University of Trento
University of Brescia
University of Padova
University of Trieste
University of Udine
University IUAV of Venezia

Giovanni Guidi (Ph. D. Student)

DISPLACEMENT CAPACITY OF LOAD-BEARING MASONRY AS A BASIS FOR SEISMIC DESIGN

Prof. Claudio Modena (Tutor)
Ass. Prof. Francesca da Porto (Co -Tutor)

2010 / 03

UNIVERSITY OF TRENTO
Engineering of Civil and Mechanical Structural Systems – XXIII Cycle

Davide Bigoni (Ph. D. Head's)

Final Examination 07 / 04 / 2011

Board of Examiners

Prof. Maurizio Piazza	(Università degli Studi di Trento)
Prof. Francesco Marotti de Sciarra	(Università di Napoli, Federico II)
Prof. Joan Ramon Casas	(Universitat Politecnica de Catalunya)

SUMMARY

The masonry still one of the widespread construction system for low-rise residential buildings even for countries prone to seismic risk. Seismic design methods yet in use are based on idea that controlling forces is better way to control earthquake induced damages. In recent decades, however, was highlighted as the differences in strength between two levels of damage is low, and therefore as the damage is better correlated to the displacement. Also, in recent years, has arose a widespread expectation for being able to control the damage based on the probability of occurrence of an earthquake or being able to base the design on different performance levels ("performance-based design").

In this context, the design of masonry buildings needs to develop these design methods. The results of experimental tests performed at the University of Padua in the recent years on different masonry systems both reinforced and unreinforced with different horizontal and vertical joints typologies, which were aimed to characterization under combined in-plane vertical and horizontal cyclic loading, were used to make different strategies of finite element modeling that reproduce and extend the experimental results using parametric analyses. These analyses allow a comparison and a validation of an analytical model which was then developed. This model is able to reproduce the envelope curves of the cyclic shear-compression tests and it is able to interpret the performances of panels linking them with limit states resulting from integration of cross-section equilibrium equations. Finally, it was applied a model able to reproduce the hysteretic behavior of masonry and were carried out dynamic analyses using the input data derived from the envelope curves. The data thus collected can be used as database and as input for displacement-based design methods.

Tutor
Prof. Claudio Modena

Co-Tutor
Ass. Prof. Francesca da Porto

Ph. D. Head’s
Prof. Davide Bigoni

SOMMARIO

La muratura rimane uno dei sistemi costruttivi più diffusi per edifici di modesta elevazione anche nei paesi inclini al rischio sismico. I metodi di progettazione anti-sismica finora in uso, sono basati sul concetto che il controllo delle forze agenti su una struttura sia il miglior approccio per controllare il danno indotto da un terremoto. Nei decenni scorsi è stato tuttavia evidenziato come la differenza in termini di forze fra due livelli di danno sia minima e come dunque il danno sia meglio correlato allo spostamento. Inoltre, negli ultimi anni, si è venuta a creare una diffusa aspettativa di poter riuscire a controllare il danno in funzione della probabilità di accadimento di un terremoto; ovvero riuscire a basare la progettazione su diversi livelli prestazionali (“performance-based design”).

In questo contesto la progettazione di edifici in muratura, necessita uno sviluppo di tali sistemi di progettazione. Usando i risultati di test sperimentali eseguiti all’Università di Padova che miravano alla caratterizzazione sotto combinazioni di carichi verticali e orizzontali ciclici agenti nel piano, su diversi sistemi di muratura sia non armata che semplice con diverse tipologie di giunto orizzontale e verticale, si sono messe a punto diverse strategie di modellazione agli elementi finiti che riproducono ed estendono i risultati sperimentali mediante analisi parametriche. Queste analisi permettono un confronto e la validazione di un modello analitico che è stato successivamente messo a punto il quale è in grado di riprodurre le curve di inviluppo delle prove a taglio-compressione e capace di interpretare le performance dei pannelli relazionandole direttamente a stati limite derivanti dall’analisi della sezione. Infine si è applicato un modello in grado di riprodurre il comportamento isteretico della muratura e si sono svolte analisi dinamiche utilizzando in input le informazioni derivate dalle curve di inviluppo trovate. I dati così ricavati possono essere utilizzati come database e come indicazione per una progettazione rivolta agli spostamenti.

DEDICATION

Ai miei genitori
Antonio e Flora
con infinita riconoscenza

ACKNOWLEDGEMENTS

First of all, I would like to acknowledge Prof. Claudio Modena, who made possible these years of doctoral studies.

The research described in the present thesis profits also from the previous work, the experience and knowledge of Ass. Prof. Francesca da Porto, Ph.D. Enrico Garbin and Ph.D. Flavio Mosele. I gratefully thank the former because she was always present in the key moments with her secure guide, the second for his invaluable help and his patience to share his deep and wide knowledge and the latter for his capacity to teach me about masonry issues with his illuminating hints.

Thanks also to Luca Nicolini, for the many interesting discussions and for his precious support in the completion of the thesis, and Massimo dalla Benetta for the support in my little parenthesis on experimental tests.

I cannot but express my sincere and deep gratitude to all my colleagues of research group for their help throughout all the phases of the research and because in many cases they were friends and not only colleagues.

In particular, my office colleagues Giulia Bettiol and Bruno Quelhas da Silva, who always endured and supported me during these years.

Thanks also to all my friends who gave me a lot of good moments to remember in these years that I'll hold always with me.

A special thought goes to my friend Enrico: I wish you were here.

I want to say a particular thanks to all my family for his support, above all to my parents Antonio and Flora and my brother Alessandro.

A last, deep and felt, thanks goes to My Mara.

CONTENTS

1. INTRODUCTION 27
1.1. Background 27
1.2. Aim and Methods 30
1.3. Thesis Organization 31

2. LITERATURE REVIEW 33
2.1. Introduction 33
2.2. Structural Behavior of Masonry Wall under Seismic Action 33
2.2.1. Unreinforced Masonry 38
2.2.2. Reinforced Masonry 42
2.3. In-Plane Modeling of Masonry Walls 50
2.3.1. Finite Element Modeling Approaches 50
2.3.2. Other Modeling Approaches 55

3. EXPERIMENTAL DATA AND RESULTS 61
3.1. Introduction 61
3.2. Unreinforced Masonry Experimental Works and Results 62
3.2.1. Basic material characterization 63
3.2.2. Standard Tests 65
3.2.3. In-plane Cyclic Tests 68
3.3. Reinforced Masonry Experimental Works and Results 73
3.3.1. Basic material characterization 74
3.3.2. Standard Tests 76
3.3.3. In-plane Cyclic Tests 78

4. FINITE ELEMENT MODELS 85
4.1. Introduction 85
4.2. Unreinforced Masonry Walls 85
4.2.1. Different Modeling Approaches Presentation 85
4.2.2. Standard Tests and In-plane Cyclic Envelopes Modeling 91
4.2.3. Parametrical Extension of Experimental Tests 100
4.3. Reinforced Masonry Walls 104
4.3.1. Modeling Approach 104

4.3.2. Uniaxial Compression and In-plane Cyclic Envelopes Modeling 106
4.3.3. Parametrical Extension of Experimental Tests 114
4.4. Analysis of results and Conclusions 121
4.4.1. Unreinforced Masonry Walls 121
4.4.2. Reinforced Masonry Walls 123
4.4.3. Summary and conclusions 127

5. ANALITICAL MODEL 129
5.1. Introduction 129
5.2. Model Hypothesis and its Capabilities 129
5.3. Model Building and Input Required 132
5.3.1. Moment-Curvature Function 132
5.3.2. Flexural Displacement Contribution 134
5.3.3. Shear Displacement Contribution to Flexural Behavior 138
5.3.4. Shear Strength and Displacement Limits 139
5.4. Analyses of Unreinforced Masonry Walls 143
5.4.1. Experimental Tests Reproductions 143
5.4.2. Parametrical Extension of Experimental Tests 150
5.5. Analyses of Reinforced Masonry Walls 159
5.5.1. Experimental Tests Reproductions 159
5.5.2. Parametrical Extension of Experimental Tests 165
5.6. Analysis of Results and Conclusions 173
5.6.1. Unreinforced Masonry Walls 176
5.6.2. Reinforced Masonry Walls 181
5.6.3. Summary and conclusions 188

6. DYNAMIC ANALYSES 191
6.1. Introduction 191
6.2. A Hysteretic Model for Masonry Walls 191
6.2.1. Experimental Cyclic Shear-Compression Tests Modeling 191
6.2.2. Arrangement of Hysteretic Model for Random Seismic Input 195
6.2.3. Seismic Input used in the analyses 197
6.3. Analysis of Results and Conclusion 199
6.3.1. Application for Reinforced Masonry System 199
6.3.2. Application for Unreinforced Masonry System 202

7. DISPLACEMENT CONSIDERATIONS IN SEISMIC DESIGN OF MASONRY FOR SDOF STRUCTURES 207
7.1. Introduction and Performance-based Design Considerations 207
7.2. Drift Limit Proposal 209

7.2.1. Further Parametrical Investigation for Unreinforced Masonry 209
7.2.2. Some Drift Limit State Design Proposals for URM 213
7.2.3. Error Estimation for Drift Formulae Proposed..218
7.3. Equivalent Viscous Damping...224
7.3.1. A Procedure to Find Hysteretic Damping of the Equivalent Elastic Substitute Structure 224
7.3.2. Discussion of Results on Experimental Walls..226
7.3.3. Extension of Results Using Analytical Model Envelopes........................232
7.4. Conclusions 233
7.4.1. Drift Limit 233
7.4.2. Equivalent Damping 234

8. CONCLUSIONS 235
8.1. Introduction...235
8.2. About Reliability of Modeling Approaches..235
8.2.1. FEM Models 235
8.2.2. Analytical Models 236
8.3. About Results of Analyses Carried Out..237
8.3.1. Unreinforced Masonry systems...237
8.3.2. Reinforced Masonry Systems 238
8.4. About Feasibility of Displacement-Based Design for Masonry 239
8.4.1. Drift limits...239
8.4.2. Damping..239
8.5. Future Work and Developments 240

9. BIBLIOGRAPHY...241

LIST OF FIGURES

Fig. 2.1. Transferring of lateral loads (wind load) from out-of-plane walls, through the rigid slab to the shear walls (from Hamid 2009). 34
Fig. 2.2. Response of simple masonry building to horizontal actions: building with deformable floors without ties (left), building with deformable floors and tied walls (middle) and building with rigid floors and tie-beams (right) (from Macchi and Magenes, 2002). 34
Fig. 2.3. Cantilever walls linked by flexible wall slabs (left), coupled shear walls with weak piers (middle) and coupled shear walls with weak spandrels (right) (from Tomaževič, 1999). 34
Fig. 2.4. Typical shear cracks in window piers of a brick-masonry building, Budva, Montenegro, 1979 (from Tomaževič, 1999). 35
Fig. 2.5. Reinforcement of the spandrel between two overlying openings (left) and reinforcement of window pier (right); 1. tie-beams, 2. reinforcement of threshold, 3. vertical reinforcement, 4. lintel reinforcement (from Giuffrè, 1980). 36
Fig. 2.6. Seismic response of masonry building, in which tie-beams, ties and rigid floors inhibit out-of-plane flexural failures (from Macchi and Magenes 2002). 36
Fig. 2.7. One-family house in San Gregorio nelle Alpi (BL, Italy) (Mosele, 2009). 37
Fig. 2.8. Residential complex in Colle Aperto (MN, Italy) (Mosele, 2009). 37
Fig. 2.9. Two-family house in Peron di Sedico (BL, Italy) (Mosele, 2009). 37
Fig. 2.10. Eight row houses in Alberi di Vigatto (PR, Italy) (Mosele, 2009). 37
Fig. 2.11. Experimental failure criteria for brick masonry walls under biaxial compression (left) and failure modes (right) for brick masonry walls under different uniaxial and biaxial stress state (after Page, 1982). 38
Fig. 2.12. Failure mechanisms of a wall portion subjected to vertical and horizontal actions (Andreaus, 1991). 39
Fig. 2.13. Main modes of a masonry pier (Tassios, 1988). 40
Fig. 2.14. Ductility vs Masonry shear resisting mechanism relationships. Maximum ductility (left) and ductility at maximum shear strength (right) (Mosele, 2009). 41
Fig. 2.15. Flexural failure mechanism: opening of the first flexural crack (left, from Macchi and Magenes, 2002) and activated vertical reinforcement (right, from Paulay and Priestley, 2009). 42
Fig. 2.16. Equilibrium of sectional forces at flexural failure of a reinforced masonry wall (from Tomaževič, 1999). 43

Fig. 2.17. Arch-beam (left) and Truss (right) mechanism of reinforced masonry wall failing in 44
Fig. 2.18. Shear failure with diagonal shear crack (left), step shape crack or crack passing through mortar joints and units (right) (from Macchi and Magenes, 2002). 44
Fig. 2.19. Mechanism of action of vertical (left) and horizontal (right) reinforcement of masonry wall failing in shear (from Tomaževič, 1999). 46
Fig. 2.20. Dowel mechanism of vertical reinforcement at shear failure of a reinforced masonry wall (Tomaževič, 1999). 46
Fig. 2.21. Sliding shear failure mechanism (left, from Macchi and Magenes, 2002) and role of reinforcement (right, from Paulay and Priestley, 1992). 49
Fig. 2.22. Different modeling strategies for masonry structures: (a) real masonry specimen, (b) detailed micro-modeling, (c) simplified micro-modeling, (d) macro modeling (Lourenço, 1996). 51
Fig. 2.23. Limit failure surfaces for interface model (Lourenço, 1996). 51
Fig. 2.24. Local failure mechanisms for masonry (Lourenço, 1996a). 52
Fig. 2.25. An example of simplified micro modeling approach for brick masonry (Lourenço, 1996a). 53
Fig. 2.26. Total Strain Rotating Crack isotropic damage model. Stress strain relation in tension (left) and in compression (right) (from De Witte, 2005). 54
Fig. 2.27. Orthotropic plasticity Rankine-Hill failure criteria (Lourenço, 1997). 54
Fig. 2.28. POR Method. Construction of storey resistance envelope on the basis of bi-linear resistance envelopes of structural walls. (Tomaževič, 1999). 56
Fig. 2.29. SAM Method: (a) equivalent frame model; (b) bi-linear relation used for masonry piers (Cattari, 2007). 56
Fig. 2.30. Equilibrium configurations of the masonry panel under compression and shear (Benedetti & Steli, 2008). 57
Fig. 2.31. Equilibrium configurations of the FRP reinforced panel under compression and shear (Benedetti & Steli, 2008). 57
Fig. 2.32. Fiber element with nonlinear shear deformations: (a) fiber strain field; (b) concrete fiber strains; (c) microplanes; and (d) tributary transverse steel reinforcement (Jiang & Kurama, 2010). 58
Fig. 2.33. Bending-Shear interaction after Priestley et al.1994: failures mode (Cosenza et al., 2010). 59
Fig. 3.1. The three masonry unit types respectively: TM TG and Po (above) and construction of a specimen for Thin-layer Masonry (below) 62
Fig. 3.2. Test of sliding along a mortar joint: shear-compression stresses diagrams for specimens failed along the joint. (da Porto et al., 2005) 64

Fig. 3.3. Typical load displacement diagrams under uniaxial compression. Masonry made with thin layer joint. Vertical measured displacements are negative (left), horizontal displacements are positive (right). 66
Fig. 3.4. Typical crack pattern under uniaxial compression. Masonry made with thin layer joint. 66
Fig. 3.5. Typical load displacement diagrams under diagonal compression. TG masonry. Vertical measured displacements are negative (left), horizontal displacements are positive (right). 67
Fig. 3.6. Typical crack pattern under diagonal compression. TG Masonry. 68
Fig. 3.7. In-plane cyclic shear-compression: (a) test set-up; (b) instrumentation scheme. 69
Fig. 3.8. Lateral load-displacement diagrams for specimens TM (left), TG (centre) and Po (right) tested under 27% ratio of applied vertical load to maximum compressive strength 69
Fig. 3.9.Crack pattern after shear-compression test. (TM 27% specimen) 70
Fig. 3.10. Shear-compression envelope curves. 70
Fig. 3.11. Details of (a) horizontally perforated unit (b) vertically perforated unit. 73
Fig. 3.12. (a) Reinforced masonry system and (b) construction phases. 73
Fig. 3.13. Specimens for compression tests: confining columns (left); plain masonry (center); complete reinforced masonry system (right) 77
Fig. 3.14. Specimens and scheme of instruments for shear compression tests: (a) plain masonry; (b) squat and (c) slender reinforced masonry walls. 79
Fig. 3.15. Shear compression test set-up (above). Horizontal displacement history (below). 80
Fig. 3.16. Crack patterns at ultimate displacement in TRHS (a), TRSa (b) and TRSb (c) under compressive stresses of 0.6 N/mm^2. 81
Fig. 3.17. Load displacement diagrams of (a) TRHS 0.6, (b) TRSa 0.6 and (c) TRSb 0.6. 81
Fig. 3.18. (a) Buckling of vertical bars in TRSa 0.4; (b) tension failure of vertical bars in SRSb 0.4; (c) transverse deformation of truss at end of test in TRHS 0.6. 82
Fig. 3.19. Limit states envelop curves of masonry specimens. 82
Fig. 3.20. Ratio of dissipated/input energy vs normalized displacement. Specimens under (a) 0.4N/mm^2 and (b) 0.6N/mm^2. 84
Fig. 3.21. Viscous damping coefficient vs normalized displacement. Specimens under (a) 0.4N/mm^2 and (b) 0.6N/mm^2. 84
Fig. 4.1. Ratio of dissipated/input energy vs normalized displacement. Scheme of iterative method of Newton-Raphson (a) convergence criterion adopted (b) (De Witte & Kikstra, 2005). 90

Fig. 4.2. Uniaxial compression: experimental and numerical load displacement diagrams. 92
Fig. 4.3. Uniaxial compression: interface model with orthotropic units. Principal tensile stresses at 50% of TM ultimate load: (a) TM, (b) TG; (c) Po. 93
Fig. 4.4. Diagonal compression: experimental and numerical load displacement diagrams. 94
Fig. 4.5. Diagonal compression: interface model with orthotropic units. Principal tensile stresses at ultimate load: (a) TM, (b) TG; (c) Po. 95
Fig. 4.6. Shear-compression. Interface model with isotropic units. Principal compression stress at maximum strength of walls: TG 27% (above) and Po 27% (below) (legend is in N/mm^2). 97
Fig. 4.7. Shear-compression, TM with vertical load of 27%: experimental crack pattern (a) and numerical principal compression stress at ultimate load (b) of compressive strength. 98
Fig. 4.8. Shear-compression envelope curves: experimental and numerical load drift-diagrams: TM with vertical load of 22% (above) and 27% (below) of compressive strength. 98
Fig. 4.9. Shear-compression envelope curves: experimental and numerical load drift-diagrams: TG with vertical load of 22% (above) and 27% (below) of compressive strength. 99
Fig. 4.10. Shear-compression envelope curves: experimental and numerical load drift-diagrams: Po with vertical load of 22% (above) and 27% (below) of compressive strength. 100
Fig. 4.11. Parametric shear-compression curves: experimental and numerical load drift-diagrams: TM with vertical load of 22% (above) and 27% (below) of compressive strength. 102
Fig. 4.12. Parametric shear-compression curves: experimental and numerical load drift-diagrams: TG with vertical load of 22% (above) and 27% (below) of compressive strength. 103
Fig. 4.13. Parametric shear-compression curves: experimental and numerical load drift-diagrams: Po with vertical load of 22% (above) and 27% (below) of compressive strength. 104
Fig. 4.14. Uniaxial compression test. Stress-strains diagrams (grey: experimental, red: numerical). 107
Fig. 4.15. Uniaxial compression test. Principal compression stresses. 108
Fig. 4.16. Axial strains at 10, 40 and 60% of maximum load (model) 109
Fig. 4.17. Scheme of shear wall finite element model. 110

Fig. 4.18. Shear-compression envelope curves. Experimental (blue) and numerical (red) load-displacement diagrams for slender walls: with vertical load of 0.4 N/mm^2 (above) and 0.6 N/mm^2 (below). 111
Fig. 4.19. Shear-compression envelope curves. Experimental (blue) and numerical (red) load-displacement diagrams for squat walls: with vertical load of 0.4 N/mm^2 (above) and 0.6 N/mm^2 (below). 112
Fig. 4.20. Crack patterns using maximum principal strains at ultimate state. 113
Fig. 4.21. Crack patterns using maximum principal strains at ultimate state. 114
Fig. 4.22. Variation of vertical load. Load – Drift curves. 116
Fig. 4.23. Variation of slenderness ratio. Load – Drift curves. 118
Fig. 4.24. Variation of vertical reinforcement ratio. Load – Drift curves. 120
Fig. 4.25. Results of parametric analyses: maximum load versus maximum drift diagrams under same vertical load (red lines) and under same ratio of vertical load to compressive strength (blue lines). 122
Fig. 4.26. Results of parametric analyses. Variation of vertical stress. 124
Fig. 4.27. Results of parametric analyses. Variation of slenderness ratio. 125
Fig. 4.28. Results of parametric analyses. Variation of vertical reinf. ratio. 126
Fig. 5.1. Masonry stress-strain relation. 131
Fig. 5.2. Moment-Curvature relation. An example of typical form. 136
Fig. 5.3. Post-peak behavior of model. 137
Fig. 5.4. Curvature along height of wall. An example of typical form. 137
Fig. 5.5. Displacement profiles along height of wall. 139
Fig. 5.6. Variation of b coefficient with base shear force. 140
Fig. 5.7. Variation of shear strength with base shear force (green line). Blue line is the masonry shear strength contribution V_m. Red line is the total shear strength V_r. (TRSa masonry with σ_0=0.6 N/mm^2, graph in kN) 141
Fig. 5.8. Post peak behavior of model in case of diagonal shear failure. Blue line: flexure capacity curve. Red line: diagonal shear post-peak curve. 142
Fig. 5.9. Po masonry. Model versus Experimental load-displacement capacity curves. 145
Fig. 5.10. TG masonry. Model versus Experimental load-displacement capacity curves. 145
Fig. 5.11. TM masonry. Model versus Experimental load-displacement capacity curves. 147
Fig. 5.12. Po masonry. Mean shear stress versus drift at different limit states of Model. 148
Fig. 5.13. TG masonry. Mean shear stress versus drift at different limit states of Model. 148

Fig. 5.14. TM masonry. Mean shear stress versus drift at different limit states of Model. 148
Fig. 5.15. Po masonry. Mean shear stress versus ductility at different limit states of Model. 149
Fig. 5.16. TG masonry. Mean shear stress versus ductility at different limit states of Model. 149
Fig. 5.17. TM masonry. Mean shear stress versus ductility at different limit states of Model. 149
Fig. 5.18. Po-17% masonry. Parametrical analyses with block strength variation. Horizontal force versus displacement. Red/yellow constant ratio, green/blue constant load combinations. 153
Fig. 5.19. Po-22% masonry. Parametrical analyses with block strength variation. Horizontal force versus displacement. Red/yellow constant ratio, green/blue constant load combinations. 153
Fig. 5.20. TG-17% masonry. Parametrical analyses with block strength variation. Horizontal force versus displacement. Red/yellow constant ratio, green/blue constant load combinations. 154
Fig. 5.21. TG-22% masonry. Parametrical analyses with block strength variation. Horizontal force versus displacement. Red/yellow constant ratio, green/blue constant load combinations. 154
Fig. 5.22. TM-17% masonry. Parametrical analyses with block strength variation. Horizontal force versus displacement. Red/yellow constant ratio, green/blue constant load combinations. 155
Fig. 5.23. TM-22% masonry. Parametrical analyses with block strength variation. Horizontal force versus displacement. Red/yellow constant ratio, green/blue constant load combinations. 155
Fig. 5.24. Po masonry. Parametrical analyses with slenderness variation. Horizontal force versus displacement. Red/yellow experimental, green/blue squat, black/grey slender walls. 158
Fig. 5.25. TG masonry. Parametrical analyses with slenderness variation. Horizontal force versus displacement. Red/yellow experimental, green/blue squat, black/grey slender walls. 158
Fig. 5.26. TM masonry. Parametrical analyses with slenderness variation. Horizontal force versus displacement. Red/yellow experimental, green/blue squat, black/grey slender walls. 159
Fig. 5.27. Reinforced masonry H/L=1.09 σ_0=0.4 N/mm^2. Model versus Experimental load-displacement capacity curves. 162
Fig. 5.28. Reinforced masonry H/L=1.09 σ_0=0.6 N/mm^2. Model versus Experimental load-displacement capacity curves. 162

Fig. 5.29. Reinforced masonry H/L=1.63 σ_0=0.4 N/mm^2. Model versus Experimental load-displacement capacity curves. 164
Fig. 5.30. Reinforced masonry H/L=1.63 σ_0=0.6 N/mm^2. Model versus Experimental load-displacement capacity curves. 164
Fig. 5.31. Vertical load variation from 0.2N/mm^2 to 3.8N/mm^2 (yellow and blue). H/L=1.63 vertical reinforcement ratio 0.134%. Model load-displacement capacity curves. 166
Fig. 5.32. Vertical load variation from 0.2N/mm^2 to 3.8N/mm^2 (red and green). H/L=1.63 vertical reinforcement ratio 0.179%. Model load-displacement capacity curves. 166
Fig. 5.33. Vertical load variation from 0.2N/mm^2 to 3.8N/mm^2 (yellow and blue). H/L=1.09 vertical reinforcement ratio 0.089%. Model load-displacement capacity curves. 168
Fig. 5.34. Vertical load variation from 0.2N/mm^2 to 3.8N/mm^2 (red and green). H/L=1.09 vertical reinforcement ratio 0.179%. Model load-displacement capacity curves. 168
Fig. 5.35. Slenderness ratio variation from 0.652 to 2.197. Vertical load 0.4N/mm^2, vertical reinforcement 0.179% (yellow) or 1Φ16 (blue). Model load-displacement capacity curves. 169
Fig. 5.36. Slenderness ratio variation from 0.652 to 2.197. Vertical load 0.6N/mm^2, vertical reinforcement 0.179% (red) or 1Φ16 (green). Model load-displacement capacity curves. 169
Fig. 5.37. Vertical reinforcement variation from 0% to 0.28%. Vertical load 0.4N/mm^2. H/L=1.63 yellow/blue, H/L=1.09 red/green. Model load-displacement capacity curves. 171
Fig. 5.38. Vertical reinforcement variation from 0% to 0.28%. Vertical load 0.6 N/mm^2. H/L=1.63 yellow/blue, H/L=1.09 red/green. Model load-displacement capacity curves. 171
Fig. 5.39. Horizontal reinforcement variation from 0 to all joint. Slenderness ratio H/L = 1.63. Model load-displacement capacity curves. 172
Fig. 5.40. Horizontal reinforcement variation from 0 to all joint. Slenderness ratio H/L = 1.09. Model load-displacement capacity curves. 172
Fig. 5.41. Displacement profiles along height of wall at masonry first non-linearity point. Red line: total displacement profile, blue line shear displacement contribution and green flexure displacement contribution. (TG masonry with σ_0=1.24 N/mm^2, H [mm] and Δ [mm]) 174
Fig. 5.42. Displacement profiles along height of wall at masonry yielding point in compression. Red line: total displacement profile, blue line shear displacement

contribution and green flexure displacement contribution. (TG masonry with σ_0=1.24 N/mm^2, H [mm] and Δ [mm]) 174
Fig. 5.43. Displacement profiles along height of wall at max strength. Red line: total displacement profile at max strength, blue line shear displacement contribution and green flexure displacement contribution. 175
Fig. 5.44. Displacement profiles along height of wall at maximum displacement. Red line total displacement profile, blue line shear displacement contribution and green flexure displacement contribution. 175
Fig. 5.45. Unreinforced masonry. Critical drift versus Vertical stress (above). Drift at maximum strength versus Vertical stress (middle). Drift at maximum displacement versus Vertical stress (below). 177
Fig. 5.46. Unreinforced masonry. Critical drift versus Masonry compressive strength (above). Drift at maximum strength versus Masonry compressive strength (middle). Drift at maximum displacement versus Masonry compressive strength (below). 179
Fig. 5.47. Unreinforced masonry. Critical drift versus Slenderness ratio (above). Drift at maximum strength versus Slenderness ratio (middle). Drift at maximum displacement versus Slenderness ratio (below). Rhombus: flexure failure, Dots: shear failure. 180
Fig. 5.48. Reinforced masonry. Critical drift versus Vertical stress (above). Drift at maximum strength versus Vertical stress (middle). Drift at maximum displacement versus Vertical stress (below). 183
Fig. 5.49. Reinforced masonry. Critical drift versus Slenderness ratio (above). Drift at maximum strength versus Slenderness ratio (middle). Drift at maximum displacement versus Slenderness ratio (below). 184
Fig. 5.50. Reinforced masonry. Critical drift versus Vertical reinforcement ratio (above). Drift at maximum strength versus Vertical reinforcement ratio (middle). Drift at maximum displacement versus Vertical reinforcement ratio (below). 186
Fig. 5.51. Reinforced masonry. Critical drift versus Horizontal reinforcement ratio (above). Drift at maximum strength versus Horizontal reinforcement ratio (middle). Drift at maximum displacement versus Horizontal reinforcement ratio (below). 187
Fig. 6.1. Idealized envelope curve (1-2-3-4) and scheme of the hysteresis loop (A-B-C-D). 192
Fig. 6.2. Degradation of stiffness K_{D-A}. 193
Fig. 6.3. Asymmetrical cycles. 195
Fig. 6.4. Definition of point E. 196
Fig. 6.5. Re-loading conditions. 197
Fig. 6.6. Eurocode 8 recommended Type 1 spectra for ground Types A to E. 198

Fig. 6.7. Synthetic time-histories used in the analyses, generated respect soil A (above) and soil D (below). 198
Fig. 6.8. Spectrum-compatibility between the mean value 10 time histories of accelerograms and Eurocode 8 type 1 spectra for soil A and D. 199
Fig. 6.9. C_1 and C_2 coefficients for RM. 200
Fig. 6.10. Experimental hysteresis loops and loops from model. Squat (left) and slender (right) specimens; σ_0=0.4 N/mm^2 (above) and σ_0=0.6 N/mm^2 (below) vertical compression load. 200
Fig. 6.11. Ratio of dissipated/input energy: comparison between experimental and modeled values. Squat (left) and slender (right) specimens; σ_0=0.4 N/mm^2 (above) and σ_0=0.6 N/mm^2 (below) vertical compression load. 201
Fig. 6.12. Some example of model results given for different soil (above), different slenderness ratios (middle) and different PGA (below). 202
Fig. 6.13. Experimental hysteresis loops and loops from model. TM (above), TG (middle) and Po (below) specimens with vertical compression load of 0.27% of their compressive strength. 203
Fig. 6.14. C_1 and C_2 coefficients for URM. 204
Fig. 6.15. Ratio of dissipated/input energy: comparison between experimental and modeled values. TM (above), TG (middle)s Po (below) specimens under vertical compression load of 0.27% of their compressive strength. 205
Fig. 6.16. Some example of model results given for different masonry type (above), different soil (middle) and different PGA (below). 206
Fig. 7.1. DDBD method from (Priestley et al., 2007) 208
Fig. 7.2. Graphical view of different drift limit states for TG masonry. Analyses of chapter 5 (a), further analyses (b). Maximum drift (blue), drift at F_{max} (red) and critical drift (green). 211
Fig. 7.3. Graphical view of different drift limit states for TM (a), TG (b) and Po (c) masonries. Slenderness analyses of Chap. 5. Max drift (blue), drift at F_{max} (red) and critical drift (green). 212
Fig. 7.4. Graphical view of different drift limit states (black dots) for mechanical parameters variation (TG masonry). Surfaces deriving from (Eq. 7.1) to (Eq. 7.5): maximum drift (blue), drift at F_{max} (red) and critical drift (green). 215
Fig. 7.5. Graphical view of different drift limit states (black dots) for slenderness variation (TM masonry). Surfaces deriving from (Eq. 7.1) to (Eq. 7.5): maximum drift (blue), drift at F_{max} (red) and critical drift (green). 216
Fig. 7.6. Graphical view of different drift limit states (black dots) for slenderness variation (TG masonry). Surfaces deriving from (Eq. 7.1) to (Eq. 7.5): maximum drift (blue), drift at F_{max} (red) and critical drift (green). 217

Fig. 7.7. Graphical view of different drift limit states (black dots) for slenderness variation (Po masonry). Surfaces deriving from (Eq. 7.1) to (Eq. 7.5): maximum drift (blue), drift at F_{max} (red) and critical drift (green). 218
Fig. 7.8. Mechanical parameters variation (TG masonry). Graphical view of differences between model and equations results (left) and the corresponding distribution of deviations from model results (right). At maximum drift (a), drift at F_{max} (b) and critical drift (c). 220
Fig. 7.9. Slenderness variation (TM masonry). Graphical view of differences between model and equations results (left) and the corresponding distribution of deviations from model results (right). At maximum drift (a), drift at F_{max} (b) and critical drift (c). 221
Fig. 7.10. Slenderness variation (TG masonry). Graphical view of differences between model and equations results (left) and the corresponding distribution of deviations from model results (right). At maximum drift (a), drift at F_{max} (b) and critical drift (c). 222
Fig. 7.11. Slenderness variation (Po masonry). Graphical view of differences between model and equations results (left) and the corresponding distribution of deviations from model results (right). At maximum drift (a), drift at F_{max} (b) and critical drift (c). 223
Fig. 7.12. Equivalent Hysteretic Damping versus Drift curves. Experimental RM walls under soil type A (above) type D (below). 227
Fig. 7.13. Equivalent Hysteretic Damping versus Ductility curves. Experimental RM walls under soil type A (above) type D (below). 228
Fig. 7.14. Equivalent Hysteretic Damping versus Drift curves. Experimental URM walls under soil type A (above) type D (below). 229
Fig. 7.15. Equivalent Hysteretic Damping versus Ductility curves. Experimental URM walls under soil type A (above) type D (below). 230
Fig. 7.16. Equivalent Hysteretic Damping versus Drift curves.RM walls under soil type A (above) type D (below). Experimental (continuous lines), analytical model (dash-dot lines). 231
Fig. 7.17. Equivalent Hysteretic Damping versus Ductility curves.RM walls under soil type A (above) type D (below). Experimental (continuous lines), analytical model (dash-dot lines). 232

LIST OF TABLES

Table 2.1. Terms of equation for reinforced masonry shear strength (Mosele, 2009).47

Table 3.1. Tests carried out on small and large size specimens. (da Porto et al., 2005) 63

Table 3.2. Mechanical properties of the units. (da Porto et al., 2005) 64

Table 3.3. Properties of the mortars. (da Porto et al., 2005) 64

Table 3.4. Uniaxial compression tests results. (da Porto et al., 2005) 65

Table 3.5. Diagonal compression tests results. (da Porto et al., 2005) 67

Table 3.6. Experimental. Lateral load, displacement and rotation angle at flexural cracking, shear cracking, maximum resistance and ultimate limit states. The values are average obtained at positive and negative displacement amplitudes (da Porto, 2005). 71

Table 3.7. Cumulative input and dissipated energy at shear cracking, maximum resistance and at collapse; values of coefficient of equivalent viscous damping at the same limit states. 72

Table 3.8. Values of coefficient of equivalent viscous damping at shear cracking, maximum resistance and at collapse. 72

Table 3.9. Mechanical properties of units with horizontal and vertical holes. 75

Table 3.10. Physical and mechanical properties of fresh and hardened mortar. 75

Table 3.11. Characteristics of specimens for uniaxial compression tests. 77

Table 3.12. Results of uniaxial compression tests. 77

Table 3.13. Specimen details for shear compression tests. 78

Table 3.14. Results of shear compression tests. 83

Table 4.1. Database of values for fracture energy of masonry. 86

Table 4.2. Parameters of orthotropic continuum model. Parameters of isotropic total strain rotating crack model can be obtained from values in y-direction. 87

Table 4.3. Parameters for interface in orthotropic discrete model and in discrete model implementing isotropic total strain rotating crack constitutive law for unit.89

Table 4.4. Parameters for unit material in orthotropic discrete model. Parameters of isotropic total strain rotating crack micro-model can be obtained from values in y-direction 89

Table 4.5. Uniaxial and diagonal compression, experimental ($P_{u,e}$) and numerical ($P_{u,m}$) ultimate loads. 91

Table 4.6. Cyclic shear-compression, experimental ($H_{max,e}$) and numerical ($H_{max,m}$) maximum load and experimental ($\theta_{u,e}$) and numerical ($\theta_{u,m}$) maximum drift. 96
Table 4.7. Parametric analyses. Parameters changed from the used relations. 101
Table 4.8. Reinforced masonry FEM model parameters. 106
Table 4.9. Comparison between experimental and FEM model at maximum strength of wall and at maximum displacement for vertical compression stress of 0.4 N/mm^2. 111
Table 4.10. Comparison between experimental and FEM model at maximum strength of wall and at maximum displacement for vertical compression stress of 0.6 N/mm^2. 112
Table 4.11. Table of parametric variations carried out. Variation of vertical load applied. 115
Table 4.12. Table of parametric variations carried out. Variation of slenderness ratio. 117
Table 4.13. Table of parametric variations carried out. Variation of vertical reinf. ratio. 119
Table 5.1. Mechanical and geometrical parameters used modeling unreinforced masonry. 144
Table 5.2. Model. Lateral load, displacement and rotation angle at first masonry non-linearity, masonry compression yielding, maximum strength and maximum displacement limit states. 150
Table 5.3. Parameters used in compressive strength parametrical analyses of unreinforced masonry. 151
Table 5.4. Summary of maximum horizontal strength in case of constant load applied. 156
Table 5.5. Parameters used in slenderness parametrical analyses of unreinforced masonry. 157
Table 5.6. Masonry mechanical and geometrical parameters in reinforced masonry system. 160
Table 5.7. Reinforcement mechanical and geometrical parameters for reinforced masonry. 160
Table 5.8. Comparison between experimental and analytical model of principal limit states at vertical compression stress of 0.4 N/mm^2. 163
Table 5.9. Comparison between experimental and analytical model of principal limit states at vertical compression stress of 0.6 N/mm^2. 163
Table 6.1. Hysteretic model parameters C_1 and C_2. 194
Table 6.2. Hysteretic model parameters for reinforced masonry system. 199
Table 6.3. Hysteretic model parameters for unreinforced masonry system. 204

Table 7.1. Drift at maximum strength for TG masonry. Parametrical analyses of chapter 5. 210
Table 7.2. Drift at maximum strength for TG masonry. Parametrical analyses of chapter 5. 210
Table 7.3. Summary of R. Columns refer to analyses type, rows refer to different limit states. 224
Table 7.4. Summary of SD. Columns refer to analyses type, rows refer to different limit states. 224
Table 7.5. Summary of RSD. Columns refer to analyses type, rows refer to different limit states. 224

1. INTRODUCTION

1.1. Background

The construction of new masonry buildings is far from being marginal in many countries of the world, including Europe, even in countries prone to seismic risk, since it is still a competitive choice for low rise residential buildings from many points of view, not necessarily all related to seismic performance, but connected to the improvement of the properties of insulation of buildings and the need of making the construction process easier and faster.

Anyhow, many collapses and deaths in recent and past earthquakes are due to unsatisfactory performance of unreinforced masonry (URM) buildings. However, it must be recognized that usually they were non-engineered, low-quality old constructions. This can partially explains why there is a rather negative attitude towards the use of structural masonry for new buildings in seismic areas and very seldom structural masonry is considered as a choice for the design of new structures in seismic areas (Magenes, 2010).

In first instance, it is essential to recognize that the majority of the collapses of URM masonry buildings in recent earthquakes involves buildings which do not comply with most of the requirements that new masonry building should satisfy according to the current seismic codes (Decanini et al., 2004). On the other hand, a huge amount of buildings, executed with modern masonry construction systems and designed according to the old codes, cannot be verified with the new seismic codes, even when they proved to sustaining earthquake actions, as it comes from the on-site experience of the author (L'Aquila, Italy, April 2009) and from the review of post-earthquake damage surveys reported in literature (Latina, 1999).

The behavior of an accurate design and construction of low rise structurally designed and engineered URM buildings should be possible also for a design PGA up to 0.3 g (Magenes, 2006). For higher seismic hazards, the solutions of confined or reinforced masonry are available, whose competitiveness and effectiveness in seismic areas is however not fully recognized in some countries.

There is, hence, the need to find a compromise between the achievement of an acceptable level of structural safety and the employment of new technologies for load bearing masonry systems, developed from traditional construction systems, which involves cultural and economic considerations.

The development of new systems for constructing unreinforced masonry walls has been driven by the market towards systems that have better thermal insulation properties and allow faster and cheaper construction processes (Hendry, 2001). Because of these developments, the latest construction technologies have replaced traditional head joints, fully filled with mortar, with preformed pockets for mortar infills at the lateral face or mortarless head joints with mechanical interlocking between units. Traditional bed joints have also been replaced by thin-layer mortar joints, which are laid on edge-ground units. These systems have been developed in countries not prone to seismic risk, but have rapidly spread throughout Europe and also beyond (Tomaževič et al., 2006). However, in the concurrent development of Italian seismic design code (DM 14/01/2008, 2008), the use of contemporary masonry systems, different from those characterized by traditional head and bed joints, is not yet regulated, when it is allowed by European seismic code (EN 1998-1: 2004. Eurocode 8, 2004). Therefore, the National and European seismic codes allow the use of reinforced masonry, but despite the seismic capabilities of these construction systems, they find very seldom diffusion in the market.

In last few years, the possibility to being able to control the damage based on the probability of occurrence of an earthquake, or to base the design on different performance levels, has arose. Limit states design approach, which has been introduced into codes of practice and is currently being adopted by the European and National Codes (DM 14/01/2008, 2008; EN 1996-1: 2005. Eurocode 6, 2005; EN 1998-1: 2004. Eurocode 8, 2004); requires the knowledge, not only of the lateral load bearing capacity, but also of the failure modes and deformability properties of masonry walls as a necessary needs for the study of the seismic response of entire masonry structures. As on example, non-linear static methods of analysis that have been developed rely on the knowledge of such characteristics.

Modern codes in seismic design or assessment of buildings, including EC8 and the Italian NTC, consider four main methods of structural analysis: linear static (or simplified modal), linear dynamic (typically multimodal with response spectrum), nonlinear static (also named “pushover”), nonlinear dynamic.

Structural analyses of masonry were mainly aimed to the in-plane behavior, since the basic principles of conceptual design of low-rise structures for earthquake resistance are based on the box-type of behavior. For global analysis of the structural system linear methods and nonlinear static methods are the ones that can be used in common practice. With the comparison between linear and nonlinear analysis results can be appreciate the limits of elastic analysis when applied to ULS seismic assessment and the reason why masonry structures were the firsts for which at a code level a simplified nonlinear approach was necessary in real applications. Among others, (Magenes et al., 2006) provides examples of such comparisons under static lateral load. In the nonlinear FEM models the calculated shears in walls show dramatic differences when compared to linear elastic FEM.

At ultimate conditions, the moderate nonlinear behavior (“ductility”) of the wall piers tends to a situation where forces not according to initial elastic stiffness.

As a consequence, both EC8 and NTC in the case of linear elastic approaches use q-factor to reduce the elastic design spectrum ordinates and consider also the introduction of the Over Strength factor (OSR), which recognize also for masonry structures the ability to sustain higher base seismic shear than elastic analysis can predict. However, as pointed out by (Morandi & Magenes, 2008) there are conceptual difficulties in defining a rational approach for the evaluation of a single conservative value of the q-factor (i.e. of the OSR) for a specific masonry.

More consistent results could be achieved only favoring nonlinear procedures, even though simplified, or the combined use of linear and nonlinear methods. In this perspective, displacement based design methods could allow a more rational solution of the problem (Magenes, 2010).

In many cases, a static nonlinear analysis can provide a more realistic simulation of the building response, besides avoiding the uncertainties related to the definition of the q-factor. Despite the explicit possibility given by EC 8 to use nonlinear static procedures only little guidance on some important design parameters, is given to the designer in EN 1998-1. No reference is given regarding the deformation/drift limits that should be used in the analysis, neither other modeling criteria.

Such information is given however in Annex C of (EN 1998-3: 2005. Eurocode 8, 2005) for existing buildings and the Italian code NTC 2008 provides drift limits for in-plane response which are consistent with EN 1998-3. However, Annex C of EN 1998-3 does not provide suggestions for confined or reinforced masonry, whereas NTC 2008 suggests increasing the limits of unreinforced masonry by 50% in the case of reinforced masonry. Some of these limits should be suitably revised on the basis of the more recent available experimental information and future advances. Some of these new finding and perspectives could be read in (Costa et al., 2008; da Porto, 2005; DISWall, 2008; ESECMaSE, 2008; Tomaževič & Weiss, 2010) for the experimental data and (Ahmad et al., 2010) as regard displacement-based approach.

Experimental work may allow the development of knowledge on seismic behavior of masonry structures built with different materials or construction systems. However, this investigation method is very costly and, in practice, it can be applied to a limited number of configurations. Another way, for understanding the behavior of masonry systems, is the development of analytical and numerical analysis methods. A wider range of configurations can be simulated using these approaches, but they must be calibrated on the basis of experimental data to be considered as reliable.

Static non-linear analysis methods for masonry buildings have improved in the last decade, but it is felt that reference values for some basic design parameters should be provided by the norms, in order to make the methods applicable in practice by the designers with more consistent results. Updated information allow adopting both force-based design approaches and more rational displacement-based design approaches for masonry buildings is progressively becoming available and could be transferred into design codes, including Eurocode 8.

In this field, the research described in the present thesis, is aimed to characterization of displacement capacity to overcome some of those code limitations and to contributing to available data for the development of displacement-based design approaches for both reinforced and unreinforced masonry. Moreover a part of present work has been included in the (DISWall, 2008) research project (coordinated by University of Padova) and is included in a more general research activity on masonry structures that is being carried out at the University of Padova since the end of the Seventies. This activity includes studies on various typologies of modern masonry, both reinforced and unreinforced, investigations on the mechanical behavior and on the strengthening techniques for historic brick and stone masonry walls, studies on special investigation techniques for the diagnosis of masonry structures, research on the seismic behavior and modeling of masonry buildings, which has created a large background on which the work carried out relies.

1.2. Aim and Methods

The main aim of the present research is that of contributing to the knowledge of the behavior under in-plane cyclic loading, i.e. as in the case of seismic actions, of various masonry systems. In particular, the behavior under in-plane vertical and horizontal cyclic load was investigated on different masonry systems focusing on displacement performances.

To this aim, an extensive modeling program was carried out based on experimental tests performed at the University of Padova in the recent years on different masonry systems. These systems includes unreinforced masonry walls made with different types of joints (head joints made with mortar pockets, dry head joints with mechanical interlocking, thin-layer mortar bed joints) and new type of reinforced masonry walls, characterized by the use of both horizontal and vertical perforated units and the use of bars or prefabricated trusses for horizontal reinforcements.

Experimental results were reproduced by different Finite Element Models approaches and by analytical model develop by author.

It was extend the experimental results using parametric analyses of both FEM and analytical models. These analyses relates to principal geometrical and mechanical parameters which mainly influence the behavior of masonry walls.

The new analytical model is a formulation of a fiber element and is cast in the general framework of the mixed method. It includes effects of shear deformation, diagonal shear failure mechanism and it is able to follow response in post-peak phase. The model is able to interpret the performances of panels linking them with limit states resulting from integration of cross-section equilibrium equations. Its results were collected proposing design equations directly related to performance levels and both geometrical and mechanical properties of URM panels.

Also dynamic models were carried out, to define the dynamic properties and to evaluate the degradation process, in particular relating damping with ductility of masonry system.

1.3. Thesis Organization

The thesis is divided into 8 chapters. The problems related to the seismic behavior of reinforced masonry buildings are briefly presented in Chapter 2, and it gives a state-of-the-art about present and past research on the in-plane behavior of masonry and some details about the background of different analysis approaches used in the thesis. Chapter 3 presents the experimental program, the data and the results of the in-plane tests carried out on systems object of the research. The tests were carried out as part of other thesis, and the author took part in both test execution and data analysis.

Chapter 4 present and discuss the Finite Element Models carried out using different approaches for reinforced and unreinforced masonry systems under investigation for the evaluation of the stress state inside the masonry walls and to provide an extension experimental results.

Chapter 5 and Chapter 6 reports the results of models carried out with analytical approaches. Respectively a static model, which was developed by the author, that leads to give capacity curves and a dynamic hysteretic model, already available from literature, focused to obtain energy dissipation characteristics.

The analysis of the results oriented to displacement-based design methods is presented and discussed in Chapter 7. Obviously the last Chapter reports the conclusions of the present research.

2. LITERATURE REVIEW

2.1. Introduction

The purpose of the present section is to give a critical overview of the recent and past research works about the in-plane and behavior of masonry. Due to the unfeasibility of treating such an extensive subject in a brief and at the same time comprehensive manner, many of the quoted topics are simply mentioned, and the reader is referred to the bibliographical references, or to the following sections of the thesis, where some of the issues are discussed more in detail.

The main topics are: (1) the main issues related to the in-plane seismic behavior of masonry walls both regarding reinforced masonry and unreinforced masonry; (2) the main issues related to the in-plane modeling of masonry walls focusing on Finite Element modeling and other analytical approaches available in literature.

2.2. Structural Behavior of Masonry Wall under Seismic Action

The modern buildings are designed for earthquake resistance following the basic principles of box-type of behavior. This assumption implies the presence of rigid diaphragms, in their own plane, able to distribute the horizontal loads to the shear walls (Shing et al., 1990). As a consequence the main seismic resistance mechanism of the building is related to the in-plane behavior of the walls (shear walls), whereas the out-of-plane behavior represent a local mechanism. In fact, the walls perpendicular to the horizontal actions are supported by floors and roofs, which transfer also these horizontal loads to the shear walls (Fig. 2.1). The connections between the walls and with the floors are fundamental to guarantee the development of the box-type behavior (Fig. 2.2).

The masonry shear walls, according to the type of construction and their configuration, solid or pierced by windows and door openings, lead to various seismic behavior and failure mechanism. Three main categories of shear walls are classified (Paulay & Priestley, 2009; Tomaževič, 1999): cantilever walls linked by flexible wall slabs, coupled shear walls with weak piers and coupled shear walls with weak spandrels (Fig. 2.3).

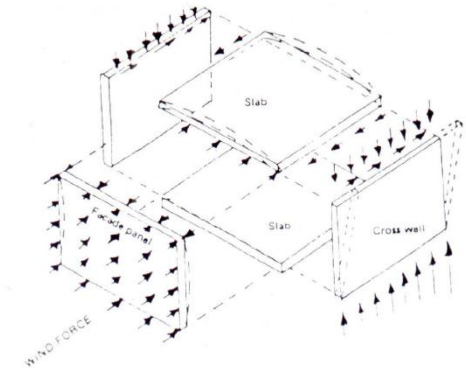

Fig. 2.1. Transferring of lateral loads (wind load) from out-of-plane walls, through the rigid slab to the shear walls (from Hamid 2009).

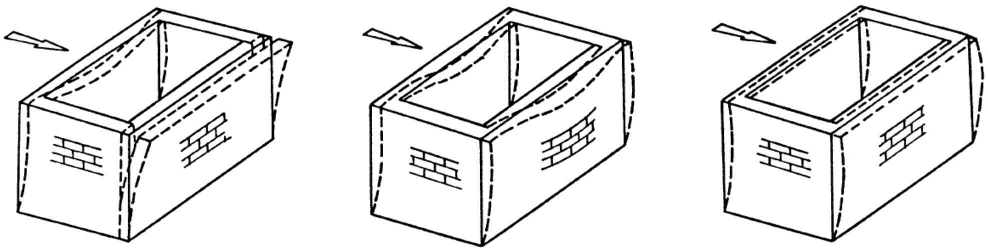

Fig. 2.2. Response of simple masonry building to horizontal actions: building with deformable floors without ties (left), building with deformable floors and tied walls (middle) and building with rigid floors and tie-beams (right) (from Macchi and Magenes, 2002).

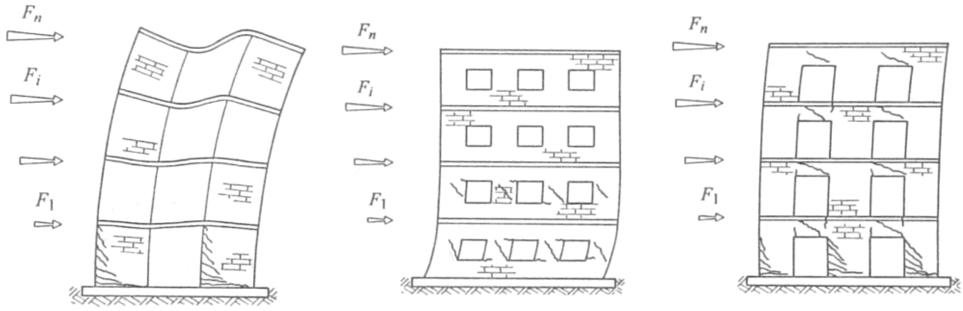

Fig. 2.3. Cantilever walls linked by flexible wall slabs (left), coupled shear walls with weak piers (middle) and coupled shear walls with weak spandrels (right) (from Tomaževič, 1999).

The former resistant model (Fig. 2.3 left) is characterized by floors rigid in their plane, but flexible in the orthogonal direction, therefore they do not transfer any moments between the shear walls. The shear walls are in this case cantilevers fixed on the bottom and free at the top of the building. The critical condition is at the base storey, where large bending moment is required. In terms of seismic response, the cantilever walls represent a suitable structural behavior, since it is dominated by flexure, and so it guarantees high ductility and energy dissipation, if carefully detailing are provided.

Usually the masonry buildings are made by shear walls (so called since they resist to the lateral shear loads with their in-plane shear capacity (Drysdale & Hamid, 2008) pierced by window and door openings, in which the spandrels connect the shear walls and transfer the horizontal loads and also bending moments. In this case two main resistant elements are identified: the spandrels, which are the portion of masonry between two overlying openings, and the piers between two next openings. Depending on the proportion of the openings, the weakest element is the piers (Fig. 2.3 middle) or the spandrels (Fig. 2.3 right). In the case of the spandrels reach the failure, they keep transferring the horizontal loads but they transfer a residual part of bending moments, so the global behavior leads towards to the structural response of cantilever walls linked by flexible wall slabs. When the piers are weaker than the spandrels, which is usually the case in traditional unreinforced masonry construction (Tomaževič, 1999), damage will first involve the piers (Fig. 2.4). The piers will fail in shear or with rocking mechanism according to the geometry, materials and vertical loads. The last failure mechanism is the more sensitive one, because the piers withstand the vertical loads and the shear failure is characterized by low energy dissipation capacity and ductility. Improvement can be provided with adequately distribute horizontal reinforcement.

Fig. 2.4. Typical shear cracks in window piers of a brick-masonry building, Budva, Montenegro, 1979 (from Tomaževič, 1999).

In the case of RM buildings, spandrels and piers can be provided with adequate vertical and horizontal reinforcement qualitatively showed in Fig. 2.5, in order to obtain predominant flexural behavior. As a result of the capacity design, the lateral resistance, the energy dissipation capacity and the ductility of the structure are increased. Moreover the hinging of the spandrels which couple the shear walls, leads to a reduction of bending moment at the base, an energy dissipation capacity distributed over the entire height of the shear walls, which allows restraining the amount of reinforcement. Therefore this mechanism is the most desirable among the three identified mechanisms (Tomaževič, 1999). In any case there are some reasons to considerate the cantilever walls system as the best, rather than coupled walls with spandrels hinging, since high ductility demand is concentrated in the coupling spandrels, and they suffer rapid strength and stiffness degradation. This leads to an uncoupling of the shear walls and results in an increase in bending moments for shear walls, which are not able to resist, if they are designed as coupled walls (Paulay & Priestley, 2009).

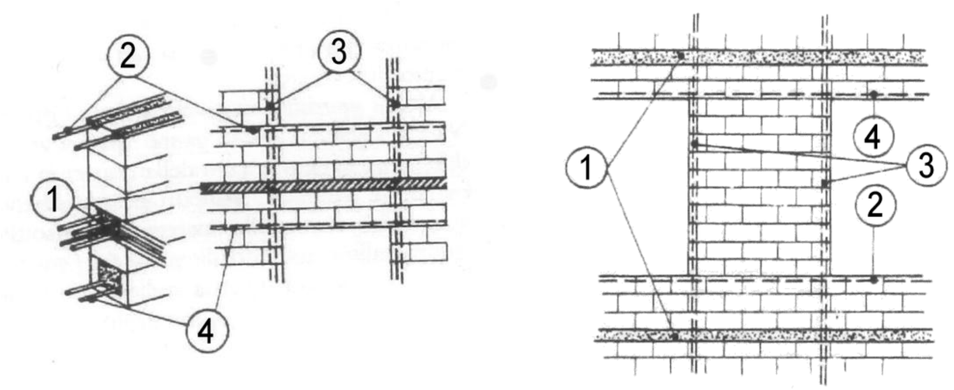

Fig. 2.5. Reinforcement of the spandrel between two overlying openings (left) and reinforcement of window pier (right); 1. tie-beams, 2. reinforcement of threshold, 3. vertical reinforcement, 4. lintel reinforcement (from Giuffrè, 1980).

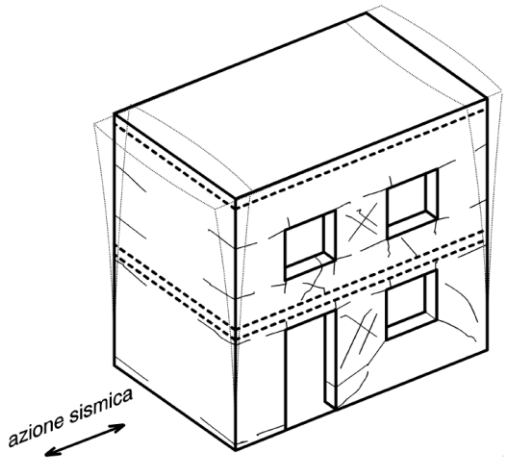

Fig. 2.6. Seismic response of masonry building, in which tie-beams, ties and rigid floors inhibit out-of-plane flexural failures (from Macchi and Magenes 2002).

In most cases load bearing masonry walls are used for residential buildings, whose configuration varies from the single occupancy house (Fig. 2.7), one or two-storey high, to the multiple-occupancy residential buildings of load-bearing masonry, which are commonly constituted by two or three-storey when they are built of unreinforced masonry, but can reach relevant height (five-storey or more) when they are built with reinforced masonry (Fig. 2.8). Intermediate types of buildings include two-storey, semi-detached two-family houses (Fig. 2.9) or attached row houses (Fig. 2.10). In these buildings, the masonry walls carry the gravity loads and they usually support concrete floor slabs and roofs, which are characterized by adequate in-plane stiffness. The inter-storey height is generally low, around 3 m.

In these structures the seismic resistance mechanism, and in general the resistance to horizontal actions, is provided by coupled shear walls (Fig. 2.6) discussed previously. Without forgetting that in certain cases, in particular for low-rise residential buildings such as single occupancy houses or two-family houses, the roof structures can be made of wooden beams and can be deformable, even in new buildings. In these cases, or in the upper storey of multi-storey (multiple-occupancy) residential buildings, wall designs can be governed by resistance to out-of-plane forces (Mosele, 2009).

Fig. 2.7. One-family house in San Gregorio nelle Alpi (BL, Italy) (Mosele, 2009).

Fig. 2.8. Residential complex in Colle Aperto (MN, Italy) (Mosele, 2009).

Fig. 2.9. Two-family house in Peron di Sedico (BL, Italy) (Mosele, 2009).

Fig. 2.10. Eight row houses in Alberi di Vigatto (PR, Italy) (Mosele, 2009).

2.2.1. Unreinforced Masonry

Some systematic studies aimed at the definition of the complete failure envelope of masonry, were developed for the entire range of combinations of ideal biaxial stress states. The first investigations were experimentally carried out with the tests on square masonry panels tested under different combination of tension and compression and different orientation of loading with respect to the head and bed joints. They allowed defining the experimental failure criteria for brick masonry (Page, 1980; Page, 1981; Page, 1983; Samarasinghe & Hendry, 1980), for concrete block masonry (Hamid & Drysdale, 1980; Hamid & Drysdale, 1981; Hegermeir et al., 1978), for masonry made of perforated clay blocks (Ganz & Thürlimann, 1984). Fig. 2.11 left shows the failure envelope found for brick masonry by (Page, 1982), where the anisotropic behavior of masonry is evidenced by the different shapes obtained varying the loading angle and by the corresponding observed failure modes (Fig. 2.11 right).

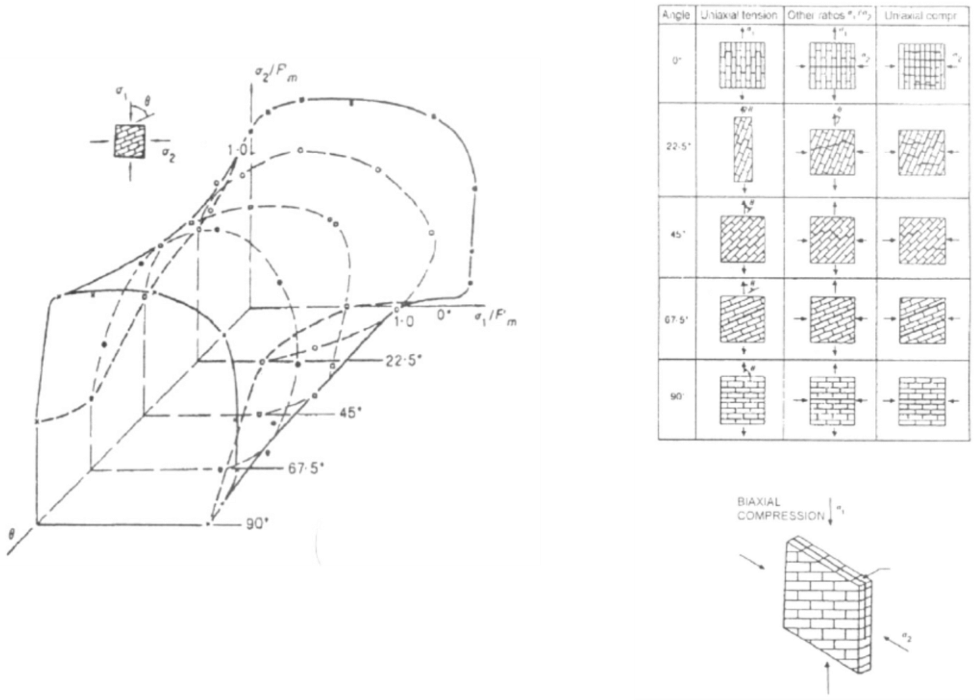

Fig. 2.11. Experimental failure criteria for brick masonry walls under biaxial compression (left) and failure modes (right) for brick masonry walls under different uniaxial and biaxial stress state (after Page, 1982).

A typical case of biaxial stress state is masonry pier under combined vertical and horizontal load (Fig. 2.12). The homogeneous stress states found e.g. by (Page,

1982) interest only a part of shear walls which are rather subjected to heterogeneous stress states. Considering that the appearance of one failure mechanism depends on parameters such as the geometry of the masonry walls and the ratio of vertical to horizontal load (Tomaževič, 1999), that failure characterizes the behavior of a masonry wall in a structure, rather than the simple material behavior.

First appearance of failure usually involves the center of shear wall or stretched corner (A and B zones in Fig. 2.12) or in the more compressed corner of pier (C zone in Fig. 2.12). It was experimentally verified from above mentioned researches that the main failure modes relevant for unreinforced masonry walls are (Fig. 2.13):

- flexural failure;
- shear failure (typically with diagonal cracks and combined with flexure);
- sliding on bed joints.

The first mechanism is characterized by the early appearance of crack in joint under tension stress state (A zone in Fig. 2.12), followed by a second limit state characterized by crushing of compressed toe of pier (C zone in Fig. 2.12).

Shear failure, on contrary, can involve different failure mechanisms, in particular: failure can involve the horizontal and vertical joints causing a stepped-crack; or failure can involve also the blocks (or bricks) giving a diagonal cracking which pass throughout masonry units and joints. The third shear failure mechanism is the sliding along bed joints with an almost horizontal crack progress. This mechanism is less frequent and can be mainly imputed to poor quality of mortar and/or low vertical stress. In general this failure mechanism do not appear for new URM made with perforated clay units (da Porto, 2005; Mosele, 2009).

Another frictional mechanism can be seen after the stepped-cracks were appeared with a sliding along the horizontal parts of crack.

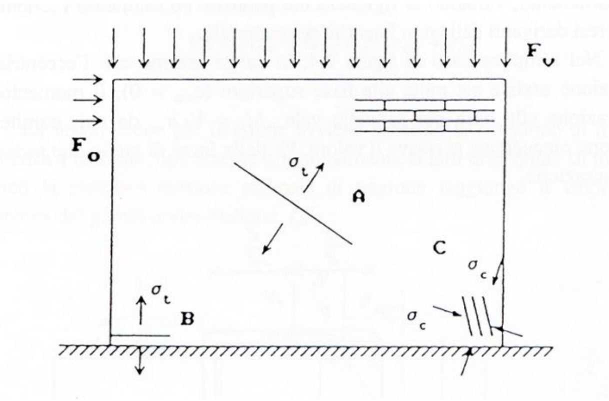

Fig. 2.12. Failure mechanisms of a wall portion subjected to vertical and horizontal actions (Andreaus, 1991).

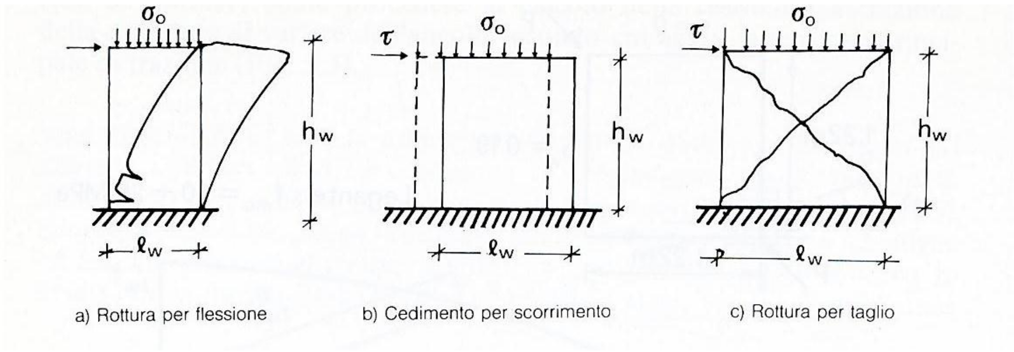

a) Rottura per flessione b) Cedimento per scorrimento c) Rottura per taglio

Fig. 2.13. Main modes of a masonry pier (Tassios, 1988).

The valuation of shear strength of plain masonry under a biaxial stress state like (V_m) is based on a Mohr-Coulomb formulation in the European, Italian and British codes and in (Tomaževič, 1999). Therefore this term implicitly take into account the level of axial load acting on the wall. Furthermore, (Tomaževič & Lutman, 1988) proposes to use, in alternative, the (Turnšek & Čačovič, 1971), i.e., to define the shear strength of URM wall on the basis of masonry tensile strength.

V_m is based on the shear stress acting on the masonry cross-section, evaluated on the basis of the aspect ratio of the wall, for the Australian standard. ACI 530 evaluates V_m as a function of square root of the masonry compressive strength f'_m and taking into account the aspect ratio M/V_l, which implicitly recalls the tensile strength of masonry. NZS 4230 takes into account, in the URM shear strength contribution, the dowel-action of vertical bars, the aspect ratio and the degradation of shear strength by respectively: C_1, C_2 and v_{bm}, which is the basic shear stress provided by masonry, still given by the square root of masonry compressive strength (see Voon & Ingham, 2007).

These terms are derived, as already explained, by (Shing et al., 1990) and (Anderson & Priestley, 1992). They both evaluated the URM contribution on the basis of the square root of masonry compressive strength. In particular, Shing et al (1990) also consider the dowel-action of vertical bars by means of ($0.0217\rho_v f_{yv}$).

American formulations are characterized by adopting tensile strength in the URM contribution, since V_m term contains $\sqrt{f'_m}$, and in particular (Anderson & Priestley, 1992) gives $1.2 \cdot \sqrt{f'_m}$, which corresponds to $1/8 \cdot \sqrt{f'_m}$, usually accepted as estimation of tensile strength of masonry (Tassios, 1988). (Tomaževič, 1999) proposed to evaluate the tensile strength as 0.03÷0.09 f_m.

These are consistent with data and observations provided by (Mosele, 2009).

(Anderson & Priestley, 1992) take into account the aspect ratio with k_1 factor, which was set not to be greater than one on the basis of experimental data, and the degradation of shear strength with k_2 factor, due to the cyclic loading in the inelastic range, which is calculated on the basis of ductility, i.e. ratio of maximum displacement to displacement at initial yield in the flexure ($\mu_{max} = \delta_{max}/\delta_{yielding}$). This factor is taken into account implicitly into the v_{bm} term by NZS 4230, and has been recently revised by Voon & Ingham (2007). Fig. 2.14 left shows the relationship between k_2 and μ_{max} for (Anderson & Priestley, 1992) and for (Voon & Ingham, 2007). For the walls of the present research, k_2 factor is equal to 1 for both the applied axial load level in the case of Anderson-Priestley proposal, and is equal to 0.91 and 0.73, respectively for the higher and lower axial load level, following the Voon-Ingham relation.

It has to be noted that both Anderson-Priestley and Voon-Ingham relations relate ductility based on maximum displacement δ_{max} therefore the reduction of shear strength is related to that limit state, whereas (Mosele, 2009) observed that, to obtain the eventual shear strength reduction at maximum load limit state, ductility has to be calculated referring to displacement at maximum load δ_{Hmax}, and becomes $\mu_{Hmax}=\delta_{Hmax}/\delta_{yielding}$. Therefore the previous values of k_2 factor valid for the maximum lateral load capacity are 1 for both the applied axial load level in the case of Anderson-Priestley proposal, and 1 and 0.9, respectively for the higher and lower axial load level, in the case of Voon-Ingham, as Fig. 2.14 right gives.

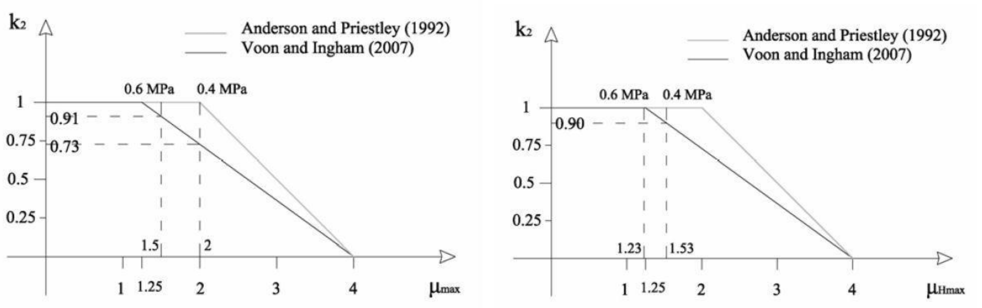

Fig. 2.14. Ductility vs Masonry shear resisting mechanism relationships. Maximum ductility (left) and ductility at maximum shear strength (right) (Mosele, 2009).

The American and New Zealand formulations also consider the axial load contribution V_P with specific terms as reported in Table 2.1. For ACI 530 this contribution was obtained by data regression, whereas for NZS 4230 from physical consideration. The New Zealand code takes into account also the reduced deformation capacity of masonry, in post-cracking phase, with increasing axial load level, observed by (Matsumura, 1988; Shing et al., 1990; Sveinsson et al., 1985). Therefore NZS 4230 limits the axial load which contributes to shear strength, as follow: $N^* \leq 0.1f'_{mtl}$, to prevent the occurrence of brittle shear failure.

2.2.2. Reinforced Masonry

Loadbearing masonry buildings can be idealized as a combination of two structural elements: piers and spandrels, which interact to withstand the lateral loads due to wind or seismic forces. The trickiest condition for masonry structures subjected to lateral loads is that of the pier, as it supports also the gravity loads and transfers them to the foundation. As a consequence the study of the seismic response of shear walls, made with a new construction system, has to be carried out first of all by means characterizing the response of piers under shear-compression loads. This is a key issue for buildings with box-type behavior (Fig. 2.6), as low/medium-rise residential buildings, in which the out-of-plane behavior needs to be verified just at local level.

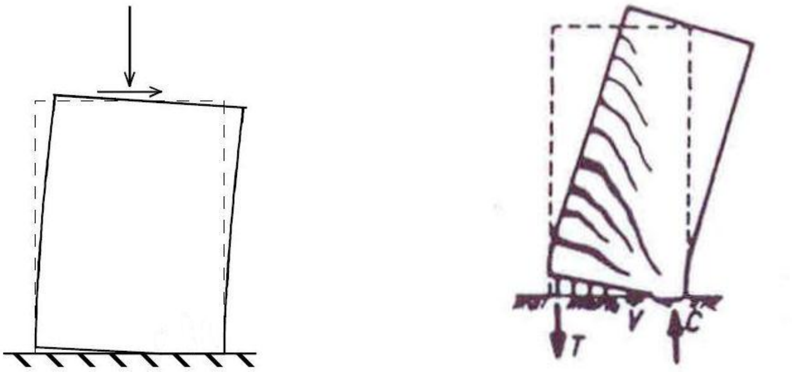

Fig. 2.15. Flexural failure mechanism: opening of the first flexural crack (left, from Macchi and Magenes, 2002) and activated vertical reinforcement (right, from Paulay and Priestley, 2009).

The pier is loaded by a combination of axial and horizontal loads, which induce both flexural and shear deformations. The failure modes associated to the reinforced masonry shear walls are essentially two: flexural or shear failure, according with the flexural strength is reached rather than the shear capacity, respectively (Drysdale & Hamid, 2008; Giuffrè, 1980; Tomaževič, 1999). The former failure mechanism develops with appearing of horizontal cracks in the bed joint of the stretched side (Fig. 2.15 left), following which the vertical reinforcement activates (Fig. 2.15 right), whereas the opposite side is under compression. The flexural failure occurs due to yielding of vertical reinforcement, which means ductile failure, if the crushing of the compressed masonry is avoided. Confinement of the compressed zone increases the crushing strength leading to a higher ductility.

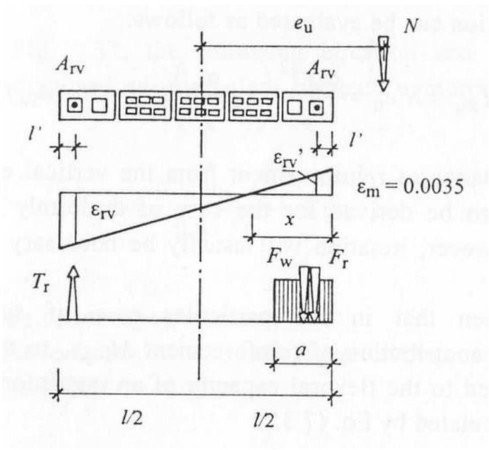

Fig. 2.16. Equilibrium of sectional forces at flexural failure of a reinforced masonry wall (from Tomaževič, 1999).

Fig. 2.16 gives the strains, stresses and loads, acting to the section of a masonry wall reinforced with symmetrical vertical reinforcement at the ends.

Under the usual hypothesis for flexure theory, such as plain sections remain plain and linear strain distribution, and assuming yielding of tension and compression vertical reinforcements, which allows the direct calculation of the depth of stress block: a, the flexural capacity of the reinforced masonry wall's section shows in Fig. 2.16, can be evaluated by (Eq. 2.1):

$$M_u = M_{u,s} + M_{rv,y} = \frac{\sigma_0 t l^2}{2}\left(1 - \frac{\sigma_0}{f}\right) + z \cdot A_{rv} f_y \tag{Eq. 2.1}$$

Where $M_{u,s}$ is the contribute of masonry and $M_{rv,y}$ is the contribute of vertical reinforcement to the flexural capacity, σ_0 is the average compression stress due to the axial load N and $z = l - 2 \cdot l'$ is the lever arm of the torque force moment of vertical reinforcement.

Some codes, such as, the Italian one (DM 14/01/2008, 2008) adopts the (Eq. 2.1) for the evaluation of bending capacity, whereas other standards, such as the US code ACI 530 (2005) indicates to neglect the contribution of compressed bars.

In the case of uniformly distribute vertical reinforcements there is a slight reduction in flexural strength, which is compensated by improved shear transfer and avoiding the bond and anchorage problems because of the limited grout space, other than reduced congestion of flexural reinforcement, in respect to the reinforcement concentrated to the wall ends (Priestley, 1986). Therefore, when it is practically possible, the distributed configuration of vertical reinforcement is preferred (Paulay & Priestley, 2009). In any case the main role of the vertical reinforcement is to avoid the rocking mechanism, which is characterized by higher displacement capacity but with low energy dissipation capacity, whereas the vertical reinforcement induce also high energy dissipation in particular in the post-yielding phase.

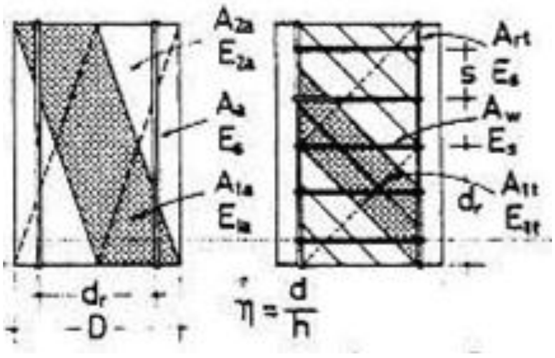

Fig. 2.17. Arch-beam (left) and Truss (right) mechanism of reinforced masonry wall failing in shear (from Wakabayashi and Nakamura, 1984).

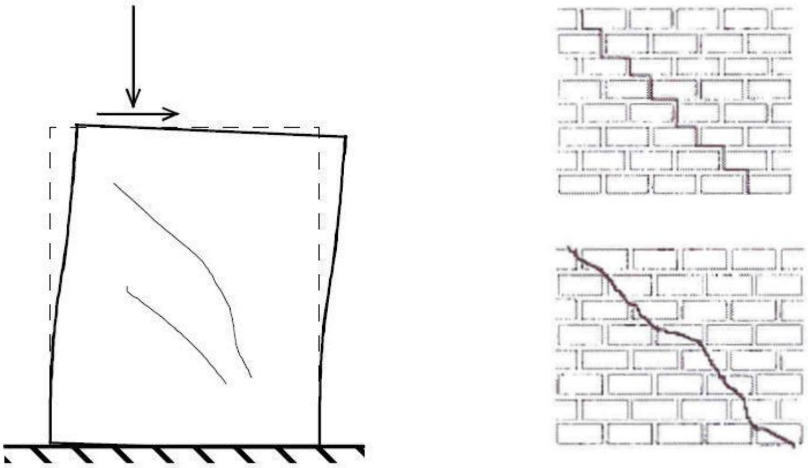

Fig. 2.18. Shear failure with diagonal shear crack (left), step shape crack or crack passing through mortar joints and units (right) (from Macchi and Magenes, 2002).

The shear failure mechanism of reinforced masonry walls is governed, at beginning, by the arch-beam mechanism (Fig. 2.17 left) due to the presence of vertical reinforcement. At a certain level of horizontal load, the diagonal crack appears on the masonry strut (Fig. 2.18), and the horizontal reinforcement prevents the separation of the wall's cracked part and provides the load transfer between the edges of the cracks, which provides therefore the interlocking mechanism between the two surfaces of each diagonal crack (Fig. 2.19 right). At this stage the combination of vertical and horizontal reinforcement and masonry leads to developing a truss mechanism (Fig. 2.17 right), and new diagonal cracks open over the entire surface of the wall. Interlocking on the diagonal cracks closed by horizontal reinforcement and the presence of reinforcement improve the energy dissipation capacity and reduce the strength degradation (which means reduced brittleness) of the unreinforced masonry.

The distributed vertical reinforcement is subjected to transversal efforts resulting in its bending, which is known as the dowel-action mechanism (Fig. 2.19 and Fig. 2.20). Part of the shear capacity of the wall can also be attributed to this mechanism by various authors, such as (Tomaževič, 1999) and (Tassios, 1988), even if it has to consider that this mechanism needs large deformations to be activated, which cannot be related to the maximum strength limit state. In the case of vertical reinforcement concentrated at the ends of the wall, which is the most common typology of RM in Italy and Europe, the dowel-action becomes very poor contribution, so it seems reasonable neglect it (Mosele, 2009). In any case, only vertical steel reinforcement is not capable of contributing to the shear resistance of masonry, as assessed in post-earthquake damage observations and through experimental indications. Walls reinforced with vertical reinforcement fail in shear, despite their predicted flexural behavior (Tomaževič, 1999).

The ultimate state of reinforced masonry wall is often reached with crushing of masonry units at the center of the wall or at the compressed toe, due to a combination of bending and shear. This indicate the fully exploitation of loadbearing capacity of masonry (Tomaževič, 1999).

Arch-beam and truss mechanism are the two main mechanisms governing the in-plane response of reinforced masonry wall, exploiting the tensile properties of vertical and horizontal reinforcement, such as the compressive characteristics of masonry. The shear response results in a global behavior in between the arch-beam and truss mechanism, this combination is made taking into account by compatibility and equilibrium conditions (Wakabayashi & Nakamura, 1984). This theoretical model was able to accurately provide the load-displacement envelop and the contribution of horizontal reinforcement (Tomaževič & Lutman, 1988; Wakabayashi & Nakamura, 1984), but, such as for other models (Shing et al., 1993; Tassios et al., 1984) the adopted equations are not always adequate for practical design, and the validity is limited to specific cases (Mosele, 2009).

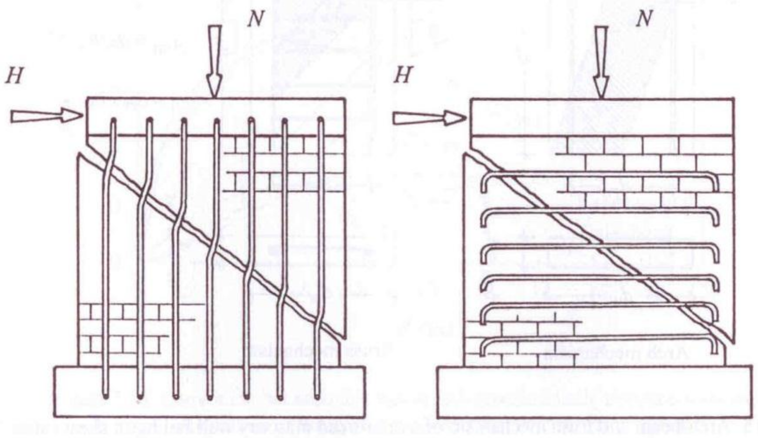

Fig. 2.19. Mechanism of action of vertical (left) and horizontal (right) reinforcement of masonry wall failing in shear (from Tomaževič, 1999).

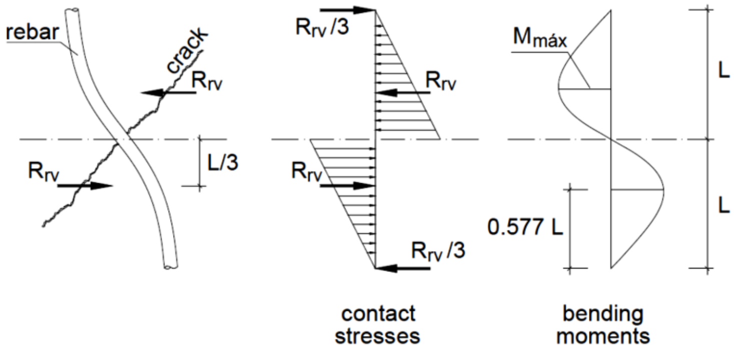

Fig. 2.20. Dowel mechanism of vertical reinforcement at shear failure of a reinforced masonry wall (Tomaževič, 1999).

The complexity of the mechanisms induced by the presence of the reinforcement, as above described, is also related to the difficult in quantifying the influence of each mechanism on shear capacity. Therefore researchers and standards evaluate the shear resistance of RM walls in a simplified way, as a sum of contributions. The usual procedure to write a shear strength formulation is to introduce terms related to the shear mechanisms and subsequent to calibrate the influence of each terms. Four main contributions are usually considered by formulations proposed to predict the nominal shear strength V_R of reinforced masonry walls: V_m is the shear strength of unreinforced masonry, V_P is the contribution of axial load, V_s is the contribution due to horizontal reinforcement and V_{dw} is the contribution due to dowel-action of vertical reinforcement, as shown by (Eq. 2.3). Formulations of this type are proposed by many standards as the (EN 1996-1: 2005. Eurocode 6, 2005), the Italian code (DM 14/01/2008, 2008), the New Zealand code NZS 4230 (2004), the US code ACI 530 (2005), the Australian Standard AS 3700 (2001) and British

Standard BS 5628-2 (2005), with some differences. The single terms in the considered formulation are reported in Table 2.1.

$$VR = V_m + V_P + V_S + V_{dw} \tag{Eq. 2.2}$$

Author	Unreinforced Masonry (V_m)	Axial Load (V_P)	Horizontal Reinf (V_s)	Dowel-action (V_{dw})
Eurocode 6 (2005)	$f_{vk} \cdot tl$	implicit	$0.9 \cdot A_{sw} f_y$	-
DM 14-01-2008	$f_{vk} \cdot td$	implicit	$0.6\left(\frac{d \cdot A_{rh} f_y}{s}\right)$	-
Tomaževič Lutman (1988)	$\left(\frac{f_t}{b} \sqrt{\frac{\sigma_0}{f_t}+1}\right) \cdot tl$	implicit	$0.3 \cdot A_{sw} f_y$	-
Tomaževič (1999)	$f_{vk} \cdot tl$	implicit	$0.3\left(\frac{0.9d \cdot A_{rh}}{s} \cdot f_y\right)$	$0.806nd_{rv}^2 \cdot \sqrt{f_m f_{yv}}$
BD 5628-2: 2005	$f_{vk} \cdot tl$	implicit	$A_{sw} f_y$	-
AS 3700-2001	$f_{vr} \cdot tl$	-	$0.8 \frac{l}{h} \cdot A_{sw} f_y$	-
ACI 530-2005	$0.083\left(4-1.75\frac{M}{Vl}\right)\sqrt{f'_m} \cdot A_n$	$0.25 \cdot \sigma_0 A_n$	$0.5 \cdot \frac{l \cdot A_{rh} f_y}{s}$	-
NZS 4230: 2004	$((C_1+C_2) \cdot v_{bm}) \cdot td$	$0.9N^* \cdot \tan\alpha$	$C_3 \cdot A_{rh} f_y \frac{d}{s}$	implicit
Shing et al. (1990)	$(0.166 + 0.0217 \rho_v f_{yv})\sqrt{f'_m} \cdot A_n$	$0.0217 \sigma_0 A_n \cdot \sqrt{f'_m}$	$\left(\frac{l-2d'}{s}-1\right) A_{rh} f_y$	implicit
Anderson Priestley (1992)	$0.12 \cdot k_1 k_2 \sqrt{f'_m} \cdot A_n$	$0.25 \cdot \sigma_0 A_n$	$0.5 \cdot \frac{d \cdot A_{rh} f_y}{s}$	evaluated to provide null contribution

Table 2.1. Terms of equation for reinforced masonry shear strength (Mosele, 2009).

The meaning of terms into the equations is given in (Mosele, 2009).

In the European, Italian, British and Australian codes, and in (Tomaževič, 1999) and (Tomaževič & Lutman, 1988), the shear strength of masonry (V_m) is evaluated on the bases of phenomenological criteria, which interpret the URM failure mode. The contribution of horizontal reinforcement (V_s) is added considering full or partial yielding of horizontal bars. Furthermore, (Tomaževič, 1999) adds the contribution of dowel-action of vertical bars (V_{dw}), which is neglected by the above mentioned codes.

On the contrary, the American and New Zealand code consider the contribution of shear strength of URM (V_m), value of axial load (V_P), and reduced effect of horizontal reinforcement (V_s), on the basis of semi-empirical relationships obtained by data-regression and physical interpretation of phenomena. They are both based on (Shing et al., 1990) and (Anderson & Priestley, 1992) proposals, being the NZS 4230 formulation a further development of the American proposal derived by the (Voon & Ingham, 2007) work.

In particular (Shing et al., 1990) proposed a formulation based on the fitting of their experimental data in order to take into account the influence of vertical bars and applied axial load, whereas they adopted simple physical concept to evaluate the shear reinforcement contribution. They also validated this equation considering the data obtained by (Sveinsson et al., 1985). Anderson & Priestley, starting from the formulation of Shing et al. and (Matsumura, 1988), proposed a new evaluation of the shear strength of reinforced masonry by means of regression analysis of data obtained by Sveinsson et al., Matsumura and Shing et al.

The term to evaluate the shear strength of plain masonry V_m can be evaluated using the formulations proposed in paragraph 2.2.1.

Tensioning of horizontal reinforcement becomes effective when the first shear crack appears, by preventing separation of cracked portions of the wall (as stated before). The contribution of the horizontal reinforcement V_s is calculated in the same way as stirrups in reinforced concrete members, as presented in (Eq. 2.3), which is directly derived by the common “truss-action”. This formula calculates the number of stirrups across the diagonal crack (assumed to be 45° sloped starting from the effective length of the resisting section), and considers that each stirrup is able to develop the maximum tensile capacity.

$$V_s = \frac{d}{s} \cdot A_{rh} \cdot f_y \qquad \text{(Eq. 2.3)}$$

In (Mosele, 2009) and in some previous researches (Tomaževič & Lutman 1998, Anderson and Priestley 1992) were demonstrated that shear reinforcement is exploited less than its maximum capacity. In particular Tomaževič & Lutman and Mosele obtained this information directly by experimental measurements, whereas Anderson and Priestley observed this through statistical data fitting. On the basis of these considerations, the horizontal reinforcement contribution V_s is calculated multiplying the second term of (Eq. 2.3) times a reduction factor C_{rh} .

The horizontal reinforcement reduction factor C_{rh} is equal to 0.6 for DM 14/01/2008, 0.8 for AS 3700 and for NZS 4230, 0.5 for ACI 530 and for Anderson and Priestley, and 0.27 for (Tomaževič, 1999).

The horizontal reinforcement reduction factor C_{rh} is equal to 0.9 and 0.3 respectively for Eurocode 6 and for Tomaževič & Lutman (1988), but in these cases it multiplies the total area of horizontal reinforcement, A_{sw} . The British Standard does not consider to apply a reduction factor to horizontal reinforcement contribution. (Shing et al., 1990) proposed to neglect the contribution of the top and bottom reinforcing bars, which do not have adequate development lengths to guarantee tensile resistance, when a diagonal crack opens. So their formulation takes into account only the inner reinforcing bars, which can develop the entire tensile strength, and these bars are considered fully effective (no reduction factor C_{rh} applies).

(Tomaževič, 1999) applies such a large reduction to horizontal reinforcement strength on the basis of experimental results, but takes into account the contribution of vertical reinforcement, by analytical evaluation of dowel-action (Priestley & Bridgeman, 1974). Dowel-action contribution is considered separately only by Tomaževič, whereas other proposals generally do not consider it or, in the case of Shing et al., Anderson & Priestley and New Zealand, implicitly take it into account in the V_m term. In particular, Shing et al. obtains small relevance of dowel contribution, with respect to other contributions.

The NZS 4230 substantially proposes the same dowel contribution of Shing et al., that for NZS 4230 also changes according to the already discussed k_2 factor. Anderson & Priestley obtained, by regression analysis, that the dowel mechanism does not affect the shear strength, so they set that term to zero. Since the ACI 530 is based on their formulation, also the American Standard does not consider the dowel action.

This is likely related to the fact that at ultimate load, the plastic zones are concentrated where the dowel mechanism acts and so its contribution is largely reduced, in particular in the case of concentrated vertical reinforcement.

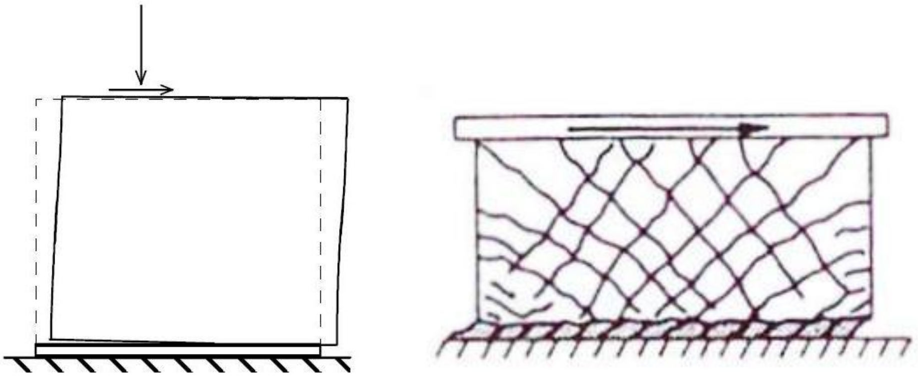

Fig. 2.21. Sliding shear failure mechanism (left, from Macchi and Magenes, 2002) and role of reinforcement (right, from Paulay and Priestley, 1992).

In case of low axial load and poor quality mortar, sliding shear failure occurs, characterized by sliding of the upper part of wall on one mortar bed joint (Fig. 2.21 left). Sliding affects mainly squat walls, in which sliding displacement can occur at the base along the flexural cracks, after significant yielding of vertical reinforcement, for a certain level of lateral load, transferred by means of dowel-action of vertical reinforcement (Fig. 2.21 left). This phase induces a reduction of both strength and stiffness of friction resistant mechanism (Paulay & Priestley, 2009). This failure mode is not frequent for RM walls since the clamping effect guaranteed by vertical reinforcement provide positive contribution. For RM walls made with clay units, the sliding failure mode is also infrequent, because the mortar is usually of high quality in order to guarantee the bond with bed joint reinforcement.

The resistance to sliding shear is proposed by authors (Paulay & Priestley, 2009; Tomaževič, 1999), to be evaluated neglecting the contribution of wall friction, and considering only the dowel-action as shear transfer mode along the base, which can be calculated adopting the V_{dw} contribution in formulation proposed by (Tomaževič, 1999) for shear strength.

2.3. In-Plane Modeling of Masonry Walls

2.3.1. *Finite Element Modeling Approaches*

Many advanced computational approaches are also available to assess seismic behavior in masonry. Non-linear finite element modeling has been recognized as a general and efficient method for analysis of the load-bearing and displacement capacity of masonry systems, and can accurately describe the pre-peak and post-peak behavior of masonry under different monotonic load combinations by adopting inelastic constitutive material models (Gambarotta & Lagomarsino, 1997a; Gambarotta & Lagomarsino, 1997b; Lourenço, 1996a; Rots, 1997). Conversely, cyclic behavior can better be described by damage-based material models (Calderini & Lagomarsino, 2008; Gambarotta & Lagomarsino, 1997a; Gambarotta & Lagomarsino, 1997b) than by those implementing plasticity concepts (Lourenço, 1996a; Rots, 1997).

In general, numeric representation of masonry can be achieved by modeling masonry constituents separately (units and mortar joints, micro-modeling approach, see Fig. 2.22b,c), or by following a global approach in which the whole structure is schematized as a continuum without any distinction between masonry constituents (macro-modeling, see Fig. 2.22d). The first approach can again be subdivided into detailed micro-modeling (Fig. 2.22b), in which units and mortar joints are represented by continuum elements and contact surfaces between units and mortar by interface elements, and simplified micro-modeling (Fig. 2.22c), in which expanded units are represented by continuum elements and non-linear behavior of mortar joints and contact surfaces is collapsed into interface elements.

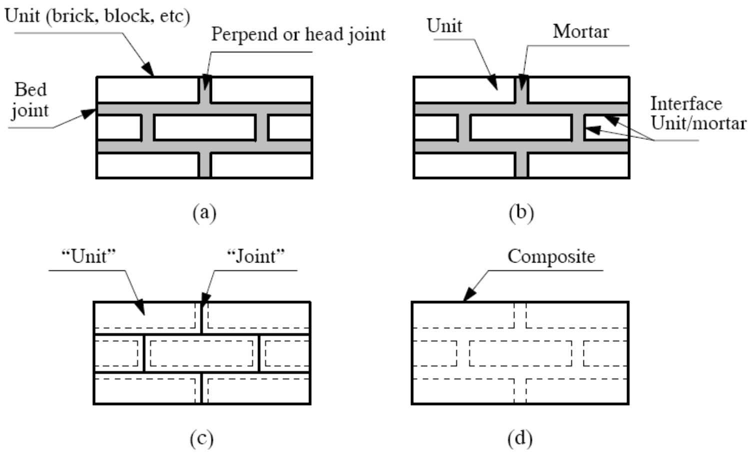

Fig. 2.22. Different modeling strategies for masonry structures: (a) real masonry specimen, (b) detailed micro-modeling, (c) simplified micro-modeling, (d) macro modeling (Lourenço, 1996).

The micro-modeling strategy for masonry has mainly focused on the development of reliable interface models, since the first introduced by Page (1978). Several constitutive laws were defined, incorporating damage and plasticity concepts (Gambarotta and Lagomarsino, 1997a; Rots, 1997) or plasticity theory only (Giambanco et al., 2001; Lotfi & Shing, 1994; Lourenço et al., 1997).

(Lourenço, 1996a) developed an interesting interface model under multi-surface plasticity theory, in which not only shear and tensile but also compressive behavior can be taken into account through a cap model (see Fig. 2.23). This interface model was further developed with a refined description of the dilatancy phenomenon by (van Zijl, 2004).

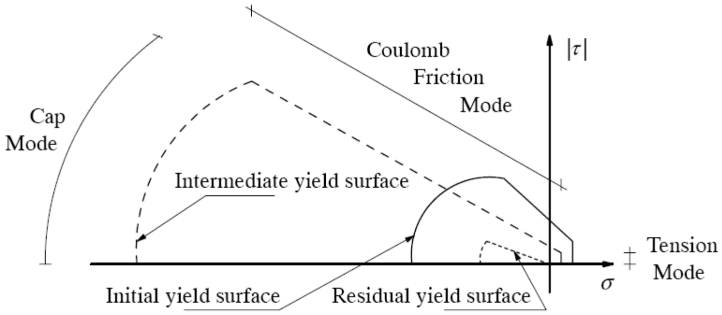

Fig. 2.23. Limit failure surfaces for interface model (Lourenço, 1996).

An accurate micro-model has to include the main local failure mechanisms for masonry (Fig. 2.24) as identified by (Lourenço, 1996a):

a) tensile failure of joints;
b) sliding along horizontal and vertical joints for low normal compression stress;
c) direct tensile failure of units;
d) diagonal cracking for medium to higher normal compression stress;
e) vertical crack, usually identified as crushing of masonry units, due to effect of dilatancy of mortar joints, which cause indirect tensile failure in the units.

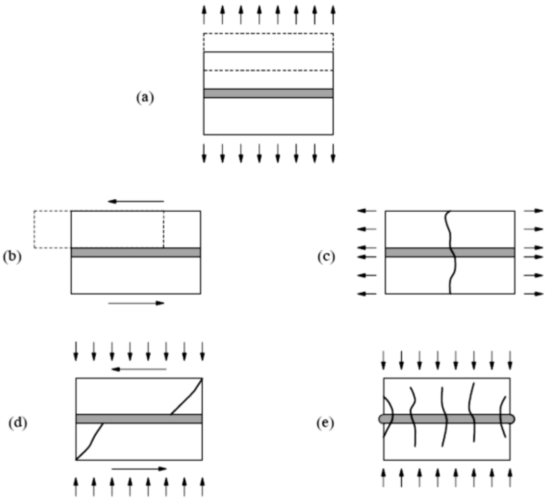

Fig. 2.24. Local failure mechanisms for masonry (Lourenço, 1996a).

Appropriate modeling of cracks through units is of basic importance, to avoid an over-stiff response and a considerable higher failure load of the numerical models than those experimentally determined (Chaimoon & Attard, 2007; Lourenço, 1996a).

Within micro-modeling, cracks through masonry units can be accommodated by employing two main strategies. In the case of bricks (Fig. 2.25), the insertion of a central potential vertical crack by means of interface elements suffices to simulate global behavior correctly (Lourenço, 1996a; Rots, 1997).

The use of smeared crack models is more appropriate for blocks that may undergo distributed cracking (Lotfi and Shing, 1994; Rots, 1997; Giambanco et al., 2001). It is worth mentioning that the first approach turned out to be very robust, whereas the second may present some convergence problems due to bifurcation (Lourenço, 1996; Rots, 1997).

Anyway in micro models with a simplified schematization there is a loss in accuracy because Poisson's effect given from mortar joint is lost. In this case the expanded unit has to average its characteristics in order to take in account the properties of joint.

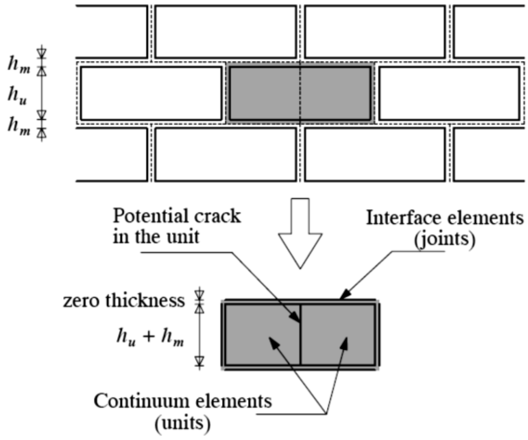

Fig. 2.25. An example of simplified micro modeling approach for brick masonry (Lourenço, 1996a).

Macro-modeling commonly uses non-linear anisotropic constitutive material models. In some simplified cases, non-linear isotropic models are also employed. Several materials models are available for masonry, incorporating either damage (Gambarotta and Lagomarsino, 1997b; de Borst, 2002; Calderini and Lagomarsino, 2008) or multi-surface plasticity theory (Rots, 1997; Lourenço et. al., 1997).

Mechanical parameters may be derived from experimental data or deduced from homogenization techniques (Pegon and Anthoine, 1997; Ma et al. 2001; Calderini and Lagomarsino, 2008). This approach becomes effective when units and mortar joints can be taken into account on average; when this is not provided, possible discrepancies between real and numerical behavior may arise (Lourenço, 1996; Lourenço et. al. 1997).

Among damage models a smeared crack constitutive model based on isotropic total strain is developed along the lines of the Modified Compression Field Theory, originally proposed by (Vecchio & Collins, 1986) which describes the stress as a function of the strain. This concept is known as hypo-elasticity when the loading and unloading behavior is along the same stress-strain path. Within the total strain-stress relationships, various approaches are possible.

One commonly used approach is the coaxial stress-strain concept, in which the stress-strain relationships are evaluated in the principal directions of the strain vector. This approach, also known as the Rotating Crack model, is applied to the constitutive modeling of reinforced concrete during a long period and has shown that the modeling approach is well suited for reinforced concrete structures. More appealing to the physical nature of cracking is the fixed stress-strain concept in which the stress-strain relationships are evaluated in a fixed coordinate system which is fixed upon cracking. Both approaches can be described in the same framework where the crack directions are either fixed or continuously rotating with the principal directions of the strain vector.

As title of example, in Fig. 2.26 are showed two relations which describe respectively the constitutive relation for tensile behavior (left) and for compressive behavior (right), in a contest of Total Strain Rotating Crack model. The first is a so called linear softening relation, while the second is a parabolic relation according to (Feenstra, 1993).

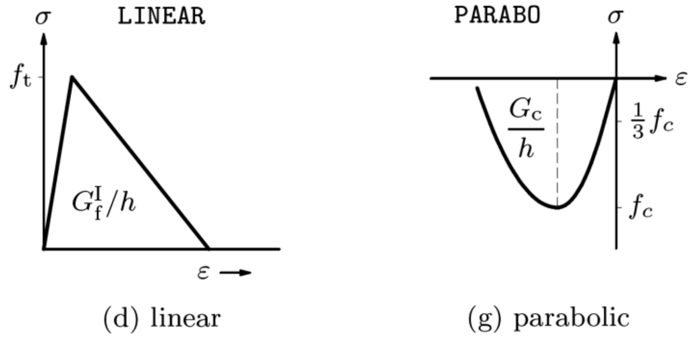

Fig. 2.26. Total Strain Rotating Crack isotropic damage model. Stress strain relation in tension (left) and in compression (right) (from De Witte, 2005).

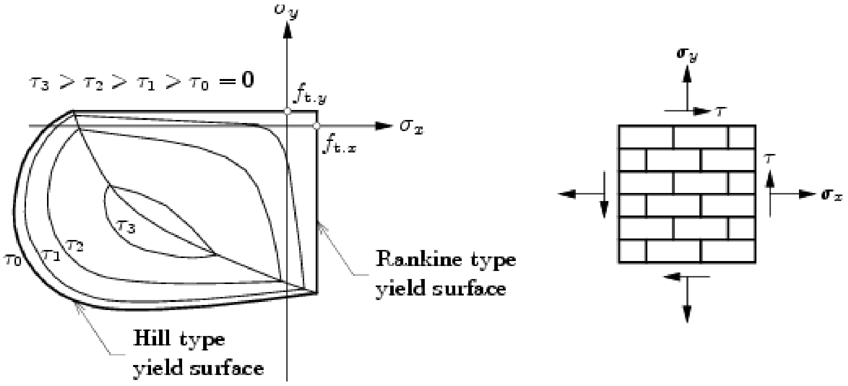

Fig. 2.27. Orthotropic plasticity Rankine-Hill failure criteria (Lourenço, 1997).

In addition to the plasticity traditional isotropic plasticity models as: Tresca (1864), Von Mises (1913), Mohr-Coulomb and Drucker-Prager (1952); the approaches of above mentioned authors a based on orthotropic multi-surface plasticity, comprising of an anisotropic Rankine yield criterion in tension combined with an anisotropic Hill criterion for compression. Masonry is an example of a material for which this criterion applies, having different strengths parallel and perpendicular to the bed joints. In Fig. 2.27 is proposed a representation of this failure surface in the usual (σ_x, σ_y, τ).

Concluding, in general micro-modeling strategy is more detailed and is a valuable tool to reproduce masonry assemblages tested during experimental research. It requires a large number of parameters, but facilitates understanding of the local behavior of masonry and parameterizing the results of experimental trials. Conversely, it is not suitable for simulating the global behavior of buildings, since the computational burden is usually excessive. The macro-modeling approach is less detailed, but depends on a limited number of parameters. It is suitable for large structures, thus becoming more attractive for practice-oriented analyses.

2.3.2. Other Modeling Approaches

Finite Element modeling can provide powerful analysis tools; however, they are computationally demanding and a large number of user-specified parameters are needed for the constitutive behavior definition.

There are other approaches for modeling nonlinear behavior of masonry structures as limit analysis where are estimated the ultimate load at collapse and the corresponding failure mechanism (Como e Grimaldi 1986, Abruzzese et al. 1992) and they are usually employed in vulnerability analyses. Other approaches follow a bi-dimensional approximation of masonry piers or spandrels using strut-and-tie models e.g (Calderoni et al., 1987 e 1989) or the more recent and sophisticated model from (Roca, 2006) which implement a primary ties for in tension and a residual model with no ties. Another class of model schematizes the structure using monodimensional elements able to deform in shear. They were first developed from (Tomaževič, 1978) and have undergone several refinements in next years (Tomaževič, 1999), and are based on so-called storey-mechanism approach (POR method) and each pier is characterized by an idealized non-linear shear-displacement curve (typically elastic perfectly-plastic with limited ductility see Fig. 2.28).

Also based on storey-mechanism approach is the so-called macro-element discretization which is based on an equivalent frame idealization of the structure (Magenes & Della Fontana, 1998) or (Lagomarsino et al., 2007). These elements represent damages, failure and displacements or rotations in pre-defined zones on the basis of mechanical assumptions and implementation of non-linear constitutive formulation of phenomenological force-displacement relations which can take in to account flexure and/or shear strength and failure determined by drift limits (SAM method see Fig. 2.29).

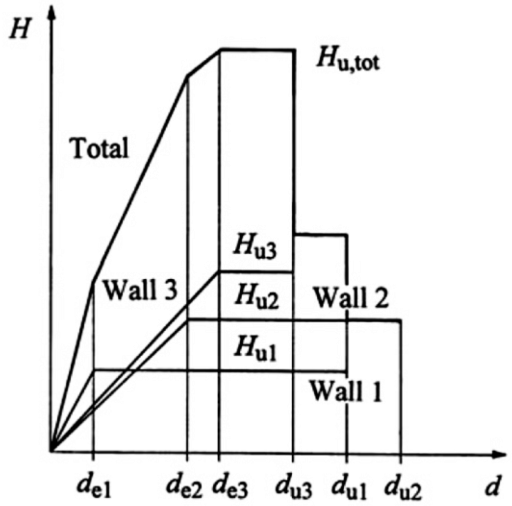

Fig. 2.28. POR Method. Construction *of storey resistance envelope on the basis of bi-linear resistance envelopes of structural walls. (*Tomaževič*, 1999).*

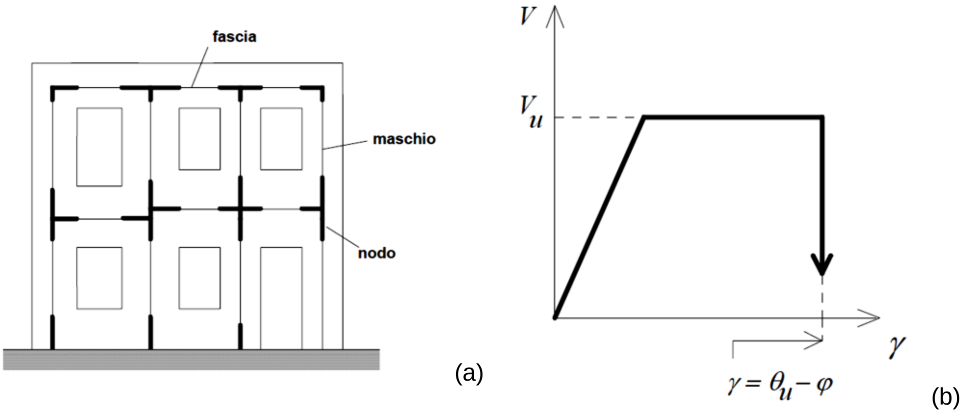

Fig. 2.29. SAM Method: (a) equivalent frame model; (b) bi-linear relation used for masonry piers (Cattari, 2007).

Another approach is proposed by (Benedetti & Steli, 2008). With a simple no-tension material and simple elastic perfectly-plastic rule for masonry and the usual hypothesis of cross section remain straight, these authors present an explicit formula for the shear-displacement curve of a URM pier, by integration of the curvature diagram. Also extend to the case of masonry with Fiber Reinforced Polymer (FRP) by introducing the hypothesis of an elastic–plastic resisting force (equal to the debonding value) of the FRP reinforcement up to the crushing of the masonry in compression.

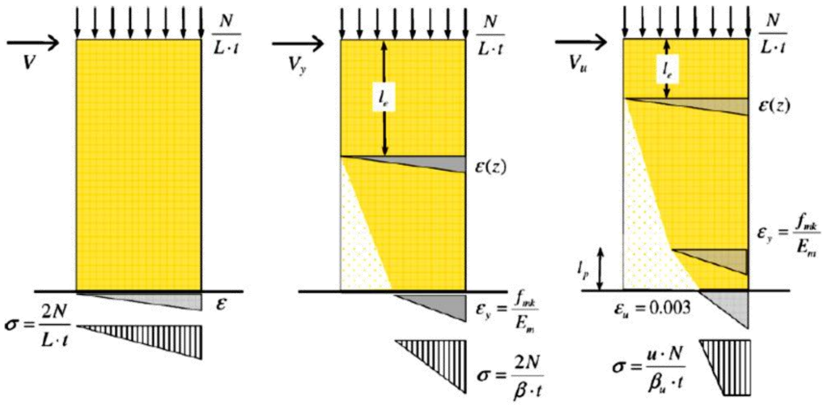

a) fully elastic b) cracked elastic c) elastic - plastic

Fig. 2.30. Equilibrium configurations of the masonry panel under compression and shear (Benedetti & Steli, 2008).

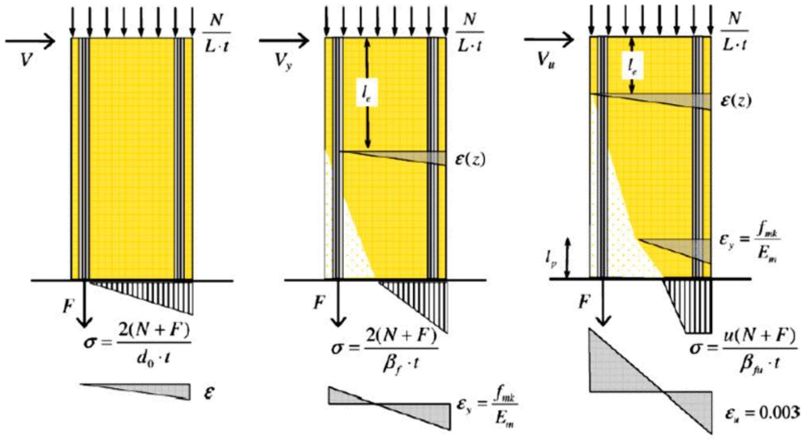

a) fully elastic b) cracked elastic c) elastic - plastic

Fig. 2.31. Equilibrium configurations of the FRP reinforced panel under compression and shear (Benedetti & Steli, 2008).

This is a very simple model includes only an elastic shear deformation and able to reproduce the behavior until the ultimate ductility only accounting a flexure failure. Anyhow it suggested that a cross sectional analysis approach can be developed also for masonry walls.

A promising approach developed for Reinforced Concrete (RC) structures is fiber element approach. They still keep the basic hypothesis of subdividing the structure in mono-dimensional elements, even though they could be defined as a hybrid between FEM and macro-models. In these models the element (such as a pier) is subdivided into longitudinal fibers. The constitutive relation of the section is not specified explicitly but it is derived by integration of the response of the fiber. These models usually assume that plain section remain plane.

Several fiber beam–column elements were developed in the last 20 years with capability of reproducing coupled axial force and flexure effects, e.g. (Spacone et al., 1996; Taucer et al., 1991). The fiber approach fits perfectly within the Euler–Bernoulli beam theory and caters for the accurate description of response of slender flexure-dominated members and full structures (Pinho & Elnashai, 2000). However, for structures with non-slender elements subjected to seismic loading the coupling between shear, axial and bending action becomes important. Recent studies (Ceresa et al., 2009; Guedes & Pinto, 1997; Jiang & Kurama, 2010; Marini & Spacone, 2006; Marmo, 2008; Mostafaei & Vecchio, 2008; Petrangeli et al., 1999; Saritas & Filippou, 2009) have attempted to overcome this limitation by introducing into the fiber approach the Timoshenko beam theory, or even a generalized beam theory coupled with multi-axial constitutive laws for material.

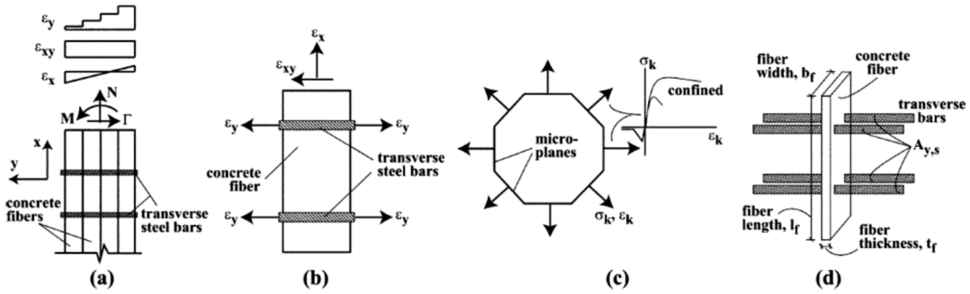

Fig. 2.32. Fiber element with nonlinear shear deformations: (a) fiber strain field; (b) concrete fiber strains; (c) microplanes; and (d) tributary transverse steel reinforcement (Jiang & Kurama, 2010).

From this literature review, it resulted that the existing modeling strategies for fiber beam–column elements with shear effects accounted for are few: they present quite different conceptual backgrounds and solution strategies with varying degrees of implementation complexity and calibration requirements. Among others, we note the well-developed efforts of Jiang & Kurama (see Fig. 2.32), which refer to Petrangeli et al. work, and formulation recently proposed by Saritas & Filippou, based on general and elegant approaches.

Some authors further introduced the bond-slip behavior between reinforcement and concrete e.g. (Cosenza et al., 2006) based on work of Manfredi & Pecce, 1998.

In plastic areas, decreasing shear strength of the element is noted, due to a decreasing or absent shear resistant mechanisms in the concrete. The influence of shear forces on the behavior of the beams was modeled by (Priestley et al., 1994); such a model is based on a reduction of the shear strength depending on the local ductility, as expressed in terms of linear variation of the curvature. The Cosenza et al. model represents an improvement of Priestley's since it enables the sectional ductility at any step of the analysis to be directly determined and then evaluates the shear strength of those sections located in the plastic regions (see Fig. 2.33).

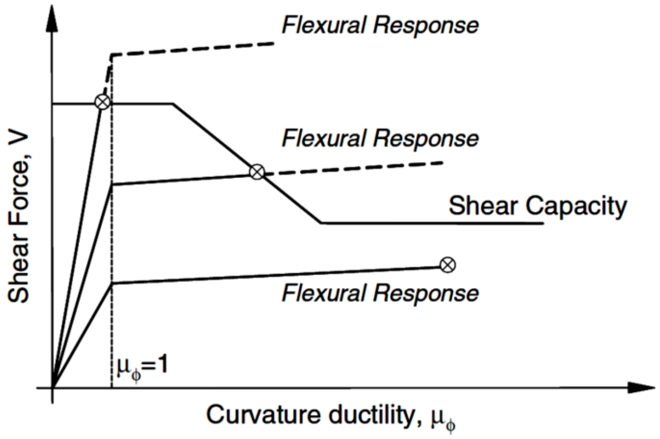

Fig. 2.33. Bending-Shear interaction after Priestley et al.1994: failures mode (Cosenza et al., 2010).

In general, if compared with finite element continuum models, the most important advantages of fiber element models are that they require a significantly reduced number of degrees of freedom and a significantly reduced number of user-defined constitutive parameters. In the nonlinear range, however, most conventional fiber models are limited to axial and flexural deformations, whereas the shear deformations are assumed to remain linear-elastic. Thus, these models are not effective in fully capturing the behavior of structures where nonlinear shear deformations play a significant role such as RC or masonry non slender walls.

3. EXPERIMENTAL DATA AND RESULTS

3.1. Introduction

The main aim of this chapter is to present the results of extensive experimental activity carried out in last few years at University of Padova, regarding the definition of in-plane behavior and seismic performances of innovative masonry construction systems. In particular masonry systems built with traditional materials but using innovative building solutions (masonry made with unit with mortar pocket infill in vertical joints, or made with thin layer mortar joints) or solutions made for seismic actions (reinforced masonry with mixed vertical and horizontal perforated clay units).

Experimental campaigns were aimed to characterize of mechanical behavior of load-bearing masonry systems. The principal research objectives were:

- experimentally evaluate mechanical performances (strength, stiffness failure modes both under compression and shear) related also to mechanical properties of joint and unit.
- define mechanical behavior of structural elements under in-plane cyclic actions, not only regarding strength and failure modes, but also to hysteretic behavior properties, as first crack stress, energy absorbed and dissipated at every cycle, stiffness degradation under cyclic actions and ductility.

This research activity was born from the fact that those new masonry typologies were not clearly recognizable with masonry systems used in common practice and which were well known in terms of performances, thus need to be investigated.

On the other hand, mechanical characterization of non-ordinary masonry systems (“ordinary” means that are made with horizontal and vertical joints filled with mortar and with thickness between 10 and 15 mm) should be done before their use as said in different Italian codes (DM 20/11/1987) and (Ordinanza P.C.M. n. 3274: 2003, 2005).

Finally as reported by (Ordinanza P.C.M. n. 3274: 2003, 2005) (and its modifications) and by clarification provided by Italian governmental organization “Protezione Civile” (SSN 0034852, 08/08/03), non-ordinary masonry systems should be tested under cyclic tests in order to verify stability under cyclic action reversals and the ductility.

3.2. Unreinforced Masonry Experimental Works and Results

The tests were carried out at the Laboratory for Structural Material Testing, at the University of Padova. Three typologies of masonry walls were studied: masonry made with thin layer joints (TM), masonry made with ordinary bed joint and interlocking (tongue and groove) units (TG), and masonry made with ordinary bed joint and units with pocket for mortar infill (Po). According to the (EN 1996-2: 2006. Eurocode 6, 2006), this last typology can be classified as having filled head joints, considering that mortar was provided over a minimum of 40% of the unit width. The main objective was to assess the cyclic behavior of masonry made with different types of head and bed joints, under in-plane loading.


TM *TG* Po

Fig. 3.1. The three masonry unit types respectively: TM TG and Po (above) and construction of a specimen for Thin-layer Masonry (below)

The unit cross section was the same for all the unit typologies, and it was designed according to the provisions for unit geometry given by the Italian seismic code valid at time of tests (Ordinanza P.C.M. n. 3274: 2003, 2005). The units contained holes having a void area equal to 43% of the gross cross-sectional area, nominal dimensions of 250x300 mm (length x width) and height equal to 250 mm for the TM units, and 225 mm for the TG and Po units. The specimens made with thin layer joints were assembled using a special premixed mortar with cement binder, methyl-cellulose polymeric additives for regular water retention and fine aggregates (size 0-0.5 mm), laid by means of the mechanical device (Fig. 3.1), in bed joints with average thickness equal to 1.3 mm. The mortar used for the reference specimens was a general purpose premixed cement-lime mortar with aggregates having maximum size equal to 4 mm, and the resulting bed joints had average thickness of about 12 mm.

The experimental phase started with accurate specimen preparation and construction. Almost 150 tests on mortars and units, 70 tests on micro-assemblages for the determination of the properties of the unit-mortar interface (couplets and crossed couplets) and more than 50 tests on large assemblages (wallettes) were carried out. Table 3.1 summarizes the main tests carried out on small and large specimens. Detailed descriptions of test procedures and results are reported elsewhere (da Porto, 2005; da Porto et al., 2005).

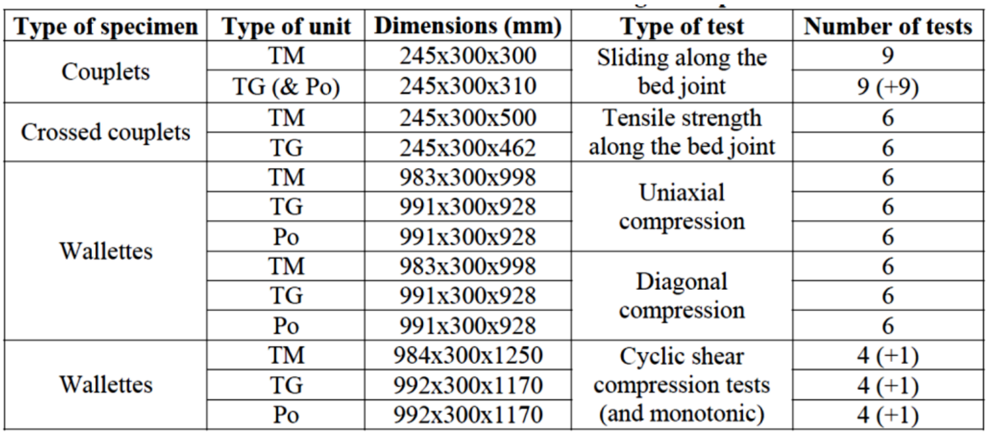

Type of specimen	Type of unit	Dimensions (mm)	Type of test	Number of tests
Couplets	TM	245x300x300	Sliding along the bed joint	9
	TG (& Po)	245x300x310		9 (+9)
Crossed couplets	TM	245x300x500	Tensile strength along the bed joint	6
	TG	245x300x462		6
Wallettes	TM	983x300x998	Uniaxial compression	6
	TG	991x300x928		6
	Po	991x300x928		6
	TM	983x300x998	Diagonal compression	6
	TG	991x300x928		6
	Po	991x300x928		6
Wallettes	TM	984x300x1250	Cyclic shear compression tests (and monotonic)	4 (+1)
	TG	992x300x1170		4 (+1)
	Po	992x300x1170		4 (+1)

Table 3.1. Tests carried out on small and large size specimens. (da Porto et al., 2005)

3.2.1. Basic material characterization

Table 3.2 and Table 3.3 summarize the main mechanical properties of the units and the mortars used: average and normalized compressive strength of the units in the direction of the vertical loads ($f_{b,m}$ and f_b) and in the horizontal direction ($f_{bh,m}$ and f_{bh}); splitting tensile strength in the direction parallel to the length and to the width of the unit calculated on the gross area ($f_{t/l}$ and $f_{t/w}$); flexural strength f_{mt} and compressive strength f_m of the mortar; elastic modulus E and Poisson's ratio v.

The tests for the determination of the shear strength under zero compressive stress were carried out on specimens made with two elements, according to the (UNI EN 1052-3, 2007).

Unit	$f_{b,m}$ [N/mm^2]	f_b [N/mm^2]	$f_{bh,m}$ [N/mm^2]	f_{bh} [N/mm^2]	$f_{t/l}$ [N/mm^2]	$f_{t/w}$ [N/mm^2]	E [N/mm^2]	v [$\varepsilon_{hl}/\varepsilon_v$]	v [$\varepsilon_{hw}/\varepsilon_v$]
TM	20.42	23.49	7.57	8.71	0.248	0.468	9328	-0.22	-0.32
TG	20.96	23.58	9.10	10.46	0.201	0.472	7997	-0.17	-0.22
Po	20.43	22.98	7.95	9.14	0.199	0.579	7887	-0.14	-0.23

Table 3.2. Mechanical properties of the units. (da Porto et al., 2005)

Mortar	Water/product ratio	Curing days	f_{mt} [N/mm^2]	f_m [N/mm^2]	E [N/mm^2]	v
Thin layer	0.35	28 60÷75	4.43 5.08	17.68 19.79	8238	0.21
General purpose	0.28	28 60÷75	3.51 4.22	11.51 14.64	9507	0.15

Table 3.3. Properties of the mortars. (da Porto et al., 2005)

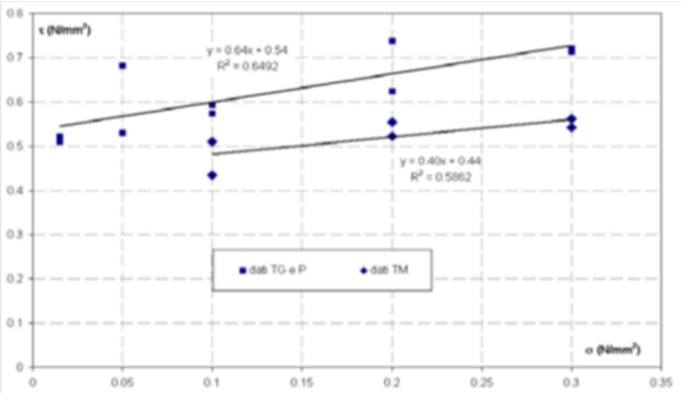

Fig. 3.2. Test of sliding along a mortar joint: shear-compression stresses diagrams for specimens failed along the joint. (da Porto et al., 2005)

The specimens were tested under 0.05, 0.10, 0.20 and 0.30 N/mm^2 confining pressure.

Higher values of confining pressure, recommended by the standard, were not applied due to premature failure of the units, occurred on three TM and eight TG-Po specimens. Coefficients of friction and cohesion were 0.40 and 0.44 N/mm^2 for six specimens with thin-layer joints (TM), which actually presented pure sliding failure. In specimens with ordinary bed joints (TG and Po), when mortar droppings in the unit holes were effective, premature failure of units occurred; when mortar droppings were not effective, sliding failure along the bed joints was observed (ten specimens). The latter specimens had a friction value of 0.64 and cohesion of 0.54 N/mm^2. When the dowel action of mortar droppings was added to this value, the estimated value of cohesion rose to 0.9 N/mm^2. The cohesion of mortar droppings was evaluated from the mortar cohesion times the net area of unit holes. Following the findings of Rots (1997) for ordinary mortar joints, the effective droppings taken into account were 35% of the total. This value was then smeared over the gross unit area, giving an estimated cohesion of mortar droppings of 0.36 N/mm^2.

Fig. 3.2 shows the shear stress-confining compressive stress diagrams that allow determining the coefficient of friction and the cohesion of the unit-mortar interface.

The tensile tests on the bed joint were carried out by adapting the crossed couplet test configuration (ASTM C952, 2002). The load was applied monotonically until failure, under displacement control (0.01 mm/s), by means of two U shaped metallic profiles. The failure occurred suddenly by separation of the two contact bed faces of the units for the thin layer joint specimens, at an average tensile stress equal to 0.20 N/mm^2 on the gross crossed unit area, equivalent to 0.36 N/mm^2 on the gross unit area. . In the case of ordinary joint masonry, mortar adhesion was generally higher than unit strength, so that cracking occurred. For specimens with contact bed face separation, failure occurred at an average tensile stress of 0.49 N/mm^2 on the gross crossed unit area, or 0.89 N/mm^2 on the gross unit area.

3.2.2. Standard Tests

The uniaxial compression tests were carried out under monotonic loading, with a load increment rate of about 0.5 kN/s (EN 1052-1, 1998). On all the specimens a 10 kN preload was applied. The specimens were instrumented with six LVDTs (±10 mm), two in the horizontal, two in the vertical direction on the main faces of the specimen, and two in the horizontal direction on the width. The results including maximum compressive stress σ_{max} (maximum applied load divided by the horizontal cross sectional area) are shown in Table 3.4. The elastic modulus, E, determined between 10-40% and 30-60% of the ultimate load and Poisson's ratio, v, evaluated on the first linear branch of the curve (10-40%) are also shown in Table 3.4.

Spec.	σ_{max} [N/mm^2]	$E_{10-40\%}$ [N/mm^2]	$E_{30-60\%}$ [N/mm^2]	v [‰]
TM	6.95	4497	4424	-0.45
TG	5.67	4924	4278	-0.36
Po	5.34	5237	4141	-0.25

Table 3.4. Uniaxial compression tests results. (da Porto et al., 2005)

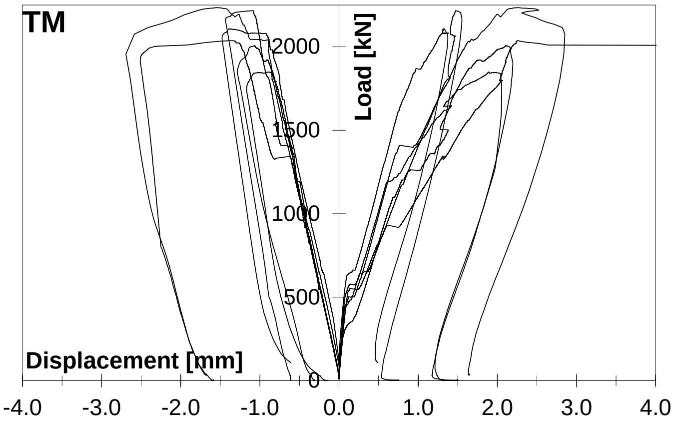

Fig. 3.3. Typical load displacement diagrams under uniaxial compression. Masonry made with thin layer joint. Vertical measured displacements are negative (left), horizontal displacements are positive (right).

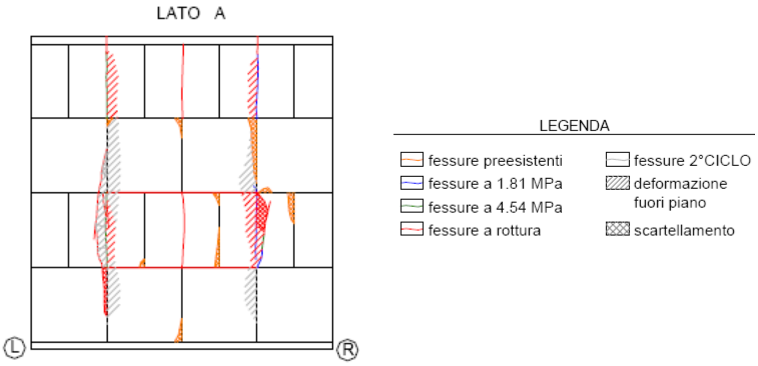

Fig. 3.4. Typical crack pattern under uniaxial compression. Masonry made with thin layer joint.

In almost all specimens, vertical cracks developed, starting from the central part of the façades, following the discontinuity of the head joints. This condition evolved until total collapse. In some cases, the test walls were completely split into columns at failure. Type of masonry did not influence the failure mode particularly. The compressive strength of TM masonry (thin-layer joints) was 23% higher than in TG (ordinary bed joint and interlocking units). TM specimens also showed lower deformability to vertical loads than TG specimens. Poisson’s coefficient (ratio between horizontal and vertical deformation) was higher by 25%. This coefficient was high in both TM and TG due to the dry mechanical interlocking between units at the head joints, which influenced the values of horizontal displacement on the first linear branch of the stress-strain curve. The compressive strength and elastic moduli of TG and Po (mortar pockets) masonry were practically equal, although the latter had lower values of compressive strength (-6%).

Fig. 3.3 shows a typical load-displacement diagram and Fig. 3.4 shows a typical crack pattern for the three types of tested specimens.

Diagonal compression tests were carried out under displacement control, at a rate of 0.01 mm/s. Loads were applied by two steel loading shoes, according to (ASTM E 519, 2007). Specimens were instrumented with four displacement transducers placed along the diagonals.

The results including nominal shear strength, τ_{max} (maximum applied load divided by the diagonal cross sectional area), shear modulus (G), shear strain (γ) evaluated between 10-40% and 30-60% of the ultimate load, shear strain $\gamma_{\tau max}$, and the vertical and horizontal strains ($\varepsilon_{v\tau max}$, $\varepsilon_{h\tau max}$) and their ratio at ultimate load are reported in Table 3.5. A typical load-displacement diagram (Fig. 3.5) shows the elastic-brittle behavior of the specimens that is due, however, also to the test configuration itself. In Fig. 3.6 is possible to see the typical crack pattern resulted from tests.

Spec.	τ_{max} [N/mm^2]	$G_{10\text{-}40\%}$ [N/mm^2]	$G_{30\text{-}60\%}$ [N/mm^2]	$\gamma_{10\text{-}40\%}$ [‰]	$\gamma_{30\text{-}60\%}$ [‰]	$\gamma_{\tau max}$ [‰]	$\varepsilon_{v\tau max}$ [‰]	$\varepsilon_{h\tau max}$ [‰]	$\varepsilon_{h\tau max}/\varepsilon_{v\tau max}$ -
TM	0.206	927	753	0.039	0.086	0.248	0.281	-0.033	-0.123
TG	0.270	1002	816	0.062	0.124	0.342	0.373	-0.032	-0.099
Po	0.537	1402	1213	0.071	0.154	0.399	0.459	-0.061	0.124

Table 3.5. Diagonal compression tests results. (da Porto et al., 2005)

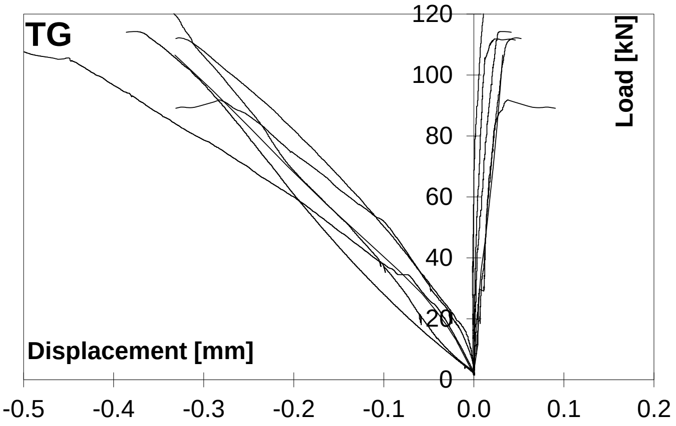

Fig. 3.5. Typical load displacement diagrams under diagonal compression. TG masonry. Vertical measured displacements are negative (left), horizontal displacements are positive (right).

In almost all specimens, collapse occurred suddenly, with the formation of stepped cracks which followed the head and bed joints along the loaded diagonal. Due to the loading configuration, displacements along the horizontal diagonal were smaller than in the vertical direction. In the case of TM, only cohesion of mortar-unit interface and friction were active. In the case of TG and Po, internal cohesion of mortar and dowel action of mortar droppings in the unit holes were also effective. The presence of mortar pockets exalted these effects. The nominal shear strength of TM masonry was 24% lower than that of TG. This was caused by the very high bond strength developing in general-purpose mortar. The nominal shear strength of Po masonry was exactly twice that of TG masonry, thanks to the resisting mechanisms which developed along the head joints.

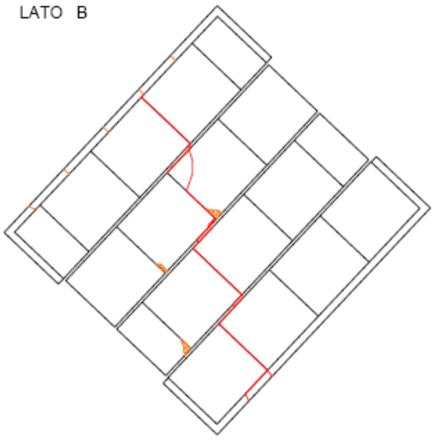

Fig. 3.6. Typical crack pattern under diagonal compression. TG Masonry.

3.2.3. In-plane Cyclic Tests

Specimens for evaluating the seismic behavior of masonry walls were sized about 1000x1250x300 mm. In-plane cyclic shear compression tests were carried out (RILEM TC76-LUMC3, 1991). Masonry walls were tested with a cantilever-type boundary condition, with fixed base and top end free to rotate, by applying centered and constant vertical loads of 17%, 22%, 27% and 33% of the mean compressive strength measured by the uniaxial compression tests. The lowest level (17%) was chosen to force rocking; the highest (27% and 33%) to obtain shear-type behavior; the intermediate level to have mixed failure mode. Horizontal cyclic displacements, with increasing amplitude and with peaks repeated three times for each displacement amplitude, were applied at a frequency of 0.004 Hz. One reference specimen per type was tested under monotonically increasing displacements. Fig.

3.7 shows the test set-up and the instrumentation scheme. For a complete description of test setup refer to (da Porto, 2005).

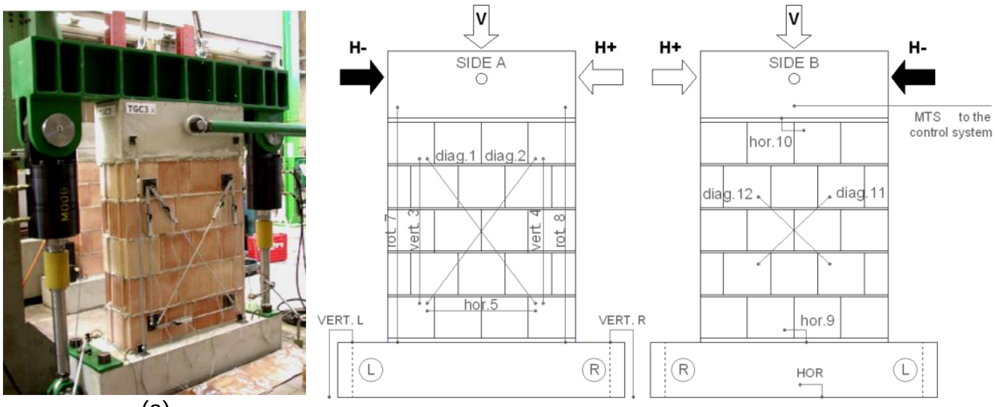

(a) (b)

Fig. 3.7. In-plane cyclic shear-compression: (a) test set-up; (b) instrumentation scheme.

During in-plane cyclic tests, the masonry walls attained four main limit states, which were used to idealize observed behavior. At first, specimen responses were linear elastic, with similar stiffness values. Rocking of specimens as rigid bodies caused the development of horizontal flexural cracks, generally located in the first mortar bed joint between the specimen and the lower concrete beam (H_f, δ_f). As tests continued, the first diagonally oriented shear crack also formed (H_{cr}, δ_{cr}). These cracks, passing both through joints and units, multiplied and increased until maximum resistance was reached (H_{max}, δ_{Hmax}). After developing their full displacement capacity, specimens reached the ultimate state (H_{dmax}, δ_{max}). In the following, this is anticipated when strength degradation of 20% occurred (H_u, δ_u). Fig. 3.8 shows the hysteresis loops of specimens tested under vertical loads of 27% of mean compressive strength; Fig. 3.9 shows the crack pattern of a TM specimen tested under the same vertical load. Finally Fig. 3.10 shows the envelope curves of experimentally obtained hysteresis loops.

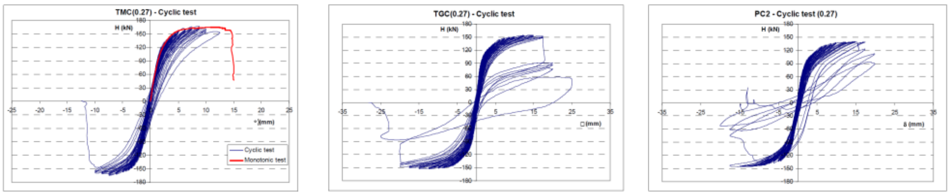

Fig. 3.8. Lateral load-displacement diagrams for specimens TM (left), TG (centre) and Po (right) tested under 27% ratio of applied vertical load to maximum compressive strength

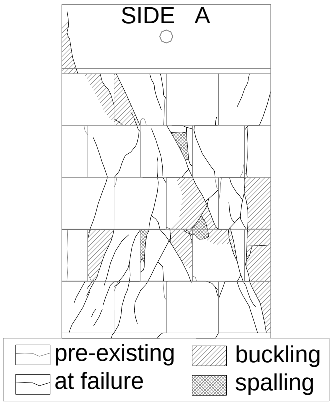

Fig. 3.9.Crack pattern after shear-compression test. (TM 27% specimen)

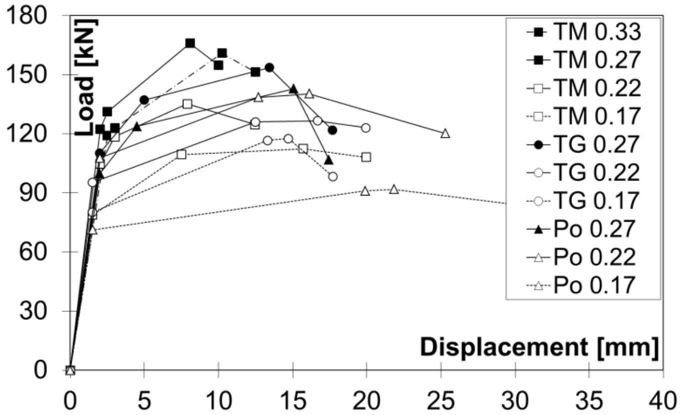

Fig. 3.10. Shear-compression envelope curves.

In terms of tensile strength, evaluated by the (Turnšek & Čačovič, 1971) criterion, differences among the three series were limited. Po masonry had tensile strength only 11% higher than the other masonry types. The rotation angle and displacement at damage limit state in Po specimens were 225% higher than in TM; in TG, they were 169% higher than in TM. The values at the ultimate limit state for Po were 103% higher than in TM; in TG, they were 44% higher than in TM. The ductility ratio, expressed as the ratio between ultimate displacement δ_u and displacement at the attainment of crack limit δ_{cr}, was high in the case of TM, although this was due to the low level of displacement at which the first shear crack opened, corresponding to a rotation angle of only 0.32%.

Table 3.6 lists the values of referential tensile strength f_t, experimental value of shear modulus G, ratio between lateral load and lateral displacements at the relevant limit states, and corresponding values of rotation angle at crack limit (θ_{cr}), maximum resistance (θ_{Hmax}) and ultimate limit state (θ_u). The dissipation capacity, evaluated both from the input and dissipated energy and the corresponding damping, and from the analysis of the hysteresis loops, was low for all the types of masonry and for a detailed descriptions of cyclic test results refers to (da Porto et al., 2009a).

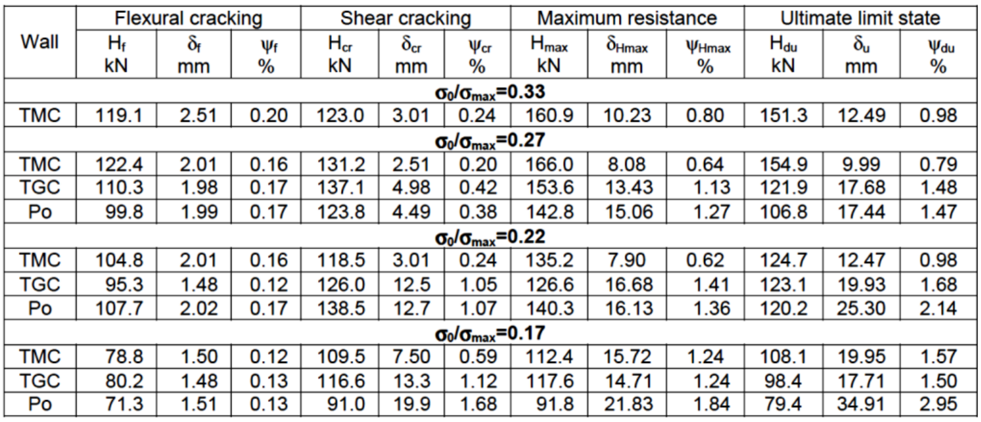

Wall	Flexural cracking			Shear cracking			Maximum resistance			Ultimate limit state		
	H_f kN	δ_f mm	ψ_f %	H_{cr} kN	δ_{cr} mm	ψ_{cr} %	H_{max} kN	δ_{Hmax} mm	ψ_{Hmax} %	H_{du} kN	δ_u mm	ψ_{du} %
σ_0/σ_{max}=0.33												
TMC	119.1	2.51	0.20	123.0	3.01	0.24	160.9	10.23	0.80	151.3	12.49	0.98
σ_0/σ_{max}=0.27												
TMC	122.4	2.01	0.16	131.2	2.51	0.20	166.0	8.08	0.64	154.9	9.99	0.79
TGC	110.3	1.98	0.17	137.1	4.98	0.42	153.6	13.43	1.13	121.9	17.68	1.48
Po	99.8	1.99	0.17	123.8	4.49	0.38	142.8	15.06	1.27	106.8	17.44	1.47
σ_0/σ_{max}=0.22												
TMC	104.8	2.01	0.16	118.5	3.01	0.24	135.2	7.90	0.62	124.7	12.47	0.98
TGC	95.3	1.48	0.12	126.0	12.5	1.05	126.6	16.68	1.41	123.1	19.93	1.68
Po	107.7	2.02	0.17	138.5	12.7	1.07	140.3	16.13	1.36	120.2	25.30	2.14
σ_0/σ_{max}=0.17												
TMC	78.8	1.50	0.12	109.5	7.50	0.59	112.4	15.72	1.24	108.1	19.95	1.57
TGC	80.2	1.48	0.13	116.6	13.3	1.12	117.6	14.71	1.24	98.4	17.71	1.50
Po	71.3	1.51	0.13	91.0	19.9	1.68	91.8	21.83	1.84	79.4	34.91	2.95

Table 3.6. Experimental. Lateral load, displacement and rotation angle at flexural cracking, shear cracking, maximum resistance and ultimate limit states. The values are average obtained at positive and negative displacement amplitudes (da Porto, 2005).

The specimens made with thin layer joints (TM) showed the lowest displacement capacity, in terms of rotation angle or drift. At each relevant limit state (shear cracking, attainment of maximum resistance and attainment of ultimate displacement) they presented values of drift respectively equal to -63%, -35%, -30% with respects to the specimens with ordinary bed joints (TG), and -69%, -45%, -51% with respects to the specimens with mortar pocket (Po). Apparently high values of ultimate ductility (ratio d_u/d_{cr}) for the specimens with thin layer joints, higher than for specimens TG and Po, are due to the very low value of displacement at the shear cracking limit d_{cr}, which corresponds to a rotation angle ψ_{cr} equal to only 0,32%. This low value can be compared to the limit value of inter-storey drift for damage limit state verification fixed by the codes, which is equal to 0.30% (Ordinanza P.C.M. n. 3274: 2003, 2005).

It can be also observed that the presence of the mortar pocket (Po) did not affect significantly the displacement capacity of the tested walls, if compared to the specimens made with ordinary bed joints and with tongue and groove indentation (TG). The comparison between the ductility indicators of the test series Po and TG at the relevant limit states (d_{cr}/d_{Hmax}, d_u/d_{Hmax}, d_u/d_{cr}), in fact, yield to the same values of ratio between the displacement at the opening of the first shear crack and the attainment of the maximum resistance (displacement capacity under increasing loads after the damage has already occurred). The values of the ratio between the ultimate displacement and the displacement at the maximum resistance and at the opening of the first shear crack are respectively 16% and 18% higher for the specimens Po than TG.

σ_0/ σ_{max} %	Sp.	Shear cracking			Maximum resistance			Specimen collapse		
		E_{inp} kNmm	E_{hys} kN mm	E_{hys} /E_{inp} %	E_{inp} kNmm	E_{hys} kN mm	E_{hys}/ E_{inp} %	E_{inp} kNmm	E_{hys} kN mm	E_{hys}/ E_{inp} %
33	TMC	4110	604	14.7	24327	3303	13.6	44181	6292	14.2
27	TMC	2953	452	15.3	26958	3698	13.7	38714	6130	15.8
	TGC	14124	1918	13.6	49112	5821	11.9	80719	12178	15.1
	PoC	9630	1208	12.5	54400	6210	11.4	62361	9697	15.6
22	TMC	3128	472	15.1	14200	1813	12.8	39534	7118	18.0
	TGC	35735	3194	8.9	54722	4554	8.3	78104	11334	14.5
	PoC	43586	4771	10.9	47186	5116	10.8	134350	20677	15.4
17	TMC	46132	5310	11.5	15198	1920	12.6	65648	10262	15.6
	TGC	23518	2914	12.4	31657	3804	12.0	86905	13620	15.7
	PoC	49911	3604	7.2	60713	4333	7.1	154170	18823	12.2

Table 3.7. Cumulative input and dissipated energy at shear cracking, maximum resistance and at collapse; values of coefficient of equivalent viscous damping at the same limit states.

σ_0/ σ_{max} %	Specimen	Shear cracking	Maximum resistance	Specimen collapse
		ξ_{cr} %	ξ_{Hmax} %	ξ_{du} %
33	TMC(0.33)	2.8	3.3	5.2
27	TMC(0.27)	2.6	3.9	5.9
	TGC(0.27)	2.6	3.0	14.7
	PC(0.27)	2.8	5.0	9.2
22	TMC(0.22)	2.9	2.9	21.8
	TGC(0.22)	2.0	2.1	13.0
	PC(0.22)	2.5	2.6	22.3
17	TMC(0.17)	2.9	37.2	10.8
	TGC(0.17)	2.8	3.0	10.9
	PC(0.17)	1.9	2.1	10.5

Table 3.8. Values of coefficient of equivalent viscous damping at shear cracking, maximum resistance and at collapse.

Regarding the energetic parameters, the values found in Table 3.7 and Table 3.8 show a low energy dissipation capacity for all the tested specimens. Apparent increases are only due to the large cycles characterized by an unstable response of the specimen before the collapse. Above all, the dissipation capacity is very similar for the three tested masonry typologies. The higher values of input and dissipated values for the specimens with ordinary joints (TG and Po) than with thin layer joints (TM) is mainly due to the higher displacements reached before collapse. However, it can be seen again that the ratio between dissipated and adsorbed energy are similar for the three tested series. For a more detailed description refer to (da Porto, 2005).

3.3. Reinforced Masonry Experimental Works and Results

The reinforced masonry system described here is based on the use of concentrated vertical reinforcement, similar to confined masonry. It is a new system of this type recently developed within the European Project (DISWall, 2008). Special clay units with horizontal holes and recesses for horizontal reinforcement are used (Fig. 3.11a). The recesses are grooves on the unit bed faces, where the horizontal reinforcement is simply laid. Mortar is used for bedding as commonly done during unreinforced masonry wall construction (Fig. 3.12). Vertically perforated units are used for the confining columns.

Vertical reinforcement in the columns is made of steel bars; horizontal reinforcement may be made of either steel bars or prefabricated steel trusses. The mortar was developed on purpose for this reinforced masonry system, in particular for what concern the properties of consistence, plasticity, and workability, to allow for a proper bed joint and recess filling and at the same time, also for a proper filling of the reinforced vertical cavities.

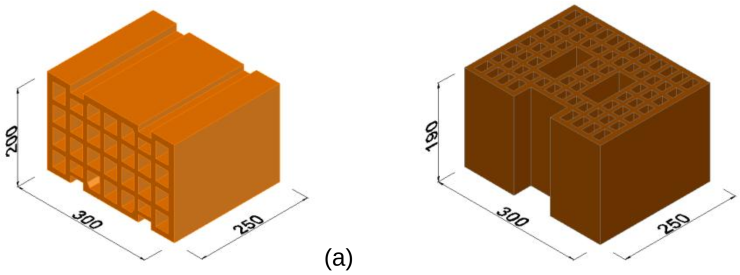

(a) (b)

Fig. 3.11. Details of (a) horizontally perforated unit (b) vertically perforated unit.

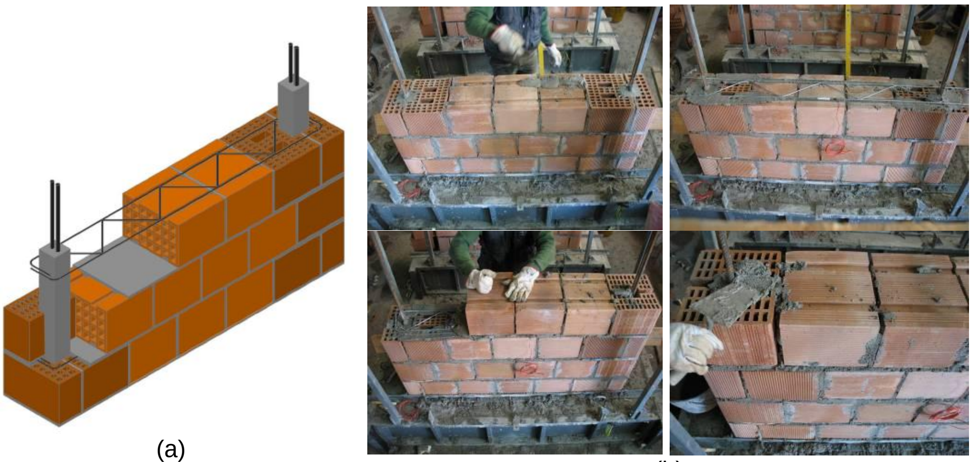

(a) (b)

Fig. 3.12. (a) Reinforced masonry system and (b) construction phases.

The main advantages of this system are related to durability and construction issues: placing the horizontal reinforcement into recesses filled with mortar improves reinforcement durability, makes the reinforcement positioning more precise and easier, allows producing good bond between mortar and units, and mortar and reinforcement. In addition, using units with horizontal holes helps fulfilling internal environment comfort conditions: this technique is traditionally adopted in the Mediterranean countries to improve thermal insulation. Units with horizontal holes could also benefit acoustic insulation, provided that head joints are covered with mortar, as it actually is.

Reinforced and confined types of masonry were developed to exploit the strength potential of masonry and to solve its lack of tensile strength, significantly improving not only resistance, but also ductility and energy dissipation capacity. In the last few decades, a great variety of reinforced and confined masonry techniques have been proposed. The various masonry systems depend on many parameters: geometric shape and material of units, composition of mortar and/or grout, and quantity and layout of reinforcement (Tomaževič, 1999).

As the new reinforced masonry system was designed for use in seismic areas, the main aim of the experimental program was to assess its behavior under in-plane cyclic actions. However, the effectiveness of horizontally perforated units in transferring horizontal loads to lateral confining columns may be reduced by unit brittleness and/or malfunctioning of the composite system at the interface between central masonry panels and confining columns. Hence, the basic properties of the constitutive materials (units, mortar and reinforcement) and the behavior of the reinforced masonry system in compression have been extensively investigated (da Porto et al., 2010b). As regards in-plane behavior under horizontal actions (i.e., seismic action), cyclic shear compression tests were carried out on fourteen full-scale specimens, differentiated by: presence or absence of vertical reinforced confining columns, use of steel bars or prefabricated trusses as horizontal reinforcement, aspect ratio (height to length ratio) of tested specimens, and value of applied axial compression loads. The tests characterized the mechanical behavior of the proposed construction system and allowed evaluation of the influence of these aspects on the main parameters (strength, ductility, energy dissipation, viscous damping, stiffness degradation) influencing the seismic behavior of reinforced masonry walls.

3.3.1. Basic material characterization

The geometry of units, physical properties of mortar, and composition of both units and mortar were especially developed for the new reinforced masonry system.

The horizontally perforated units were developed to optimize the behavior under in-plane actions, following the concept of robustness mentioned in (EN 1998-1: 2004. Eurocode 8, 2004) and in (Tomaževič et al., 2006) and (da Porto et al., 2010a).

The unit webs and shells were rectilinear and continuous, according to Italian seismic requirements (DM 14/01/2008, 2008) and were 12 mm thick. Web connections had a high curvature radius, and hole percentage was less than 45%. Nominal dimensions were 250 x 300 x 200 mm (length, width, height). The units contained 20% of tuff. This composition avoided shrinkage problems. Their mean compressive strength in the direction of vertical loads (f_{bm}) was 9.26 N/mm^2 and in the direction orthogonal to vertical loads, in the plane of the wall (f_{bhm}), it was 13.24 N/mm^2. Table 3.9 lists the mechanical properties of units.

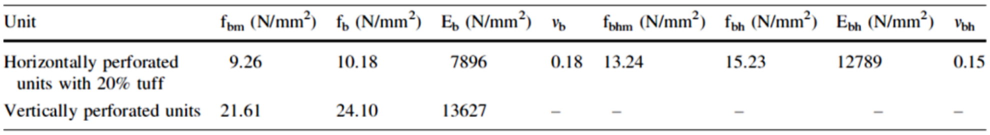

Unit	f_{bm} (N/mm^2)	f_b (N/mm^2)	E_b (N/mm^2)	ν_b	f_{bhm} (N/mm^2)	f_{bh} (N/mm^2)	E_{bh} (N/mm^2)	ν_{bh}
Horizontally perforated units with 20% tuff	9.26	10.18	7896	0.18	13.24	15.23	12789	0.15
Vertically perforated units	21.61	24.10	13627	–	–	–	–	–

Table 3.9. Mechanical properties of units with horizontal and vertical holes.

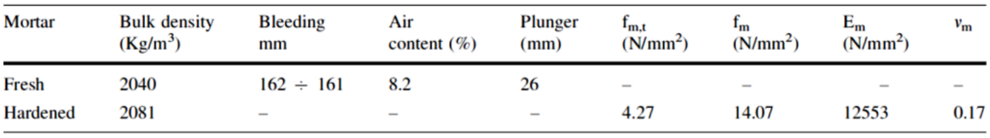

Mortar	Bulk density (Kg/m^3)	Bleeding mm	Air content (%)	Plunger (mm)	$f_{m,t}$ (N/mm^2)	f_m (N/mm^2)	E_m (N/mm^2)	ν_m
Fresh	2040	162 ÷ 161	8.2	26	–	–	–	–
Hardened	2081	–	–	–	4.27	14.07	12553	0.17

Table 3.10. Physical and mechanical properties of fresh and hardened mortar.

The main objective of mortar development was to use a single product, suitable for laying the horizontally perforated units and filling the vertical reinforced cavities. Mortar requirements were: compressive strength higher than 10 N/mm^2, as recommended by (EN 1998-1: 2004. Eurocode 8, 2004) and (DM 14/01/2008, 2008); balanced consistence, plasticity, and workability for bed and head joints and vertical cavities; good adhesion to units and reinforcement. Starting from two general-purpose M10 mortars, with hydraulic binder and aggregates with a maximum diameter of 4 mm, various modified mortars were produced, with plasticizing additives, which made fresh mortar more plastic, soft, workable and aerated, or powders for dispersal, which increased adhesion properties. During this developmental stage, a large variety of physical and chemical tests were carried out to check workability, bleeding properties, bulk density, air content, workable life. The mean flexural ($f_{m,t}$) and compressive (f_m) strengths of the final product after 28 days' curing were 4.27 N/mm^2 and 14.07 N/mm^2, respectively Table 3.10.

The horizontal reinforcement was made of B450C hot-rolled steel with yielding stress (f_y) of 500 N/mm^2 and elastic modulus of 204.4 kN/mm^2; the truss reinforcement had yielding stress of 486 N/mm^2 and elastic modulus of

203.7 kN/mm^2. The vertical reinforcement was made of B450 cold-drawn steel, with yielding stress of 501 N/mm^2 and elastic modulus of 189 kN/mm^2.

The detailed description of the basic mechanical tests is reported elsewhere (da Porto et al., 2010b; Mosele et al., 2008).

3.3.2. Standard Tests

As the new reinforced masonry system was designed for use in seismic areas, the main aim of the experimental program was to assess its behavior under in-plane cyclic actions. However, to give an assessment of the mechanical behavior a specific part of the experimental program was dedicated to the behavior of the system under uniaxial compression. The main aims of these tests were to gather information on material properties, to study the interactions between the various masonry portions under simple stress states, and to assess the overall performance in compression of the composite system, before more complex in-plane cyclic shear compression tests were carried out. The behavior of the reinforced masonry system in compression was studied both on specimens of the entire system and on its single components, i.e., confining columns and masonry panels without confining columns. The confining columns were built and tested with 3 (C3) and 5 (C5) rows of units. The masonry panels without confining columns were built using only horizontally perforated units, and adopting two types of horizontal reinforcement. In one series (SRHC), the horizontal reinforcement was made up of two ribbed reinforcing bars with 6-mm diameter. In the other series (TRHC), prefabricated truss reinforcement was used. In all specimens, the horizontal reinforcement was distributed at 400-mm intervals. Similarly, tests on specimens of the entire system were repeated on two series, one with two steel bars with 6-mm diameter at 400-mm intervals (SRC), and the other with prefabricated truss reinforcement at 400-mm intervals (TRC). The difference between SRHC–TRHC and SRC–TRC is that the latter also had vertical confining columns, reinforced with two ribbed steel bars with 16-mm diameter, at each edge. The amount of horizontal and vertical reinforcement was the same of that used in specimens for in-plane cyclic shear-compression tests, described in (da Porto et al., 2010b; Mosele, 2009). That amount was obtained following the provisions of the Italian code (DM 14/01/2008, 2008), taking the minimum prescribed horizontal reinforcement, and calculating the vertical reinforcement to force the shear failure of specimens. Table 3.11 lists the compression tests carried out and gives the specimen geometry. Fig. 3.13 shows the details of the elements tested in compression.

Name	Dimension (mm)	Horizontal reinf.	ρ_w (%)	Vertical reinf.	ρ_l (%)	No of tests
C3	380 × 300 × 650	–	–	–	–	3
				2Φ16	0.353	1
C5	380 × 300 × 1070			–	–	3
				2Φ16	0.353	1
SRHC	1030 × 300 × 1080	Rebar	0.035	–	–	3
TRHC	1030 × 300 × 1080	Truss	0.031	–	–	3
SRC	1550 × 300 × 1710	Rebar	0.045	4Φ16	0.173	1
TRC	1550 × 300 × 1710	Truss	0.040	4Φ16	0.173	1

Table 3.11. Characteristics of specimens for uniaxial compression tests.

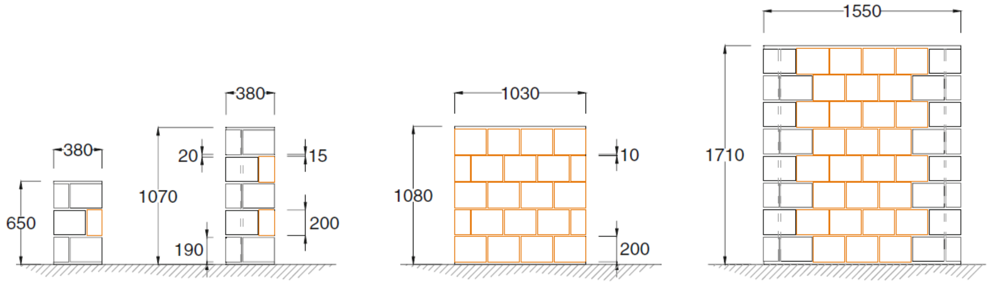

Fig. 3.13. Specimens for compression tests: confining columns (left); plain masonry (center); complete reinforced masonry system (right)

Table 3.12 lists compressive strength f_c (maximum load divided by gross horizontal cross-sectional area), elastic modulus E, between 10 and 40% of the maximum load, and Poisson's ratio v, evaluated on the first linear branch of the stress-strain curves. For a full detailed description of tests refers to (da Porto et al., 2010b; Mosele, 2009).

Test series	f_c (N/mm^2)	$E_{10-40\%}$ (N/mm^2)	v
C3[a]	5.44	7781	0.23
C5[a]	5.73	7587	0.23
Mean	5.58	7684	0.23
SRHC[a]	2.95	4225	0.18
TRHC[a]	2.48	4427	0.20
Mean	2.71	4326	0.19
SRC	4.11	6492	0.10
TRC	3.69	5231	0.12
Mean	3.90	5861	0.11

[a] Average on test series

Table 3.12. Results of uniaxial compression tests.

3.3.3. In-plane Cyclic Tests

The specimens were tested with a cantilever-type boundary condition, with fixed base and top end free to rotate, by applying centered and constant vertical loads of 11% and 16% of the measured maximum compressive strength of the reinforced masonry walls, corresponding to 15% and 22% of the measured maximum compressive strength of the walls without confining columns. The corresponding compressive stress levels (0.4 and 0.6 N/mm^2) are adequate to represent typical vertical loads for buildings from two to four storeys in height. Two specimens, one for each pre-compression level, constitute each series listed in Table 3.13.

Name	Dimension (mm)	Horizontal Reinf.	ρ_w (%)	Vertical Reinf.	ρ_l (%)	n° of tests
HS	1550x300x1690	-	-	-	-	2
SRHS	1550x300x1690	Rebar	0.045	-	-	2
TRHS	1550x300x1690	Truss	0.040	-	-	2
SRSa	1550x300x1690	Rebar	0.045	4Φ16	0.173	2
TRSa	1550x300x1690	Truss	0.040	4Φ16	0.173	2
SRSb	1030x300x1690	Rebar	0.045	2Φ16	0.130	2
TRSb	1030x300x1690	Truss	0.040	2Φ16	0.130	2

Table 3.13. Specimen details for shear compression tests.

Specimens were instrumented with 24 potentiometric displacement transducers to measure displacements, wall flexural and shear deformations, base uplift and relative sliding between wall and footing. Four strain-gauges were used to measure strains in both vertical and horizontal reinforcement bars at characteristic sections of the wall (see Fig. 3.14). Lateral and vertical loads were measured by means of load cells with the three hydraulic actuators used. The lateral displacement at the top of the wall was measured by a magnetostrictive displacement transducer, which was also used for retro-activation of the actuators. Fig. 3.14 (a, b, c) shows the instrumental scheme.

Fig. 3.15 (above) shows a view of the test set-up. Horizontal cyclic displacements, of increasing amplitude and with peaks repeated three times for each displacement amplitude, were applied at a frequency of 0.004 Hz (Fig. 3.15, below). Further details on tests setup, instrumentation and procedure are available in (Mosele, 2009).

During experimental tests, the attainment of four limit states, which can be used to idealize the behavior of the masonry wall, were observed. These limit states correspond to changes in how the specimens resist the progressive increment of applied lateral displacement.

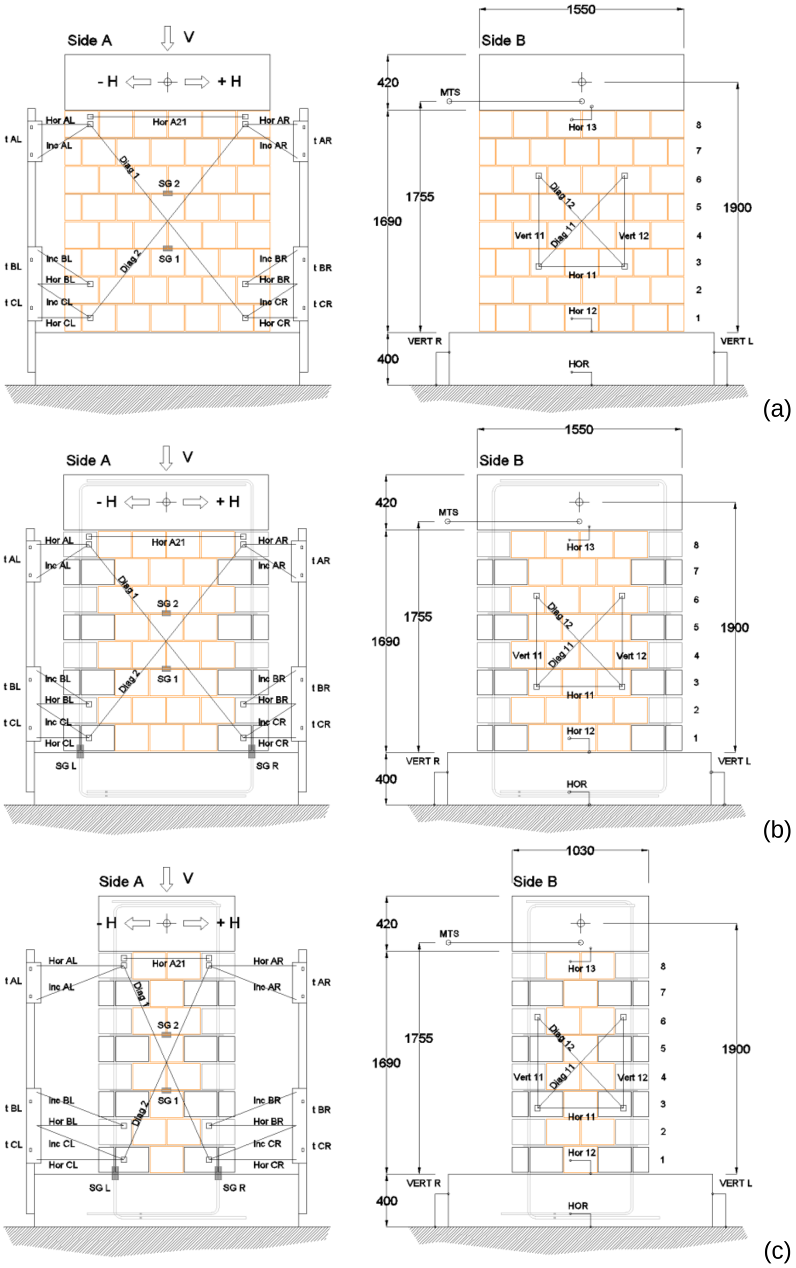

Fig. 3.14. Specimens and scheme of instruments for shear compression tests: (a) plain masonry; (b) squat and (c) slender reinforced masonry walls.

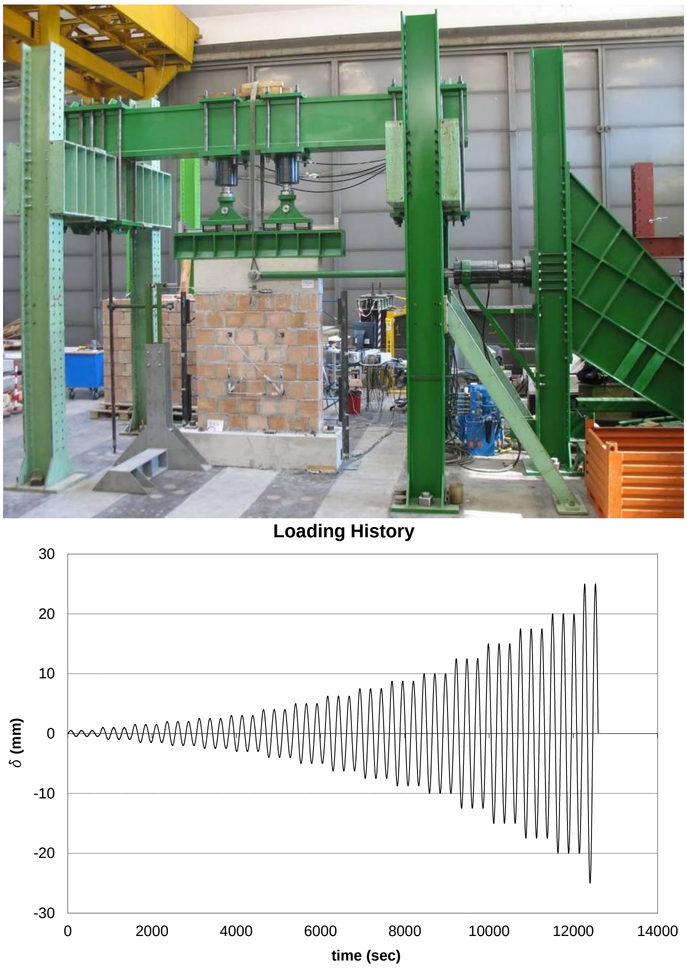

Fig. 3.15. Shear compression test set-up (above).
Horizontal displacement history (below).

This idealization, purposely developed for plain masonry (Abrams, 2001), was adapted to our reinforced masonry wall specimens.

Fig. 3.16 shows three specimens (TRHS, TRSa and TRSb) tested under compressive stresses of 0.6 N/mm^2, Fig. 3.17 shows the corresponding load-displacement diagrams, and Fig. 3.18 shows some details at failure. Fig. 3.19 compares limit states and the idealized envelope curves of all tested specimens. Lastly, Table 3.14 lists the values of lateral loads (H) and corresponding rotation angles ($\psi = \delta / H$) at the four limit states, the main load and ductility ratios, and observed failure modes.

The first non-linearity, due to the first cracks opening on the bottom bed-joints (H_f, δ_f), occurred at displacements of about 1 - 2 mm (mean rotation angle $\psi = 0.075\%$), independently of type of specimen or applied axial load.

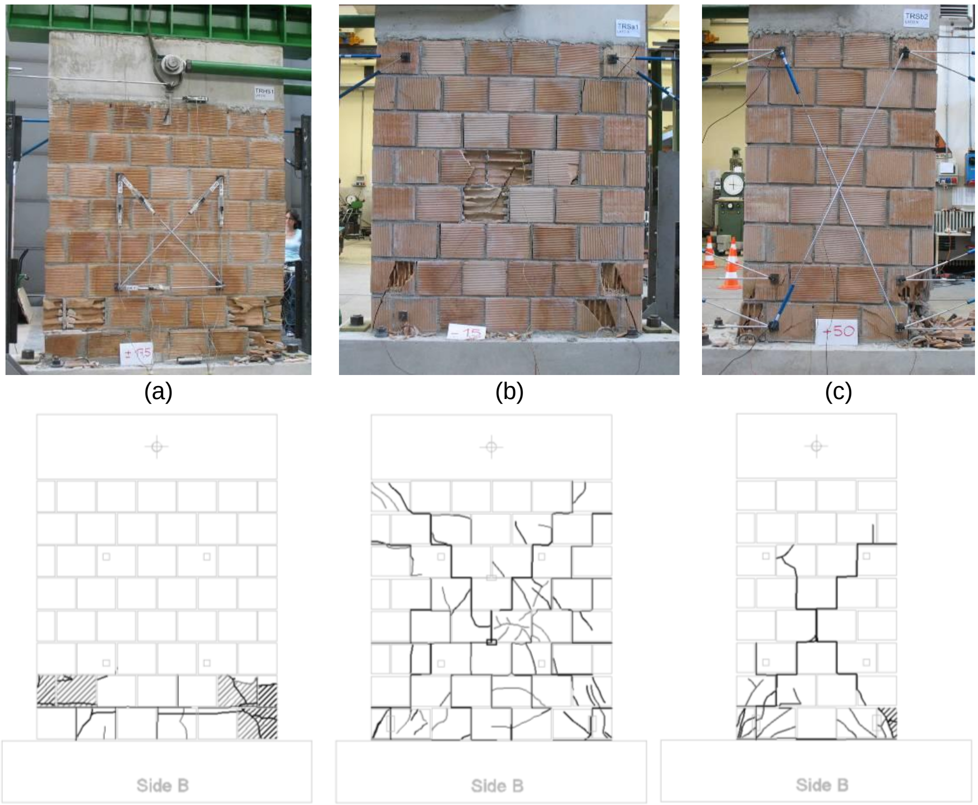

(a) (b) (c)

Fig. 3.16. Crack patterns at ultimate displacement in TRHS (a), TRSa (b) and TRSb (c) under compressive stresses of 0.6 N/mm^2.

In slender specimens, which were characterized by flexural failure and damage concentrated at the compressed toe (Fig. 3.16c), the following crack limit state (H_{cr}, δ_{cr}) occurred when the vertical bars yielded, at displacements of 9-12 mm (ψ = 0.50-0.70%), according to axial loads and type of horizontal reinforcement.

In squat specimens, characterized by shear failure mode (Fig. 3.16b), the second non-linearity took place when the first diagonal crack opened and strains of shear reinforcement simultaneously increased. This occurred at displacements of 5 mm (ψ=0.30%), independently of applied axial load.

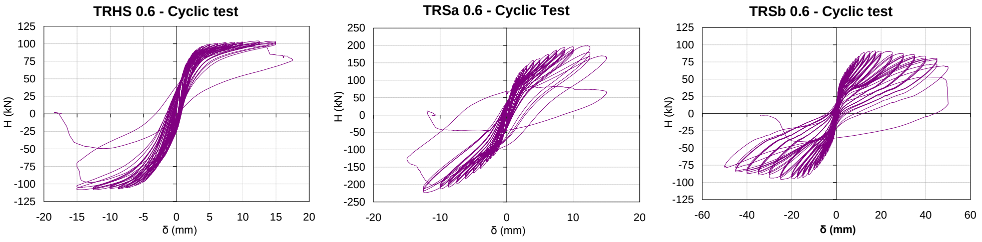

(a) (b) (c)

Fig. 3.17. Load displacement diagrams of (a) TRHS 0.6, (b) TRSa 0.6 and (c) TRSb 0.6.

(a) (b) (c)

Fig. 3.18. (a) Buckling of vertical bars in TRSa 0.4; (b) tension failure of vertical bars in SRSb 0.4; (c) transverse deformation of truss at end of test in TRHS 0.6.

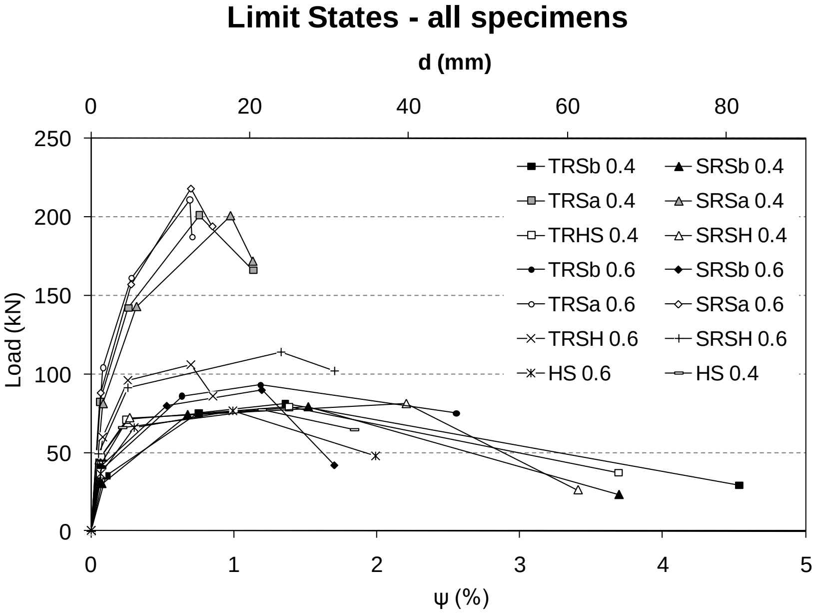

Fig. 3.19. Limit states envelop curves of masonry specimens.

Subsequently, in slender walls, loads increased gradually until maximum load (H_{max}) and the relevant displacement (δ_{Hmax}, Fig. 3.17c and Fig. 3.19) were reached. This condition represents the third limit state, and is characterized by crushing of masonry.

Conversely, squat specimens reached this state with consistently increased loads (Fig. 3.17b and Fig. 3.19), and with the formation of a diagonal strut, defined by cracks which crossed units and mortar joints. Spalling of units was also observed (Fig. 3.16b). At the lower axial load level, damage of the compressed toes due to buckling of vertical bars also occurred (Fig. 3.18a).

Specimen	H_f	ψ_f	H_{cr}	ψ_{cr}	H_{max}	ψ_{Hmax}	H_u	ψ_u	$H_{cr}/$	$H_u/$	$\psi_{cr}/$	$\psi_u/$	Failure
	kN	%	kN	%	kN	%	kN	%	H_{max}	H_{max}	ψ_{Hmax}	ψ_{cr}	mode
σ_0=0.6 N/mm²													
HS 06	36	0.07	66	0.31	77	0.99	48	1.99	0.86	0.63	0.31	6.42	R
TRHS 06	60	0.09	96	0.26	106	0.70	86	0.85	0.91	0.81	0.36	3.33	R
SRHS 06	49	0.06	91	0.26	114	1.33	102	1.71	0.80	0.89	0.20	6.58	R
TRSa 06	104	0.09	169	0.31	207	0.73	166	0.86	0.82	0.80	0.42	2.77	S
SRSa 06	88	0.06	159	0.31	217	0.74	182	1.04	0.73	0.84	0.41	3.41	S
TRSb 06	40	0.09	86	0.68	93	1.28	81	2.71	0.92	0.88	0.53	4.00	F
SRSb 06	41	0.08	80	0.53	89	1.20	70	1.81	0.90	0.79	0.44	3.42	F
σ_0=0.4 N/mm²													
HS 04	45	0.08	66	0.22	77	1.20	65	1.85	0.86	0.84	0.18	8.41	R
TRHS 04	47	0.07	71	0.25	79	1.39	37	3.69	0.90	0.47	0.18	14.76	R
SRHS 04	45	0.06	72	0.27	81	2.21	26	3.41	0.89	0.32	0.12	12.63	R
TRSa 04	82	0.07	144	0.30	199	0.70	160	1.25	0.72	0.80	0.44	4.13	S/F*
SRSa 04	81	0.09	137	0.30	200	1.04	149	1.45	0.68	0.75	0.29	4.80	S/F*
TRSb 04	32	0.10	74	0.73	79	1.18	68	3.29	0.94	0.87	0.62	4.53	F
SRSb 04	30	0.08	67	0.53	78	1.46	70	2.70	0.86	0.90	0.36	5.07	F

R = rocking, F = flexure, S = shear, S/F = combined shear/flexure mechanism

Table 3.14. Results of shear compression tests.

This phenomenon took squat specimens to the ultimate limit state with high strength degradation (10-15%) and low displacement capacity (12-20 mm, corresponding to ψ=0.70-1.14%, according to axial compression load). This ultimate limit state corresponded to the values of displacements δ_u (and loads H_u), at which the specimens still showed stable behavior, before reaching maximum experimental displacement and collapse. Slender walls had high displacement capacity (30-60mm, ψ=1.70-3.70%) and hence ductile behavior, due to flexural failure mode, which occurred with fracture of vertical bars, according to axial load (Fig. 3.18b).

In walls without vertical reinforcement, high values of ultimate displacements were due to rocking, and damage was concentrated at the bottom of the specimen (Fig. 3.16a and Fig. 3.18c).

The values of rotation angles at the ultimate limit state were weighed against those proposed by the Italian standard (DM 14/01/2008, 2008) for non-linear static analysis of reinforced masonry buildings. 1.2% assumed for flexural behavior and 0.6% assumed for shear behavior are moderately conservative, compared with the experimental values.

Lastly, the seismic response of buildings is related not only to strength and displacement capacity, i.e., ductility, of the structural members, but also to typical parameters of cyclic behavior, such as energy dissipation capacity, stiffness degradation and viscous damping coefficient, according to damage propagation. The energy dissipation capacity of our reinforced masonry system was lower than that usually reported for reinforced masonry walls (Bernardini et al., 1997; Magenes et al., 1996; Tomaževič et al., 1996). The ratio between dissipated and input energy of the complete reinforced masonry system ranges between 20% and 40% (Fig. 3.20). In any case, these values are still higher than those generally given for unreinforced masonry (da Porto et al., 2009a; Magenes & Calvi, 1997). The trend of the viscous damping coefficient is generally similar to that of energy dissipation capacity (Fig. 3.21). The viscous damping coefficient was about 5%, and tended to increase in the post-peak phase in reinforced masonry walls (TRS and SRS), whereas it remained constant for specimens without vertical reinforcement (HS series).

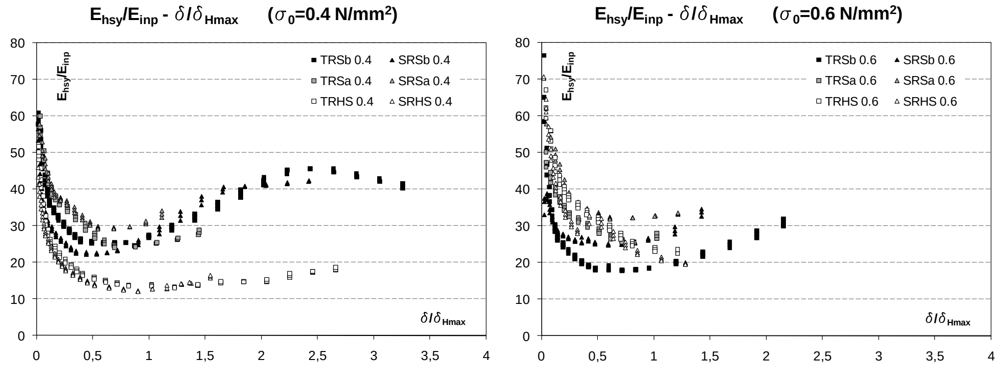

(a) (b)

Fig. 3.20. Ratio of dissipated/input energy vs normalized displacement. Specimens under (a) 0.4N/mm^2 and (b) 0.6N/mm^2.

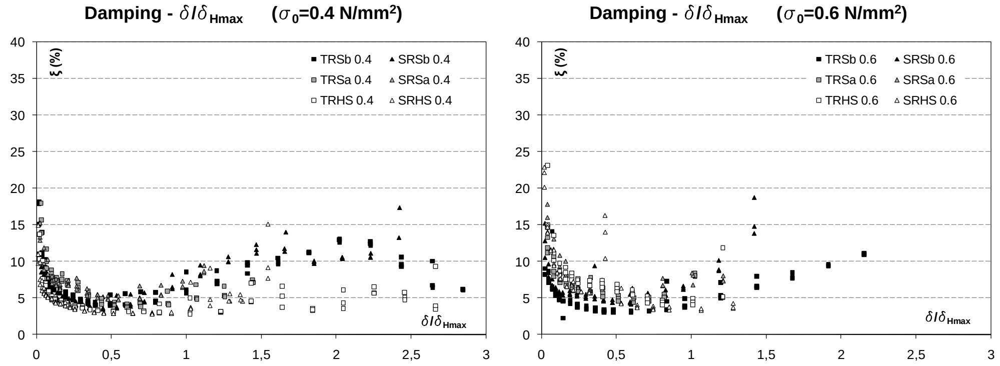

(a) (b)

Fig. 3.21. Viscous damping coefficient vs normalized displacement. Specimens under (a) 0.4N/mm^2 and (b) 0.6N/mm^2.

4. FINITE ELEMENT MODELS

4.1. Introduction

According to experimental results of extensive campaigns presented in previous chapter, aimed to defining the mechanical behavior of different load-bearing masonry systems both reinforced and unreinforced, a methodical process of Finite Element Model (FEM) calibration was carried out.

The procedure was done in order to obtain one single set of parameters that can be used with different modeling strategies and able to describe various types of test.

Experimental behavior was reproduced by different types of non-linear FEM models. Both macro- and micro-modeling strategies, implementing either the isotropic damage or orthotropic plastic model, were adopted.

Results allow some conclusions to be drawn about the behavior of the three unreinforced masonry types and the reinforced masonry system under investigation (in particular for shear-compression behavior) and the reliability of the modeling strategies.

Finally, in order to investigate the influence of principal geometrical and mechanical parameters on in-plane behavior of these load-bearing masonry systems, were extended the experimental results performing different parametrical analyses.

All FEM analyses were carried out using code DIANA™ release 9.3.

4.2. Unreinforced Masonry Walls

4.2.1. Different Modeling Approaches Presentation

Experimental results were reproduced by means of both macro- and micro-modeling strategies. A plane stress state was assumed in all adopted models, implementing actual experimental boundary conditions and loading schemes. Eight-node elements with a Gauss integration scheme were used in continuum models and for masonry units in micro models. In the discrete micro-models, six-node interface elements with the Lobatto integration scheme were also adopted.

The macro-modeling strategy implemented two types of constitutive laws: the isotropic total strain rotating crack model (Rots, 1997) and the orthotropic plastic model developed by (Lourenço et al., 1997). The first was implemented with linear softening in tension and parabolic curve in compression; the second applied the Rankine-Hill failure criterion. The simplified micro-modeling strategy implemented continuum elements, adopting both the above-mentioned constitutive laws for the expanded units. “Expanded” means that the head and bed joints were collapsed into zero-thickness interface elements and units were expanded to maintain the global geometry (Rots, 1997). The Coulomb friction criterion with parabolic compression cap and tension cut-off describes interface behavior (Lourenço & Rots, 1997). For a description of modeling background refer to paragraph 2.3.1.

Various simplified criteria were proposed to calibrate the numerical models.

The fracture energies of masonry in tension (G_{ft}) and compression (G_{fc}) were not experimentally evaluated but are needed by models approaches. These inelastic parameters were defined according to an extensive literature research for masonry and using Model Code 90 for concrete (FIP CEB, 1991), and were summarized into a database valid for masonry structures (da Porto et al., 2010a; Guidi, 2006) and summarized in Table 4.1.

The isotropic continuum model does not need any other parameter, as other elastic and strength values (elastic and shear modules and corresponding Poisson’s coefficient, masonry compressive and tensile strength) were experimentally determined.

Material / Fracture energy	G_{ft} N/mm	G_{fc} N/mm
Masonry unit	0.020 ÷ 0.080	15 ÷ 50
Masonry	0.018 ÷ 0.050	5 ÷ 20
Unit/joint interface	0.006 ÷ 0.018	5 ÷ 20

Table 4.1. Database of values for fracture energy of masonry.

Instead, the orthotropic plastic continuum model with Rankine-Hill failure criterion implements more parameters. To define the orthotropic values of elastic and strength parameters, one set of values was again based on the experimental results. The values along the orthogonal axis were evaluated by assuming direct proportionality with the net areas in the two orthogonal directions (Eq. 4.1):

$$\Pi_x = \Pi_y \cdot \left(\frac{A_{net,x}}{A_{net,y}} \right) \qquad \text{(Eq. 4.1)}$$

where $A_{net,x}$ and $A_{net,y}$ are net areas in the horizontal and vertical directions, taking into account the actual geometry of the perforated units, and Π_x and Π_y are generic mechanical properties in the horizontal and vertical directions. This simple criterion was assumed on the basis of the fragile nature of units.

According to the experimental data, the (EN 1992-1-1, 2004) at point 4.2.1.3.3(5) and (Lourenço, 1996b) recommendations, the value of strain at peak compressive strength for masonry was on average -2.2‰. Based on this value, it was possible to evaluate κ_p, which is the equivalent plastic strain at peak compressive strength, as required by the implemented failure criterion.

Other parameters had to be estimated are α, β and γ, which define the envelope of the Rankine-Hill failure criterion. For their evaluation, biaxial tests should be carried out. The values proposed by (Lourenço, 1996a) according to the experimental works of (Page, 1981; Page, 1983) on clay brick masonry and (Ganz & Thürlimann, 1982; Ganz & Thürlimann, 1984) on perforated clay block masonry, were assumed. Table 4.2 lists the parameters adopted by the orthotropic continuum model. The parameters of the isotropic continuum model can be inferred from the values in the vertical direction (y subscript).

Series	E_x N/mm^2	ν -	f_{tx} N/mm^2	G_{ftx} N/mm	f_{cx} N/mm^2	G_{fcx} N/mm	α -	γ -
TM	3191	0.45	0.177	0.018	4.93	17.03	0.71	2.13
TG	3143	0.36	0.158	0.018	3.62	16.51	0.64	1.91
Po	3185	0.25	0.167	0.018	4.93	16.36	0.61	1.82
	E_y N/mm^2	G_{xy} N/mm^2	f_{ty} N/mm^2	G_{fty} N/mm	f_{cy} N/mm^2	G_{fcy} N/mm	β -	κ_p ‰
TM	4497	1551	0.249	0.018	6.95	17.81	-1	0.65
TG	4924	1810	0.247	0.018	5.67	17.32	-1	1.05
Po	5237	2095	0.274	0.018	6.95	17.19	-1	1.18

Table 4.2. Parameters of orthotropic continuum model. Parameters of isotropic total strain rotating crack model can be obtained from values in y-direction.

The procedure of unit expansion and mortar joint collapse in the interface models defines the linear stiffness k_n and k_s (respectively normal and tangential) of the interface elements. Classical formulations in the literature lead to overestimation of stiffness values. These are generally reduced to carry out analysis (Chaimoon & Attard, 2007; Lourenço, 1996a; Rots, 1997). In the present study, this procedure was based on the correction factor Δ, based on experimentally measured displacements (Eq 4.2):

$$\Delta = \left(\frac{h_u + h_m}{E_{\exp}} \right) - \left(\frac{h_u}{E_u} + \frac{h_m}{E_m} \right) \qquad \text{(Eq. 4.2)}$$

where h_u and h_m are, respectively, the heights of unit and mortar joint, E_{exp} is the global experimental elastic modulus of masonry, and E_u, E_m are the experimental elastic moduli of units and mortar. Mathematical models assume that there is perfect contact at the interface, whereas the correction takes into account the fact that, in reality, obvious irregularities are found in mortar joints and unit-joint interfaces (Vermeltfoort, 2005). The elastic material displacement (Δl_{tot}), seen as the sum of the ideal elastic displacement of unit and mortar, thus becomes (Eq 4.3):

$$\Delta l_{tot} = \sigma \frac{h_u}{E_u} + \sigma \frac{h_m}{E_m} + \sigma\Delta = \sigma \frac{h_u}{E_u^{'}} + \sigma \frac{h_m}{E_m^{'}} \qquad \text{(Eq. 4.3)}$$

where σ represents the stress state; E'_u and E'_m are the corrected elastic moduli of units and mortar, that are assumed to be reciprocally proportional to the ratio of the corresponding displacement to the elastic material displacement. The common equivalence between elastic material displacement and model displacement yielded the elastic moduli of expanded unit, E'_u (Eq. 4.4a), and mortar, E'_m (Eq. 4.4b). Applying the basic equations of mechanics, the interface normal k_n and shear stiffness k_s were thus evaluated.

$$E_u^{'} = \frac{h_u}{\frac{h_u}{E_u} + \left(\frac{\Delta}{L} \cdot \frac{h_m}{E_m}\right)} \quad \text{(a)} \qquad E_m^{'} = \frac{h_m}{\frac{h_m}{E_m} + \left(\frac{\Delta}{L} \cdot \frac{h_u}{E_u}\right)} \quad \text{(b)} \qquad \text{(Eq. 4.4)}$$

The other parameters needed to define the failure criterion were chosen according to the literature. Dilatancy angle (ψ) was assumed to be zero, as it tends toward zero with the increase in normal stresses. This choice also avoids non-conservative predictions of shearing resistance (Rots, 1997; van Zijl, 2004).

C_s defines the contribution of shear stresses to failure (Lourenço, 1996a); its value was chosen in order to fit the cap model with the experimental results. The values of fracture energy in tension (G_{ft}) and compression (G_{fc}) were found as explained above. In addition, for mode II fracture energy in shear (G_{fs}), the formulation proposed by (Lourenço, 1996a) was used. To complete the interface definition, the equivalent plastic strain was evaluated following the same criteria already explained for the continuum model. Table 4.3 lists the interface parameters in both isotropic and orthotropic discrete models. For TM and TG, some head joint interface properties are set with values close to zero, to simulate the absence of mortar in vertical joints, without losing friction and compression properties.

Complete definition of the interface model also requires setting constitutive laws for expanded units. In this case, the model relies on the properties of the single units and not on those of the masonry walls. For the isotropic interface model, the elastic and strength properties of the units were experimentally determined. The inelastic parameters were found as explained previously. For the interface model with orthotropic plastic failure of units, orthotropic properties were defined by applying the criterion expressed by (Eq. 4.1). Table 4.4 lists the unit parameters adopted in the orthotropic discrete model. The parameters implemented by the isotropic discrete model correspond to values in the y-direction.

Bed joint interface	k_n N/mm^3	k_s N/mm^3	f_t N/mm^2	f_c N/mm^2	G_{ft} N/mm	G_{fc} N/mm
TM	34.90	14.42	0.36	25	0.026	20
TG	57.13	24.88	0.89	25	0.050	20
Po	69.46	30.17	0.89	25	0.063	20
	c N/mm^2	tgφ -	tgψ -	C_s -	G_{fs} N/mm	κ_p ‰
TM	0.44	0.40	0	16	0.044	1.40
TG	0.90	0.64	0	16	0.090	0.34
Po	0.90	0.64	0	16	0.090	0.67
Head joint interface	k_n N/mm^3	k_s N/mm^3	f_t N/mm^2	f_c N/mm^2	G_{ft} N/mm	G_{fc} N/mm
TM	25.10	10.36	0.00025	11	0.00002	19.29
TG	33.00	14.34	0.00025	11	0.00002	19.29
Po	38.20	16.62	0.21	11	0.018	19.29
	c N/mm^2	tgφ -	tgψ -	C_s -	G_{fs} N/mm	κ_p ‰
TM	0.05	0.09	0	16	0.005	0.42
TG	0.05	0.09	0	16	0.005	0.86
Po	0.36	0.64	0	16	0.036	1.04

Table 4.3. Parameters for interface in orthotropic discrete model and in discrete model implementing isotropic total strain rotating crack constitutive law for unit.

Unit	E_x N/mm^2	ν -	f_{tx} N/mm^2	G_{ftx} N/mm	f_{cx} N/mm^2	G_{fcx} N/mm	α -	γ -
TM	6615	0.22	0.332	0.024	7.57	17.03	0.71	2.13
TG	5104	0.17	0.300	0.022	9.10	16.51	0.64	1.91
Po	4797	0.14	0.352	0.025	7.95	16.36	0.61	1.82
	E_y N/mm^2	G_{xy} N/mm^2	f_{ty} N/mm^2	G_{fty} N/mm	f_{cy} N/mm^2	G_{fcy} N/mm	β -	κ_p ‰
TM	9269	3799	0.468	0.034	20.42	17.81	-1	0.90
TG	7767	3319	0.472	0.034	20.96	17.32	-1	0.36
Po	7704	3379	0.579	0.042	20.43	17.19	-1	0.45

Table 4.4. Parameters for unit material in orthotropic discrete model. Parameters of isotropic total strain rotating crack micro-model can be obtained from values in y-direction

The geometry meshing took advantage of specimen regularity. Structured regular mesh was, thus, used. The mesh sensitivity problem was also taken in to account, but with a reasonable number of subdivision model showed a good stability response. Actually, mesh refinement had a neglectable influence on global response of models. This is in agreement with the used implementation of fracture energies in DIANA™. Material constitutive laws were based on fracture energy by the definition of the crack bandwidth (*h*) of the element, for which DIANA™ assumes a value *h* related to the square root of the area of the element (De Witte & Kikstra, 2005).

Iterative process of FEM analyses was conducted using Newton-Raphson method (see Fig. 4.1a) with indirect displacement control, i.e. applying force but using arch-length algorithm able to describe snap-back behaviors. Line-search algorithm was also used to improve both stability and speed of convergence process.
Furthermore during the analysis procedure was used a DIANA™ option able to auto-adapt the load step magnitude based on previous step number of iteration (in a given range).

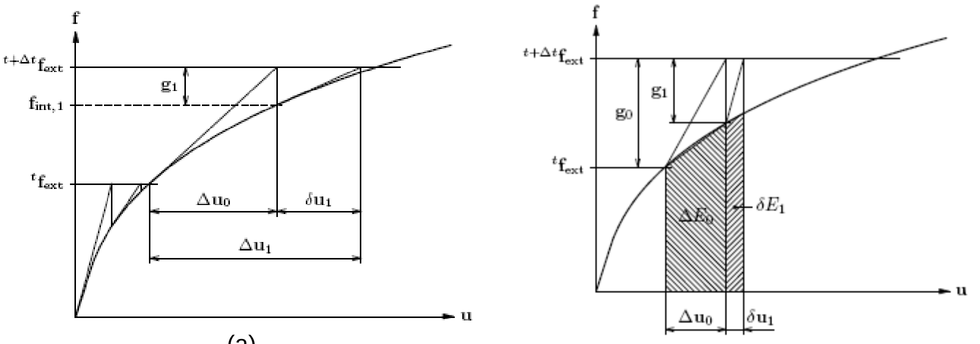

(a)

(b)

Fig. 4.1. Ratio of dissipated/input energy vs normalized displacement. Scheme of iterative method of Newton-Raphson (a) convergence criterion adopted (b) (De Witte & Kikstra, 2005).

An energetic convergence criterion was adopted. It is based on ratio between norm of internal forces and displacement product at current iteration, and norm of internal forces and displacement product at the start of load step (Fig. 4.1b). Tolerance was imposed to be less than 10^{-4} with reference to (Eq. 4.5).

$$\left\| \frac{\delta u_i^T \left(f_{\text{int},i+1} + f_{\text{int},i} \right)}{\Delta u_0^T \left(f_{\text{int},1} + f_{\text{int},0} \right)} \right\| < 10^{-4} \qquad \text{(Eq. 4.5)}$$

4.2.2. Standard Tests and In-plane Cyclic Envelopes Modeling

All type of FEM models, described in previous section, were used to analyze the experimental tests presented in paragraph 3.2.

The uniaxial compression tests analyses, carried out with these different models, gave similar results, apart from the isotropic continuum model. The latter can reproduce the behavior of masonry walls until first crack opening, but cannot reach the ultimate state, whereas the other models can very well reproduce both the value of the experimental ultimate load ($P_{u,e}$, Table 4.5) and deformability along the direction of loading.

Series	Exp.	Continuum Orthotropic		Continuum TSRCM		Micro-model Orthotropic		Micro-model TSRCM	
	$P_{u,e}$ kN	$P_{u,m}$ kN	$P_{u,m}/P_{u,e}$ %	$P_{u,m}$ kN	$P_{u,m}/P_{u,e}$ %	$P_{u,m}$ kN	$P_{u,m}/P_{u,e}$ %	$P_{u,m}$ kN	$P_{u,m}/P_{u,e}$ %
Uniaxial compression									
TM	2050	2036	99	1307	64	2041	99	2047	100
TG	1686	1674	99	1307	78	1679	99	1685	100
Po	1583	1577	99	1253	79	1588	100	1588	100
Diagonal compression									
TM	86	491	568	165	191	85	99	86	100
TG	114	356	314	162	143	119	105	92	81
Po	211	327	155	190	90	223	106	203	96

Table 4.5. Uniaxial and diagonal compression, experimental ($P_{u,e}$) and numerical ($P_{u,m}$) ultimate loads.

The models reproduce vertical displacements (negative in Fig. 4.2) better for TG and Po specimens than for TM specimens, where they are stiffer than real walls. They correctly estimate horizontal displacements (positive in Fig. 4.2) until the opening of the first crack, but then underestimate them. This happens because experimental horizontal displacements undergo a sudden discontinuity when the first crack opens. The continuum orthotropic model is the only one that is able to average the trend of horizontal displacements before and after crack opening. Regardless of masonry type, the test set-up induces concentration of stresses in the center of specimens. The experimentally observed occurrence of the first cracks at that point confirms the results of the numerical simulation.

The main difference in the behavior of the three tested masonry types lay in the presence of the vertical mortar joint in Po specimens, which produces better distribution of tensile stresses induced by compression (Fig. 4.3, where the mesh was hidden in order to highlight stress distribution). However, due to the higher tensile stresses which filled head joints can transfer to units, collapse occurs earlier and the ultimate load correspondingly decreases, when compared with TG specimens (Table 4.5), matching experimental evidence.

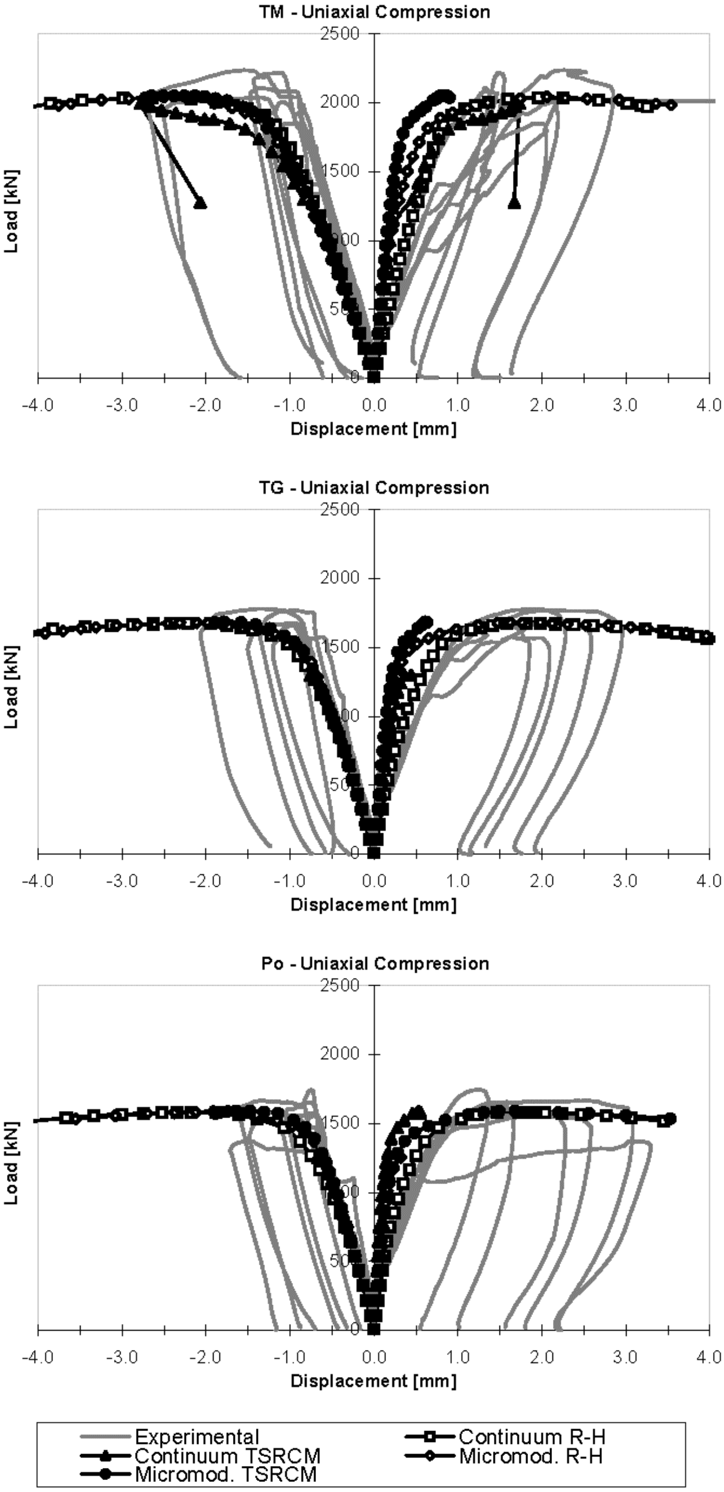

Fig. 4.2. Uniaxial compression: experimental and numerical load displacement diagrams.

Only micro-models can describe this particular behavior, as they adequately reproduce stress concentrations in units and joints. Masonry with ordinary bed joints (TG) and thin-layer joints (TM) do not show particular differences in terms of stress distribution, although at the same level of applied load, thin joints induce lower tensile stresses in the block (Fig. 4.3), thus causing the experimentally observed increase in compressive strength with respect to TG specimens.

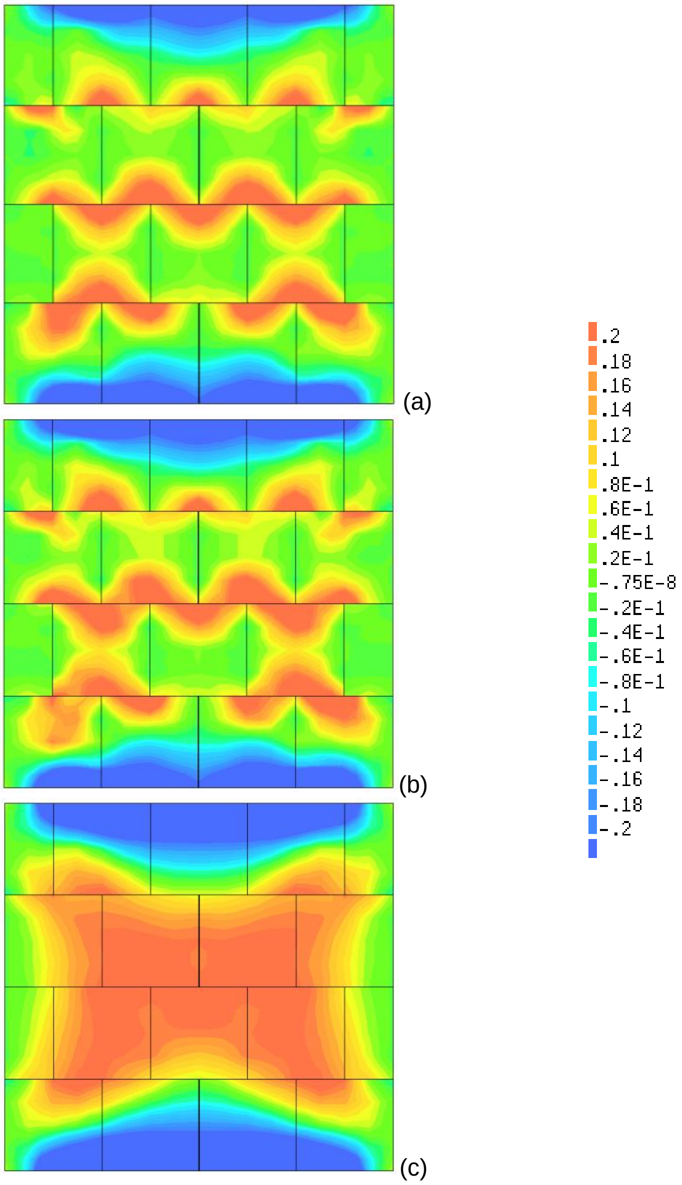

Fig. 4.3. Uniaxial compression: interface model with orthotropic units. Principal tensile stresses at 50% of TM ultimate load: (a) TM, (b) TG; (c) Po.

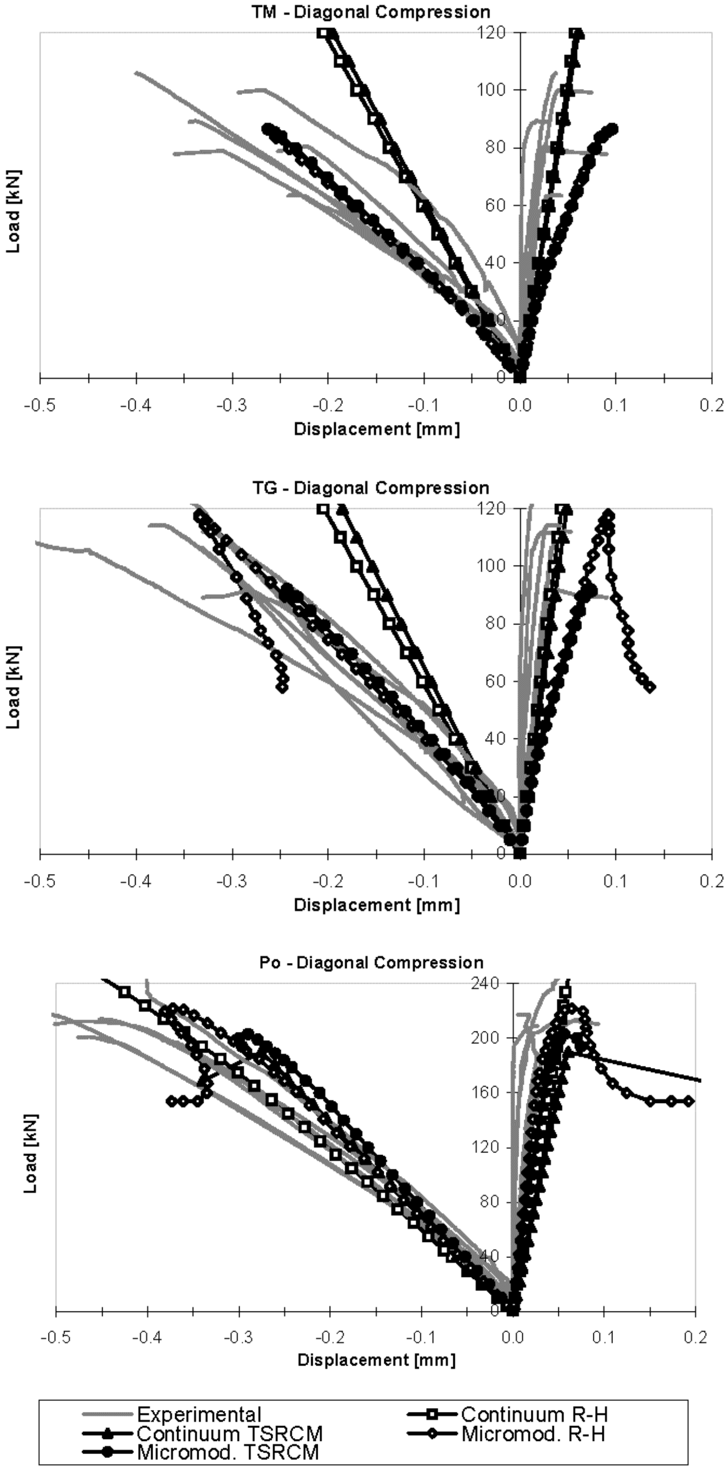

Fig. 4.4. Diagonal compression: experimental and numerical load displacement diagrams.

Diagonal compression tests gave differing results. In terms of both stiffness (Fig. 4.4) and ultimate load ($P_{u,e}$, Table 4.5), micro-models generally showed good agreement with experimental behavior, whereas continuum models significantly overestimated ultimate loads. Experimental horizontal displacements were lower than numerical ones, but their small extent, close to measuring device sensitivity, should be taken into account. When first setting of joints occurs, between 20 and 40 kN, micro-models show decreased stiffness.

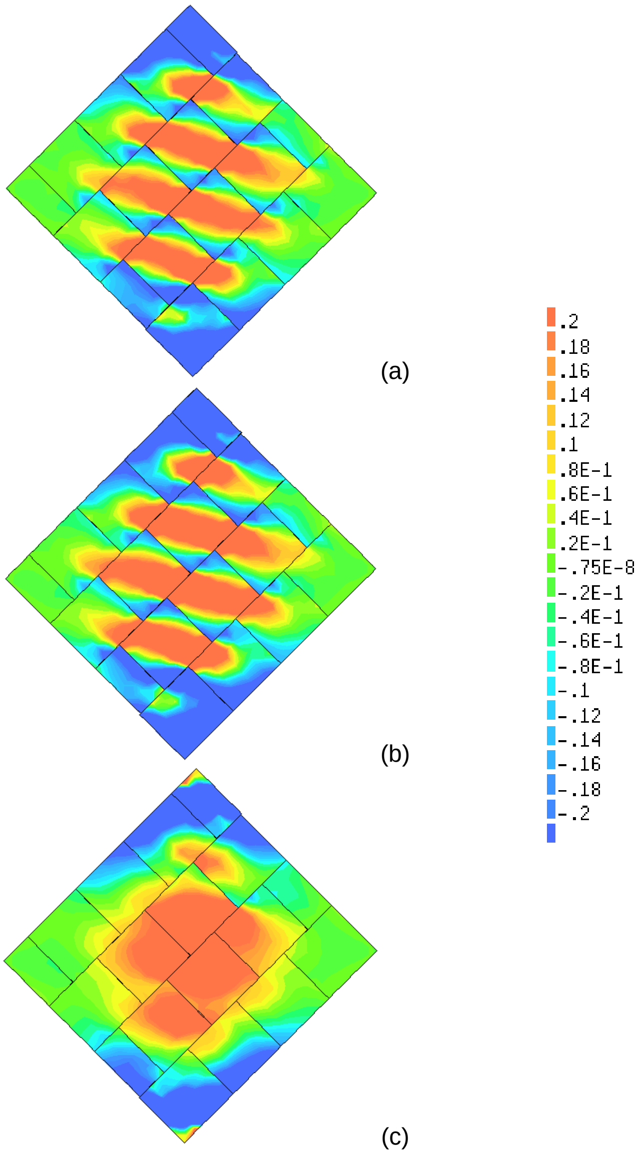

Fig. 4.5. Diagonal compression: interface model with orthotropic units. Principal tensile stresses at ultimate load: (a) TM, (b) TG; (c) Po.

The absence of filled head joints in the TG and TM specimens leads to a distribution of principal stresses which differs from homogeneous distributions of continuum materials. Stresses are concentrated in parallel diagonal bands that can be identified only by micro-models. These stress bands follow the masonry texture, not the main geometric diagonal of walls. Therefore, areas close to head joints are almost completely unloaded (Fig. 4.5a, b). This distribution is favored by unit geometry (shape and dimension) and masonry bond arrangement (one-layer masonry with simple overlap and unfilled head joints). Collapse thus occurs in both experimental tests and micro-models, due to concentration of tensile stresses in bed joints around the central unit. Failure is initially located there, then other joints along the same direction fail and the specimens separate into two portions. Thanks to its mortar pockets, Po masonry shows a stress distribution that is closer to that of homogeneous solids (Fig. 4.5c). Strength thus increases, as experimentally observed, and the results of continuum and discrete models become similar (Table 4.5). In addition, all the proposed modeling strategies are able to reproduce the experimental stiffness values (Fig. 4.4).

In general, all models confirm the fragility of the collapse mode, but isotropic micro-models describe deformation behavior better. The models also highlight the fact that, when a diagonal test set-up is applied to masonry walls made with large units and unfilled head joints, the resulting stress distribution strongly influences specimen behavior. As already observed by (Bosiljkov, 2001), specimen failure modes depend on the most unfavorable combination of possible failure mechanisms, and may significantly differ from failure modes observed on real walls.

Series	Exp. 22%	Continuum TSRCM		Micro-model TSRCM		Exp. 27%	Continuum TSRCM		Micro-model TSRCM	
	$H_{max,e}$ kN	$H_{max,m}$ kN	$H_{max,m}/H_{max,e}$ %	$H_{max,m}$ kN	$H_{max,m}/H_{max,e}$ %	$H_{max,e}$ kN	$H_{max,m}$ kN	$H_{max,m}/H_{max,e}$ %	$H_{max,m}$ kN	$H_{max,m}/H_{max,e}$ %
TM	135	134	99	139	103	166	160	96	158	95
TG	127	119	94	123	97	154	142	92	147	96
Po	140	111	79	118	84	143	132	92	142	99

Series	Exp. 22%	Continuum TSRCM		Micro-model TSRCM		Exp. 27%	Continuum TSRCM		Micro-model TSRCM	
	$\theta_{u,e}$ %	$\theta_{u,m}$ %	$\theta_{u,m}/\theta_{u,e}$ %	$\theta_{u,m}$ %	$\theta_{u,m}/\theta_{u,e}$ %	$\theta_{u,e}$ %	$\theta_{u,m}$ %	$\theta_{u,m}/\theta_{u,e}$ %	$\theta_{u,m}$ %	$\theta_{u,m}/\theta_{u,e}$ %
TM	0.89	0.54	61	0.85	95	0.72	0.57	79	0.65	90
TG	1.43	1.13	79	1.21	85	1.27	0.73	57	1.18	93
Po	1.64	0.93	57	1.49	91	1.25	0.76	61	1.25	100

Table 4.6. Cyclic shear-compression, experimental ($H_{max,e}$) and numerical ($H_{max,m}$) maximum load and experimental ($\theta_{u,e}$) and numerical ($\theta_{u,m}$) maximum drift.

In shear-compression tests simulation the horizontal load was applied as a controlled displacement at the central node in the top concrete beam.

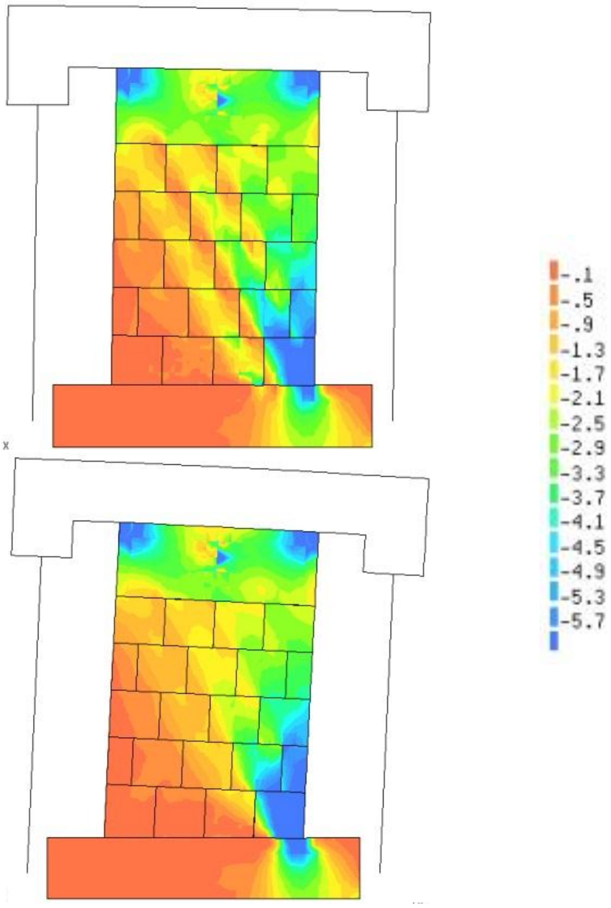

Fig. 4.6. Shear-compression. Interface model with isotropic units. Principal compression stress at maximum strength of walls: TG 27% (above) and Po 27% (below) (legend is in N/mm^2).

The analyses of continuum models were very sensitive to parameters defining tensile strength and, due to concentration of stresses in the compressed toe of masonry, also to those defining compressive strength. Particularly the orthotropic continuum model presented anticipated failure and also modified the experimentally observed sequence of damage mechanisms.

Isotropic micro-models reproduced experimental behavior fairly well without any correction of parameters extracted by the previous model calibration phase, i.e. the standard test reproduction. Instead, orthotropic micro-models did not reproduce experimental behavior very well, and also presented anticipated failure very often. For this type of model and loading scheme, the adopted calibration procedure, which gave good results for monotonic and diagonal compression, was not effective. However, all the various models were able to reproduce initial elastic stiffness fairly well, although continuum models were always slightly stiffer than micro-models. Comparison of the various masonry types showed that their behavior was similar.

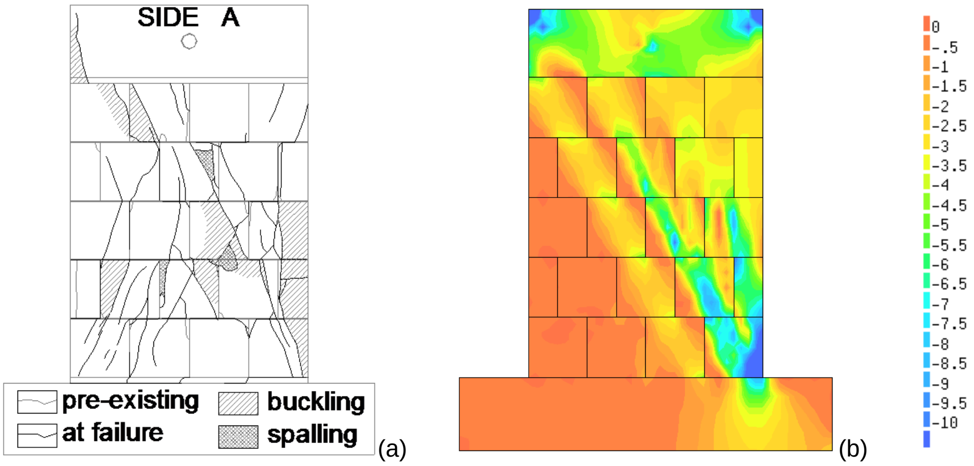

Fig. 4.7. Shear-compression, TM with vertical load of 27%: experimental crack pattern (a) and numerical principal compression stress at ultimate load (b) of compressive strength.

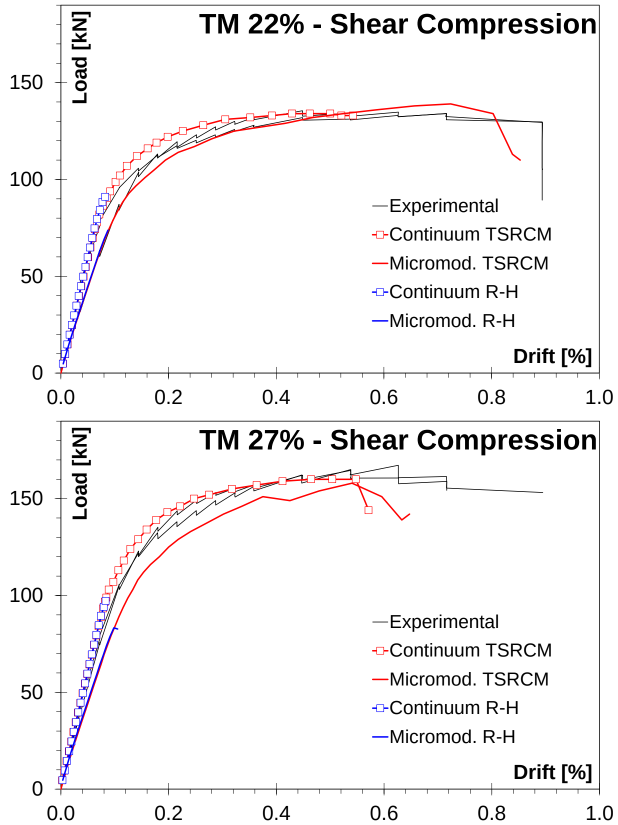

Fig. 4.8. Shear-compression envelope curves: experimental and numerical load drift-diagrams: TM with vertical load of 22% (above) and 27% (below) of compressive strength.

The only difference was seen in masonry with mortar pockets (Po) that again showed better stress distribution than the other masonry types, and a higher tendency to rocking, as experimentally observed (see as example Fig. 4.6).
From Fig. 4.8 to Fig. 4.10 are show the comparison between experimental behavior, represented by the envelope of the hysteresis loops, and numerical results, for the three masonry types and for specimens tested under compressive loads of 22% and 27% of their compressive strength. Both isotropic models, which gave the best results, reproduced stiffness and maximum horizontal loads very well, which were only slightly underestimated (generally between -1% and -8%). Isotropic micro-models were also able to estimate maximum displacement with an acceptable error, between 0% and -15% (see Table 4.6). Both these modeling strategies could reproduce the observed sequence of failure mechanisms and, in particular, the isotropic micro-models presented crack patterns consistent with experimental ones (see, for example, Fig. 4.7a and b).

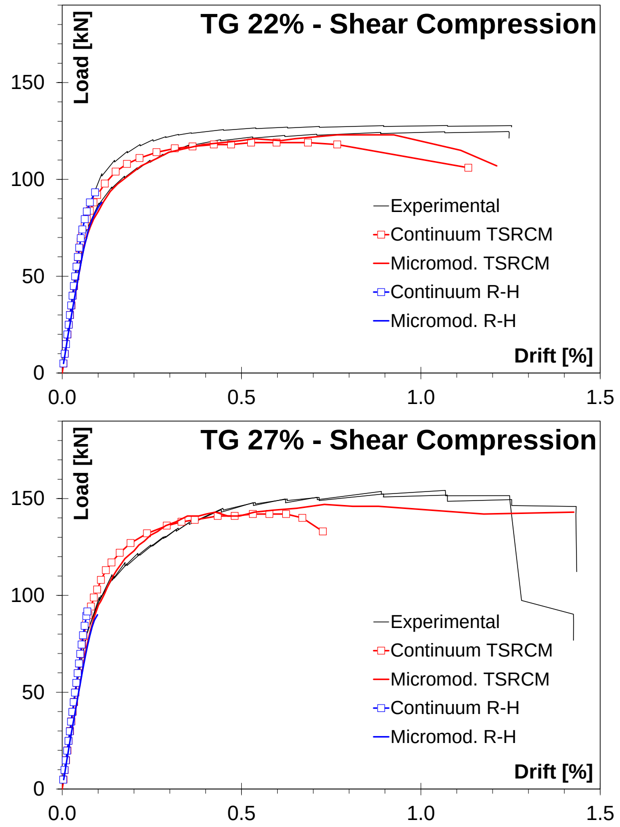

Fig. 4.9. Shear-compression envelope curves: experimental and numerical load drift-diagrams: TG with vertical load of 22% (above) and 27% (below) of compressive strength.

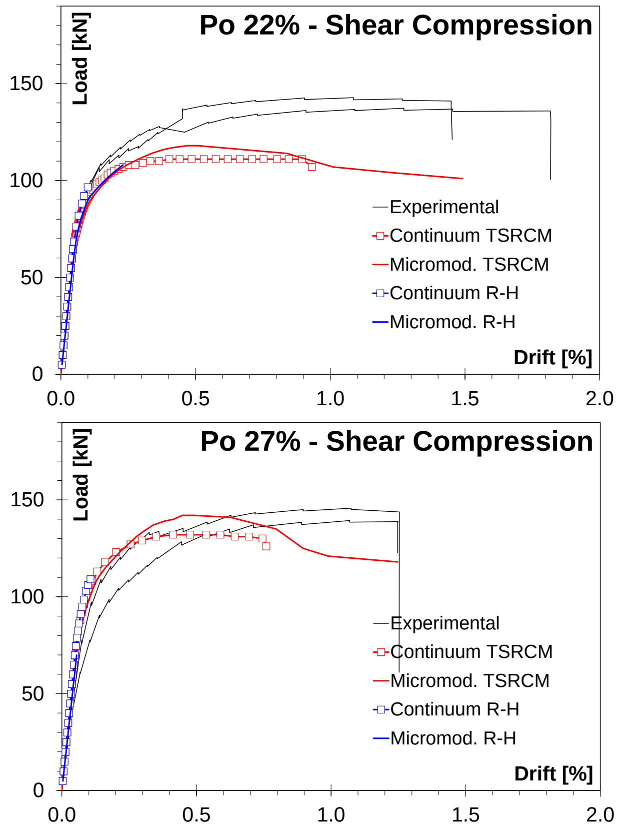

Fig. 4.10. Shear-compression envelope curves: experimental and numerical load drift-diagrams: Po with vertical load of 22% (above) and 27% (below) of compressive strength.

4.2.3. Parametrical Extension of Experimental Tests

The experimental perforated clay units were designed on purpose for this research, following the principles of 'robustness' given by recent seismic codes (DM 14/01/2008, 2008; EN 1998-1: 2004. Eurocode 8, 2004; Ordinanza P.C.M. n. 3274: 2003, 2005). They had compressive strength of about 20 N/mm^2, whereas the compressive strength of perforated clay units used in practice varies over a range of about 20 to 5 N/mm^2. Therefore, in order to study the influence of unit compressive strength (f_{cu}) on the global shear behavior of the three masonry types, analyses were repeated with units with compressive strength of 20, 15, 10 and 5 N/mm^2. From the results of model calibration, the simplified micro-modeling strategy, with total strain rotating crack law for units, turned out to be the most suitable to reproduce the cyclic shear behavior of masonry monotonically. The parametric analyses thus implemented this model. The adopted models simplify the unit mortar interaction, and their results are influenced by some parameters, such as unit fracture energy, that were assumed. However, the methodical approach followed for model calibration and the comparison between numerical and experimental results, allowed the parametric study of the three masonry types.

A database of unit properties was created to estimate the mechanical characteristics of the theoretical units. It contains values reported in the literature for about 100 perforated clay units characterized by similar percentages of holes (da Porto, 2005; DISWall, 2008). The fitting process used relationships similar to those proposed by Eurocode 2 for concrete (EN 1992-1-1, 2004). They were adapted to estimate unit elastic modulus E_u (Eq. 4.6) and unit tensile strength ftu (Eq. 4.7), starting from unit compressive strength f_{cu}. (Eq. 4.6) and (Eq. 4.7) refer to the gross area of units.

$$E_u = 3041\sqrt[3]{f_{cu}} \qquad \text{(Eq. 4.6)}$$

$$f_{tu} = 0{,}087 \cdot f_{cu}^{\;0.58} \qquad \text{(Eq. 4.7)}$$

For each masonry type and each value of unit compressive strength, analyses were repeated by applying the same vertical load used in the experimental and numerical phases of the research, or a vertical load corresponding to the same ratio between applied load and compressive strength of masonry. In the latter case, it was possible to compare the behavior of each masonry type, varying the unit compressive strength, when stresses inside the walls had comparable intensity.

To evaluate the pre-compression load on the models with different masonry compression strength (with correlation to different unit strength) an adapted version of the (Guidi, 1954) relation (Eq 4.8) was used, and fitted with the experimental data. For further details about this formula refer to (da Porto, 2005; da Porto et al., 2010b). The adopted version of the equation used the following values: a=4.52, b=1 and c=2.75. Table 4.7 shows the parameters used in the parametric analyses that were changed from the models used to reproduce the experimental tests.

$$\mathrm{f_{c,m}} = \frac{\mathrm{f_{cu}}}{\mathrm{a}} \cdot \log(\mathrm{b} \cdot \mathrm{f_m} + \mathrm{c}) \qquad \text{(Eq. 4.8)}$$

N/mm^2	TM				TG				Po			
f_{cu}	20.42	15.00	10.00	5.00	20.96	15.00	10.00	5.00	20.43	15.00	10.00	5.00
f_{tu}	0.47	0.42	0.33	0.22	0.47	0.42	0.33	0.22	0.58	0.42	0.33	0.22
$f_{c,m}$	6.95	5.16	3.44	1.72	5.67	4.12	2.74	1.37	5.34	4.12	2.74	1.37
σ_0 22%	1.53	1.14	0.76	0.38	1.25	0.91	0.60	0.30	1.17	0.91	0.60	0.30
27%	1.88	1.39	0.93	0.46	1.53	1.11	0.74	0.37	1.44	1.11	0.74	0.37

Table 4.7. Parametric analyses. Parameters changed from the used relations.

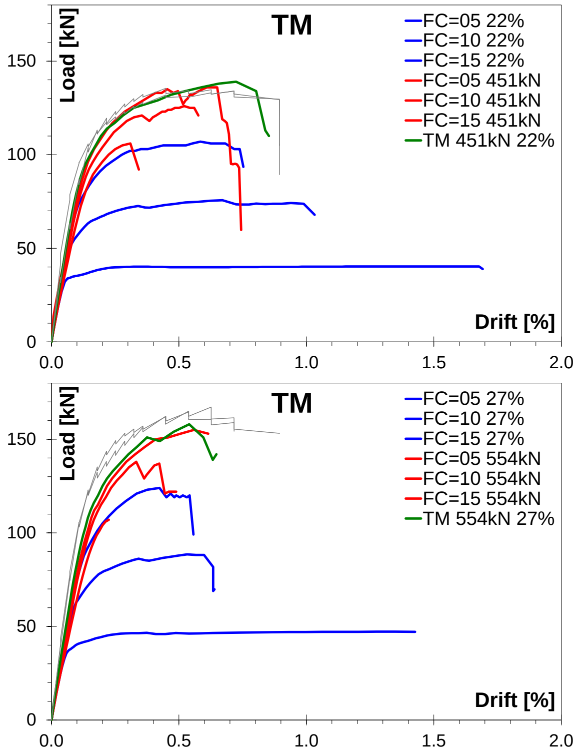

Fig. 4.11. Parametric shear-compression curves: experimental and numerical load drift-diagrams: TM with vertical load of 22% (above) and 27% (below) of compressive strength.

From Fig. 4.11 to Fig. 4.13 are presented the capacity curves found with parametrical analyses (blue and red lines) carried out for the three masonry type (TM, TG and Po respectively) together with experimental results (grey lines) and relatives numerical model (green line).

When the applied vertical load changes in order to keep the ratio with masonry compressive strength constant (blue lines), the effect of unit strength and of the concurring applied vertical load can be appreciated. In TM, the maximum horizontal load decrease is almost linear with unit strength decrease (-22% at f_c=15 N/mm^2, -45% at f_c=10 N/mm^2, and -70 at f_c=5 N/mm^2). In TG and Po, the maximum horizontal load decrease is less pronounced when unit strength is higher, but is exactly the same in TM at the lowest unit strength (-11% at f_c=15 N/mm^2, -40% at f_c=10 N/mm^2, and -70 at f_c=5 N/mm^2). Behavior in terms of maximum displacement is similar in the three types. For unit strength of 15 N/mm^2, displacement is 11% smaller than for unit strength of 20 N/mm^2, due to whole capacity of wall to sustain loads decreases. At lower unit strength (10 and 5 N/mm^2), the effect of the lower vertical load applied becomes evident (rocking mechanism), and maximum displacement increases by 12% and 110% respectively.

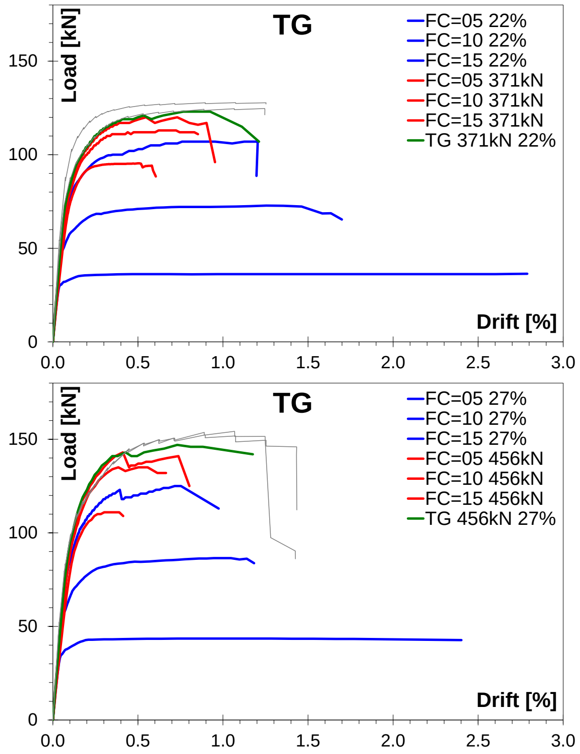

Fig. 4.12. Parametric shear-compression curves: experimental and numerical load drift-diagrams: TG with vertical load of 22% (above) and 27% (below) of compressive strength.

When the applied vertical load is the same as in the experimental tests (red lines), besides the effect of unit strength, the behavior of the various masonry types can be appreciated. For TM masonry, maximum horizontal load decreases by -5%, -11%, and -28% for unit strengths of 15, 10 and 5 N/mm^2 (compared with the case with unit strength of 20 N/mm^2). For TG and Po masonry, it decreases by about -2%,-7% and -23%. It worth to point out the great strength decay, when unit with 5 N/mm^2 of compressive strength were used.

The behavior in terms of drift at ultimate limit state (maximum drift) is different in the various types. As expected, at the lowest unit strength, maximum drift decrease was higher in TM (-63%) than in TG and Po (-57%). However, at higher unit strength, this trend changes, and the maximum drift decrease was -28% and -17% for TM at unit strength of 10 and 15 N/mm^2, but -38% and -26% for TG and Po.

Also here it has to be noted the nonlinear decrease unit with 5 N/mm^2 of compressive strength were used.

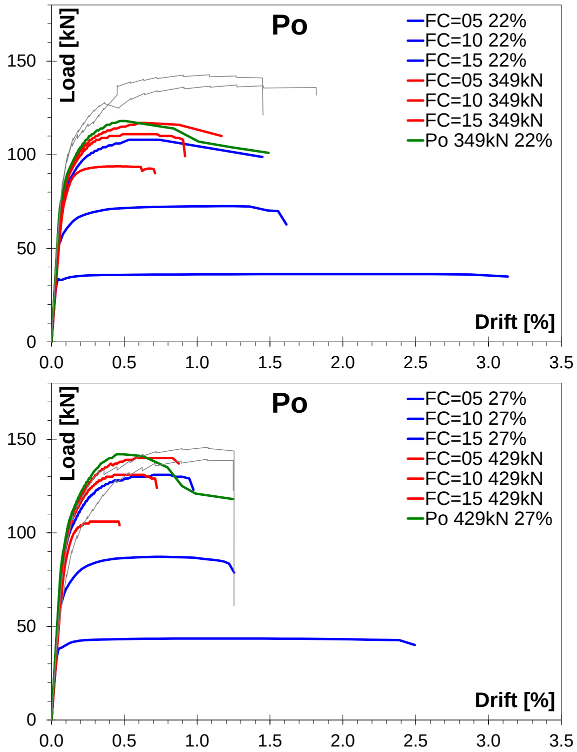

Fig. 4.13. Parametric shear-compression curves: experimental and numerical load drift-diagrams: Po with vertical load of 22% (above) and 27% (below) of compressive strength.

4.3. Reinforced Masonry Walls

4.3.1. Modeling Approach

For modeling the reinforced masonry walls under study, a simplified micro-modeling strategy with continuum elements and no unit-mortar interface elements was adopted. This strategy was slightly different from previously adopted (and described in paragraph 4.2.1) with the aim of broadening the spectrum of adopted approaches.

The constitutive laws of mortar and blocks were implemented using the Total Strain Rotating Crack isotropic damage model (Rots, 1997), which describes the tensile and compressive behavior with one stress-strain relationship. The steel reinforcement behavior was described by means of elasto-plastic Von Mises yield criterion, without hardening.

Eight-node isoparametric plane-stress elements with Gauss integration scheme were used in the models. The Newton-Raphson iteration procedure was used (it was also used the so called line-search algorithm) with an energetic convergence criterion (as previously done for URM masonry, see paragraph 4.2.1). For standard compression tests were imposed vertical force using arch length method, whereas for shear compression tests simulation was used a displacement control applying it as in experimental tests.

The reinforcement had the shape of a line and was considered fully bonded and embedded in all the plane stress elements that define the wall geometry (as provided by DIANA™ version 9.3 used to carry out these analyses). Considering the type of model used, it was not possible to make a distinction between the truss and the bar reinforcement used.

Each different material was defined by following properties: elastic modulus (E) equal in compression and in tension; Poisson's coefficient (v); tensile and compressive strengths (σ_t and σ_c respectively); fracture energies in tension and compression (G_{ft} and G_c respectively). Being a plane stress model, the presence of vertical columns filled by mortar used to cast vertical reinforcements, did not directly take in to account. It was done by averaging throughout wall thickness the properties of different materials, weighing them in proportion to their thickness over the whole wall thickness.

The fracture energy of masonry in tension (G_{ft}) and in compression (G_{fc}) are parameters needed into the continuum model implementing the isotropic total strain rotating crack constitutive law that have not been experimentally evaluated. These values have been found using the criteria and data described in paragraph 4.2.1.

Other parameters, which are not directly available from the experimental tests, are the tensile strengths of the masonry components. The values of the tensile strengths were evaluated indirectly from the numerical model developed for the uniaxial compression tests (wallettes without confining columns, confining columns and complete RM system walls). The tensile strength to be assigned to the vertical joints (and with good approximation, even horizontal joints) was assessed by means of matching the opening of the first crack in the vertical joints, seen as a discontinuity in the load displacement curve (see Fig. 4.14a). To get an estimate of other tensile strength the same procedure was adopted. Furthermore, the obtained parameters were in agreement with those available both in the literature (Rots, 1997) and with those resulting from equations proposed for concrete by the EC2 (EN 1992-1-1, 2004). It should be noted that the tensile strength assigned to the joints is not the mortar strength, but an assessment of the strength of the interface between the mortar and the blocks (which is less).

Finally, a structured regular mesh was used. Mesh sensitivity problem was also taken in to account, but still valid the observations made in paragraph 4.2.1 and mesh refinement had a neglectable influence on global response of models.

4.3.2. Uniaxial Compression and In-plane Cyclic Envelopes Modeling

The validation of the numerical model has been based on the experimental results. Material properties are derived from experimental tests carried out on masonry materials and, in a later stage, on standard tests of masonry macro-assemblages (i.e. uniaxial compression and shear compression tests on wallettes).

The use of a continuum model requires the calibration of the material properties through homogenization procedures in order to get results in agreement with the experimental ones (i.e. between the vertical mortar columns at the wall edges, used for casting the vertical reinforcement, and the vertically perforated units that contain it). This process yielded to a reduction of about 30% for the elastic moduli derived from the tests on materials, which mainly took into account the absence of interface elements in the model (Rots, 1997). Whereas the Poisson's ratios were equal to experimental ones. In the case of the unit, to take into account the compressive failure accompanied by web detachment and the effects of the complex tri-dimensional stress state on the unit orthotropy, the compressive strength was also reduced by about 50%. As introduced before, the tensile strength assigned to the joints was assessed from the strength of the interface between mortar and units, backcalculating the values of stresses when the first cracks in the vertical joints, seen as a discontinuity in the load displacement curve, occur (see Fig. 4.17a), Horizontal holes). By matching this crack pattern into the numerical model, the mortar-block (see also Fig. 4.15) interface appeared to have a tensile strength of approximately 0.2 N/mm^2 (see Table 4.8). To get an estimate of other tensile strength the same procedure was adopted.

The experimental condition of reinforcement-mortar bond is not realistically modeled with the full-bonded hypothesis used for embedded reinforcements available in DIANA™. In order to take into account this fact, the elastic modulus of the steel reinforcement was also reduced by about 40%, with respect to experimental values. (see Table 4.8)

Material	E N/mm^2	v -	f_t N/mm^2	f_c N/mm^2	G_{ft} N/mm	G_{fc} N/mm
Horizontal preforated units	5381	0.15	0.90	2.90	0.0170	2.0
Vertical preforated units	9085	0.18	0.85	9.70	0.0170	6.0
Mortar bed joints	8370	0.17	0.30	12.00	0.0064	6.0
Mortar head joints	8370	0.17	0.21	12.00	0.0045	6.0
Vertical preforated units with mortar pocket (homogenized)	8895	0.17	1.13	9.60	0.0200	6.0
Horizontal reinforcements	122700	/	460		/	/
Vertical reinforcements	116300	/	510		/	/

Table 4.8. Reinforced masonry FEM model parameters.

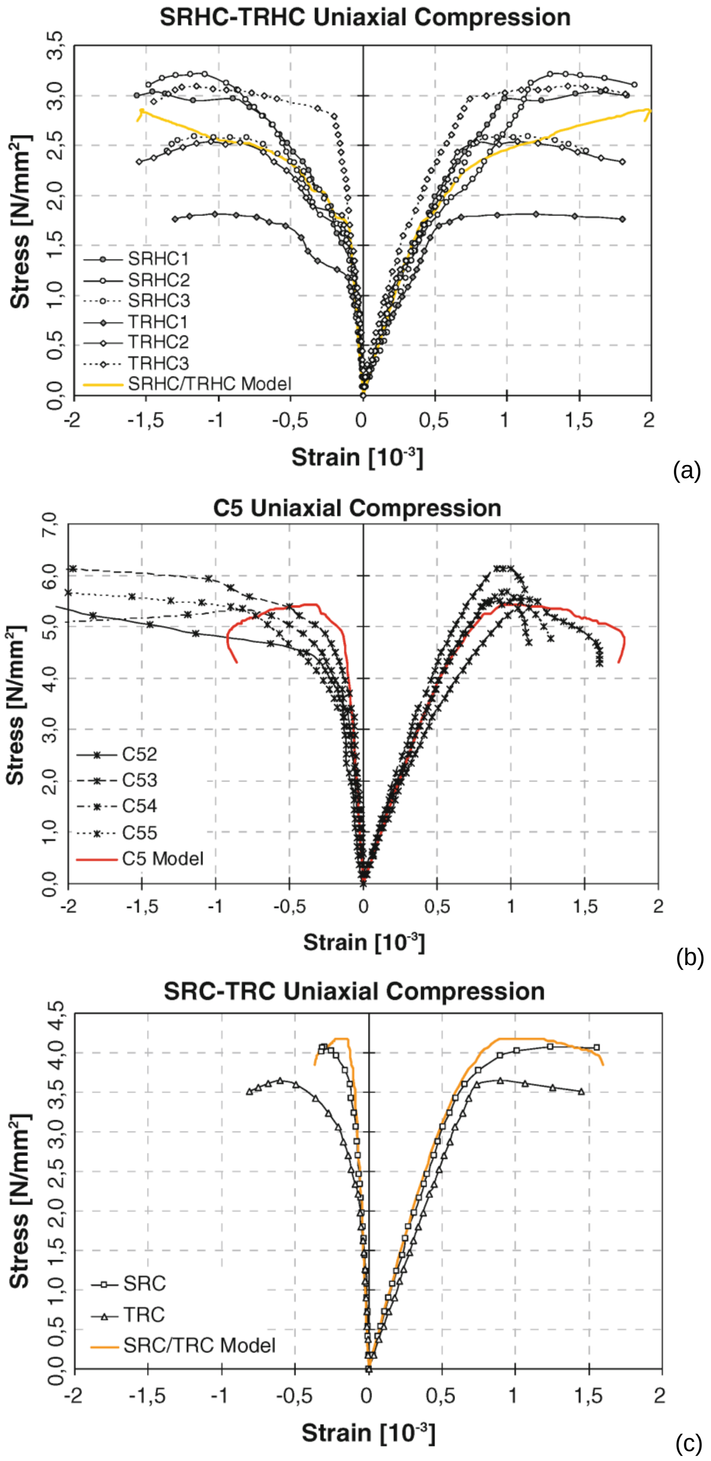

Fig. 4.14. Uniaxial compression test. Stress-strains diagrams (grey: experimental, red: numerical).

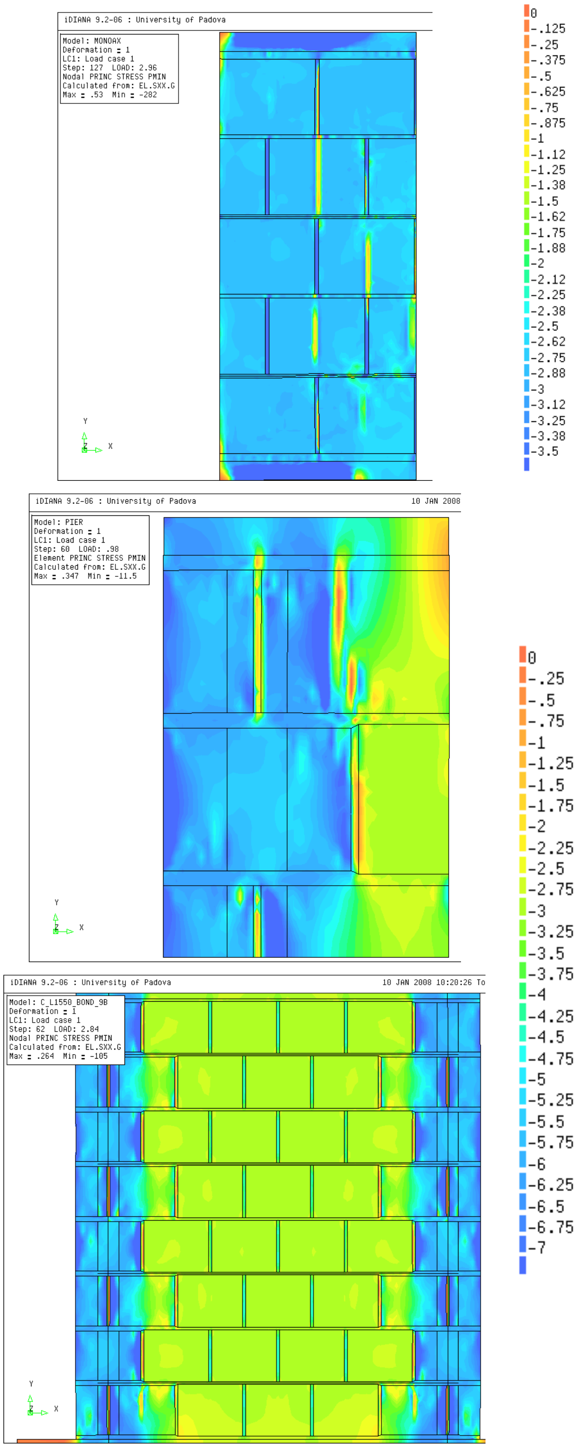

(a)
Horizontal Holes
(half of specimen)

(b)
Columns
(quart of specimen)

(c)
Complete System

Fig. 4.15. Uniaxial compression test. Principal compression stresses.

The comparison between the experimental results and the numerical models for the uniaxial compression tests, gives the following results. Fig. 4.14 compares experimental and numerical stress-strain curves. The models reproduced the various test series fairly well. The compressive strengths of columns (C5) and wall with horizontally perforated blocks (SRHC-TRHC) were, respectively, underestimated and overestimated by 5%. The compressive strength of the entire reinforced masonry system was overestimated by about 7%. The elastic modulus and experimental and model strains were almost identical for C5 and SRHC–TRHC. The elastic modulus of the entire reinforced masonry system was overestimated by 10% (SRC-TRC). C5 and SRHC-TRHC reproduced experimental behavior very well, with cracks opening in vertical joints and propagating in the units (Fig. 4.15).

As expected, the compressive stresses of SRC-TRC were concentrated in the confining columns, which were stiffer than the central masonry portion. Also in this case, the model simulated experimental behavior very well. The first cracks opened at the interface between the two components of the systems. The state of stress at this interface remained high during the entire analysis, but later vertical cracks also appeared on the central masonry panel (Fig. 4.15c). The model properly reproduced the experimental strains of the confining columns and central masonry portion. Fig. 4.16 shows the model axial strains along the wall, on four courses (the third, fourth, fifth and sixth from the bottom), and their average, at three load levels (10, 40 and 60% of maximum load). The mean values in the central part of the wall were higher than those in the confining columns. This change in behavior occurred between 250 and 380 mm of wall length (and symmetrically between 1170 and 1300 mm), i.e., where vertically and horizontally perforated units alternated on each unit course. For further details refer to (da Porto et al., 2010b).

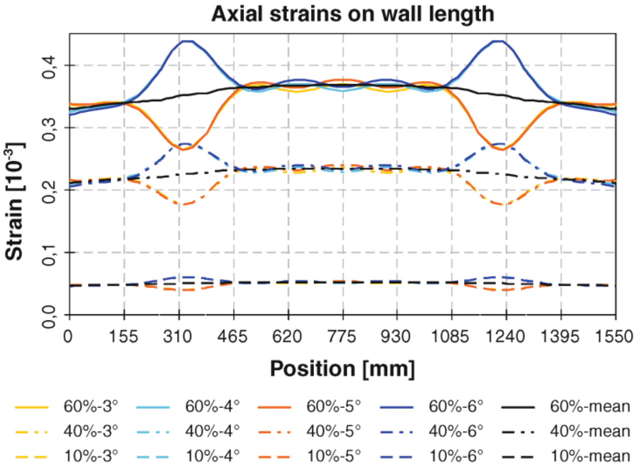

Fig. 4.16. Axial strains at 10, 40 and 60% of maximum load (model)

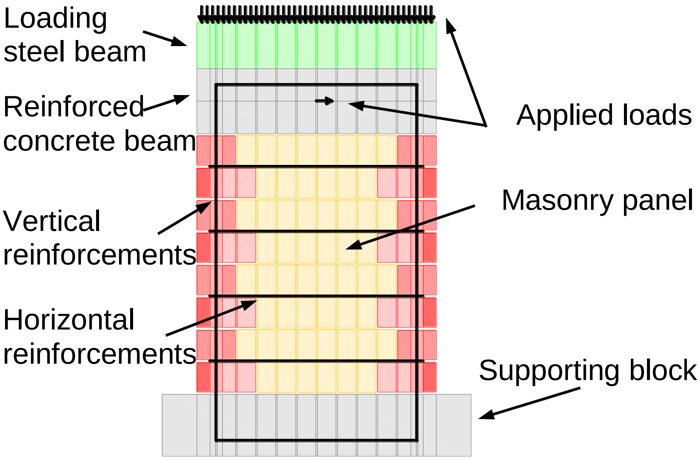

Fig. 4.17. Scheme of shear wall finite element model.

The set of parameters defined was adopted for the simulation of shear-compression tests (Table 4.8). The specimens were tested with cantilever type boundary condition and applying a centered and constant vertical load (see section 3.3.3 and Fig. 3.15). The top steel girder, the top r.c. beam and the bottom bond beam are modeled with linear-elastic elements. The vertical forces are converted into a normal distributed load over the complete length of the top concrete beam. The horizontal load is applied as a controlled displacement. The central node in the top r.c beam has been chosen to apply the horizontal displacement as during the experimental tests (see Fig. 4.17).

Considering the type of model used, it was not possible to make a distinction between the truss and the bar reinforcement used. This was chosen as experimental results showed substantially the same behavior of the specimens reinforced with the two different types of horizontal reinforcement (see section 3.3.3). The analyses aimed at reproducing the experimentally observed shear-compression behavior of the reinforced masonry system were carried out under incremental displacement (pushover analyses). This type of analysis is adequate to reproduce the experimental envelope curve obtained by means of the tests.

Fig. 4.18 and Fig. 4.19 show the average of the experimental hysteresis loops envelope (blue color) obtained by the shear compression tests, and the comparison with the numerical results (red curves), respectively for the slender and the squat specimens. Table 4.9 and Table 4.10 compare the main experimental and numerical results, for specimens with applied vertical load of 0.4 and 0.6 N/mm^2.

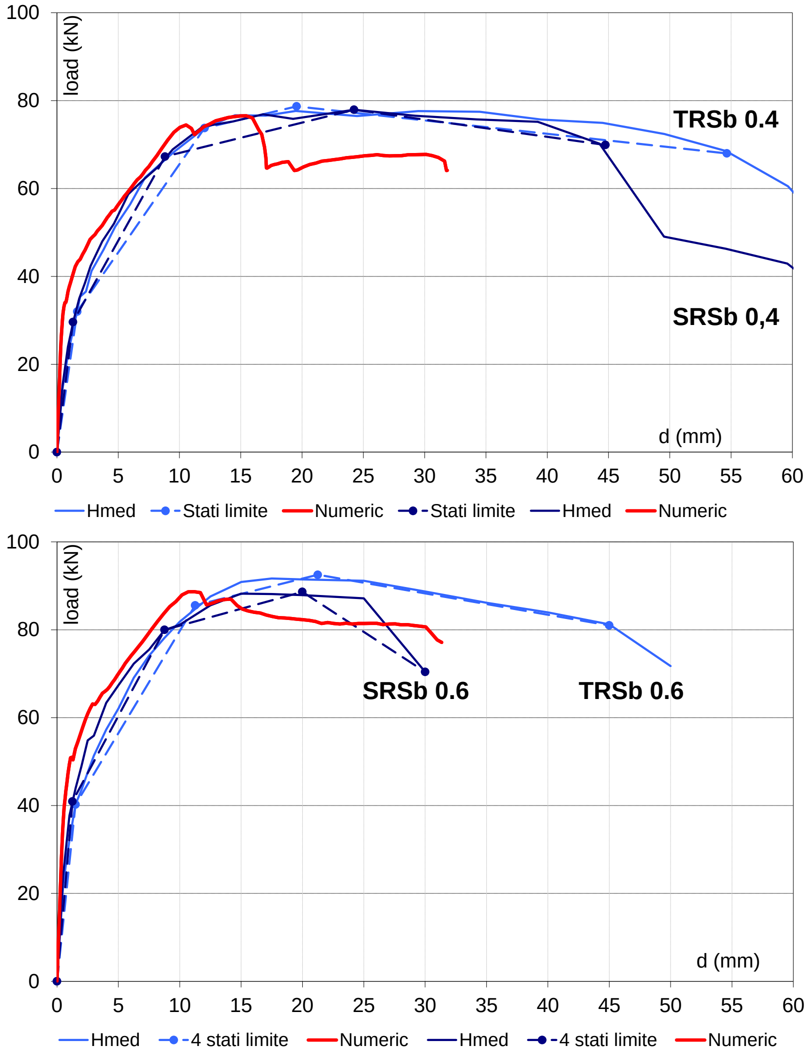

Fig. 4.18. Shear-compression envelope curves. Experimental (blue) and numerical (red) load-displacement diagrams for slender walls: with vertical load of 0.4 N/mm^2 (above) and 0.6 N/mm^2 (below).

vertical compression 0.4 *N/mm*^{2}	F_{max} *kN*	d_{Fmax} *mm*	F_{dmax} *kN*	d_{max} *mm*
TRSa	199	11.67	166	19.99
SRSa	200	17.23	172	19.99
Model	200	10.87	156	16.83
error	*+0%*	*-25%*	*-8%*	*-16%*
TRSb	79	19.55	68	54.65
SRSb	78	24.24	70	44.75
Model	77	15.45	64	31.85
error	*-2%*	*-29%*	*-7%*	*-36%*

Table 4.9. Comparison between experimental and FEM model at maximum strength of wall and at maximum displacement for vertical compression stress of 0.4 N/mm^2.

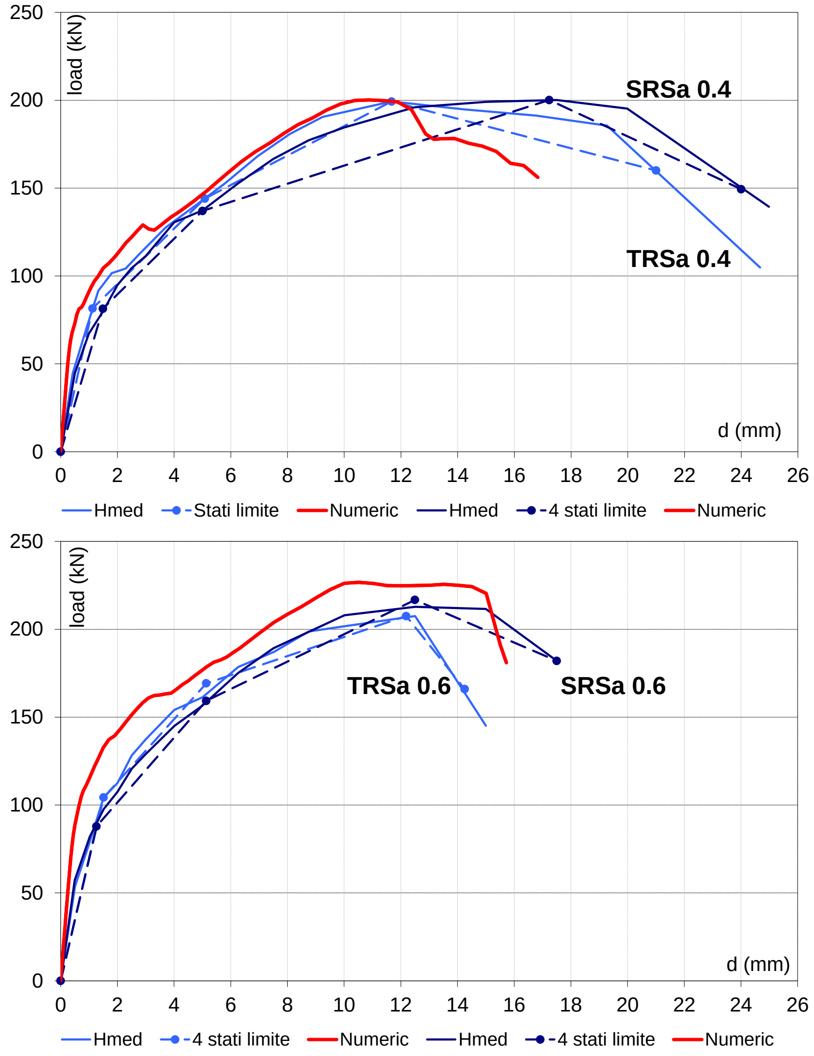

Fig. 4.19. Shear-compression envelope curves. Experimental (blue) and numerical (red) load-displacement diagrams for squat walls: with vertical load of 0.4 N/mm^2 (above) and 0.6 N/mm^2 (below).

vertical compression 0.6 *N/mm^2*	F_{max} *kN*	d_{Fmax} *mm*	F_{dmax} *kN*	d_{max} *mm*
TRSa	207	12.19	166	14.25
SRSa	217	12.50	182	17.50
Model	227	10.51	181	15.73
error	*+7%*	*-15%*	*+4%*	*-1%*
TRSb	93	21.25	81	45.00
SRSb	89	19.99	70	30.00
Model	89	11.18	77	31.34
error	*-2%*	*-46%*	*+2%*	*-16%*

Table 4.10. Comparison between experimental and FEM model at maximum strength of wall and at maximum displacement for vertical compression stress of 0.6 N/mm^2.

The models slightly overestimate the initial stiffness and reproduce the maximum horizontal load with an absolute average error of about 3%.

Due to the higher initial model stiffness, the numerical displacements at maximum load are underestimated up to -40%. However, the maximum errors are found in slender specimens where the envelopes curves showed a relative long branch with almost constant load, and taking in to account experimental variability, definition of displacement at maximum load can varies.

Furthermore, the values of maximum displacement at collapse for high vertical compression level (0.6 N/mm^2), when a sudden drop of strength occurs as observed during the experimental tests (da Porto et al., 2009b; Mosele, 2009), are in agreement (absolute average error 9%, see Table 4.10) with the experimental ones. For flexural specimens under lower vertical stress level, the maximum displacement is underestimated (average error about -26%, see Table 4.9).

However, from the interpretation of the model results, it can be said that the failure modes and the crack pattern are in agreement with those observed in the experimental phase (see Fig. 4.20 and Fig. 4.21 which gives the principal tensile stress on cracks for the masonry for squat specimen models).

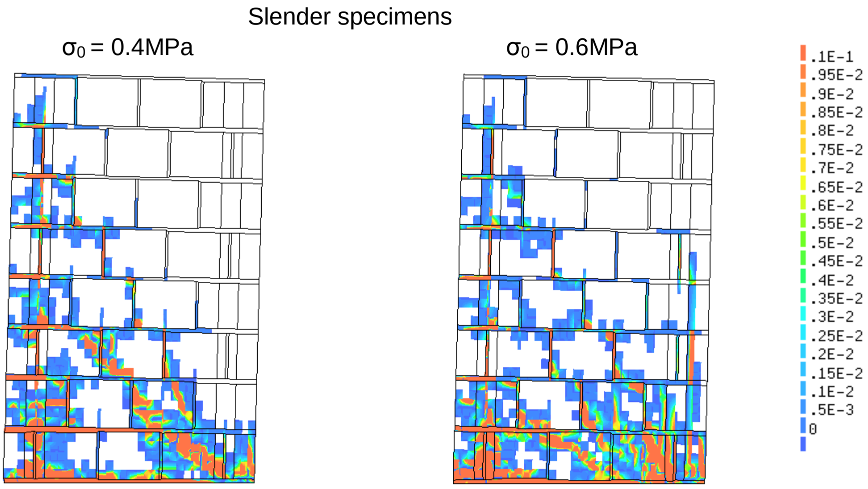
Slender specimens

σ_0 = 0.4MPa

σ_0 = 0.6MPa

Fig. 4.20. Crack patterns using maximum principal strains at ultimate state.

The reduction of axial load level allows to observe, for squat specimen, a change of failure mode from shear to shear/flexural mode, pointed out by the less clear diagonal strut and higher concentration of stresses on the compressed toe of masonry. The same reduction in vertical load induces, in the slender specimens, a less concentration of stresses at the base of the wall, together with a higher exploitment of the stretched vertical reinforcement.

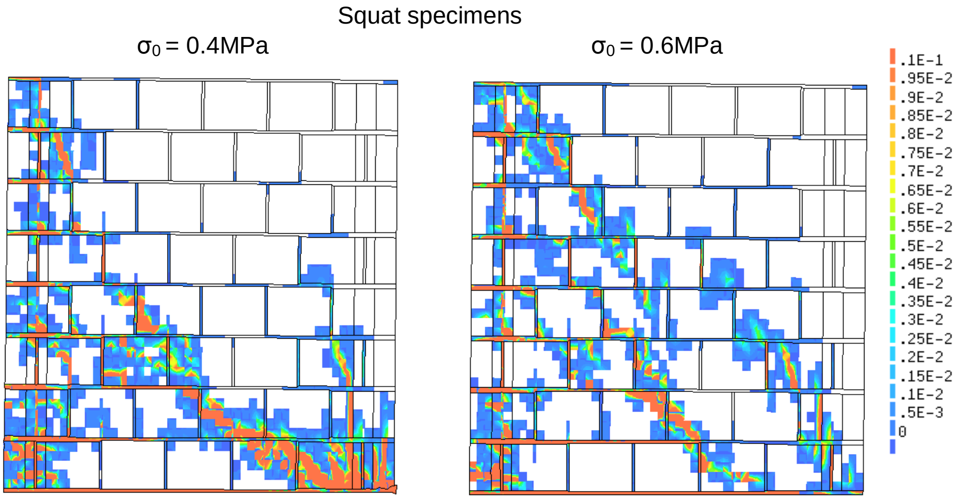

Fig. 4.21. Crack patterns using maximum principal strains at ultimate state.

4.3.3. Parametrical Extension of Experimental Tests

The influence of three parameters on the behavior of analyzed reinforced masonry system was investigated: axial load level, slenderness and percentage of reinforcement. For each parameter, a specific series of numerical analyses was carried out.

To check the influence of different vertical load level on the behavior of the analyzed reinforced masonry system, a series of numerical analyses were carried out, where the vertical load on the wall was changed to obtain a vertical stress level from 0.2 to 2.0 N/mm^2. That corresponds, in reality, to a different number of storeys above ground or to a different building use.

These analyses were carried out on walls having the same slenderness (H/L 1.09 and 1.64) and the same ratio of vertical reinforcement (0.17% and 0.13%) of the experimental specimens, and also with vertical reinforcement ratio just above the minimum required as in the Italian standard (DM 14/01/2008, 2008), which is 0.05%. We did not take in to account the requirement of 200 mm^2 in each side of the wall. Thus, the parametric combinations were extended within a reasonable range in order to analyze the principal failure mechanisms and the changes in masonry behavior. In the analyses code in Fig. 4.22 and Table 4.11 (e.g., 164_45_073_08), the first number gives the wall slenderness (1.64 in this example), the second and third numbers show the horizontal (0.045%) and the vertical (0.073%) reinforcement ratios, the fourth number, finally, shows the vertical stress level (0.8 N/mm^2) at which the analysis is carried out. An overall number of 32 analyses were carried out for this study.

name	H/L -	Hor. Reinf. %	Ver. Reinf. %	σ_0 N/mm^2	τ_{max} N/mm^2	Drift$_{max}$ %	H_{max} kN	d_{max} mm
109_45_066_02	1.09	0.045	0.066	0.2	0.20	0.625	93	14.37
109_45_066_04	1.09	0.045	0.066	0.4	0.27	0.862	125	19.84
109_45_066_06	1.09	0.045	0.066	0.6	0.34	0.827	157	19.01
109_45_066_08	1.09	0.045	0.066	0.8	0.41	0.782	189	18.00
109_45_066_10	1.09	0.045	0.066	1.0	0.47	0.516	218	11.86
109_45_066_12	1.09	0.045	0.066	1.2	0.53	0.475	247	10.93
109_45_066_16	1.09	0.045	0.066	1.6	0.66	0.371	305	8.52
109_45_066_20	1.09	0.045	0.066	2.0	0.74	0.242	342	5.56
109_45_173_02	1.09	0.045	0.173	0.2	0.35	0.442	164	10.16
109_45_173_04*	1.09	0.045	0.173	0.4	0.43	0.732	200	16.83
109_45_173_06*	1.09	0.045	0.173	0.6	0.49	0.684	227	15.73
109_45_173_08	1.09	0.045	0.173	0.8	0.56	0.661	259	15.21
109_45_173_10	1.09	0.045	0.173	1.0	0.62	0.574	288	13.21
109_45_173_12	1.09	0.045	0.173	1.2	0.65	0.500	301	11.50
109_45_173_16	1.09	0.045	0.173	1.6	0.74	0.438	346	10.07
109_45_173_20	1.09	0.045	0.173	2.0	0.80	0.344	370	7.90
164_45_073_02	1.64	0.045	0.073	0.2	0.14	0.802	44	18.45
164_45_073_04	1.64	0.045	0.073	0.4	0.19	1.234	59	28.39
164_45_073_06	1.64	0.045	0.073	0.6	0.23	1.216	72	27.96
164_45_073_08	1.64	0.045	0.073	0.8	0.27	1.159	85	26.66
164_45_073_10	1.64	0.045	0.073	1.0	0.31	0.700	97	16.10
164_45_073_12	1.64	0.045	0.073	1.2	0.35	0.657	109	15.11
164_45_073_16	1.64	0.045	0.073	1.6	0.43	0.565	134	13.00
164_45_073_20	1.64	0.045	0.073	2.0	0.51	0.376	156	8.65
164_45_130_02	1.64	0.045	0.130	0.2	0.21	0.873	64	20.08
164_45_130_04*	1.64	0.045	0.130	0.4	0.25	1.385	77	31.85
164_45_130_06*	1.64	0.045	0.130	0.6	0.29	1.363	89	31.34
164_45_130_08	1.64	0.045	0.130	0.8	0.33	1.283	101	29.51
164_45_130_10	1.64	0.045	0.130	1.0	0.37	0.921	113	21.18
164_45_130_12	1.64	0.045	0.130	1.2	0.40	0.765	125	17.58
164_45_130_16	1.64	0.045	0.130	1.6	0.46	0.616	142	14.17
164_45_130_20	1.64	0.045	0.130	2.0	0.52	0.535	161	12.32
* analysis that corresponds to an experimental condition								

Table 4.11. Table of parametric variations carried out. Variation of vertical load applied.

Fig. 4.22 shows the load-drift curves with variation of vertical compression load. The lines with dots represent the FEM analyses which reproduce experimental walls.

As expected, the maximum shear stress increases for increasing applied vertical stresses (see Fig. 4.22). The maximum horizontal displacement in the wall decreases with the increase of the vertical compression level (see Fig. 4.22 and Table 4.11). This indicates that the applied vertical load directly influences the mechanism of failure in the walls.

For vertical loads corresponding to 0.2 N/mm^2, the models show a large decrease of maximum drift when compared to higher vertical stresses (Fig. 4.22). This can be imputed to the change of behavior from flexure (in slender models) or mixed shear/flexure (in squat models) to crushing of compressed toe.

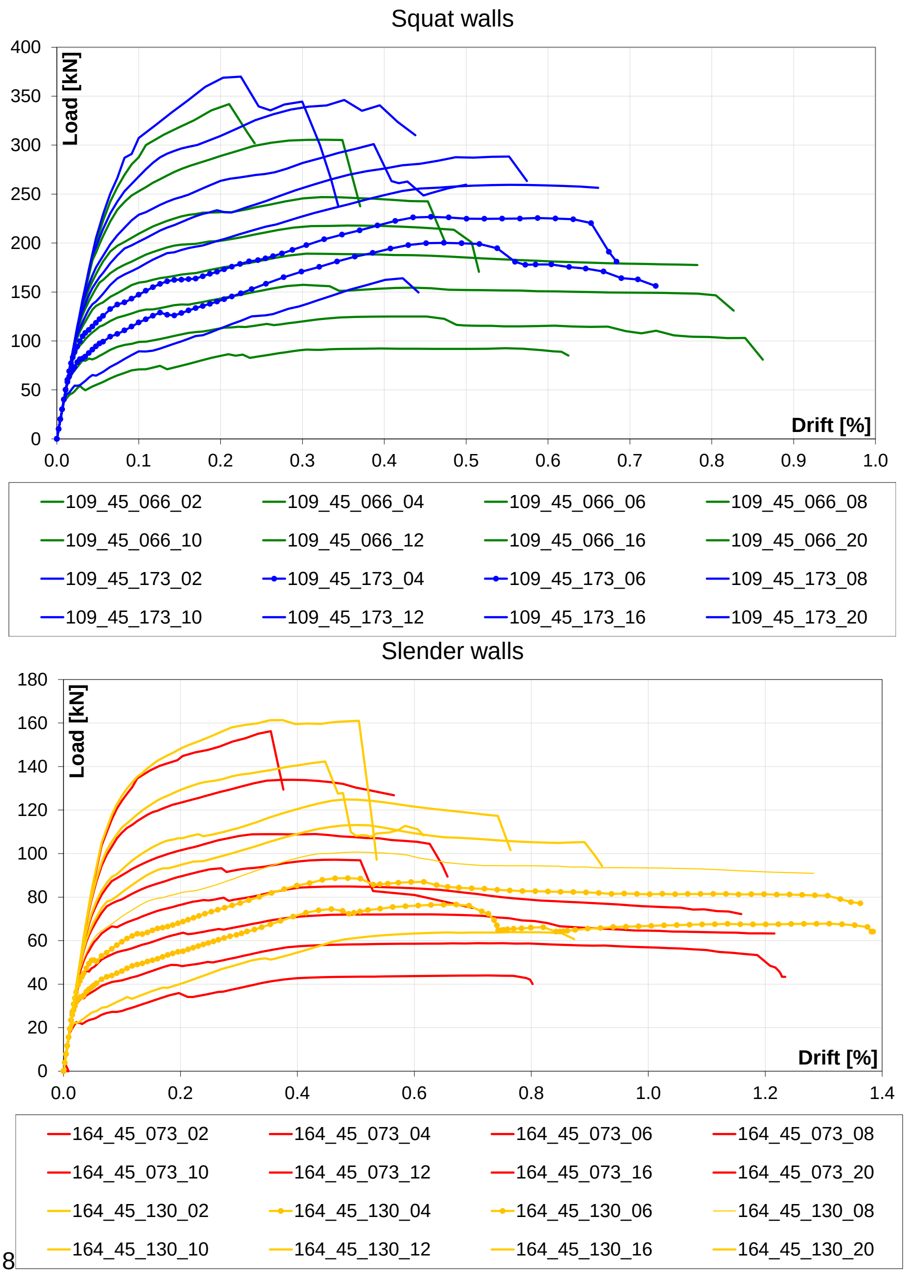

Fig. 4.22. Variation of vertical load. Load – Drift curves.

name	H/L -	Hor. Reinf. %	Ver. Reinf. %	σ_0 N/mm^2	τ_{max} N/mm^2	Drift$_{max}$ %	H_{max} kN	d_{max} mm
065_45_052_04	0.65	0.045	0.052	0.4	0.41	0.433	320	9.96
065_45_052_06	0.65	0.045	0.052	0.6	0.52	0.394	404	9.06
065_45_162_04	0.65	0.045	0.162	0.4	0.57	0.301	447	6.93
065_45_162_06	0.65	0.045	0.162	0.6	0.63	0.278	489	6.41
082_45_050_04	0.82	0.045	0.050	0.4	0.32	0.723	198	16.63
082_45_050_06	0.82	0.045	0.050	0.6	0.42	0.636	258	14.63
082_45_164_04	0.82	0.045	0.164	0.4	0.50	0.451	312	10.36
082_45_164_06	0.82	0.045	0.164	0.6	0.65	0.443	404	10.20
109_45_066_04	1.09	0.045	0.066	0.4	0.27	0.862	125	19.84
109_45_066_06	1.09	0.045	0.066	0.6	0.34	0.827	157	19.01
109_45_173_04*	1.09	0.045	0.173	0.4	0.43	0.732	200	16.83
109_45_173_06*	1.09	0.045	0.173	0.6	0.49	0.684	227	15.73
164_45_073_04	1.64	0.045	0.073	0.4	0.19	1.234	59	28.39
164_45_073_06	1.64	0.045	0.073	0.6	0.23	1.216	72	27.96
164_45_130_04*	1.64	0.045	0.130	0.4	0.25	1.385	77	31.85
164_45_130_06*	1.64	0.045	0.130	0.6	0.29	1.363	89	31.34
219_45_098_04	2.19	0.045	0.098	0.4	0.16	1.153	36	26.53
219_45_098_06	2.19	0.045	0.098	0.6	0.19	1.094	44	25.15
219_45_174_04	2.19	0.045	0.174	0.4	0.20	0.590	46	13.56
219_45_174_06	2.19	0.045	0.174	0.6	0.24	0.902	56	20.74
* analysis that corresponds to an experimental condition								

Table 4.12. Table of parametric variations carried out. Variation of slenderness ratio.

To check the influence of different wall geometry on the behavior of the analyzed reinforced masonry system (that corresponds, in reality, to the different wall length that can be found in a building), a series of numerical analyses were carried out where the length and thus the slenderness of the walls were changed. The H/L values were varied between 0.65 and 2.19 which correspond to walls with length varying from 2.60 to 0.75m. In these analyses, the vertical load was kept constant and equal to the two values adopted for the experimental tests (0.6 N/mm^2 and 0.4 N/mm^2) and again the vertical reinforcement ratios used were 0.13% and 0.17%, consistently with the experimental tests, or minimum requirement similar to the Italian building code (0.05%). The label codes of the analyses in Fig. 4.23 and Table 4.12 can be read as explained in the previous section. An overall number of 20 analyses were carried out in this case.

The maximum shear stress increases with the length of the wall (see Fig. 4.23 and Table 4.12). However, the simultaneous increase of vertical reinforcement causes higher increase of shear resistance (Fig. 4.23), accompanied by higher fragility. Pure shear limit can be observed for 065_45_162_06 and 082_45_164_06, i.e. the squatter walls with highest vertical stresses and reinforcement.

In addition, for slenderness of 2.19, which represents the minimum length for the masonry system under investigation, the behavior changes again and the maximum drift shows a large decrease (see Fig. 4.23). This can be imputed to the change of behavior from flexure to crushing of compressed toe.

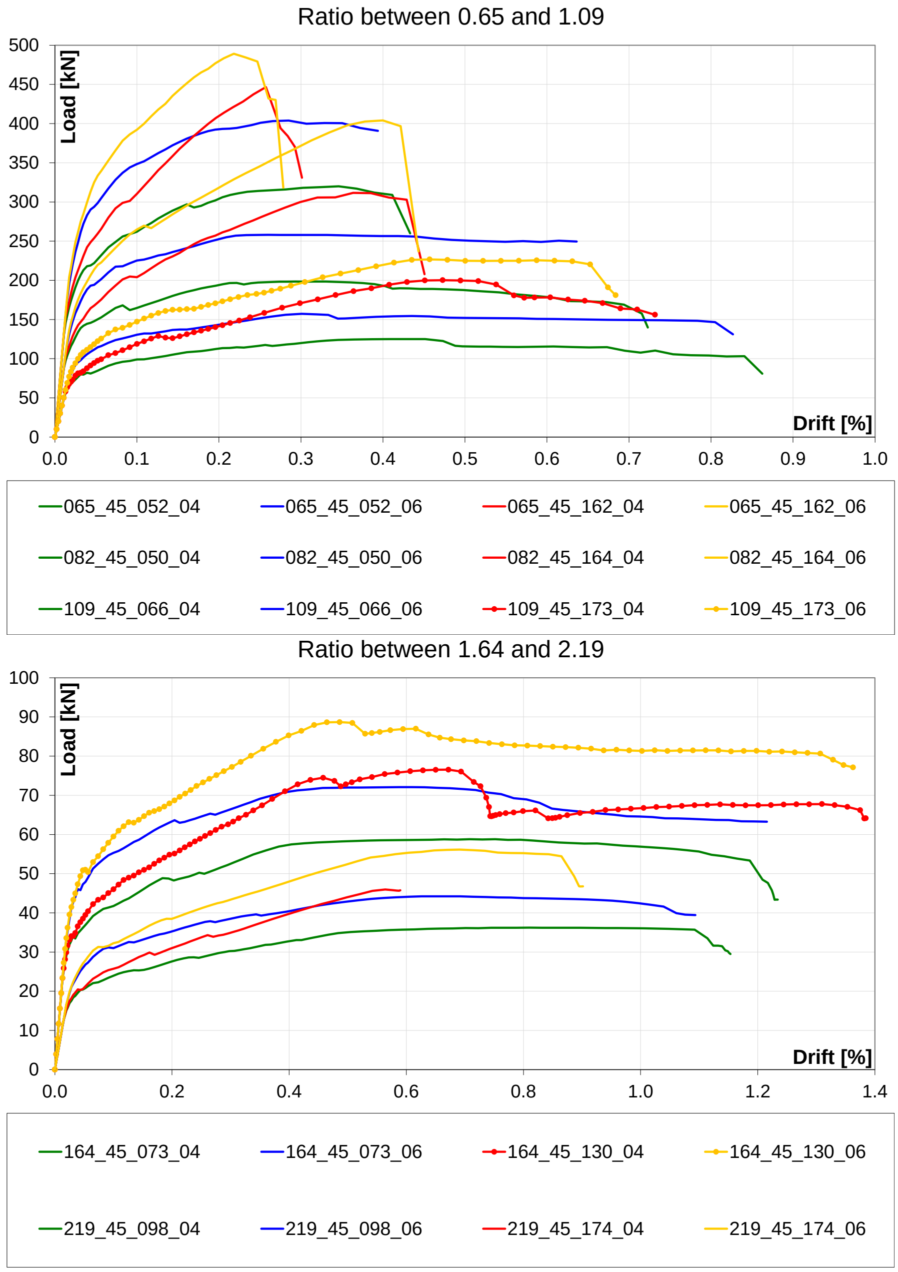

Fig. 4.23. Variation of slenderness ratio. Load – Drift curves.

A further parametric analysis was carried out in order to determine the influence of the vertical reinforcement percentage on the behavior of the analyzed reinforced masonry system (from 0 to 0.27%). In this study, the horizontal reinforcement, the vertical load (0.6 N/mm^2 and 0.4 N/mm^2) and the slenderness ratio (H/L 1.09 and 1.64), remained constant and consistent with the experimental value. The codes of the analyses in Fig. 4.24 and Table 4.13 are consistent with the previous ones; the overall number of analyses carried out was 28.

Fig. 4.24 shows the obtained results. The walls with reinforcement ratio lesser than 0.13% (4Φ14 for squat and 2Φ16 for slender models) exhibited crushing of the compressed toe after yielding of flexural reinforcement. Conversely, the walls with vertical reinforcement ratio higher than 0.2% (4Φ18 for squat and 2Φ14+2Φ16 for slender models), failed in shear with a limited ductility (see Fig. 4.24 and Table 4.13). For the walls without vertical reinforcement, the behavior changed dramatically. A rigid rocking mechanism developed, accompanied by premature crushing of compressed toe, reduction of the ultimate drift capacity, and consequent numerical instability.

name	H/L -	Hor. Reinf. %	Ver. Reinf. %	σ_0 N/mm^2	τ_{max} N/mm^2	Drift$_{max}$ %	H_{max} kN	d_{max} mm
109_45_000_04	1.09	0.045	0.000	0.4	0.16	0.592	74	13.62
109_45_066_04	1.09	0.045	0.066	0.4	0.27	0.862	125	19.84
109_45_097_04	1.09	0.045	0.097	0.4	0.33	0.836	151	19.23
109_45_132_04	1.09	0.045	0.132	0.4	0.38	0.737	175	16.96
109_45_173_04*	1.09	0.045	0.173	0.4	0.43	0.732	200	16.83
109_45_219_04	1.09	0.045	0.219	0.4	0.49	0.570	228	13.10
109_45_270_04	1.09	0.045	0.270	0.4	0.54	0.492	249	11.32
109_45_000_06	1.09	0.045	0.000	0.6	0.23	0.507	109	11.66
109_45_066_06	1.09	0.045	0.066	0.6	0.34	0.827	157	19.01
109_45_097_06	1.09	0.045	0.097	0.6	0.39	0.815	180	18.75
109_45_132_06	1.09	0.045	0.132	0.6	0.44	0.795	202	18.30
109_45_173_06*	1.09	0.045	0.173	0.6	0.49	0.684	227	15.73
109_45_219_06	1.09	0.045	0.219	0.6	0.54	0.626	250	14.39
109_45_270_06	1.09	0.045	0.270	0.6	0.58	0.573	268	13.18
164_45_000_04	1.64	0.045	0.000	0.4	0.10	0.558	32	12.85
164_45_073_04	1.64	0.045	0.073	0.4	0.19	1.234	59	28.39
164_45_100_04	1.64	0.045	0.100	0.4	0.22	1.540	68	35.41
164_45_130_04*	1.64	0.045	0.130	0.4	0.25	1.385	77	31.85
164_45_173_04	1.64	0.045	0.173	0.4	0.29	1.297	89	29.83
164_45_230_04	1.64	0.045	0.230	0.4	0.34	0.683	105	15.71
164_45_260_04	1.64	0.045	0.260	0.4	0.37	0.676	113	15.56
164_45_000_06	1.64	0.045	0.000	0.6	0.15	0.510	47	11.74
164_45_073_06	1.64	0.045	0.073	0.6	0.23	1.216	72	27.96
164_45_100_06	1.64	0.045	0.100	0.6	0.26	1.642	80	37.76
164_45_130_06*	1.64	0.045	0.130	0.6	0.29	1.363	89	31.34
164_45_173_06	1.64	0.045	0.173	0.6	0.33	0.973	101	22.39
164_45_230_06	1.64	0.045	0.230	0.6	0.37	0.675	115	15.53
164_45_260_06	1.64	0.045	0.260	0.6	0.39	0.656	120	15.09

* analysis that corresponds to an experimental condition

Table 4.13. Table of parametric variations carried out. Variation of vertical reinf. ratio.

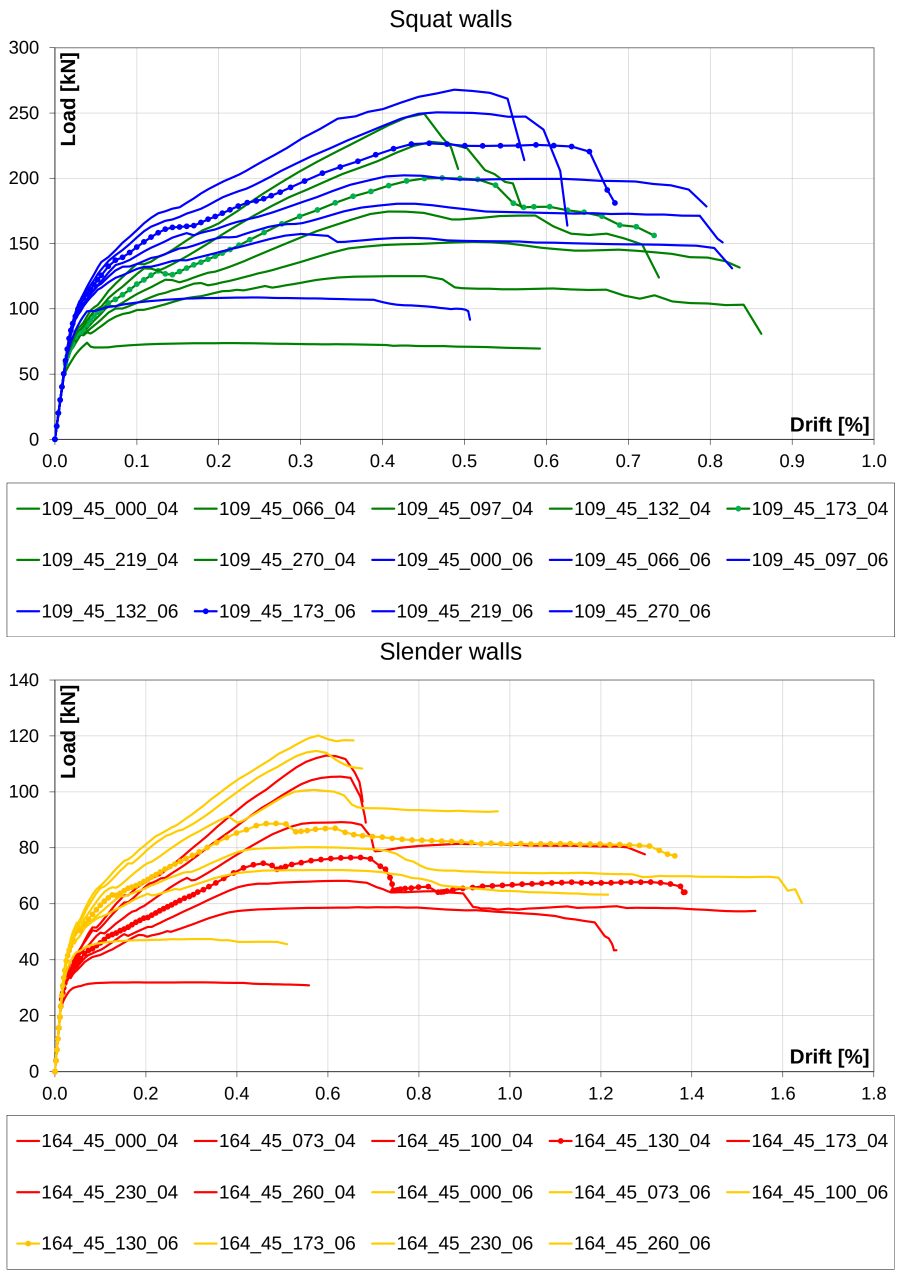

Fig. 4.24. Variation of vertical reinforcement ratio. Load – Drift curves.

4.4. Analysis of results and Conclusions

4.4.1. Unreinforced Masonry Walls

In Fig. 4.25 are summarized the results of parametric analyses in the three masonry types. The dots represent the performance of each numerically analyzed wall in terms of maximum resistance (H_{max}) and drift at ultimate limit state (θ_u). Red curves correspond to analyses carried out by applying the same vertical load used in the experimental tests. Blue curves show analyses carried out under vertical load, corresponding to the same ratio between applied load and masonry compressive strength. The four dots in each curve correspond to results of analyses carried out on walls made with units of different strength (20, 15, 10 and 5 N/mm^2) and, obviously, decreases in maximum load correspond to lower unit strength.

In general, all masonry types showed an almost linear variation in maximum horizontal force of wall with the compressive strength of unit (and wall, in broad sense) when the latter was used in constant ratio with vertical compression load (blue lines). The bends of blue curves depend of drift behavior conditioned from rocking when the effects of lower vertical load became prevalent. Despite of this fact the distribution and the evolution of stresses inside the walls did not change in this case.

When the applied vertical load is the same as in the experimental tests (red lines) the strong, non-linear maximum load decrease that all masonry types showed at the lowest unit strength indicates that, for modest unit strength, wall behavior becomes more brittle independently of masonry type, and this occurs when unit strength is between 10 and 5 N/mm^2 (the differences between masonry types are due to the greater brittleness of thin-layer joint masonry).

Combined with maximum drift decrease, this fact is reflected in the red curves of Fig. 4.25 and depends on the different failure modes of the masonry types. The curves bend sharply in the case of TG and Po masonry, indicating that failure mode changes with different unit strength.

The model results show that flexural/rocking behavior prevails at higher unit strength, whereas brittle failure develops and prevents rocking from occurring at lower unit strength. In the case of TM, the red curves of Fig. 4.25 are almost linear, in this case shear failure dominates at high unit strength range and confirms the brittleness of this type of masonry.

In facts, comparison of the three masonry types in Fig. 4.25 shows that maximum drift in TM, is always lower than in Po and TG.

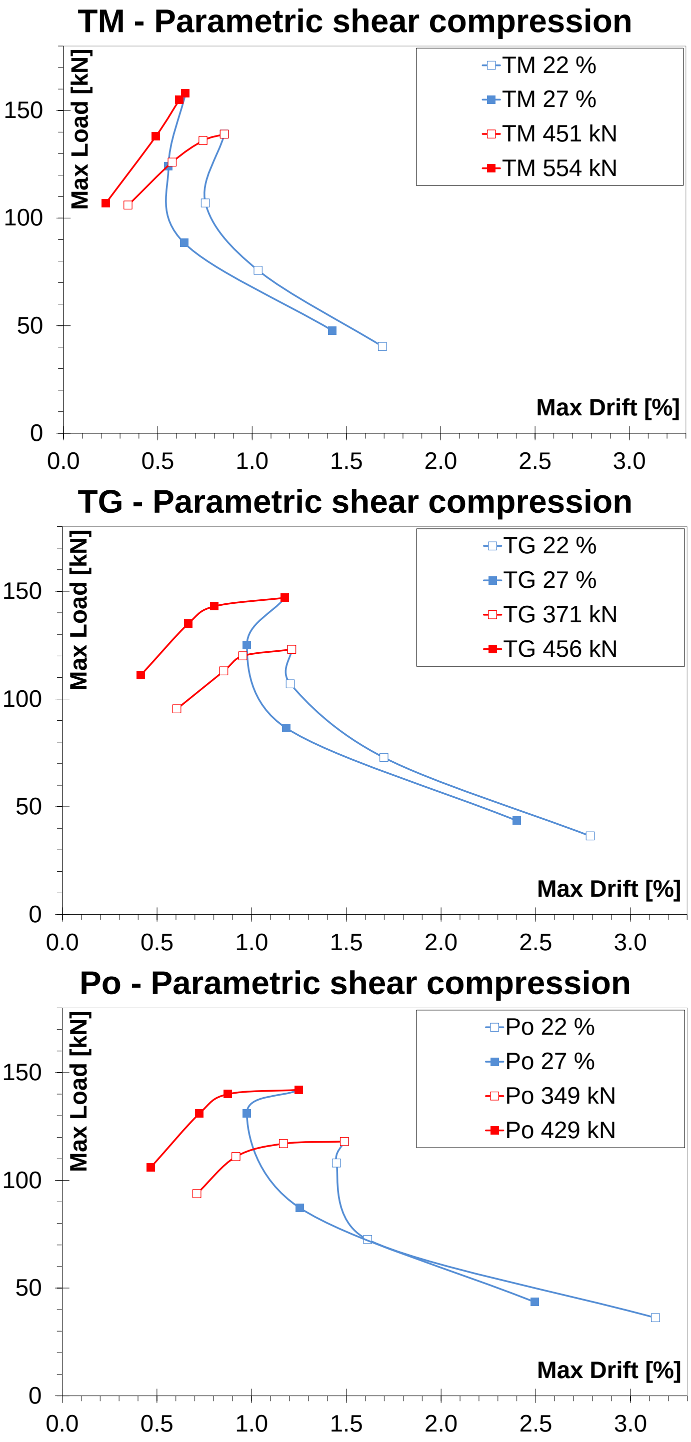

Fig. 4.25. Results of parametric analyses: maximum load versus maximum drift diagrams under same vertical load (red lines) and under same ratio of vertical load to compressive strength (blue lines).

Regard the above observations, it has to be noted that the Italian codes require a minimum characteristic compressive strength of unit of 5 N/mm^2, for the use in seismic areas (DM 14/01/2008, 2008). The European seismic code also recommends a minimum normalized compressive strength of masonry units of 5 N/mm^2 (EN 1998-1: 2004. Eurocode 8, 2004).

However, the former, being a characteristic strength, refers to an average strength which is higher than 5 N/mm^2 (and for sure comprised between 10 and 5 N/mm^2).

Instead, the latter, being a normalized compressive strength, refers to an average compressive strength of unit, which is even lower than 5 N/mm^2 considering the unit dimensions generally found in the construction market and the procedures adopted to obtain this strength from tests (EN 772-1: 2000, 2007).

4.4.2. Reinforced Masonry Walls

The Fig. 4.26, Fig. 4.27 and Fig. 4.28 summarize the results of analyses presented in paragraph 4.3.3 in terms of mean maximum shear stress and maximum drift plotted against parameter was changed in parametrical analyses.

As expected, the maximum shear stress increases for increasing applied vertical stresses (see Fig. 4.26). The increment is almost linear and is greater for the squat than for the slender models. The maximum horizontal displacement in the wall decreases with the increase of the vertical compression level (see Fig. 4.26 and Table 4.11). This indicates that the applied vertical load directly influences the mechanism of failure in the walls. After the toe crushing and under higher compression loads, the wall change its failure mode from a ductile one, as observed in the curves with vertical load lesser than 1.0 N/mm^2, to a brittle shear mode, with reduced inelastic deformation capacity beyond the peak load. The slender walls are more sensitive to this change of failure mode (see Fig. 4.26).

For vertical loads corresponding to 0.2 N/mm^2, the models show a large decrease of maximum drift when compared to higher vertical stresses (Fig. 4.26). This can be imputed to the change of behavior from flexure (in slender models) or mixed shear/flexure (in squat models) to crushing of compressed toe and the model was not able to follow displacement after this. The slender models (with greater H/L ratio) are more sensitive to this effect.

When was varied the slenderness ratio the maximum shear stress increases with the length of the wall (see Fig. 4.27 and Table 4.12). This occurs because the relative contributions of bending and shear deformations depend on the wall aspect ratio (H/L) and, consequently, the relative stiffness vary with the length of the wall (see Fig. 4.27).

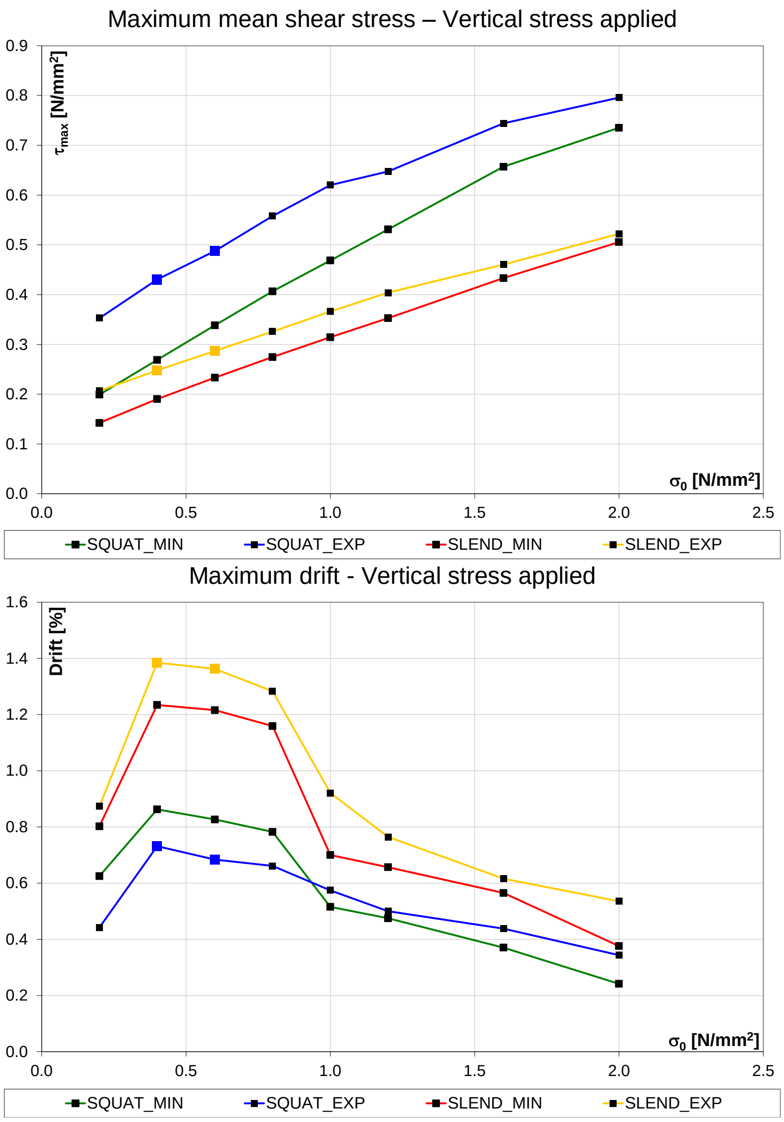

Fig. 4.26. Results of parametric analyses. Variation of vertical stress.

However, the increase is not linear and for smaller slenderness (H/L), the simultaneous increase of vertical reinforcement causes higher increase of shear resistance (Fig. 4.27), accompanied by higher fragility. Pure shear limit can be observed for 065_45_162_06 and 082_45_164_06, i.e. the squatter walls with highest vertical stresses and reinforcement. Indeed, by analysis for H/L ratio lesser than 1.09, there is greater ultimate displacement with minimum reinforcement rather than with the percentage of reinforcement used in experimental tests (Fig. 4.27 and Table 4.12). This turns into similar displacement capacity for a slenderness ratio H/L equal to 1.09, and this trend reverses (larger displacement capacity with higher reinforcement ratio) when H/L ratio is higher than 1.09.

In the case of slenderness ratio equal to 1.64, due to the flexural-type behavior, with the lower reinforcement ratio the walls are under-reinforced, and collapse occurs due to failure of reinforcement in tension. In addition, for slenderness of 2.19, which represents the minimum length for the masonry system under investigation, the behavior changes again and the maximum drift shows a large decrease (see Fig. 4.27). This can be imputed to the change of behavior from flexure to crushing of compressed toe. The models with larger vertical reinforcement ratio are more sensitive to this effect.

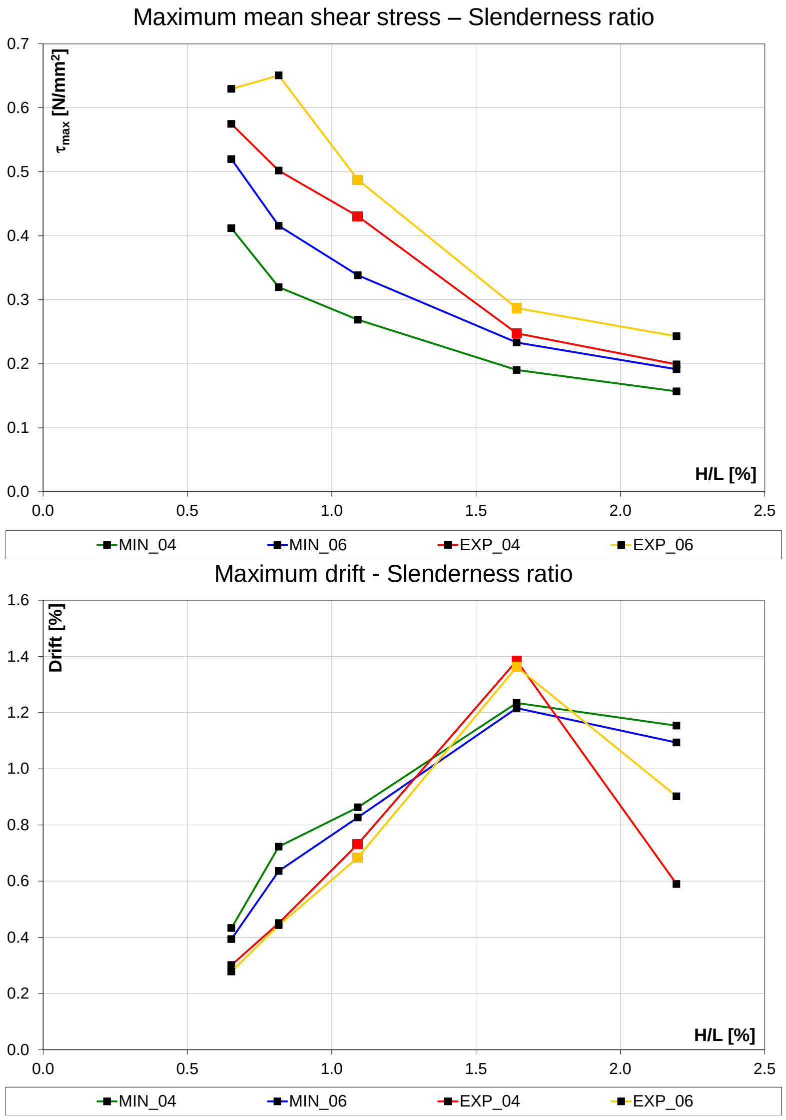

Fig. 4.27. Results of parametric analyses. Variation of slenderness ratio.

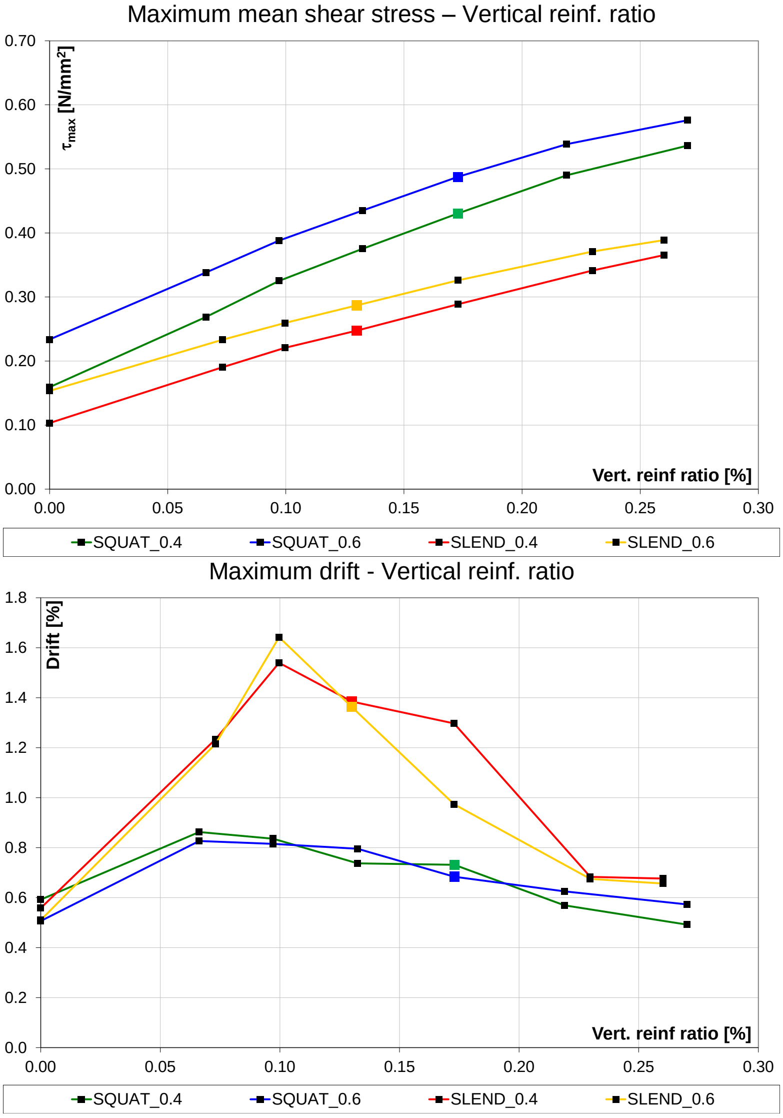

Fig. 4.28. Results of parametric analyses. Variation of vertical reinf. ratio.

Fig. 4.28 shows the obtained results of parametric analyses carried out in order to determine the influence of the vertical reinforcement percentage.

Maximum mean shear stress increases almost linearly with vertical reinforcement ratio. The walls with reinforcement ratio lesser than 0.13% (4Φ14 for squat and 2Φ16 for slender models) exhibited crushing of the compressed toe after yielding of flexural reinforcement. Conversely, the walls with vertical reinforcement ratio higher than 0.2% (4Φ18 for squat and 2Φ14+2Φ16 for slender models), failed in shear with a limited ductility (see Fig. 4.28). This worsening of the wall behavior is more significant for slender rather than for squat specimens. The maximum displacements of the two series become even similar, for vertical reinforcement ratio higher than 0.2% (Fig. 4.28). For the walls without vertical reinforcement, the behavior changed dramatically. A rigid rocking mechanism developed, accompanied by premature crushing of compressed toe, reduction of the ultimate drift capacity, and consequent numerical instability.

Hence, the increase of the vertical reinforcement has a positive influence on the ultimate strength of the walls. Up to a certain quantity, the increase of reinforcement ratio increases both strength and the available displacement capacity otherwise the walls would be under reinforced. After a certain limit, the increase of reinforcement still increases the ultimate load capacity, but it reduces the available ductility (see Fig. 4.28).

4.4.3. Summary and conclusions

Three types of load-bearing un-reinforced masonry walls, made with perforated clay units and differing types of head and bed joints were experimentally tested under in-plane cyclic loads. Four different types of non-linear models, which follow macro- and micro-modeling strategies and implement isotropic damage or orthotropic plastic criteria for materials, were calibrated. The main mechanical parameters were extracted by common tests, used in practice to characterize materials and simulate actual loading conditions in structural masonry walls, and were applied without arbitrary corrections.

Inelastic parameters, which can be obtained by means of more complex test procedures and are useful for theoretical studies of masonry behavior, were defined according to an extensive literature survey.

Lastly, some simple criteria to evaluate mechanical properties of expanded units in micro-models and to obtain orthotropic parameters from isotropic ones were defined. The first criterion is based on the net area ratio that characterizes masonry cross-sections and influences masonry anisotropy when perforated units are used. The second allows micro-model interface parameters to be found and they can be applied to the analyses without any correction, by systematically introducing the experimental correction due to mortar joint and mortar-unit interface irregularity into the numerical models.

In the case of uniaxial compression, three out of the four models reproduced experimental behavior fairly well. Orthotropic models and the isotropic micro-model are more suitable. Experimental behavior under diagonal compression was properly described only by micro-models, both orthotropic and isotropic. In particular the isotropic micro-model described shear compression tests accurately. The type of test that is being simulated influences the accuracy of numerical results more than masonry type itself. In general, at least one modeling strategy simulated each type of test very well, and allowed differences in stress distribution and behavior due to the type of masonry bond arrangement to be appreciated. Analyses confirmed that the various test configurations used to study the shear behavior of masonry walls (i.e., diagonal compression and shear compression tests) leads to different stress distributions, clearly, but they also showed that the types of tested masonry could emphasize this effect (i.e. unit dimension and joints arrangements).

Thanks to the methodical approach followed, it was possible to define a reliable modeling strategy for analysis of in-plane loaded masonry. Parametric analyses showed how wall performance under combined shear and compression depend on unit strength and masonry type. In general, maximum horizontal load and drift at ultimate state decrease with unit strength. For masonry with ordinary bed joints (Po and TG), the decrease in unit strength also corresponds to a change in dominant failure mode, from flexure/rocking to shear whereas, in the case of more brittle thin-joint masonry (TM), a more brittle failure prevails throughout the unit strength range. In all masonry types, critical behavior arises at unit strengths between 10 and 5 N/mm^2. If the ratio of applied vertical load to masonry compressive strength is kept constant, maximum drift may increase at lower unit strength, as vertical load decreases and rocking behavior prevails but, in any case, the displacement capacity of thin-layer joint masonry remains lower than in other masonry types.

Analyses on a newly perforated clay unit reinforced masonry system were done with the aim of modeling the envelope of cyclic shear compression tests carried out. The results of the analyses carried out were discussed and the main results are in the following:

- finite element and experimental results were compared and good agreement was found in terms of load, displacements, failure modes and crack patterns;
- the calibrated model was used to carry out some parametric analyses in order to investigate the influence of vertical load, slenderness and vertical reinforcement ratio on the behavior of the masonry system under investigation;
- the maximum horizontal load capacity of the walls changes, as expected, with the variation of these parameters and their combinations.
- in general, it was possible to find linear relation between the maximum shear stress and both the vertical load and the vertical reinforcement percentage.
- the maximum shear stress presented a non-linear decrease with increase of H/L ratio.
- the ultimate drift curves generally presented a non-linear trend in relation to these parameters, due to the variation of ductility caused by the change of failure mechanisms in the reinforced masonry walls.

5. ANALITICAL MODEL

5.1. Introduction

In order to simplify the approaches described in previous chapter an analytical model able to reproduce the force-displacement behavior of URM and RM masonry walls was built.

For masonry wall (S.D.o.F. structure) under in plane both vertical and horizontal forces, the model is able to take in to account the deformability (also shear deformation), that relates the wall behavior with section curvature. The model can reproduce both flexural and shear failures, and identifies the achievement of various limit states which represent the performances of masonry walls (i.e. serviceability, damage control, ultimate, and collapse prevention), related with cross-section or whole panel limit states.

5.2. Model Hypothesis and its Capabilities

The model is a formulation of a fiber element and is cast in the general framework of the mixed method. The proposed state determination is based on a non-linear algorithm that always maintains static equilibrium within the element and converges to a state that satisfies the element constitutive relation within a specified tolerance.

The proposed solution algorithm is particularly suitable for the analysis of the highly non-linear behavior of softening members, such as reinforced and unreinforced masonry piers under varying axial load.

The formulation of the wall element is based on the assumption of linear geometry. The element is divided into a discrete number of cross sections. Plane sections remain plane and normal to the longitudinal axis during the element deformation history. While this hypothesis is acceptable for small deformations of elements composed of homogeneous materials, it does not properly account for phenomena which are characteristic of masonry elements (such as cracking). The effect of cracking can be included in the model by an appropriate modification of the stress-strain relation of masonry according to the smeared crack concept of finite element analysis. This effect is only significant in the pre-yield phase of response and can be neglected in studies which focus on the hysteretic behavior under large inelastic deformation reversals (Spacone et al., 1996).

From the assumption that sections remain plane and normal to the longitudinal axis, all strains and stresses act parallel to this axis. Since the reference axis is fixed, this implies that the geometric centroids of the sections form a straight line that coincides with the reference axis. It is worth pointing out that the section subdivision into fibers derives from the numerical solution of the integrals for the determination of the section stiffness and resisting force from the corresponding stresses and strains. This point is discussed in more detail in the in the next paragraph (5.3).

The validity of the analytical results depends therefore on the accuracy of the material models. Since the present study is limited to the behavior of masonry members and the effect of bond-slip on reinforcement bars is neglected, only two material models are required: one for masonry and one for reinforcing steel (if reinforcement is present). The element formulation simplifies the task of material model selection to uniaxial behavior, which is thoroughly studied and well established to date. Three-dimensional effects on material behavior can be included into the uniaxial model by appropriate modification of the parameters that define the monotonic envelope. This could be important in the case of confined masonry, where confinement has a significant effect on the stress-strain behavior, but is not the case for masonry systems which this thesis refers. The model does not take into account the effect of confinement by transverse reinforcement because this phenomenon was not possible for the reinforced masonry construction system which this study refers (Mosele, 2009). Actually this is true for reinforced clay masonry walls in general, since the reinforcements are placed into horizontal joints and they not be able to develop a full bond and confinement effect as reinforced concrete. Therefore shear deformation of masonry element does not take into account the contribution of horizontal reinforcements (if they are present) until shear failure occurs.

Strength deterioration of masonry members under large deformation reversals depends largely on the capacity of masonry to sustain stresses in the strain range beyond achievement of maximum strength. This requires the use of a refined even simple material model. The model used in this study is shown in Fig. 5.1. The monotonic envelope of masonry in compression is a 4 branch multi-linear curve (plus a residual strength which is intended only for numerical stability) and was neglected the masonry contribution in tension. Even though more accurate and complete models have been published since the (Kent & Park, 1971) model, this approximation represents a good compromise between simplicity and accuracy.

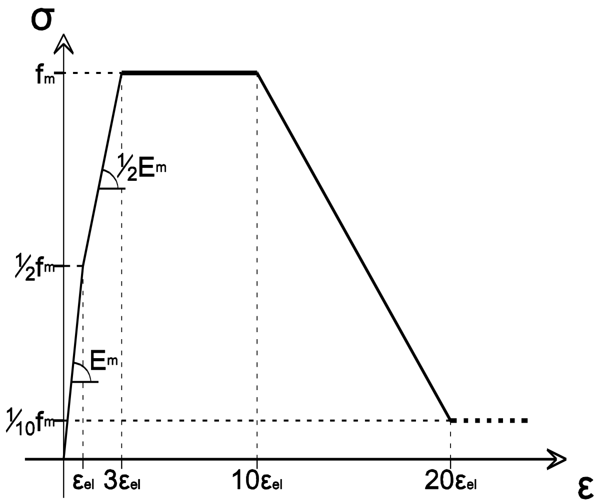

Fig. 5.1. Masonry stress-strain relation.

The non-linear behavior of the proposed element derives in part from the material constitutive laws and in part from shear stiffness degradation effect. Therefore shear effects are also included, which is a reasonable approximation for normal height to depth ratios of the masonry member (it will be discuss more in detail in 5.3.3).

The model takes into account possible shear failures at wall level, using the phenomenological approach proposed by (Turnšek & Čačovič, 1971) and modified by (Tomaževič & Lutman, 1988). This approach refers to a diagonal shear failure induced by a tensile failure of masonry panel. It takes into account of effect of axial load and, coupled with information provided by this model (namely relation between overturning moment and load eccentricity), it can change shear distribution factor (*b*) and update the shear strength of panel with horizontal force variation. The choice using only diagonal indirect tensile failure mechanism in shear can be justified in the light of observed failure modes in tests under consideration and in others experimental works present in literature (da Porto et al., 2009b; Magenes et al., 2008; Tomaževič, 2009). If shear failure occurs the model approximates empirically the post-peak load-displacement curve of element in a similar way to criteria proposed by (Anderson & Priestley, 1992) and (Voon & Ingham, 2007) and taking in to account (Mosele, 2009) observations. It does point out however, that the criteria presented by these authors aimed to assess the maximum shear strength for a given ductility, while the aim of this model is to describe the decay of strength with increasing displacement (and therefore also of ductility in the broad sense) after the maximum strength achievement (it will be discuss more in detail in 5.3.4).

Summarizing, the model start from Moment-Curvature analysis of panel with isostatic boundary conditions (fixed to the base) and considers masonry wall as isotropic homogeneous material. Then, from pure flexural analysis, considering (if present) the contribution of vertical reinforcement bars at wall ends to the flexural strength and displacement, the model adds shear deformation contribution.

Therefore the model follows the wall behavior in the post-peak branch of capacity curve and takes into account possible indirect tensile diagonal shear failure of panel and the strength contribution of horizontal reinforcement bars (if they are present) and approximates shear strength decay with increasing displacements.

5.3. Model Building and Input Required

5.3.1. Moment-Curvature Function

In order to build the moment and curvature functions the inputs required are geometrical, material properties and boundary condition definition. Respectively these are L, H, t for length, height and thickness of wall (geometrical), f_m, E_m and G which define compressive strength, elastic and shear modulus of masonry (material properties) and σ_0 the vertical compression stress (boundary condition). Of course, when reinforcements are present there are more inputs required such as the area of vertical and horizontal re-bars (A_s and A_{sh} respectively). In addition, for vertical re-bars, positioning with respect to the wall edge (d') and spacing between horizontal re-bars (s), and also steel material properties, such elastic moduli (E_s and E_{sh} respectively) and steel yield strengths (f_{ys} and f_{ysh})

Imposing equilibrium equations it is possible, for a generic cross-section, moment and curvature related to a specific strain (i.e. at the maximum compressed side). In this way it is possible to identify some limit states related to cross-section performances even though limited to flexure response. Observing that shear deformation don't affect curvature, moment and curvature previously calculated are still valid even when shear deformation is added. Therefore isostatic boundary conditions of panel suggest that these cross-section limit states related to base section of wall will give, at least, the first indicators of whole panel behavior. Furthermore, imposing that compression strain grows (at compressed toe), it is possible to control the whole moment curvature curves and by simply imposing equilibrium equations.

In details, imposing vertical translation equilibrium equation and ε (the masonry strain at compressed edge of section) the model is able to find the correct cross-section part under compression (named β) using the following equations (from Eq. 5.1 to Eq. 5.6):

$$d = L - d' \qquad \text{(Eq. 5.1)}$$

$$N = \sigma_0 \cdot (L \cdot t) \qquad \text{(Eq. 5.2)}$$

$$C(\varepsilon, \beta) = \begin{cases} t \cdot \int_0^{\beta} \sigma\left(\frac{x}{\beta} \cdot \varepsilon\right) dx\,, & \beta \leq L \\ t \cdot \int_{\beta - \mathrm{L}}^{\beta} \sigma\left(\frac{x}{\beta} \cdot \varepsilon\right) dx\,, & \beta > L \end{cases} \qquad \text{(Eq. 5.3)}$$

$$S(\varepsilon, \beta) = \begin{cases} \left(\frac{\beta - d}{\beta} \cdot \varepsilon\right) \cdot E_s \cdot A_s\,, & \left|\frac{\beta - d}{\beta} \cdot \varepsilon\right| \leq \varepsilon_{ys} \\ \left(\frac{\beta - d}{\beta} \cdot \varepsilon\right) / \left|\frac{\beta - d}{\beta} \cdot \varepsilon\right| \cdot f_{ys} \cdot A_s\,, & \left|\frac{\beta - d}{\beta} \cdot \varepsilon\right| > \varepsilon_{ys} \end{cases} \qquad \text{(Eq. 5.4)}$$

$$S'(\varepsilon, \beta) = \begin{cases} \left(\frac{\beta - d'}{\beta} \cdot \varepsilon\right) \cdot E_s \cdot A_s\,, & \left|\frac{\beta - d'}{\beta} \cdot \varepsilon\right| \leq \varepsilon_{ys} \\ f_{ys} \cdot A_s\,, & \left|\frac{\beta - d'}{\beta} \cdot \varepsilon\right| > \varepsilon_{ys} \end{cases} \qquad \text{(Eq. 5.5)}$$

$$N = C + S + S' \qquad \text{(Eq. 5.6)}$$

Where d is the distance between vertical reinforcement in tension and the edge of section in compression, N the total vertical force applied to masonry panel (it is constant as σ_0), C is the total compressive reaction force provided by masonry, S is the reaction of vertical reinforcement in tension (negative in this reference system) and S’ the reaction of vertical reinforcement in compression (which is positive).

The solutions was achieved using MathCad 14 (from PTC software) environment with non-linear solver that uses Levemberg-Marquardt method and a numerical tolerance of 10^{-5}N for (Eq. 5.6) and integrals of (Eq. 5.2).

For each strain imposed to masonry in compression (which always grows during a push-over analysis) model can relate an effective compression depth (β(ε)) starting from a strain ε_0 due to initial σ_0 stress state using the following equations (from Eq. 5.7 to Eq. 5.9) in the previous (Eq. 5.6).

$$C(\varepsilon_0) = t \cdot \mathrm{L} \cdot \sigma(\varepsilon_0) \qquad \text{(Eq. 5.7)}$$

$$S(\varepsilon_0) = \begin{cases} \varepsilon_0 \cdot E_s \cdot A_s, & |\varepsilon_0| \leq \varepsilon_{ys} \\ f_{ys} \cdot A_s, & |\varepsilon_0| > \varepsilon_{ys} \end{cases} \qquad \text{(Eq. 5.8)}$$

$$S'(\varepsilon_0) = S(\varepsilon_0) \qquad \text{(Eq. 5.9)}$$

When compression depth is known is possible to calculate the position of resultant provided by masonry contribution. With (Eq. 5.10) it was calculate this position referring to compressed end of section.

$$j(\varepsilon) = \begin{cases} \beta(\varepsilon) - \left(\frac{t}{C(\varepsilon,\beta(\varepsilon))}\right) \cdot \left[\int_0^{\beta(\varepsilon)} x \cdot \sigma\left(\frac{x}{\beta(\varepsilon)} \cdot \varepsilon\right) dx\right], & \beta(\varepsilon) \leq L \\ \beta(\varepsilon) - \left(\frac{t}{C(\varepsilon,\beta(\varepsilon))}\right) \cdot \left[\int_{\beta(\varepsilon)-\mathrm{L}}^{\beta(\varepsilon)} x \cdot \sigma\left(\frac{x}{\beta(\varepsilon)} \cdot \varepsilon\right) dx\right], & \beta(\varepsilon) > L \end{cases} \qquad \text{(Eq. 5.10)}$$

Then, imposing rotational equilibrium to section, it was find out the bending moment as a function of maximum compression strain in masonry compressed end of section (M(ε)) with following equation (Eq. 5.11):

$$M(\varepsilon) = \left(N \cdot \frac{L}{2}\right) - \left[\left(j(\varepsilon) \cdot C(\varepsilon)\right) + \left(d \cdot S(\varepsilon)\right) + \left(d' \cdot S'(\varepsilon)\right)\right] \qquad \text{(Eq. 5.11)}$$

Using a more general form (with the above mentioned hypothesis that section remains plane), it was also calculated the curvature as function of maximum masonry compression strain (φ(ε)) by (Eq. 5.12)

$$\varphi(\varepsilon) = \varepsilon / \beta(\varepsilon) \qquad \text{(Eq. 5.12)}$$

Furthermore, as common practice, model limits the post-peak response with some additional controls:

a) maximum strength loss is 20% of bending moment at peak;
b) vertical reinforcements in compression do not yield ($S' < \mathrm{f_{ys}} \cdot \mathrm{A_s}$).

The first point above find reference in a manifold of codes and research works (Ordinanza P.C.M. n. 3274: 2003, 2005; Tomaževič, 1999).

Instead point b) gives a raw approximation for the model and is un-conservative limit for possible buckling effects of compressed vertical reinforcements. Correctly evaluate the buckling length (and consequently buckling load) is an hard task because mortar columns, where vertical reinforcements are arranged, might be in a non-linear range of stress-strain relation and also horizontal reinforcements don't provide a full constraint when reinforcement bars can buckle.

5.3.2. Flexural Displacement Contribution

Despite both bending moment and curvature are functions of same maximum masonry compression strain, it should be pointed out that the model cannot relate them straightforward. This is an issue that imposes to leave a pure analytical solution for a less fascinating but practically suitable numerical way. This would be objective of future improvements of model.

Anyhow, we can observe that for a non-linear solution, which is the target of this model, the curvature profile along the height (H) of masonry wall is *a prioi* unknown. Then it is useless to relate bending moment directly to curvature (M(φ)) because even if it is theoretically possible by cross-section equilibrium equations it is not when model need integration along wall height to obtain the global response.

Furthermore, bending moment profile along wall height is known, thanks to isostatic boundary conditions, and varies linearly from 0 at top of the wall up to maximum at base of masonry pier. So it is possible to relate and integrate curvature with bending moment, but during the strength-loss branch of Moment-Curvature (and/or Force-Displacement curves), the solution becomes not unique and φ(M) function does not have a straightforward analytical solution.

Therefore, this model adopts a workaround of these problems:

a) approximating φ(M) function obtained from linear interpolation of φ(ε)-M(ε) functions at cross-section level;
b) dividing φ(M) function in two branches one before and one after the maximum bending moment.

Linear interpolation of functions φ(ε) and M(ε) is made with φ as dependent value from M value and where each couple refers to the same maximum masonry strain in compression. The operation of dividing these functions in two branches was intended to have two monotone functions and furthermore made possible a handily way to manipulate post-peak moment profile (Fig. 5.2 provides a typical form of Moment curvature relation). Actually both these procedure was applied for all variables e.g. C, S, S’, β in order to refer all of them directly to cross-section bending moment and not only for curvature.

As stated above, due isostatic boundary conditions, model can refer to base bending moment (and of course base shear force) without losing any information about moment variation along wall height because it is always linear. This makes possible to describe curvature profile for a given base shear force and hence integrate it to obtain a rotation profile and, with a second integration process, the displacement profile.

Therefore, model draws shear force versus displacement curve or rather a capacity curve of wall. To be precise only flexural capacity curve was found until shear deformation contribution to displacements is also added.

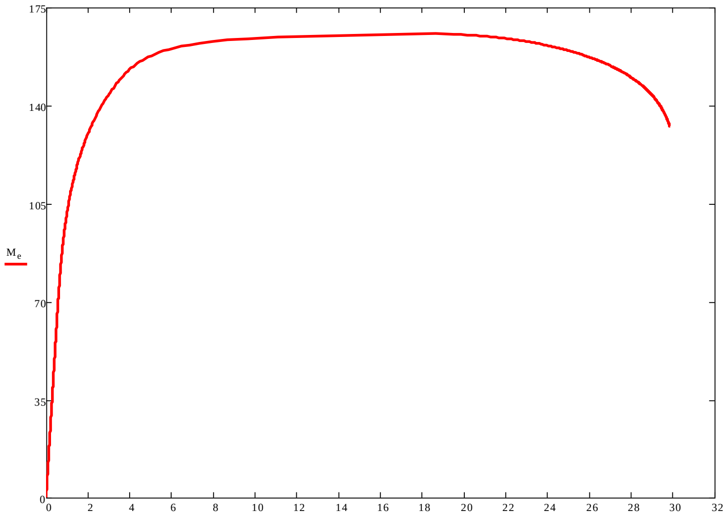

Fig. 5.2. Moment-Curvature relation. An example of typical form.
(TG masonry with σ_0=1.55 N/mm^2, M [kNm] and φ[10^6/mm])

There are a couple of issues about post-peak response treatment and integration process that have to be pointed out. First, when the wall reaches maximum bending moment at base cross-section (according to moment-curvature function found), rest of the wall has lower moment. Then, in the next step (see Fig. 5.3), base-wall bending moment decreases following moment-curvature function (start softening branch). Instead other cross-sections have different behavior because their moment decreases even though it did not reach maximum moment. Hence base section behaves following found moment curvature function and its curvature grows with strength softening when it is not for the rest of wall. Model does not provide a loading-unloading stress-strain function, so needs to approximate this phenomenon with one more hypothesis at moment-curvature level. A good and accepted in literature hypothesis (Benedetti et al., 1982; Del Piero, 1983) describes compression unloading for masonry as linear.

This model introduces the hypothesis of constant curvature unloading for all cross-sections above the wall base, hence with a further approximation. This is justified from observation that curvature of elastic branch is negligible against more stressed cross-sections (see Fig. 5.4 where the green line represents the elastic curvature profile or an estimate of error introduced introducing this hypothesis).

To describe post-peak capacity curve it was built a matrix where the curvature of base cross-section follows the full moment-curvature function whereas sections above base keep constant for each horizontal shear force applied at top of wall.

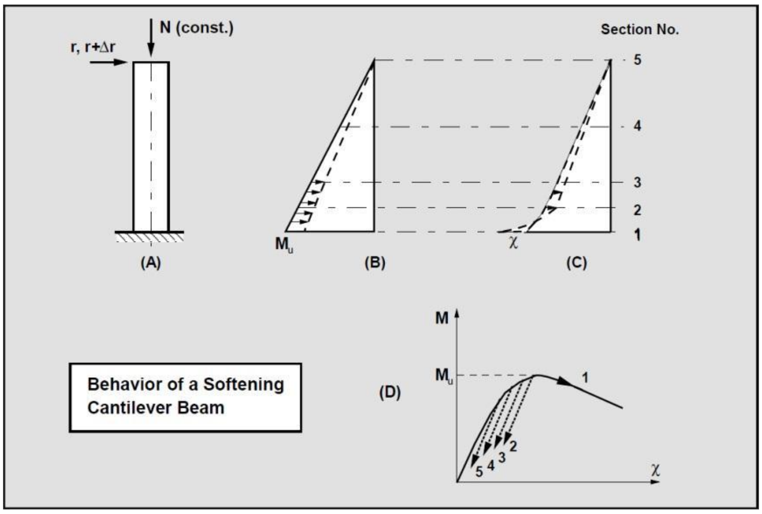

Fig. 5.3. Post-peak behavior of model.
(A) Member and loading; (B) Moment distribution; (C) Curvature distribution; (D) Moment-Curvature relation. (Taucer et al., 1991)

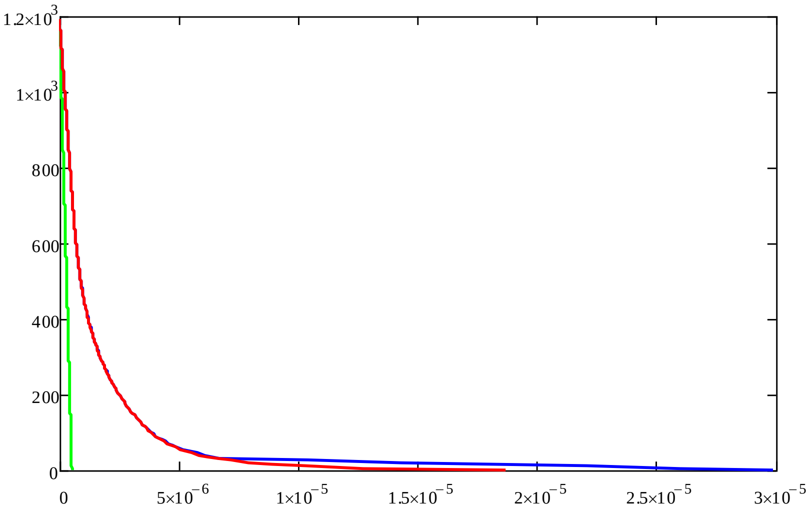

Fig. 5.4. Curvature along height of wall. An example of typical form.
Red line curvature profile at max strength, blue line at ultimate strength and green elastic curvature. (TG masonry with σ_0=1.55 N/mm^2, H [mm] and φ [1/mm])

In general this this kind of approaches bear to discretization sensitivities when integrating the functions along height of wall because section base curvature (the only one where curvature increases beyond maximum moment) has more or less influence in whole response (the integrated one) with change of discretization size. This problem was found in other works in literature (Jiang & Kurama, 2010; Taucer et al., 1991) but with a reasonable number of subdivision along the wall and especially close to the base (where are the non-linarites concentrated), the response of wall becomes stable.

5.3.3. Shear Displacement Contribution to Flexural Behavior

After the calculation of pure flexural response the model adds the deflection induced by shear. This was estimated by integration along wall height too, but using (Eq. 5.13) that express angular deflection due to shear:

$$\gamma(M) = \frac{\chi \cdot F}{G(M) \cdot t} \cdot \frac{1}{\beta(M)} \tag{Eq. 5.13}$$

Where χ indicates shear coefficient that is constant and equal to 6/5=1.2 for rectangular sections used in this model; F is horizontal force applied and β is the neutral axis position of cross-section measured from compressed end of section. This form of equation was used for directly taking into account the actual section involved in the shear-flexure deformations as soon as the material is (by hypothesis) not resisting to traction.

Fixed the force applied (F), β varies along the height of the wall, from whole section length (L) in the upper part of panel, that is still elastic, and decreases with increasing of moment up to the base section. Hence, when masonry reaches elastic limit (ε_{el}) and starts non-linear part of stress-strain curve, shear modulus do not still as remaining constant. Besides since G is an elastic modulus, it acts only in the cross section part that is still in the elastic range (masonry compression strain smaller than ε_{el}).

This two observations are translated in the following (Eq. 5.14 and 5.15):

$$\beta_{el}(M) = \begin{cases} \beta(M), & \left[\frac{\varepsilon_{el}}{\varphi(M)}\right] \geq \beta(M) \\ \left[\frac{\varepsilon_{el}}{\varphi(M)}\right], & \left[\frac{\varepsilon_{el}}{\varphi(M)}\right] < \beta(M) \end{cases} \tag{Eq. 5.14}$$

$$G_{red}(M) = \mathrm{G} \cdot \frac{\beta_{el}(M)}{\beta(M)} \tag{Eq. 5.15}$$

So, previous (Eq. 5.13) becomes the following (Eq. 5.16):

$$\gamma(M) = \frac{\chi \cdot F}{G_{red}(M) \cdot t} \cdot \frac{1}{\beta_{el}(M)} \tag{Eq. 5.16}$$

Integrating this equation (using the same recommendations presented in previous paragraph 5.3.2) along the height of wall bears to find shear displacement contribution (an example in Fig. 5.5).

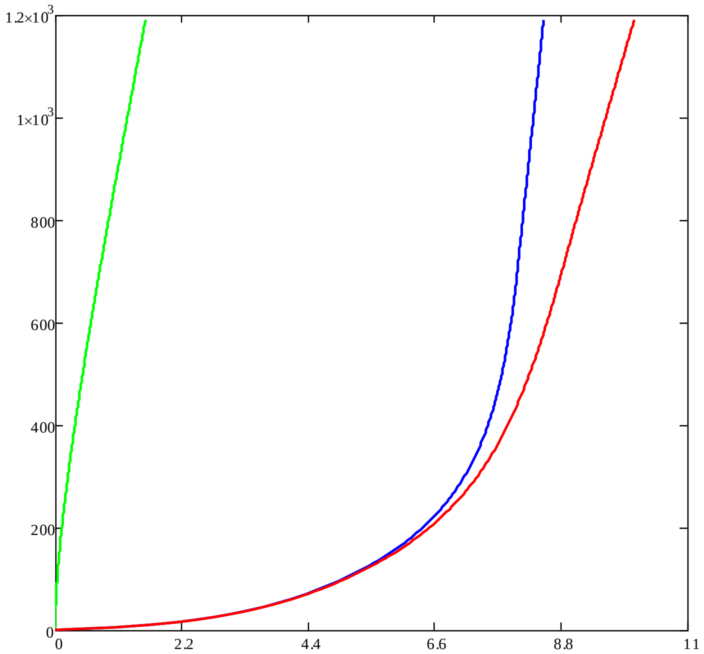

Fig. 5.5. Displacement profiles along height of wall.
Red line: total displacement profile at max strength, blue line shear displacement contribution and green flexure displacement contribution.
(TG masonry with σ_0=1.55 N/mm^2, H [mm] and Δ [mm])

5.3.4. Shear Strength and Displacement Limits

Mixed method proposed with the model calculates flexure behavior by successive integrations to get the response of masonry wall, starting from section equilibrium equations while possible shear failure is evaluated considering masonry pier subjected to a global mechanism. Model follows a phenomenological approach that considers masonry shear failure as truss tensile-induced failure and indirectly takes into account vertical load (Tomaževič & Lutman, 1988; Turnšek & Čačovič, 1971). Furthermore, in present model masonry shear strength is not considered constant because it can calculate for every single bending moment value and eccentricity of load resultant (e) over cross-section. According with formulation proposed in (Bernardini et al., 1982a; Bernardini et al., 1982b) the (Eq. 5.17)

$$b(e) = \begin{cases} 1.5 - 0.48 \cdot \frac{2 \cdot e}{H}, & \frac{H}{L} \leq 1.5 \\ 1.5, & \frac{H}{L} > 1.5 \end{cases} \qquad \text{(Eq. 5.17)}$$

Where b is the factor that refers to maximum tangential stress distribution with respect the mean one. It varies between 1.5 for slender cantilever walls ($H/L \geq 1.5$)

and 1 for squat cantilever walls $H/L \leq 1$. Therefore factor b is function of eccentricity ($e = M/N$) and indirectly function of bending moments (see Fig. 5.6).

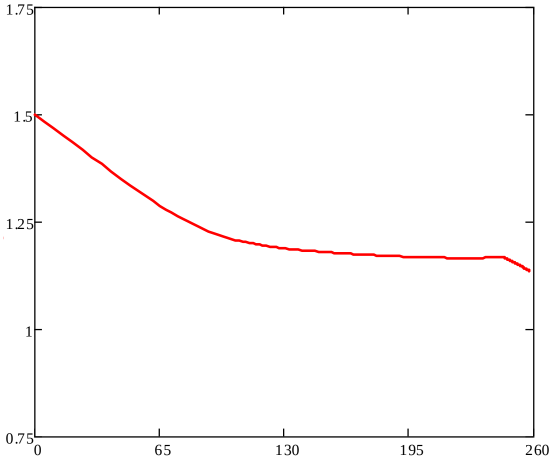

Fig. 5.6. Variation of b coefficient with base shear force. (TRSa masonry with σ_0=0.6 N/mm^2, b [-] and F [kN])

Accordingly to this, shear strength (V_r) is a summation of two contributions: masonry shear strength (V_m) and horizontal reinforcements (V_{sh}) if they are present. First term is calculated from (Eq. 5.18):

$$V_m(\mathrm{M}) = \left(\frac{f_{mt}}{b(M)} \cdot \sqrt{\frac{\sigma_0}{f_{mt}} + 1}\right) \cdot t \cdot L \qquad \text{(Eq. 5.18)}$$

With f_{mt} is indicated tensile strength of masonry (considered as homogeneous material) and it is evaluated from (Eq. 5.19):

$$f_{mt} = \sqrt{f_m}/10 \leq 0.2\ \mathrm{N/mm^2} \qquad \text{(Eq. 5.19)}$$

This definition is a refinement of American formulations that are characterized by adopting tensile strength in the URM contribution, since V_m term contains $\sqrt{f_m}$, and in particular (Anderson & Priestley, 1992) gives $1.2 \cdot \sqrt{f_m}$, which corresponds to $1/8 \cdot \sqrt{f_m}$, usually accepted as estimation of tensile strength of masonry (Tassios, 1988).

(Tomaževič, 1999) proposed to evaluate the tensile strength as 0.03÷0.09 f_m. These are consistent with data and observations provided by (Mosele, 2009). This model provides also a limitation of 0.2 N/mm^2 that improves the best fitting for all masonry systems under investigation in this thesis (both URM and RM system).

Shear contribution due to horizontal reinforcements is given by (Eq. 5.20):

$$V_s = C_r \cdot \left(\frac{d}{s} \cdot A_{sh} \cdot f_{ysh}\right) \tag{Eq. 5.20}$$

This formula calculates the number of stirrups across the diagonal crack (assumed to be 45° sloped starting from the effective length of the resisting section: d). Spacing between two horizontal reinforced joints was named s and C_r is reduction coefficient that takes into account efficiency of stress transfer among horizontal reinforcements and masonry (Anderson & Priestley, 1992; Mosele, 2009; Tomaževič & Lutman, 1997) and it is equal to 0.6 in agreement with (Ordinanza P.C.M. n. 3274: 2003, 2005). In this way model can calculate shear strength of masonry panel (V_r) associated to each bending moment (M). The isostatic boundary conditions bear that shear strength of pier must be confronted with wall base bending moment or rather the flexure capacity of masonry wall. Then it is possible to verify whether shear failure occurs in the wall that is whether shear strength is lesser then flexure capacity (Fig. 5.7).

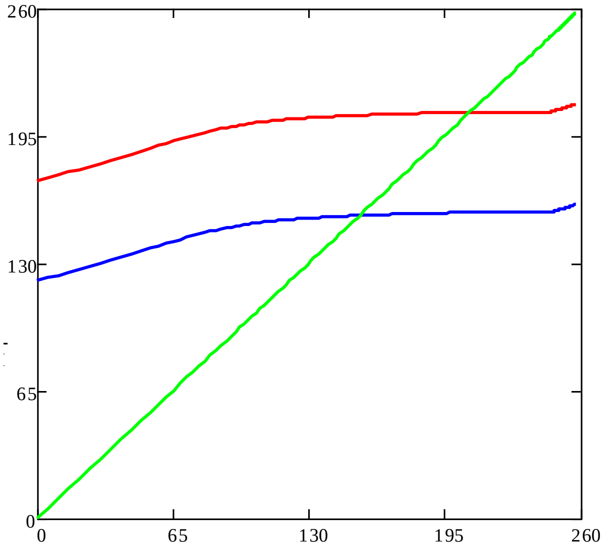

Fig. 5.7. Variation of shear strength with base shear force (green line). Blue line is the masonry shear strength contribution V_m. Red line is the total shear strength V_r. (TRSa masonry with σ_0=0.6 N/mm^2, graph in kN)

When shear failure occurs, model follows the capacity curve until this point. After that it needs to describe post-peak behavior in terms of strength decay and displacements.

As introduced above (paragraph 5.2) force-displacement relation is composed by two branches. The first where strength still constant with displacement increasing and a second branch where a parabolic decay of strength, with displacement increasing, take place until the ultimate displacement fixed at 20% of strength decay respect to maximum shear capacity (see Fig. 5.8).

The displacement of two points where model change between these branches were found with following equations (Eq. 5.21 to Eq. 5.24):

$$\Delta_0^* = \left[\frac{\Delta V_m}{\Delta M_{max}} \cdot \left(\frac{\Delta M_{max} - \Delta M_{ult}}{\Delta M_{ult}}\right)\right] \cdot [\mu_{0a} \cdot \Delta V_m + \mu_{0b} \cdot (\Delta V_r - \Delta V_m)] \qquad \text{(Eq. 5.21)}$$

$$\Delta_0 = \begin{cases} \Delta V_r, & \Delta_0^* \leq \Delta V_r \\ \Delta_0^*, & \Delta_0^* \leq \Delta M_{max} \\ \Delta M_{max}, & \Delta_0^* > \Delta M_{max} \end{cases} \qquad \text{(Eq. 5.22)}$$

Where Δ_0 is the displacement point where constant strength ends when shear failure occurs. It was found limiting Δ_0^* function between two constraint point given by: ΔV_r the displacement where shear failure starts to develop and ΔM_{max} the displacement of maximum flexure capacity.

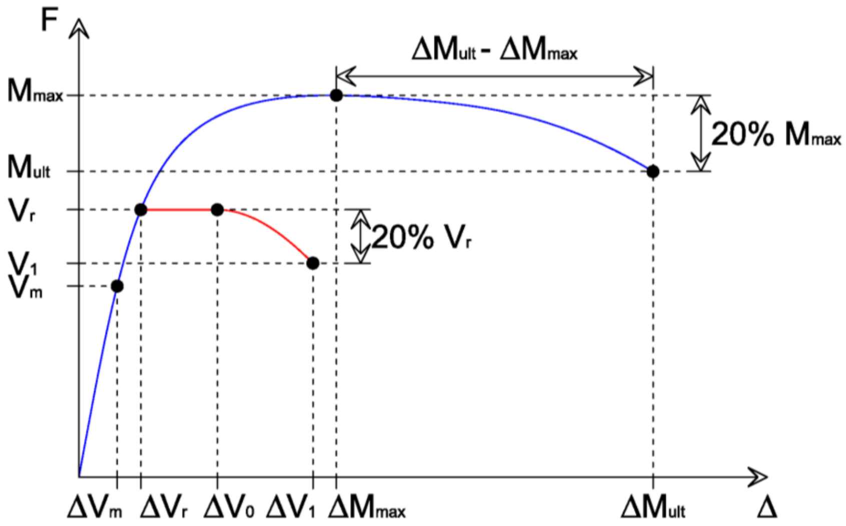

Fig. 5.8. Post peak behavior of model in case of diagonal shear failure.
Blue line: flexure capacity curve. Red line: diagonal shear post-peak curve.

The function Δ_0^* is characterized by two components. The first factor is a ratio controls how much masonry shear capacity is far from flexure capacity (without horizontal reinforcement contribution) and how much “ductile” would be flexure post-peak response if shear failure did not occur. Second factor of Δ_0^* is a sum of displacement due to masonry shear strength and displacement due to horizontal reinforcement contribution (left over to ΔV_r). These two addends are magnified by

μ_{0a} and μ_{0b} resulting from best fitting of experimental results of both reinforced and unreinforced masonry systems under investigation which had a shear failure.

$$\Delta_1^{*}=\left[\frac{\Delta V_m}{\Delta M_{max}}\cdot\left(\frac{\Delta M_{max}-\Delta M_{ult}}{\Delta M_{ult}}\right)\right]\cdot\left[\mu_{1a}\cdot\Delta V_m+\mu_{1b}\cdot(\Delta_0-\Delta V_m)\right] \qquad \text{(Eq. 5.23)}$$

$$\Delta_1=\begin{cases}1.15\cdot\Delta_0, & \Delta_1^{*}\leq 1.15\cdot\Delta_0\\ \Delta_1^{*}, & \Delta_1^{*}\leq 2\cdot\Delta M_{max}\\ 2\cdot\Delta M_{max}, & \Delta_1^{*}>2\cdot\Delta M_{max}\end{cases} \qquad \text{(Eq. 5.24)}$$

Δ_1 is the ultimate displacement when shear failure occurs after the parabolic decay which starts after Δ_0 point. It was found limiting Δ_1^{*} function between two constraint point given by: $(1.15\cdot\Delta_0)$ considered as a minimum multiplier factor of displacement Δ_0 (in according with experimental data) and $(2\cdot\Delta M_{max})$ appear as reasonable limit for shear failure ductility. Again Δ_1^{*} has the same form of Δ_0^{*} but it is fitted with experimental results using different coefficients μ_{1a} and μ_{1b} which magnify respectively ΔV_m and the displacement contribution of stirrups $(\Delta_0-\Delta V_m)$.

The coefficients μ_{0a}, μ_{0b}, μ_{1a} and μ_{1b} were fitted using both reinforced and unreinforced masonry which had shear failure and their values proposed are respectively: $\mu_{0a}=2.8$, $\mu_{0b}=27.5$, $\mu_{1a}=5.6$ and $\mu_{1b}=31$.

5.4. Analyses of Unreinforced Masonry Walls

To validate the analytical model described in previous paragraph (5.3) were done a series of analyses focused to reproduce the experimentally observed data.

Afterwards was carried out a series of parametrical analyses aimed to extend the experimental results and investigate the influence of different parameters on masonry behavior.

5.4.1. Experimental Tests Reproductions

The input required for the model are described in paragraph 5.3.1 and summarized in Table 5.1 there are those used for different unreinforced masonry Po, TG and TM. The calibration process was quite easy because of simplified hypotheses used in the model and consequent limited number of parameters needed.

The model uses, obviously, the same geometrical and boundary conditions of experimental test set-up (namely L, H, t, σ_0). The mechanical parameters are the same resulting from experimental tests for compressive strength (f_m), elastic modulus of masonry (E_m). The only parameter used to calibrate the model is the shear elastic modulus (G). Starting from standard diagonal compression test results G was corrected (lowering about 20%) to catch the initial stiffness of elastic branch of capacity curves. It was found a good agreement with shear modulus extrapolate form shear-compression tests which is quite lower from the former one as observed in (da Porto et al., 2009b; Mosele, 2004).

Wall	f_m	E_m	G	L	H	t	H/L
	N/mm^2	N/mm^2	N/mm^2	mm	mm	mm	-
TM	6.95	4497	700	984	1271	300	1.292
TG	5.67	4983	600	992	1187	300	1.196
Po	5.34	5113	550	993	1184	300	1.192

Table 5.1. Mechanical and geometrical parameters used modeling unreinforced masonry.

Fig. 5.9 Fig. 5.10 and Fig. 5.11 show the comparison between experimental behaviors, represented by the envelope of the hysteresis loops, and modeling results, for the three masonry types (respectively for Po, TG and TM) and for specimens tested under different compressive load. Dashed lines are the experimental positive and negative envelopes, the continuous lines are the modeled capacity curves and dots represent some limit states in the model.

The model was able to well reproduce initial elastic stiffness. Comparison of the various masonry types showed that their behavior was similar. In general model highlight that for all masonry types the sequence of limit states is not constant with different vertical load. When low vertical stress ratio was applied first limit state is horizontal cracking at base, with reduction of cross-section that actually responds to compression. The response still almost linear until second limit state, first non-linearity in masonry (see Fig. 5.1), was achieved for most stressed element in compression. On the contrary for higher vertical stress ratios model come out from masonry stress-strain linear branch before the wall base cross-section show the first horizontal crack.

Therefore in general model underestimates the experimental strengths (except for TM-33% wall but only with 2% of error). The model is in fairly good agreement with experimental results in term of maximum strengths and maximum displacements. In strength the average error is about 7% and maximum error is about 20%, in terms of maximum displacement the average error is about 26% (and 20% if exclude one TM-22%).

With a closer look on Po walls (Fig. 5.9) is possible to observe that model of wall Po-17% (i.e. with $\sigma_0/f_m = 0.17$) had lower ultimate displacement capacity compared with experimental (error about 34%). This fact can be imputed to rocking prevailing behavior which is difficult to catch with the model. Other Po analyses with different vertical axial loads were able to reproduce correctly the flexural behavior. Despite Po-22% analysis show a higher error in term of strength (about 20%) respect other analyses.

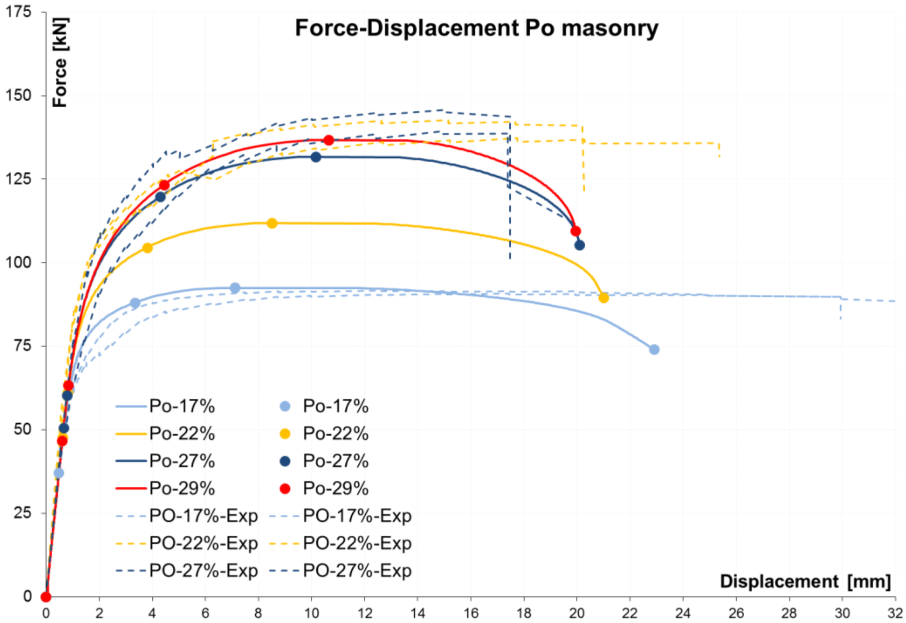

Fig. 5.9. Po masonry. Model versus Experimental load-displacement capacity curves.

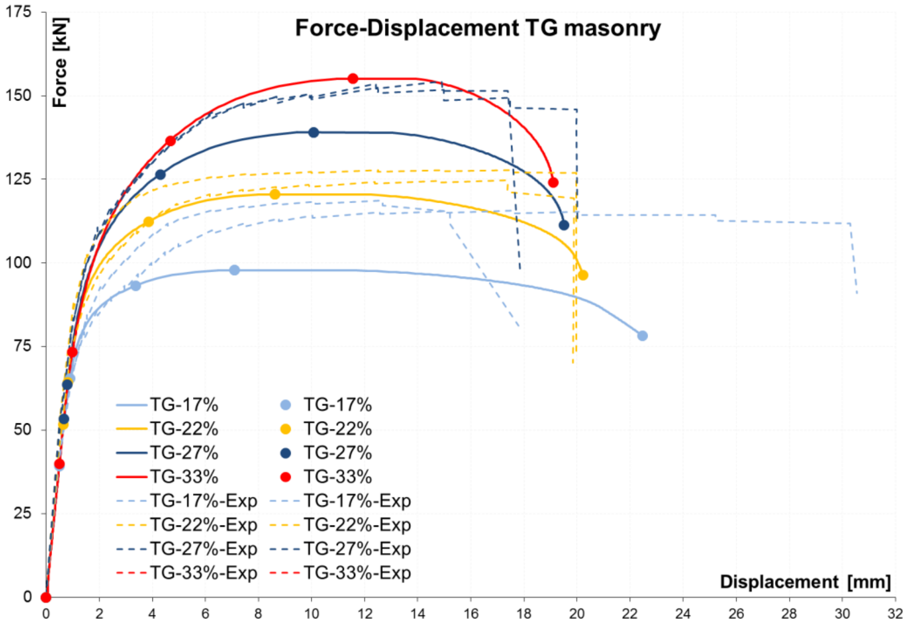

Fig. 5.10. TG masonry. Model versus Experimental load-displacement capacity curves.

Furthermore it can be noted that the choice to put critical limit state when maximum masonry compression stress in the wall (at compressed toe) reaches the masonry compressive strength ($\sigma_{m.max} = f_m$) is supported by a great change in stiffness between before and after this point and also from observation of some discontinuities in experimental capacity curves close to this point.

Even though TG-27% shows an error in term of maximum horizontal force of about 20%, TG wall analyses (Fig. 5.10) confirm flexural-type behavior experimentally observed with good agreement in terms both of maximum displacement (average error 12%) and of horizontal strength (average error about 11%). Still valid the observations pointed out for Po masonry type which had a similar behavior to TG masonry.

Fig. 5.11 shows the TM masonry analyses compared with experimental envelope curves. The curves are in very good agreement until maximum strength both in terms of displacement and force. Anyway it can be noted that analysis of TM-27% wall has a lower maximum strength than TM-33% wall on contrary experimental specimens had for TM-27% a higher maximum horizontal force than TM-33%. Despite this fact model load error is still lower than 7% at maximum strength. Moreover the model is able to catch both flexural-type of failure for TM-17% and TM-22% and shear failure for TM-27% and TM-33% walls.

The simplified approach used to describe shear failure, which is controlled by only one parameter (tensile strength f_{mt}), is able to catch experimental specimens which were subjected to this kind of failure. This is consistent with the idea that shear cracks in masonry are generally related to principal tensile stresses derived by bi-axial stress state. This type of stress state is adequately described by (Turnšek & Čačovič, 1971), which considers not only the tensile strength influence, but also the effect of different axial stresses and is consistent with that obtained (Anderson & Priestley, 1992) by data regression and with the experimental data.

Analyses of TM-27% and TM-22% in particular have a higher displacement capacity compared with the experimental tests related to. Actually this is the major difference showed by the model, but it is worth to point out that those analyses refer to a boundary zone between shear failure and flexural failure and this fact together with experimental variability could be a partial explanation of this difference.

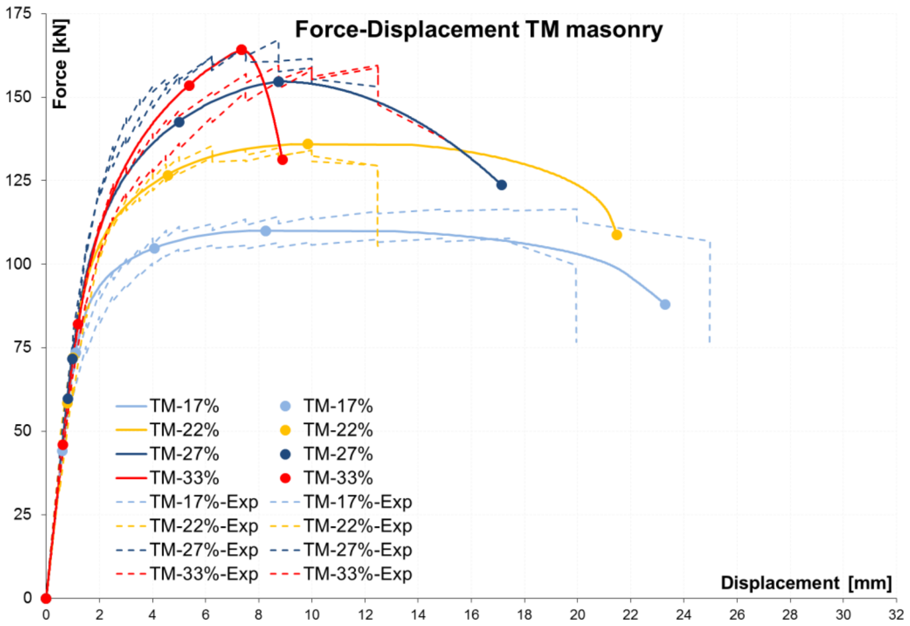

Fig. 5.11. TM masonry. Model versus Experimental load-displacement capacity curves.

Table 3.6 summarizes the experimental limit states. It shows lateral load, displacement and rotation angle (drift) related to first observed flexural cracking, shear cracking, maximum resistance and displacement of last stable cycle. These are obtained averaging values at positive and negative displacement amplitudes.

Table 5.2 summarizes the modeling analysis limit states showing same parameters but it can be noted that the choice of limit state was slightly different for first two limit states. In facts, model can highlight earlier the first non-linearity than experimental tests and data observation, because it can highlight the reaching of a selected limit state for a single cross-section. On contrary during tests, and from data obtained, is possible to notice when mechanism changes wall behavior involving at least a part of wall and not only one section. This explains why experimental limit state named flexural cracking was always after both first non-linearity of masonry in compression and the first horizontal crack due to reduction of compressed zone.

Since model is able to find the exit from masonry linear elastic behavior this is considered more significant limit state than the appearance of first horizontal crack.

The second, and fundamental, limit state refers to the attainment of masonry compressive strength and start of yielding branch (see Fig. 5.1) at maximum compressed zone, i.e. at toe of wall. Here masonry stress-strain curve enters in a plastic phase and wall leaves completely the linear behavior. For this reason this limit state was chosen as critical limit state which ductility parameter (μ) refers to (see from Fig. 5.15 to Fig. 5.17).

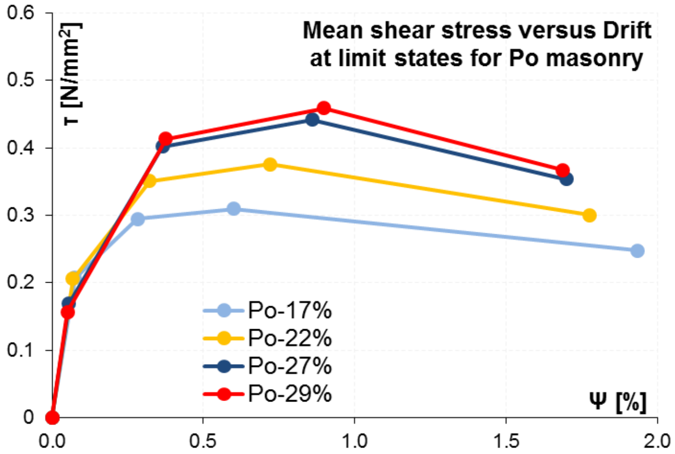

Fig. 5.12. Po masonry. Mean shear stress versus drift at different limit states of Model.

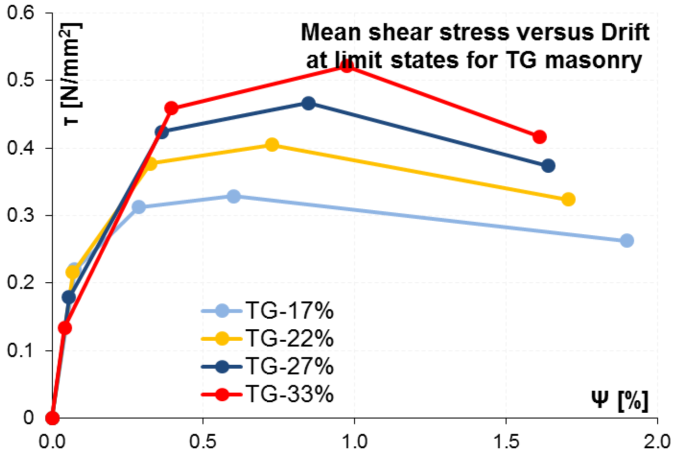

Fig. 5.13. TG masonry. Mean shear stress versus drift at different limit states of Model.

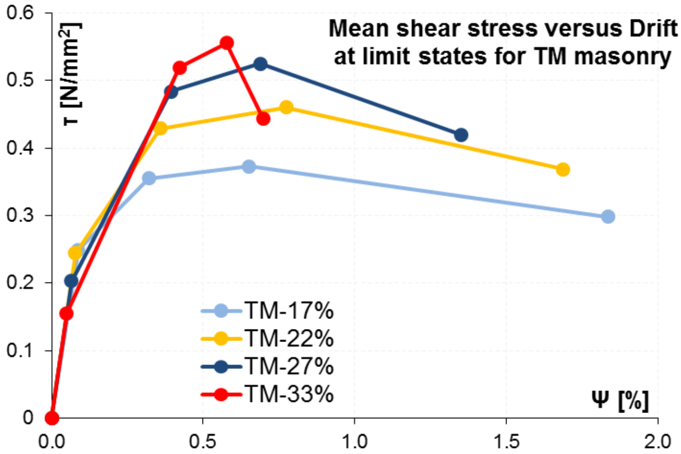

Fig. 5.14. TM masonry. Mean shear stress versus drift at different limit states of Model.

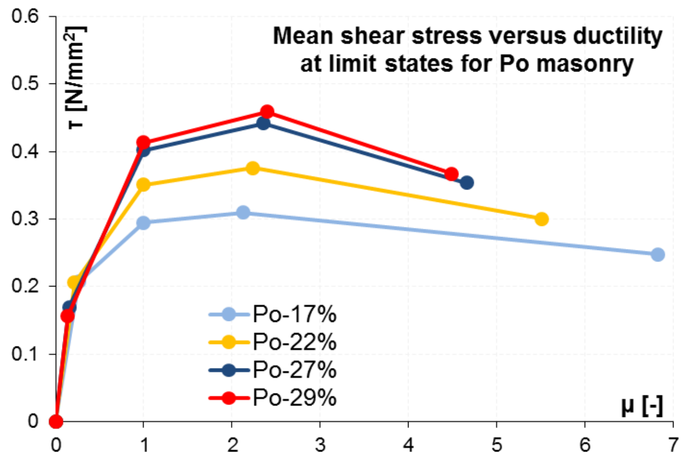

Fig. 5.15. Po masonry. Mean shear stress versus ductility at different limit states of Model.

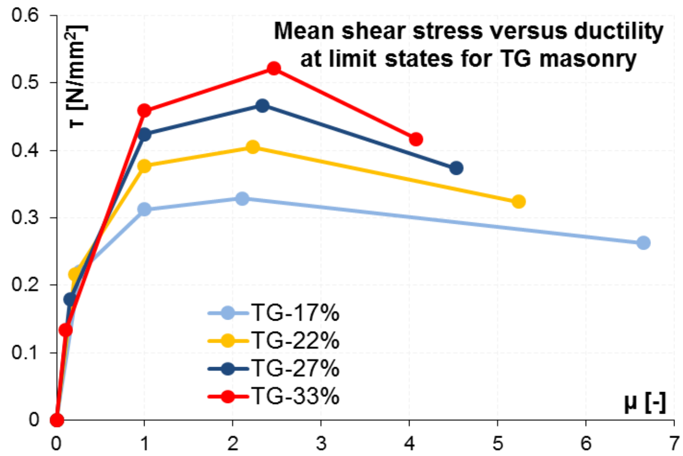

Fig. 5.16. TG masonry. Mean shear stress versus ductility at different limit states of Model.

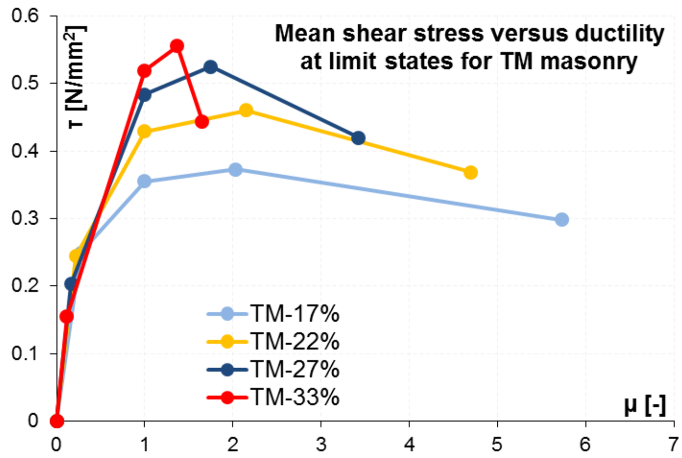

Fig. 5.17. TM masonry. Mean shear stress versus ductility at different limit states of Model.

Wall	1^{st} non-linearity			Masonry Yielding			Maximum Strength			Max displacement		
	H_e	δ_e	Ψ_e	H_{cr}	δ_{cr}	Ψ_{cr}	H_{max}	δ_{Hmax}	Ψ_{Hmax}	$H_{\delta max}$	δ_{max}	$\Psi_{\delta max}$
	kN	mm	%	kN	mm	%	kN	mm	%	kN	mm	%
σ_0/f_m = 0.33												
TM-33%	46.0	0.63	0.05	153.4	5.38	0.42	164.2	7.35	0.58	131.3	8.88	0.70
TG-33%	40.0	0.50	0.04	136.6	4.69	0.39	155.1	11.55	0.97	124.1	19.11	1.61
Po-33%	46.7	0.61	0.05	123.2	4.45	0.38	136.7	10.64	0.90	109.4	19.96	1.69
σ_0/f_m = 0.27												
TM-27%	59.8	0.82	0.06	142.5	5.00	0.39	154.7	8.74	0.69	123.7	17.14	1.35
TG-27%	53.3	0.67	0.06	126.4	4.31	0.36	139.0	10.08	0.85	111.2	19.52	1.64
Po-27%	50.4	0.66	0.06	119.7	4.31	0.36	131.6	10.17	0.86	105.3	20.10	1.70
σ_0/f_m = 0.22												
TM-22%	72.0	1.00	0.08	126.6	4.57	0.36	135.9	9.85	0.77	108.8	21.48	1.69
TG-22%	64.2	0.82	0.07	112.3	3.87	0.33	120.5	8.61	0.73	96.4	20.23	1.70
Po-22%	61.1	0.81	0.07	104.4	3.81	0.32	111.8	8.52	0.72	89.5	21.00	1.78
σ_0/f_m = 0.17												
TM-17%	73.5	1.11	0.09	104.7	4.07	0.32	110.0	8.26	0.65	88.0	23.29	1.83
TG-17%	65.4	0.90	0.08	93.1	3.37	0.28	97.8	7.10	0.60	78.3	22.46	1.90
Po-17%	61.9	0.89	0.07	88.0	3.36	0.28	92.5	7.13	0.60	74.0	22.91	1.93

Table 5.2. Model. Lateral load, displacement and rotation angle at first masonry non-linearity, masonry compression yielding, maximum strength and maximum displacement limit states.

5.4.2. Parametrical Extension of Experimental Tests

The analyses done with the numerical model approach reported in paragraph 4.2.3 were repeated and extended using the analytical model proposed in this chapter, besides other parametrical analyses were done aimed to investigate the influence of slenderness on global shear behavior of the three masonry types TM, TG and Po. Furthermore a series of analyses with the purpose to find a better definition of displacement in case of flexural failure needed in the section 7.1 will presented.

In the first series of analyses was changed, as in paragraph 4.2.3, the unit compressive strength (f_{cu}) between 5 and 20 N/mm^2.

In the micro modeling FEM strategies adopted, the model inputs required were compressive strength, elastic modulus (E_u) and tensile strength (f_{tu}) of blocks. In order to calibrate unit elastic modulus and tensile strength a formulation relating them to the unit compressive strength was adopted. The analytical model proposed in this chapter is a homogenized macro model then needs to relate compressive strength of unit to compressive strength, elastic modulus, shear modulus and tensile strength of masonry wall (f_m).

This issue was overcome using a formulation first proposed from (Guidi, 1954) and recently calibrated on basis of wide database (da Porto, 2005; DISWall, 2008) using the equation following (Eq. 5.25) where f_{cm} is the compressive strength of mortar:

$$f_m = \frac{f_{cu}}{4.52} \cdot \log_{10}(f_{cm} + 2.75) \qquad \text{(Eq. 5.25)}$$

The elastic modulus was calibrated starting from calculated f_m using (Eq. 5.26) which was fitted with experimental data. The shear modulus G was supposed proportional to E_m and linearly varied with. Finally evaluation of tensile strength of masonry (f_{mt}) uses the (Eq. 5.19) previously described.

$$E_m = 2692 \cdot \sqrt[3]{f_m} \qquad \text{(Eq. 5.26)}$$

Table 5.3 lists the mechanical parameters used during compressive strength parametrical analyses.

For each masonry type and each value of unit compressive strength, analyses were repeated by applying the same vertical load used in the experimental tests, or a vertical load corresponding to the same ratio between applied load and compressive strength of masonry. In the latter case, it was possible to compare the behavior of each masonry type, varying the unit compressive strength, when stresses inside the walls had comparable intensity. Hence, three types of masonry, two levels of vertical compression stress and four unit compressive strength repeated in two combinations (with same ratio and same magnitude used in experimental tests) yield a total analyses number of 48.

[N/mm^2]	f_{cu}	f_m	E_m	G
Po	20	5.49	4748	511
	15	4.12	4314	464
	10	2.74	3769	405
	5	1.37	2991	322
TG	20	5.49	4748	572
	15	4.12	4314	519
	10	2.74	3769	454
	5	1.37	2991	360
TM	20	5.99	4888	761
	15	4.49	4441	691
	10	2.99	3880	604
	5	1.50	3079	479

Table 5.3. Parameters used in compressive strength parametrical analyses of unreinforced masonry.

For these analyses vertical compression ratios corresponding to 17% and 22% of masonry compressive strength were used. This choice was slightly different from corresponding FEM parametrical analysis, because this analytical model is oriented to find masonry behavior close to cases which are more often present in practical design of unreinforced masonry buildings (low-rise building bears to a quite low vertical load), more than inspect masonry capabilities in term of stress and strain inside the wall. In the next will be indicate a wall with label composed by three parts: first indicate the type of masonry, second the vertical stress applied (in percentage or indicating e.g. σ_0 = 0.89 N/mm^2 as “089”) and third number the compressive strength of unit considered (indicating e.g. f_{cu} = 5 N/mm^2 as “05”, f_{cu} = 10 N/mm^2 as “10”, …)

Fig. 5.18 shows the analyses for Po masonry with reference to vertical stress ratio of 17% of compressive strength of this masonry (in yellow and red), approximates with (Eq. 5.25) and also the analyses done with vertical load applied in experimental tests which was 0.89 N/mm^2 (in green and blue). Obviously the horizontal forces and maximum displacements tend to increase with masonry compressive strength in both vertical load combinations.

It can be noted that walls with constant ratio between vertical load and compressive strength (in yellow and red), tend to have the same behavior with the same sequence of limit states (showed with markers) despite capacity of masonry increase significantly with masonry compressive strength increments. Furthermore these increments are almost linear both in terms of force and displacement capacity.

The limit state sequence showed in these analyses was:

1. horizontal cracking of wall at base section (F_{hc});
2. masonry leaves its elastic part of stress-strain curve at base section (F_e);
3. masonry yields in compression at toe of wall (F_{cr});
4. wall reaches maximum horizontal shear strength (F_{max});
5. maximum displacement capacity (δ_{max}).

If vertical load was kept constant (in green and blue), the masonry behavior changes with compressive strength of masonry: from ductile flexure, when high unit strength was used, to brittle flexure when low unit strength was used. When compressive strength was between 10 and 20 N/mm^2 maximum shear resistance of walls was changed about 20% between walls with f_{cu} = 20 and 10 N/mm^2 and a great decrease was found when f_{cu} = 5 N/mm^2.

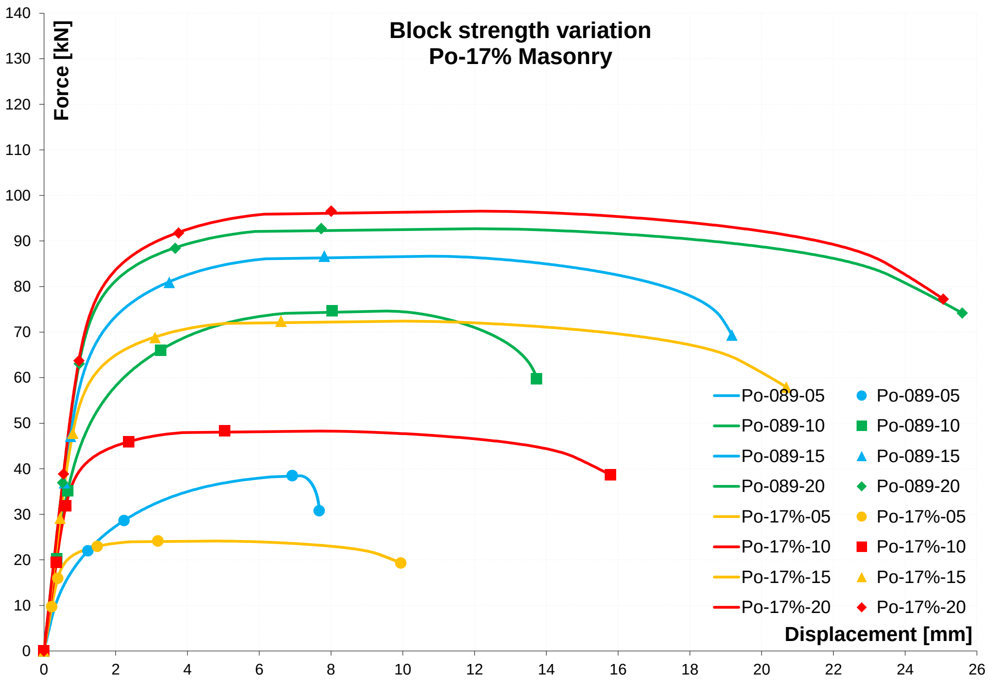

Fig. 5.18. Po-17% masonry. Parametrical analyses with block strength variation. Horizontal force versus displacement. Red/yellow constant ratio, green/blue constant load combinations.

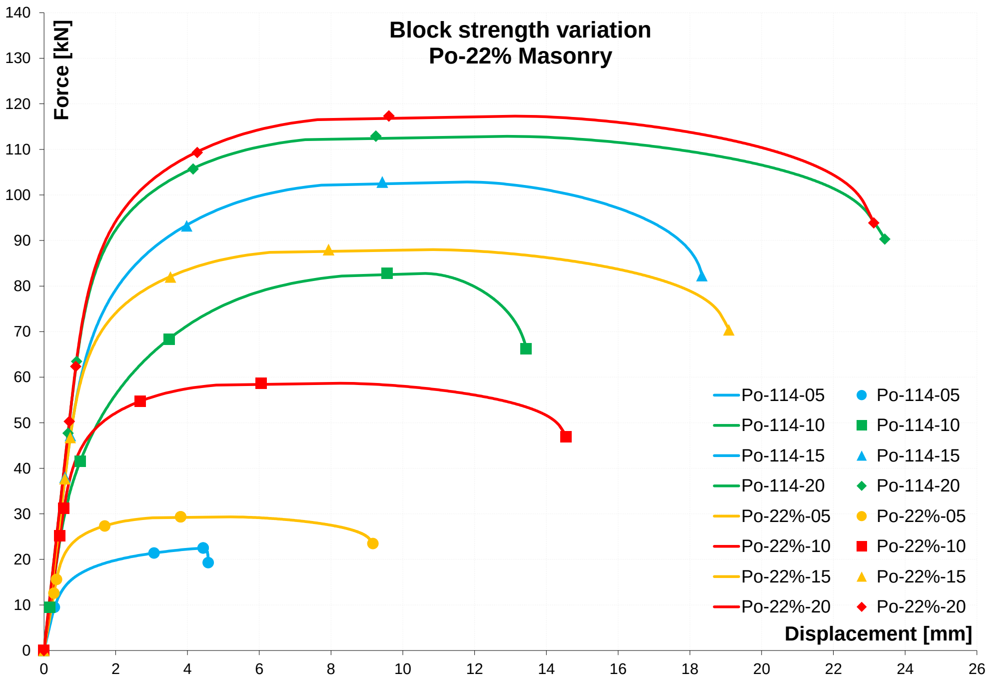

Fig. 5.19. Po-22% masonry. Parametrical analyses with block strength variation. Horizontal force versus displacement. Red/yellow constant ratio, green/blue constant load combinations.

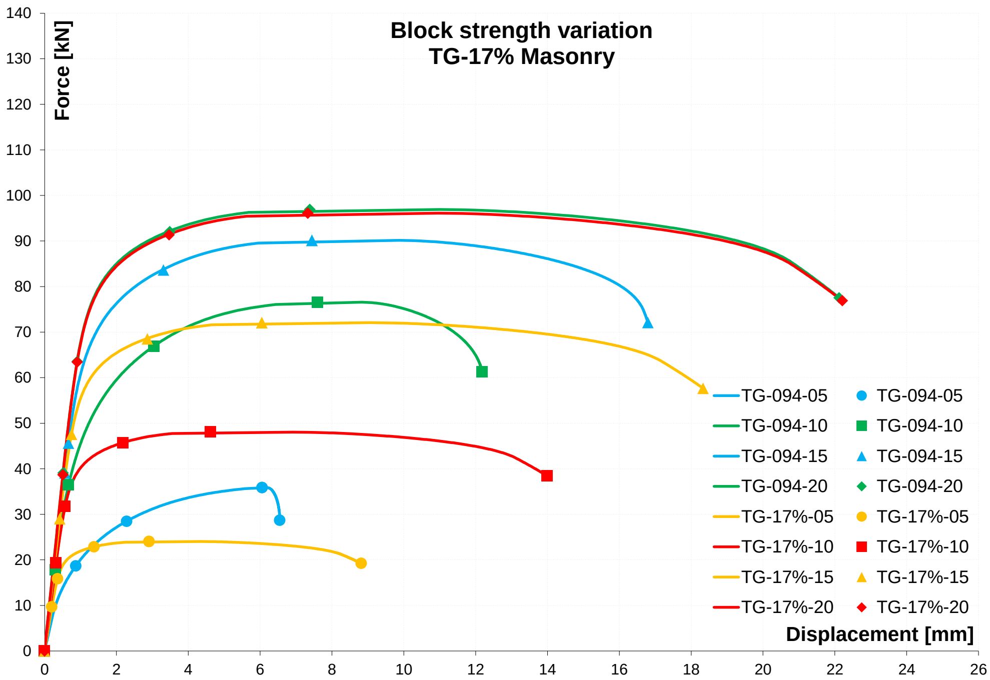

Fig. 5.20. TG-17% masonry. Parametrical analyses with block strength variation. Horizontal force versus displacement. Red/yellow constant ratio, green/blue constant load combinations.

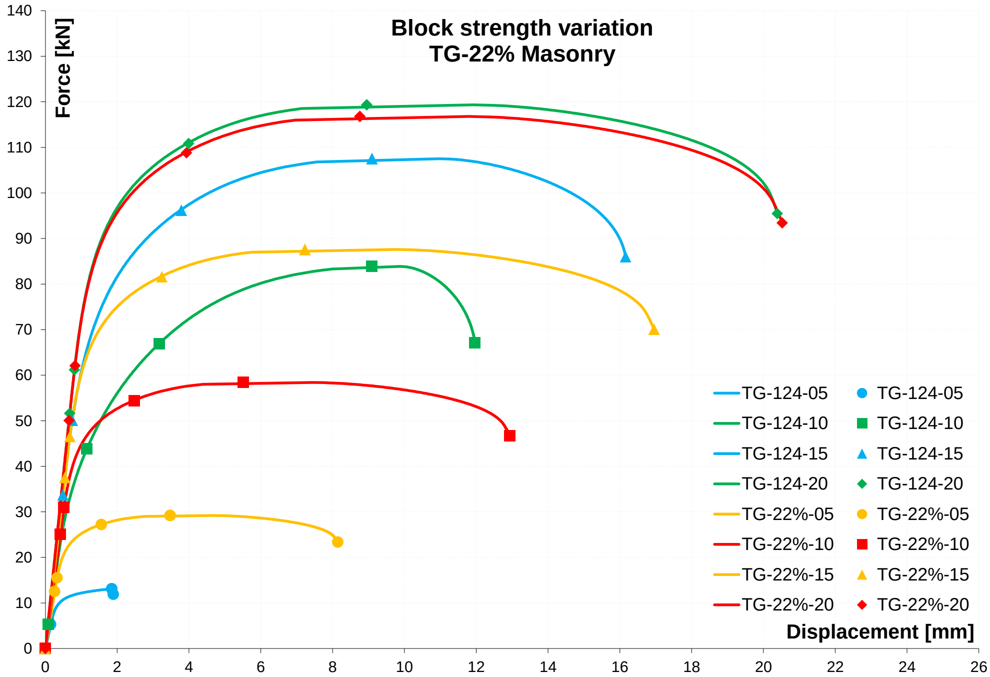

Fig. 5.21. TG-22% masonry. Parametrical analyses with block strength variation. Horizontal force versus displacement. Red/yellow constant ratio, green/blue constant load combinations.

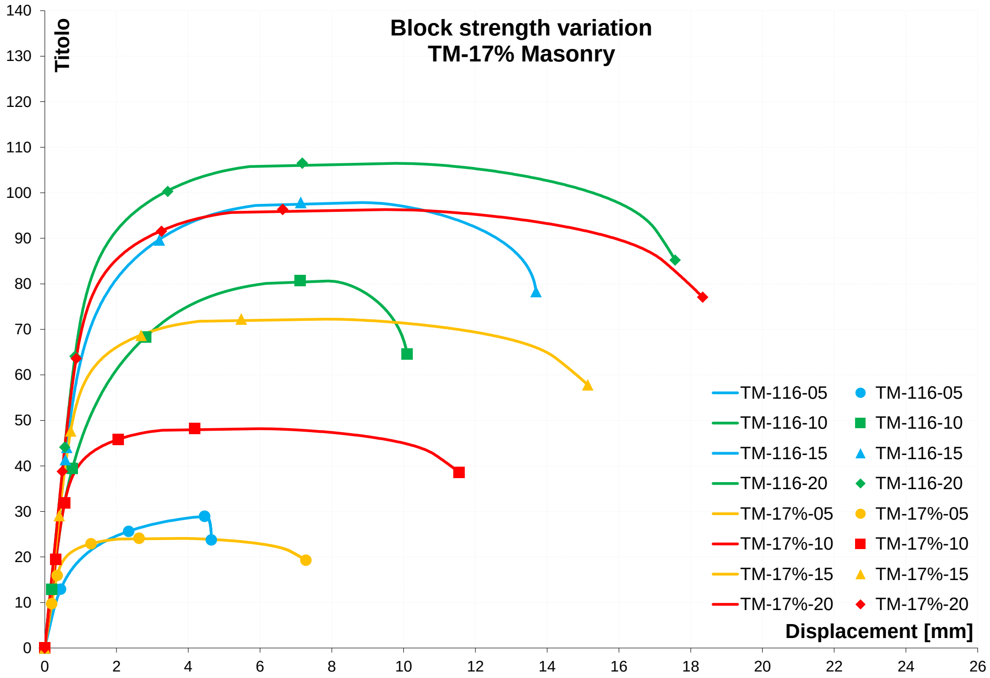

Fig. 5.22. TM-17% masonry. Parametrical analyses with block strength variation. Horizontal force versus displacement. Red/yellow constant ratio, green/blue constant load combinations.

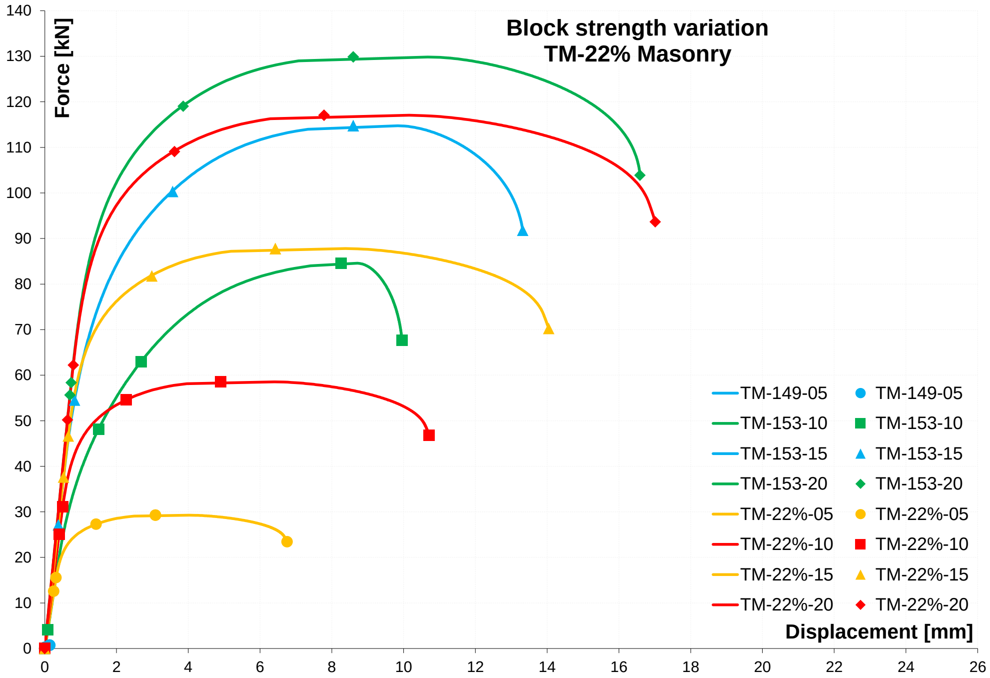

Fig. 5.23. TM-22% masonry. Parametrical analyses with block strength variation. Horizontal

force versus displacement. Red/yellow constant ratio, green/blue constant load combinations.

In this vertical load combination the sequence of limit states previously described is not always valid. F_{hc} and F_e were achieved in different order, as with the same vertical load F_e tends to be reached earlier if compressive strength decreases. When lowest unit compressive strength was used, wall started to displaces when it was already in nonlinear phase of masonry stress-strain relationship and this fact causes a low initial stiffness.

Fig. 5.19 shows Po masonry analyses carried out with vertical loads of 22% of vertical compressive strength and with constant vertical load of 1.14 N/mm^2. Observations done for Fig. 5.18 are still valid also in this case and it is worth to point out that strong loss of masonry capacity, both in term of strength and displacement, shown when constant load was applied and unit compressive strength was 5 N/mm^2, became more important with this higher vertical load.

	f_{cu} N/mm^2	F_{max} kN	F_{max}/ F_{max20} %	F_{max} kN	F_{max}/ F_{max20} %
Po		σ_0 = 0.89 N/mm^2		σ_0 = 1.14 N/mm^2	
	20	92.7	100	112.9	100
	15	86.7	93	102.8	91
	10	74.6	80	82.8	73
	5	38.5	41	22.5	20
TG		σ_0 = 0.94 N/mm^2		σ_0 = 1.24 N/mm^2	
	20	96.9	100	119.3	100
	15	90.1	93	107.5	90
	10	76.6	79	83.9	70
	5	35.9	37	13.1	11
TM		σ_0 = 1.16 N/mm^2		σ_0 = 1.53 N/mm^2	
	20	106.5	100	129.9	100
	15	97.9	92	114.8	88
	10	80.6	76	84.6	65
	5	28.9	27	0.7*	0.5*

Table 5.4. Summary of maximum horizontal strength in case of constant load applied.

Analyses done for TG masonry are showed in Fig. 5.20 and Fig. 5.21 respectively with ratios of 17% and 22% of masonry compressive strength and with constant loads of 0.94 N/mm^2 and 1.24 N/mm^2. Besides, Fig. 5.22 and Fig. 5.23 show parametric analyses of TM masonry. When constant loads were used, compression stress was respectively 1.16 N/mm^2 and 1.53 N/mm^2. Also for TM masonry previous remarks are still valid but it can be noted as σ_0 = 1.53 N/mm^2 is higher than masonry compressive strength for f_{cu} = 5 N/mm^2 so an analysis with σ_0 = 1.49 N/mm^2 was performed. Results (marked with *) are reported in Table 5.4 with a summary of maximum horizontal strength in case of constant load applied.

The second series of parametrical analyses, as outlined before, concerns variation of wall slenderness, namely the wall length (L). It was changed from experimental length adding or removing a unit. Hence from four unit as in the original walls, to 3 unit, named slender walls (suffix SL), and 5 unit, named squat walls (suffix SQ).

Combination for this kind of parametric analysis includes three masonry types, four ratios of vertical load and three wall slenderness's for a total number of 36 analyses. Table 5.5 summarizes the different wall lengths used in these analyses and indicates corresponding slenderness ratio (H/L).

Wall	suffix	L mm	H mm	H/L -
TM	SL	738	1271	1.722
		984		1.292
	SQ	1230		1.033
TG	SL	744	1187	1.595
		992		1.196
	SQ	1240		0.957
Po	SL	745	1184	1.589
		993		1.192
	SQ	1241		0.954

Table 5.5. Parameters used in slenderness parametrical analyses of unreinforced masonry.

From Fig. 5.24 to Fig. 5.26 the results of slenderness parametrical analyses are presented in terms of force-displacement curves with markers used to indicate principal limit states. With black and grey lines was show slender walls (SL), with green and blue the squat walls (SQ) and in red and yellow experimental analyses reproductions.

In general, all three masonry types with slender walls exhibited a flexure failure. Furthermore, in general when slenderness ratio decreases masonry wall capacity to sustain lateral load tends to increase together with displacement capacity until shear failure takes place.

Excluding Po-17%-SQ and TG-17%-SQ other squat walls exhibited a shear failure. Moreover Po-22%-SQ, TG-22%-SQ and TM-17%-SQ had a shear failure which demonstrated a certain amount of ductility reserve. Actually in these analyses maximum shear strength was reached after critical limit state (fixed when masonry yields in compression at wall base), that ensures that flexural damage develops before shear failure takes place. On the contrary, other squat walls showed a very sudden shear failure before masonry reached maximum compressive strength in any cross section along the wall. Also at maximum displacement these walls denoted a poor ductility with a strong drop of strength immediately after the shear failure.

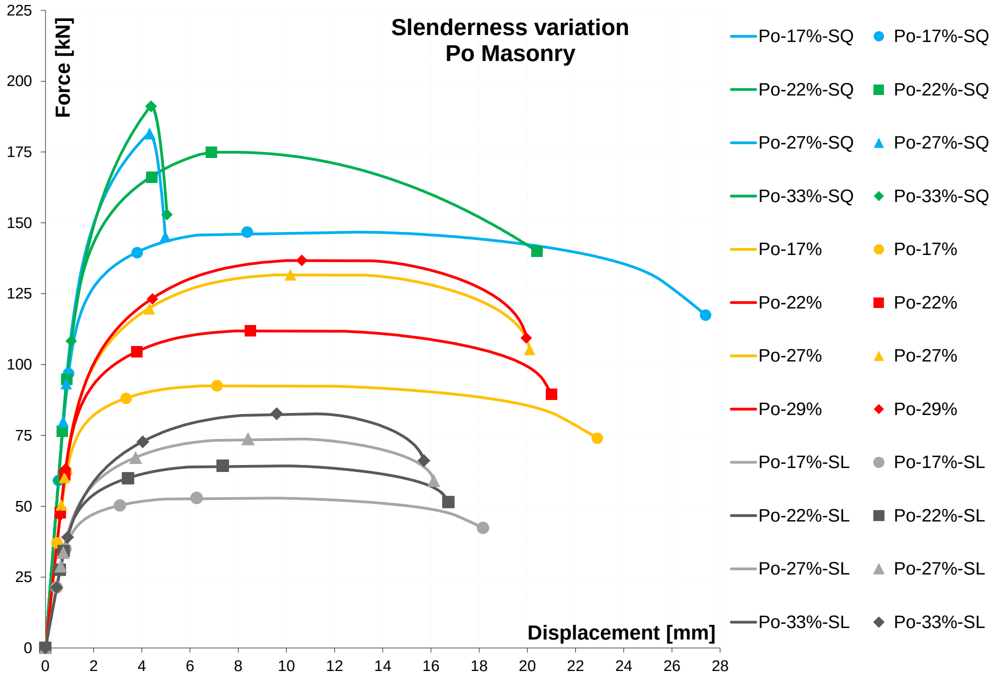

Fig. 5.24. Po masonry. Parametrical analyses with slenderness variation. Horizontal force versus displacement. Red/yellow experimental, green/blue squat, black/grey slender walls.

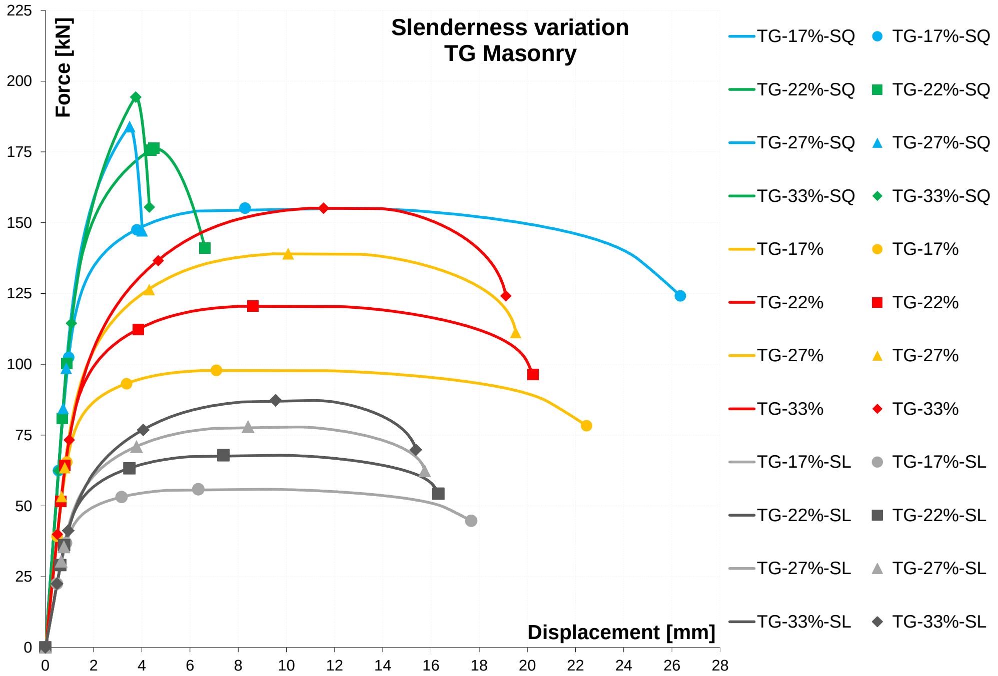

Fig. 5.25. TG masonry. Parametrical analyses with slenderness variation. Horizontal force versus displacement. Red/yellow experimental, green/blue squat, black/grey slender walls.

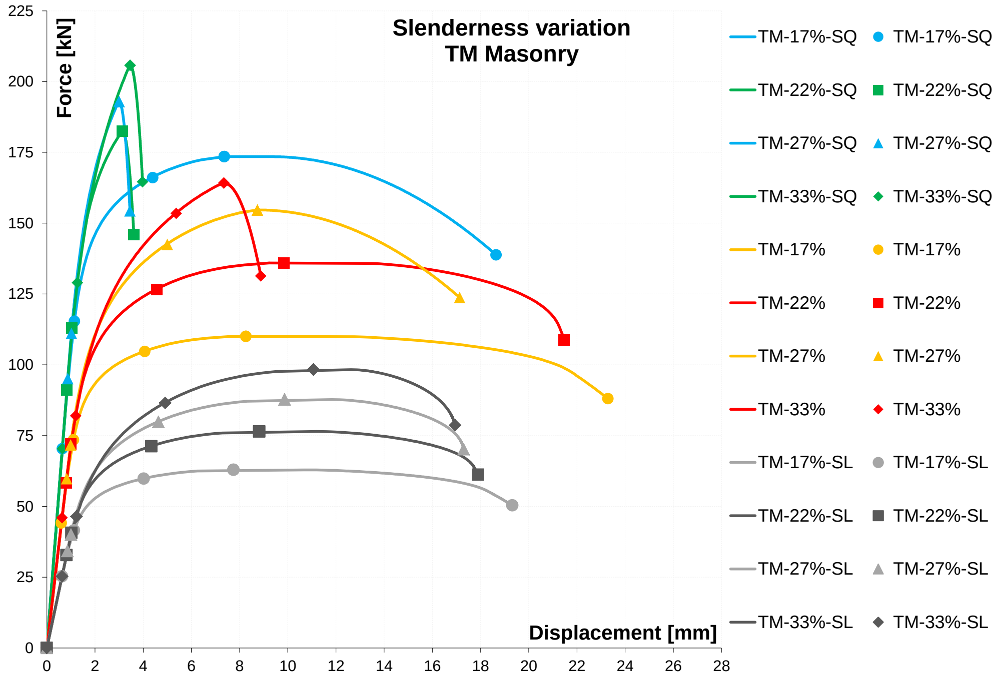

Fig. 5.26. TM masonry. Parametrical analyses with slenderness variation. Horizontal force versus displacement. Red/yellow experimental, green/blue squat, black/grey slender walls.

5.5. Analyses of Reinforced Masonry Walls

To validate the analytical model described in previous paragraph (5.3) for RM walls a series of analyses focused to reproduce the experimentally observed data were done.

Afterwards, a series of parametrical analyses aimed to extend the experimental results and investigate the influence of different parameters on reinforced masonry behavior was carried out.

5.5.1. Experimental Tests Reproductions

The input required for the model are described in paragraph 5.3.1 and summarized in Table 5.6 there are those used for reinforced masonry. The calibration process was quite easy because of simplified hypotheses used in the model and consequent limited number of parameters needed.

The model uses, obviously, the same geometrical and boundary conditions of experimental test set-up (namely L, H, t, σ_0). The mechanical parameters result from experimental tests done, as elastic modulus (E_m) and compressive strength (f_m) of masonry, or vertical and horizontal reinforcements yield stress (f_{ysv} and f_{ysh} respectively) and elastic moduli (E_{sv} and E_{sh} respectively).

It can be noted that f_m was chosen slightly higher (2%) than average compressive strength resulting from experimental uniaxial compression tests. This was due to observation that wall specimen which showed an earlier failure that affected the mean value, also showed a better crack pattern and moreover only two uniaxial experimental tests were done. Hence f_m value was rounded to 4 N/mm^2.

From test results G was calibrated in order to catch the initial stiffness of capacity curves.

Masonry and reinforcement details are summarized in Table 5.6 and Table 5.7 respectively. It is worth to remember that model cannot reproduce the complex 3D interaction developed in masonry joints when truss horizontal reinforcement was used and hence model cannot catch differences between single bar and truss behavior except for the effects of their different cross-section reinforcement area (or percentage over wall area).

f_m	E_m	G	Wall	L	H	t	H/L	σ_0
N/mm^2	N/mm^2	N/mm^2		mm	mm	mm	-	N/mm^2
4.00	5835	650	SRSa04	1530	1657	290	1.083	0.4
			TRSa04	1530	1675	293	1.095	0.4
			SRSa06	1530	1680	295	1.098	0.6
			TRSa06	1525	1666	298	1.092	0.6
			SRSb04	1015	1660	295	1.635	0.4
			TRSb04	1017	1660	291	1.632	0.4
			SRSb06	1020	1660	295	1.627	0.6
			TRSb06	1015	1660	295	1.635	0.6

Table 5.6. Masonry mechanical and geometrical parameters in reinforced masonry system.

E_{sv}	f_{ysv}	d'	Wall	Vertical Reinf.		Horizontal Reinf.		E_{sh}	f_{ysh}
N/mm^2	N/mm^2	mm		Reinf.	%	Reinf.	%	N/mm^2	N/mm^2
188760	501	125	SRSa04	4Φ16	0.181	2Φ6/40cm	0.047	204400	500
			TRSa04	4Φ16	0.179	1 truss/40cm	0.041	203700	486
			SRSa06	4Φ16	0.178	2Φ6/40cm	0.046	204400	500
			TRSa06	4Φ16	0.177	1 truss/40cm	0.040	203700	486
			SRSb04	2Φ16	0.134	2Φ6/40cm	0.046	204400	500
			TRSb04	2Φ16	0.136	1 truss/40cm	0.041	203700	486
			SRSb06	2Φ16	0.134	2Φ6/40cm	0.046	204400	500
			TRSb06	2Φ16	0.134	1 truss/40cm	0.041	203700	486

Table 5.7. Reinforcement mechanical and geometrical parameters for reinforced masonry.

Fig. 5.27 shows the comparison between experimental behaviors, represented by the envelope of the hysteresis loops, and modeling results, for the slenderness ratio

H/L=1.09 and under vertical compression load σ_0=0.4N/mm^2. Dashed lines represent the experimental positive and negative envelopes, continuous lines show the modeled capacity curves and dots represent some limit states in the model.

The model was able to well reproduce initial elastic stiffness. Model had same sequence of limit states both for truss and single bar horizontal reinforcements. They are in sequence: horizontal crack at base cross-section, first non-linearity in masonry (see Fig. 5.1 and named F_e), achievement of shear masonry strength (V_m), maximum horizontal wall strength (F_{max}) and maximum displacement (d_{max} fixed in model when horizontal force decay to 80% of F_{max}). See Table 5.8 for details on main limit states. It has to be noted that critical limit state was set equal to V_m contrary to unreinforced masonry (URM) systems described in previous paragraph. This was due to the fact that these walls reach V_m before masonry yielding in compression and obviously because for URM V_m correspond to F_{max}.

The response was still almost linear until second limit state was achieved and failure occurred because walls reached their shear limit (V_r).

Therefore model underestimates the experimental strengths with error of 6.7% for truss horizontal reinforcement and of 3.4% for single re-bar. The model is in fairly good agreement with experimental results also in term of maximum displacements, corresponding global trend of post peak capacity curve (average error 14.5%).

Other main limit states are summarized in Table 5.8. Altought these are in good agreement with experimental ones, some differences are to be considered as normal because model limit states refer to cross-section achievement (at wall base) of fixed condition, conversely experimental limit states was fixed after that at least a part of wall was involved.

Fig. 5.28 shows experimental versus model comparison for analyses where the slenderness ratio H/L=1.09 and under vertical compression load σ_0=0.6N/mm^2. As before, model was able to well reproduce initial elastic stiffness.

Model had same sequence of limit states both for truss and single bar horizontal reinforcements. They are in sequence: horizontal crack at base cross-section, first non-linearity in masonry (F_e), achievement of shear masonry strength (V_m), masonry yielding in compression (F_{ym}), maximum horizontal wall strength (F_{max}) and maximum displacement (d_{max}). See Table 5.9 for details on main limit states. Also here the response still almost linear until second limit state was achieved.

Therefore model underestimates the experimental strengths but with negligible maximum error of 1.1%. These modeled walls are in fairly good agreement with experimental results also in terms of maximum displacements seeing global trend of post peak capacity curve (average error 15.5%).

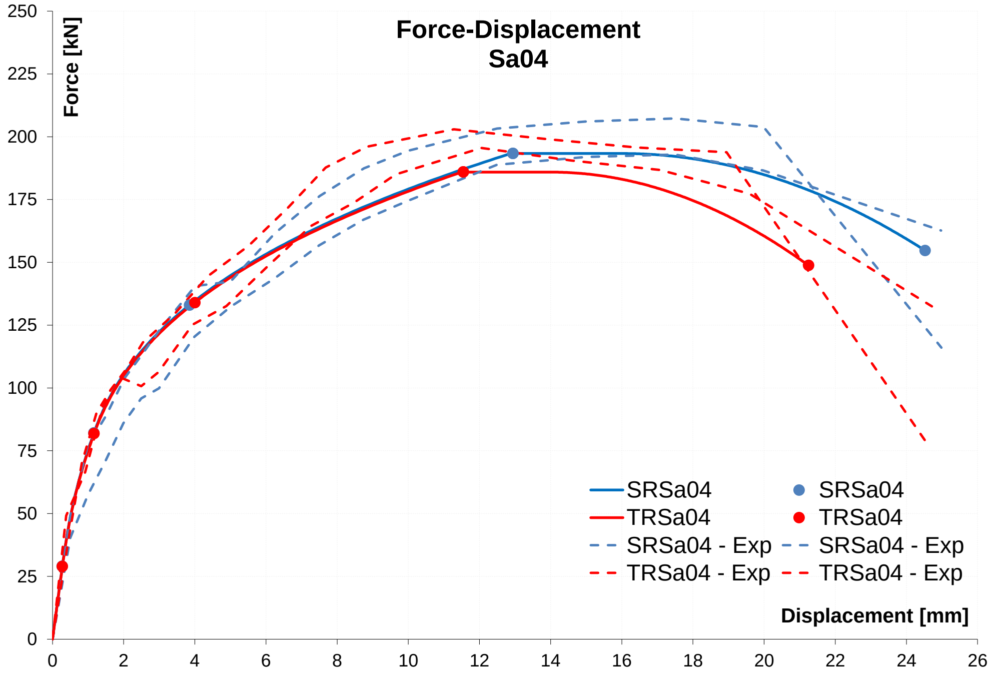

Fig. 5.27. Reinforced masonry H/L=1.09 σ_0*=0.4 N/mm*^{2}*.*
Model versus Experimental load-displacement capacity curves.

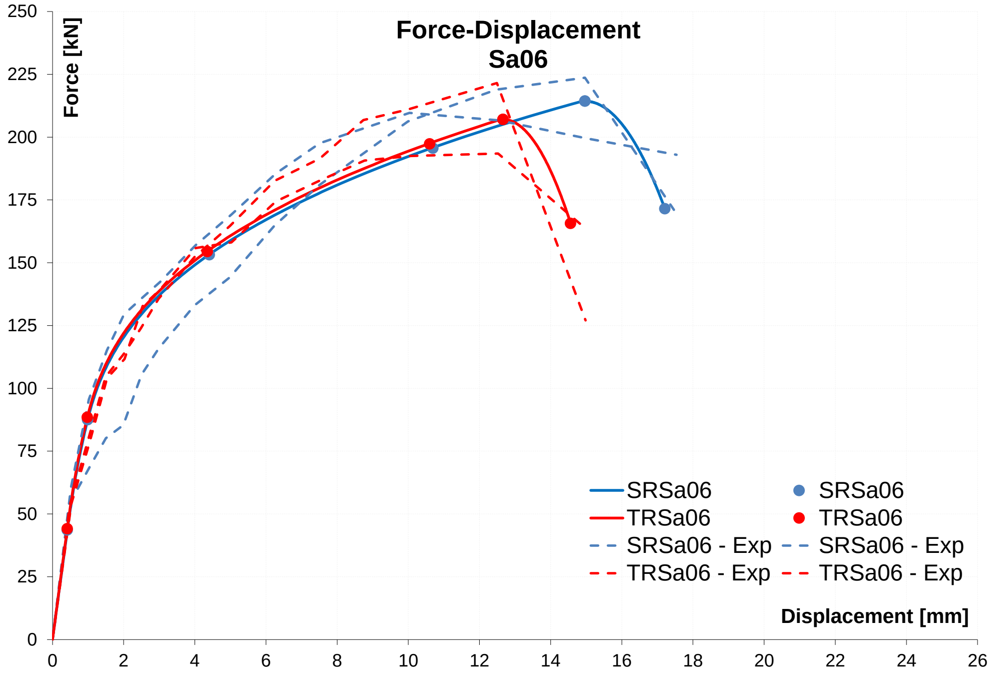

Fig. 5.28. Reinforced masonry H/L=1.09 σ_0*=0.6 N/mm*^{2}*.*
Model versus Experimental load-displacement capacity curves.

All wall analyzed with slenderness ratio of 1.09 had a shear failure and it is worth to point out that for both vertical compression stress adopted the vertical reinforcements in tension did not reach their yielding stress (f_{ysv}). This fact confirms experimental evidences and walls cannot completely profit of presence of vertical reinforcement due to shear strength limitations.

vertical compression 0.4 *N/mm*^{2}		F_e	D_e	F_{cr}	d_{cr}	F_{max}	d_{Fmax}	F_{dmax}	d_{max}
		kN	*mm*	*kN*	*mm*	*kN*	*mm*	*kN*	*mm*
TRSa	Experim.	82	1.12	144	5.08	199	11.67	166	19.99
	Model	82	1.17	134	4.01	186	11.55	149	21.25
SRSa	Experim.	81	1.49	137	5.00	200	17.23	172	19.99
	Model	82	1.17	133	3.86	186	12.94	155	24.53
TRSb	Experim.	32	1.66	74	12.04	79	19.55	68	54.65
	Model	33	0.99	68	7.98	79	14.77	75	40.98
SRSb	Experim.	30	1.31	67	8.82	78	24.24	70	44.75
	Model	33	0.99	69	8.11	79	14.61	75	40.73

Table 5.8. Comparison between experimental and analytical model of principal limit states at vertical compression stress of 0.4 N/mm^2.

vertical compression 0.6 *N/mm*^{2}		H_f	d_{Hf}	H_{cr}	d_{cr}	H_{max}	d_{Hmax}	H_{dmax}	d_{max}
		kN	*mm*	*kN*	*mm*	*kN*	*mm*	*kN*	*mm*
TRSa	Experim.	104	1.51	169	5.13	207	12.19	166	14.25
	Model	88	0.98	154	4.36	207	12.66	166	14.56
SRSa	Experim.	88	1.26	159	5.13	217	12.50	182	17.50
	Model	87	0.99	153	4.41	214	14.97	171	17.21
TRSb	Experim.	40	1.51	86	11.25	93	21.25	81	45.00
	Model	37	0.85	80	9.38	92	19.20	89	32.06
SRSb	Experim.	41	1.26	80	8.76	89	19.99	70	30.00
	Model	37	0.85	74	6.91	93	19.22	90	31.99

Table 5.9. Comparison between experimental and analytical model of principal limit states at vertical compression stress of 0.6 N/mm^2.

Fig. 5.29 and Fig. 5.30 show experimental versus model comparison for analyses where the slenderness ratio H/L=1.63 and under vertical compression load σ_0=0.4 N/mm^2 and σ_0=0.6 N/mm^2 respectively.

As in previous analyses, model was able to fairly well reproduce initial elastic stiffness. Even if TRSb04 and SRSb04 analyses slightly overestimate experimental stiffness. Model had same sequence of limit states both for truss and single bar horizontal reinforcements and for both vertical stress applied. They are in sequence: horizontal crack at base cross-section, first non-linearity in masonry (F_e), achievement of shear masonry strength (V_m), masonry yielding in compression (F_{ym}), yielding of vertical reinforcements in tension (F_{ys}), maximum horizontal wall strength (F_{max}) and maximum displacement (d_{max}).

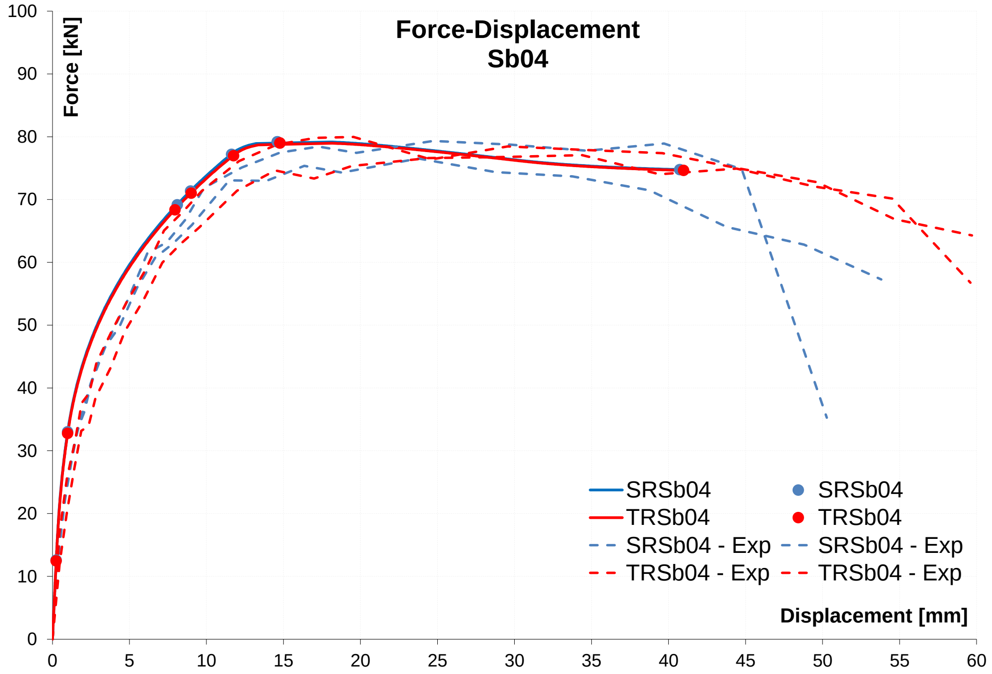

Fig. 5.29. Reinforced masonry H/L=1.63 σ_0=0.4 N/mm^2.
Model versus Experimental load-displacement capacity curves.

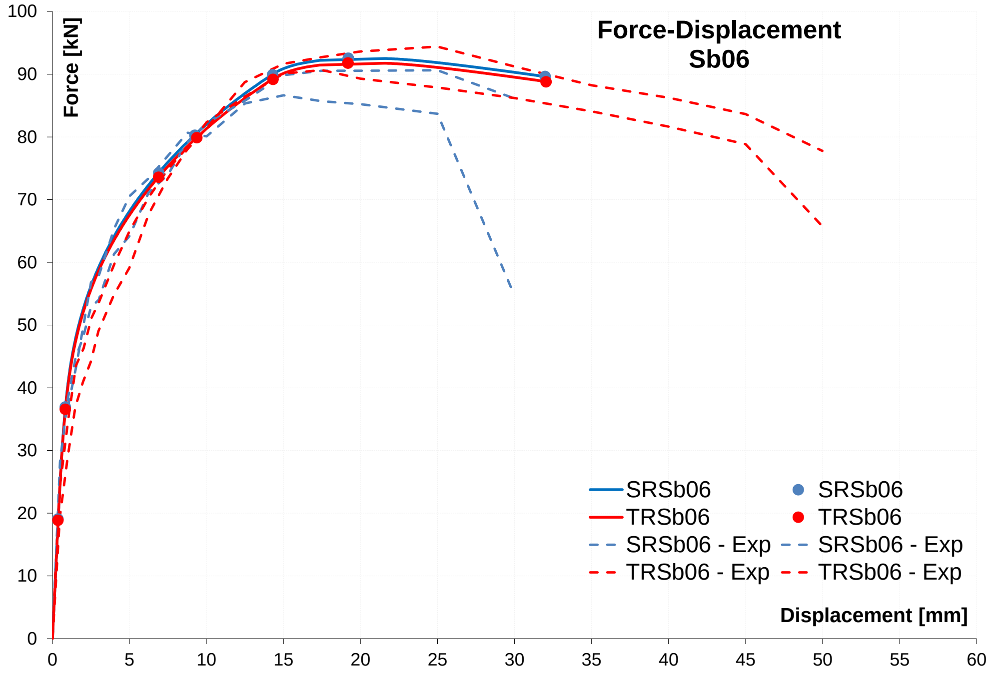

Fig. 5.30. Reinforced masonry H/L=1.63 σ_0=0.6 N/mm^2.
Model versus Experimental load-displacement capacity curves.

Also here the response is still almost linear until second limit state was achieved. Therefore model overestimates the experimental strengths with the negligible maximum error of 1.5%. These modeled walls are in fairly good agreement with experimental results also in terms of maximum displacements seeing global trend of post peak capacity curve (average error 18%). It has to be noted that after walls reached the horizontal force applied F_{ys} (vertical re-bars yielding), capacity curve became almost horizontal presenting a kind of "ideal plastic" branch, denoting the great influence of vertical reinforcements on these walls which failed in flexure. Notwithstanding, reinforcement yielding in tension was not chosen as critical point which refers ductility ratio because it is not always presents in all walls and, if used, makes non unique the definition of ductility ratio.

In general, with reference to Table 5.8 and Table 5.9 it can be noted that for σ_0 = 0.4 N/mm^2 analyses (except for TRSa04) definition of displacement when maximum horizontal force was reached is rather lower from experimental evidence with an average error of about 30%. However, because these walls are strongly influenced by the fact that load is close to maximum for a certain portion of capacity curve, hence the definition of displacement at maximum experimental load may differ from the analytical definition.

5.5.2. Parametrical Extension of Experimental Tests

112 shear compression parametrical analyses of reinforced masonry panels were performed using the analytical model proposed in this chapter, which resume and expand FEM model analyses.

These analyses were aimed to inspect main parameters characterizing mechanical behavior of this construction system which are:

- vertical load applied (40 analyses combinations);
- slenderness of wall (20 analyses combinations);
- vertical reinforcement ratio (28 analyses combinations);
- horizontal reinforcement ratio (24 analyses combinations).

All combinations were repeated for two different series: one with vertical reinforcement ratio similar to that used in experimental tests and another with minimum vertical reinforcement ratio following prescriptions of Italian building code (Ordinanza P.C.M. n. 3274: 2003, 2005). Nevertheless, it was limited the total number of combination using only the single bar horizontal reinforcement solution. This choice was made because, as before mentioned, model cannot compute the complex three dimensional effects of truss in mortar joint and observing analyses done reproducing experimental behavior gave similar results for both truss and single rebar systems.

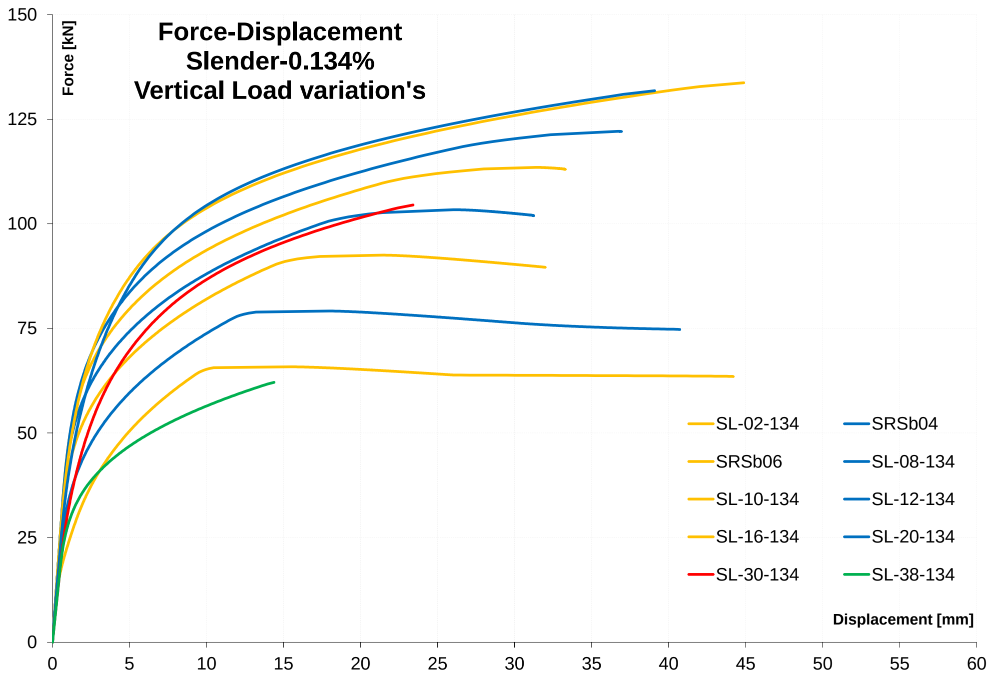

Fig. 5.31. Vertical load variation from 0.2N/mm^2 to 3.8N/mm^2 (yellow and blue). H/L=1.63 vertical reinforcement ratio 0.134%. Model load-displacement capacity curves.

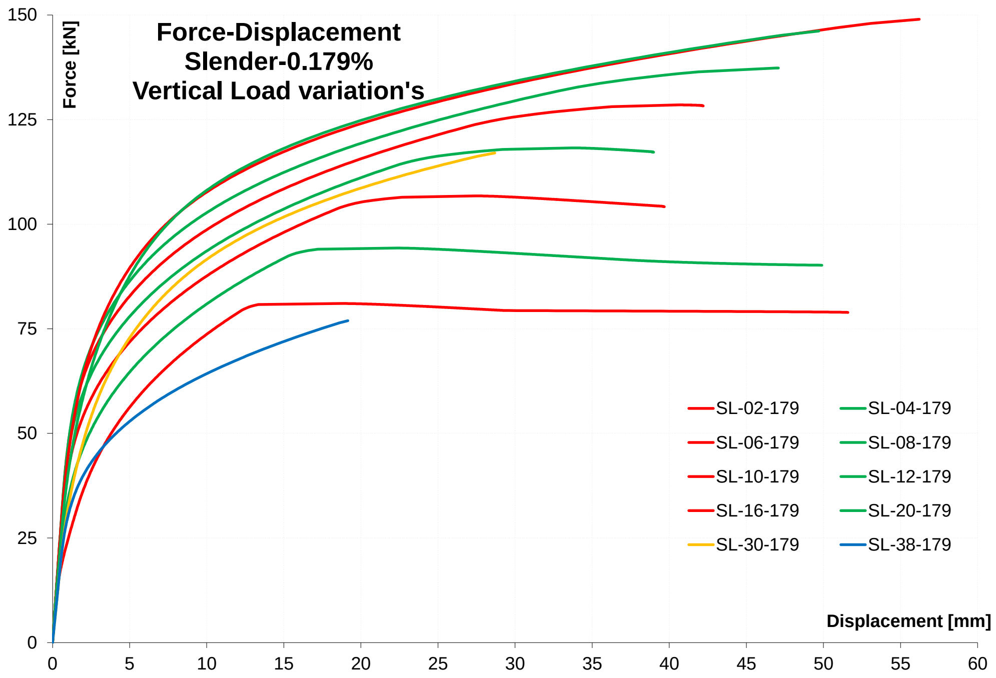

Fig. 5.32. Vertical load variation from 0.2N/mm^2 to 3.8N/mm^2 (red and green). H/L=1.63 vertical reinforcement ratio 0.179%. Model load-displacement capacity curves.

Furthermore truss reinforcement masonry was not inspected also with FEM analysis.

As done for unreinforced masonry, also in this case will be indicating the walls using labels composed by three parts. Experimental walls still using original label and “SQ” indicates other squat walls and “SL” other slender walls.

The analyses done by changing vertical compression load are presented from Fig. 5.31 to Fig. 5.34. Vertical load varies from 0.2 N/mm^2 to 2 N/mm^2 and in addition was performed two further analyses with vertical load of 3 N/mm^2 and 3.8 N/mm^2. Hence vertical load over vertical compressive strength (or vertical stress ratio) varies from 5% to 50% plus two analyses at 75% and 95%.

The four graphs respectively refer to: slender walls with minimum reinforcement ratio for (Ordinanza P.C.M. n. 3274: 2003, 2005) which is at least 1Φ16 at both end of wall (Fig. 5.31), slender walls with experimental reinforcement ratio (Fig. 5.32), squat walls with 1Φ16 at both end of wall (Fig. 5.33) and squat walls with experimental reinforcement ratio (Fig. 5.34). In general, load and displacement capacity increases with vertical load, except for analyses with $\sigma_0/f_m \geq 40\%$. Only squat walls with vertical reinforcement ratio of 0.179% presented diagonal shear failure (see Fig. 5.34). Other walls failed in flexure but with a wide range of ductility capacity. In fact, with vertical load ratio greater than 25%, analyses have shown a little displacement capacity after maximum horizontal load. But, when $\sigma_0/f_m \geq 40\%$ maximum load and displacement capacity were limited by yielding of vertical reinforcement in compression before maximum flexural capacity achievement. This model is not able to consider possible buckling of vertical reinforcement in compression and to stop analysis when it yields. This condition bears to a sudden and brittle failure of walls, and should therefore be avoided.

Fig. 5.35 and Fig. 5.36 show results of slenderness parametrical analyses. Slenderness ratios correspond to: S1 with H/L=2.20, S2 with H/L=1.63, S3 with H/L=1.09, S4 with H/L=0.82 and S5 with H/L=0.65. Obviously, S2 and S3 correspond to experimental slenderness ratio. Fig. 5.35 shows walls subjected to vertical load of 0.4 N/mm^2 and Fig. 5.36 walls with 0.6 N/mm^2.

Obviously initial stiffness and maximum load tend to increase with decrease of H/L ratio (S1 has less stiffness and strength of S5). Yellow and red lines correspond to analyses with almost constant vertical reinforcement ratio of 0.179%, while green and blue line indicate that minimum vertical reinforcement was used (1Φ16).

All walls analyzed, for H/L ratio greater than 1.63 shown a flexural failure.

As expected, high vertical reinforcement ratio tends to cause diagonal shear failure. Besides, walls with minimum reinforcement ratio and H/L<1.09 were limited from yielding of vertical reinforcement in compression before developing their maximum flexural capacity.

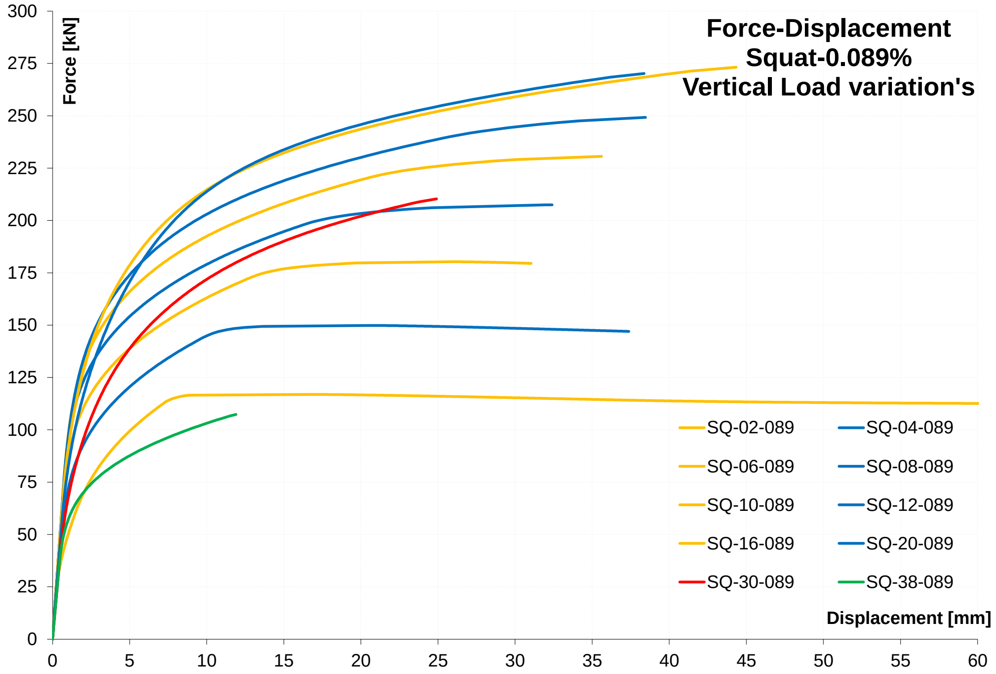

Fig. 5.33. Vertical load variation from 0.2N/mm^2 to 3.8N/mm^2 (yellow and blue). H/L=1.09 vertical reinforcement ratio 0.089%. Model load-displacement capacity curves.

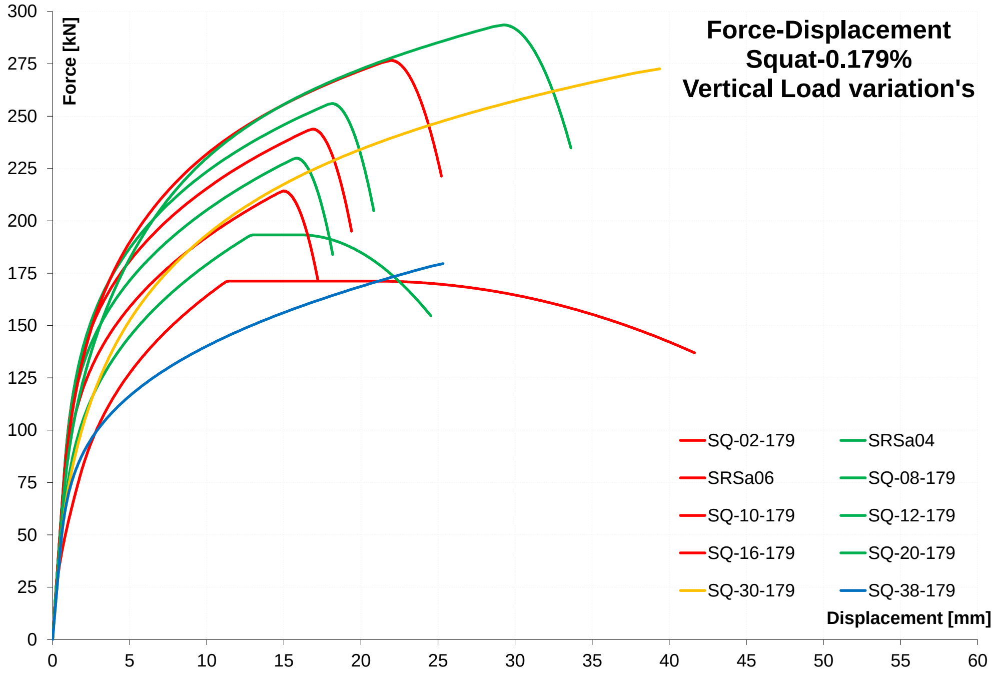

Fig. 5.34. Vertical load variation from 0.2N/mm^2 to 3.8N/mm^2 (red and green). H/L=1.09 vertical reinforcement ratio 0.179%. Model load-displacement capacity curves.

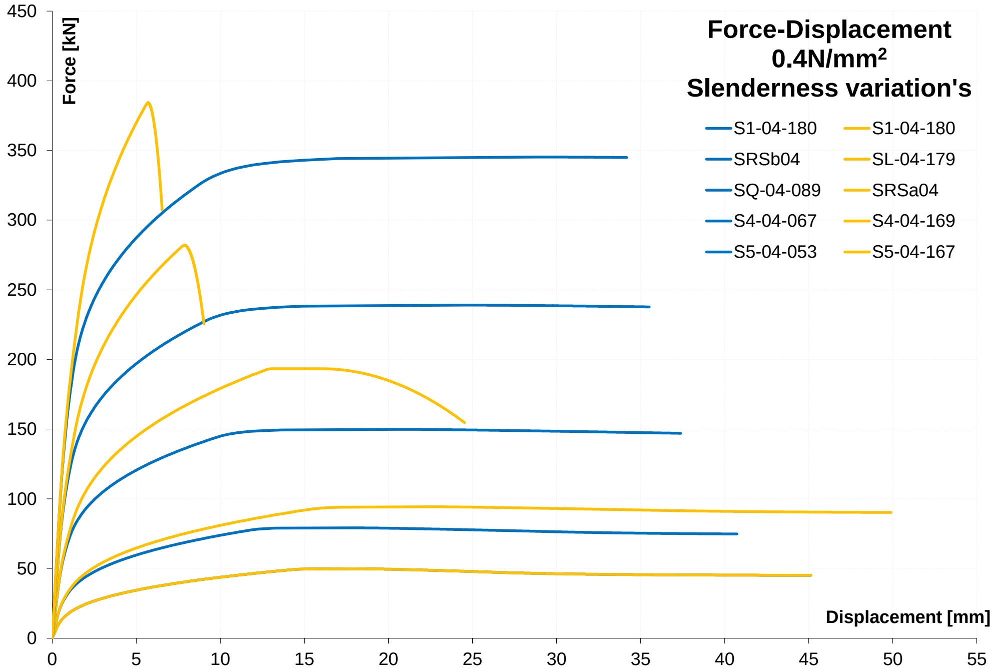

Fig. 5.35. Slenderness ratio variation from 0.652 to 2.197. Vertical load 0.4N/mm^2, vertical reinforcement 0.179% (yellow) or 1Φ16 (blue). Model load-displacement capacity curves.

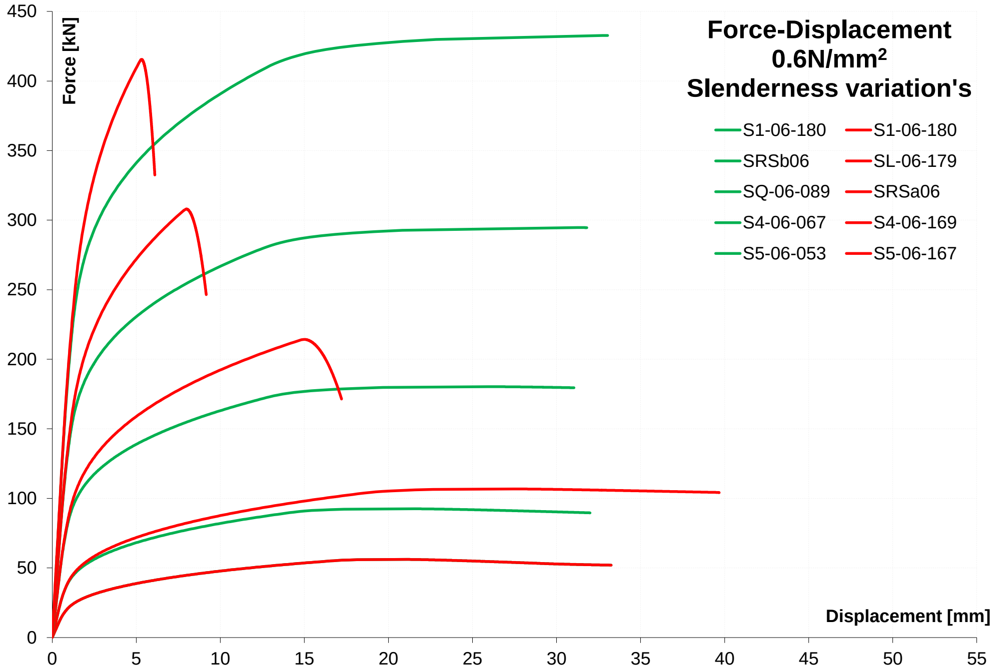

Fig. 5.36. Slenderness ratio variation from 0.652 to 2.197. Vertical load 0.6N/mm^2, vertical reinforcement 0.179% (red) or 1Φ16 (green). Model load-displacement capacity curves.

Despite this fact, it is worth to point out that for σ_0 = 0.6 N/mm^2 analyses with minimum vertical reinforcement ratio presented a good ductility capacity and their maximum strength became greater than other walls with more flexural reinforcements when H/L decreases because the latter were limited by diagonal shear strength.

Fig. 5.37 and Fig. 5.38 show the analyses done varying vertical reinforcement ratio. First graph shows walls subjected to a vertical load of 0.4 N/mm^2, while second shows walls with σ_0 = 0.6 N/mm^2.

For each graph it can be noted two distinct groups of results which refer to slender walls (in yellow and blue) and squat walls (in red and green).

In general, with increasing of vertical reinforcement ratio walls have a stiffer response (and this make easy distinguishing each wall in the graphs). Also the vertical compression ratio, as highlighted with previous parametrical analyses, had an influence on results.

It was used realistic combination of vertical re-bars from 0 (but horizontal reinforcements stilled present) to 0.27% and 0.28% for slender and squat wall respectively. For slender walls these percentages correspond to: 1Φ12, 1Φ14, 1Φ16, 1Φ14+1Φ16 and 2Φ16 at each wall side. Besides, for squat walls: 2Φ12, 2Φ14, 2Φ16, 2Φ18 and 2Φ20 at each wall side.

First of all it can be noted the dramatic influence of vertical reinforcement presence on global behavior of shear walls seeing the walls, both slender and squat and both with low and high vertical load, without vertical reinforcement. They are still in a range with about half strength and displacement capacity showed from average of other walls.

In general, with the increase of vertical re-bar ratio also maximum load and displacement capacities increase, but the tendency of diagonal shear failure also increases, which limits both loads and displacements. Except wall failed with diagonal shear mechanism and walls with no vertical reinforcements, all walls that failed in flexure were limited in maximum displacement from yielding of compressed vertical reinforcements but after showing a good ductility capacity.

Fig. 5.39 and Fig. 5.40 show all possible combinations considering slender and squat walls, with two experimental vertical load ratio and two vertical reinforcement ratio (minimum gave from Italian code and ratio used in experimental tests) for a total of 8 walls. These walls were analyzed with horizontal reinforcements in all joints, or every second joint, or without horizontal reinforcement (vertical reinforcement still present). In these analyses one more part was added to labels indicating different walls. Respectively “000” when was used no horizontal reinforcement and “ALL” when all horizontal joints are reinforced.

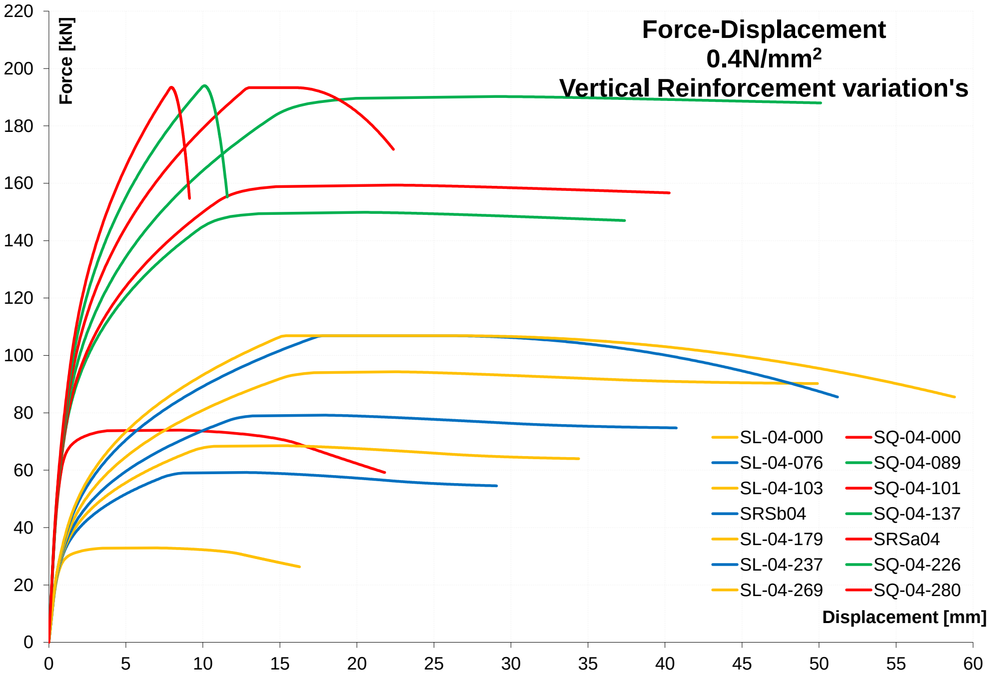

Fig. 5.37. Vertical reinforcement variation from 0% to 0.28%. Vertical load 0.4N/mm^2. H/L=1.63 yellow/blue, H/L=1.09 red/green. Model load-displacement capacity curves.

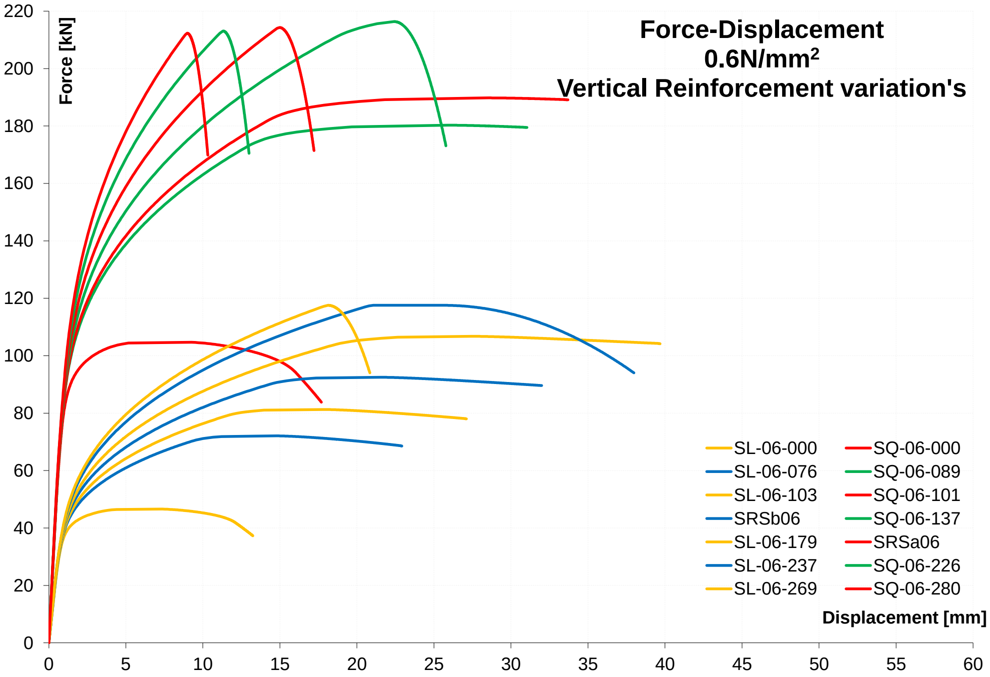

Fig. 5.38. Vertical reinforcement variation from 0% to 0.28%. Vertical load 0.6 N/mm^2. H/L=1.63 yellow/blue, H/L=1.09 red/green. Model load-displacement capacity curves.

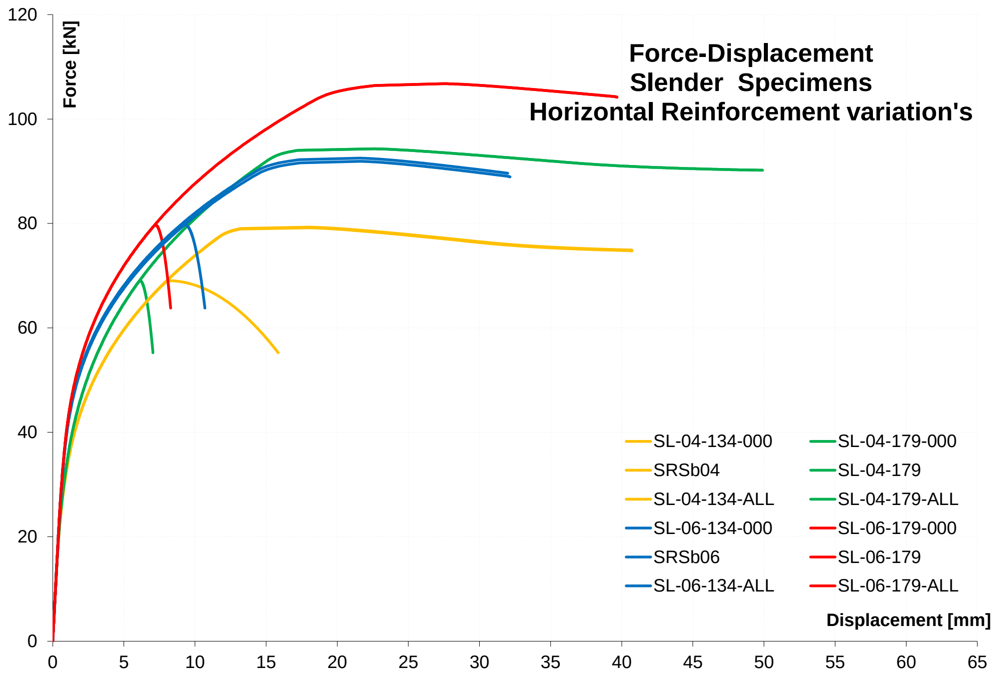

Fig. 5.39. Horizontal reinforcement variation from 0 to all joint. Slenderness ratio H/L = 1.63. Model load-displacement capacity curves.

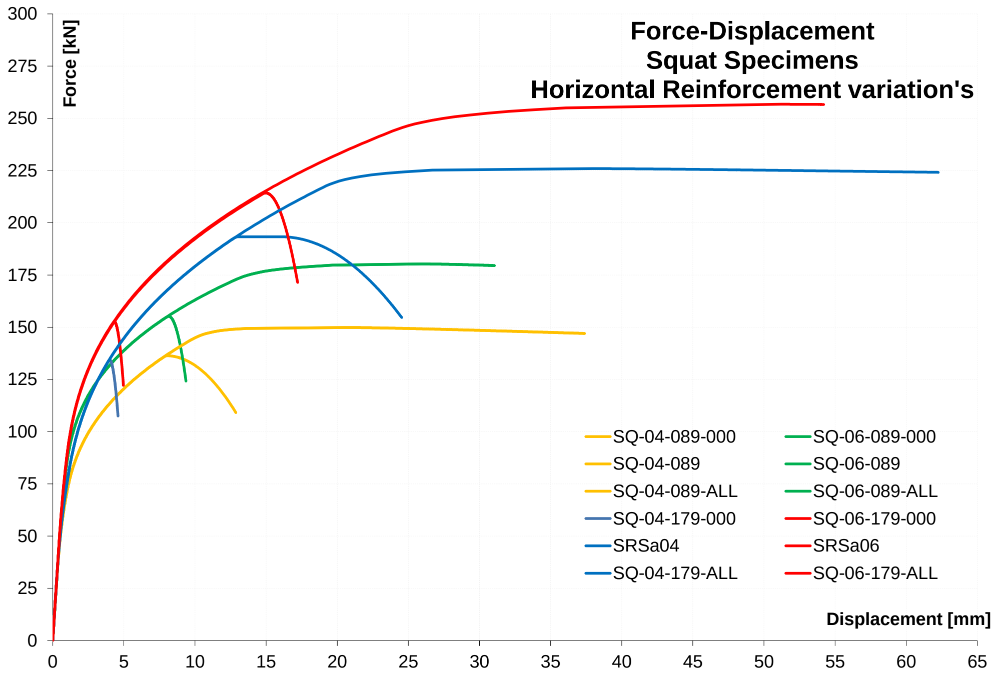

Fig. 5.40. Horizontal reinforcement variation from 0 to all joint. Slenderness ratio H/L = 1.09. Model load-displacement capacity curves.

When no horizontal reinforcement was present in the walls failure occurred for diagonal shear mechanism with all vertical reinforcement, vertical loads and slenderness considered. When re-bars every second joint were added, slender walls change their failure to flexure with a great increase of displacement and strength capacity.

Furthermore, for squat walls (Fig. 5.40 different behavior between minimum and experimental vertical re-bars ratio) took place. Respectively, in first case (green and yellow curves) flexural failure occurred when horizontal reinforcements (as highlighted for slender walls) were added, whereas walls with higher vertical reinforcement ratio (red and blue curves) required reinforcements in all horizontal joints to avoid shear failure.

In general, introducing or increasing horizontal reinforcement hinders shear failure of walls (especially for high vertical reinforcement ratio) and increases global performances in terms of strength and displacement in comparison with the same walls with lower horizontal reinforcement ratio.

5.6. Analysis of Results and Conclusions

The model presented was validated reproducing experimental tests (see 5.4.1 and 5.5.1) and through parametrical analyses done in paragraphs 5.4.2 and 5.5.2 it is was possible to collect interesting data regarding displacements and limit states of both unreinforced and reinforced masonry walls (S.D.o.F. structure) subjected to in-plane actions.

This simplified model can take into account shear deformation contribution and possible diagonal shear failure mechanism. Furthermore it is able to describe the achievement of predetermined limit states relate to cross-section condition or, generally, to global performance (e.g. shear strength contribution of masonry V_m) of walls. In this way it becomes easy to relate these limit conditions to design performance limit states (i.e. serviceability, damage control, ultimate, and collapse prevention).

An aspect that is worth to emphasize, and not noticed before, is that the model allows figuring out displacement profile of wall along its height, besides model can show flexural and shear deformation contribution to total displacement. Fig. 5.41 to Fig. 5.44 show these contributions in the case of TG-22% (used as example) masonry analysis with change of horizontal force applied corresponding to above mentioned limit states: first non-linearity and yielding of masonry in compression, attainment of maximum horizontal resistance and maximum displacement.

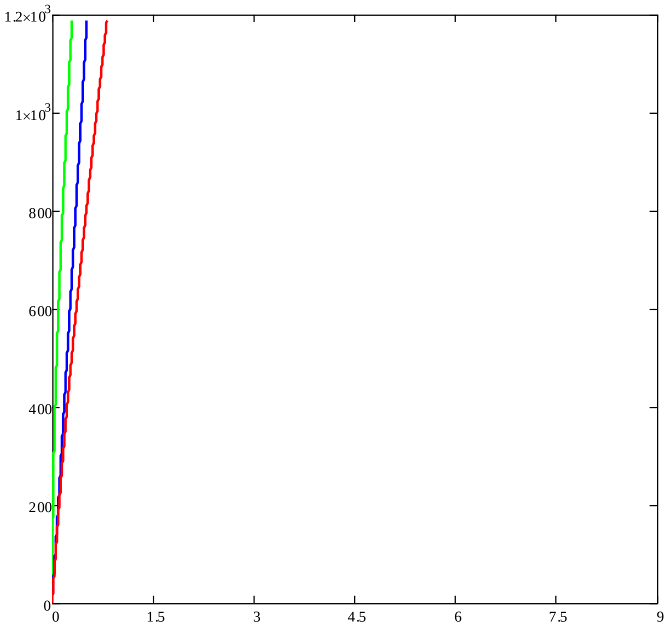

Fig. 5.41. Displacement profiles along height of wall at masonry first non-linearity point. Red line: total displacement profile, blue line shear displacement contribution and green flexure displacement contribution. (TG masonry with σ_0=1.24 N/mm^2, H [mm] and Δ [mm])

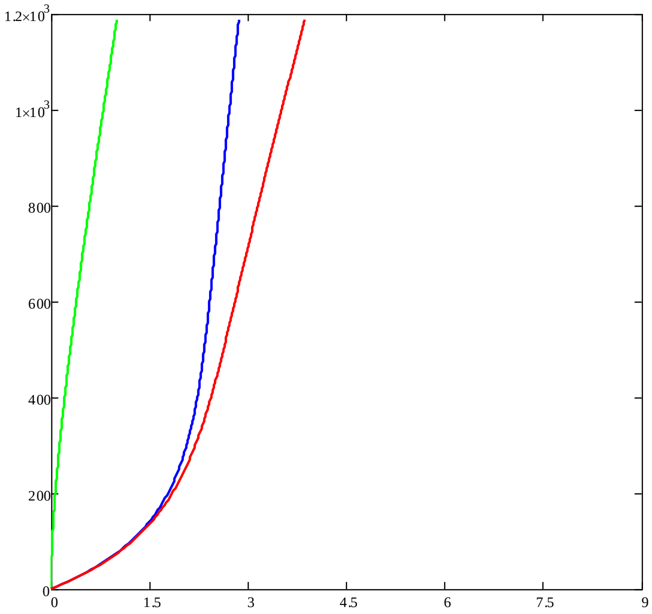

Fig. 5.42. Displacement profiles along height of wall at masonry yielding point in compression. Red line: total displacement profile, blue line shear displacement contribution and green flexure displacement contribution. (TG masonry with σ_0=1.24 N/mm^2, H [mm] and Δ [mm])

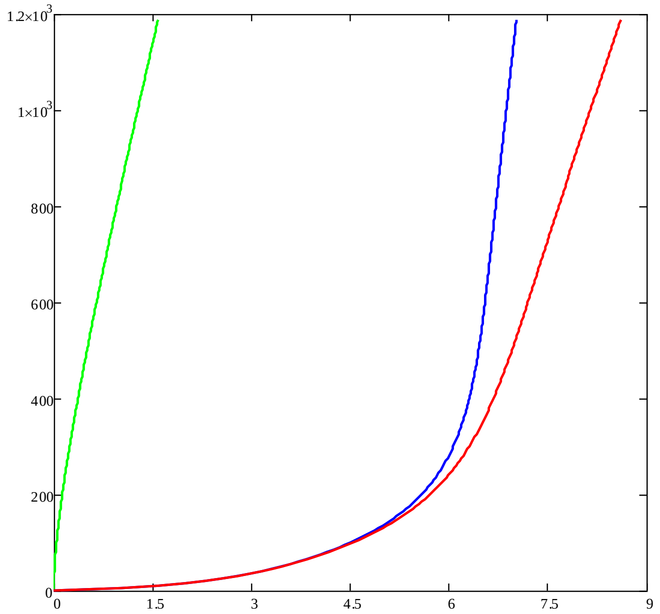

Fig. 5.43. Displacement profiles along height of wall at max strength. Red line: total displacement profile at max strength, blue line shear displacement contribution and green flexure displacement contribution. (TG masonry with σ_0=1.24 N/mm^2, H [mm] and Δ [mm])

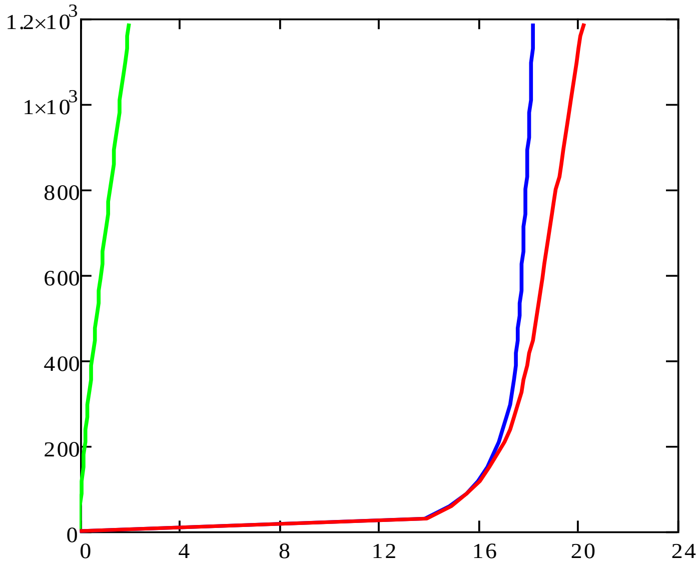

Fig. 5.44. Displacement profiles along height of wall at maximum displacement. Red line total displacement profile, blue line shear displacement contribution and green flexure displacement contribution. (TG masonry with σ_0=1.24 N/mm^2, H [mm] and Δ [mm])

It is clear that shear contribution plays a major role already at the end of elastic phase, even though total displacement profile is still flexure-like. When applied horizontal force increases, shear displacement contribution becomes prevailing and the total displacement profile becomes shear-like already at critical limit state (Fig. 5.42).

From this point to ultimate displacement, the contribution of shear grows quickly compared to flexural contribution and in the end it is about 6-9 times (Fig. 5.44). This tendency is valid in case of flexure failure for all three unreinforced masonry types (TM, TG and Po) but also for reinforced masonry system. For walls failing in shear, this kind of comparison is still valid until the achievement of maximum horizontal resistance because it is inherent to model construction that after this point displacement is only approximates in an empirical way. At maximum horizontal force, the ratio between shear and flexure displacement contributions to total displacement at the top of wall, range around 3-4 for all walls.

In general modeled walls are greatly influenced by shear deformation and shear deformation is controlled by a great extent from shear modulus (G). Despite this sensitivity, model was in good agreement with experimental G obtained from shear-compression tests and with lower bound of values provided by (Circolare 2/02/2009 n. 617 C.S.LL.PP., 2009).

5.6.1. Unreinforced Masonry Walls

In this section will be presented analysis results in terms of drift ($\psi=\delta/H$), at each main limit state, comparing different parameters which were varied in order to see the influence of these mechanical and geometrical conditions on displacement capacity of masonry walls under in-plane actions.

Fig. 5.45 shows vertical stress variation when critical drift was achieved (above), at maximum horizontal strength of wall (middle) and at maximum displacement (below). The results were grouped by masonry compressive strength (using different colors) and by masonry type (using different marker sign).

Critical drift (ψ_{cr}) has about linear function with vertical stress, when it is proportional with masonry strength (left part of chart). On the contrary, when vertical stress is still constant and masonry compressive strength is low, critical drift has nonlinear function with vertical stress (right part of chart). It is possible to see this nonlinear decrease of drift already when unit compressive strength correspond 10 N/mm^2 but it become important when f_{cu} was set to 5 N/mm^2.

In these analyses critical drift ranges between 0.1% and 0.35%.

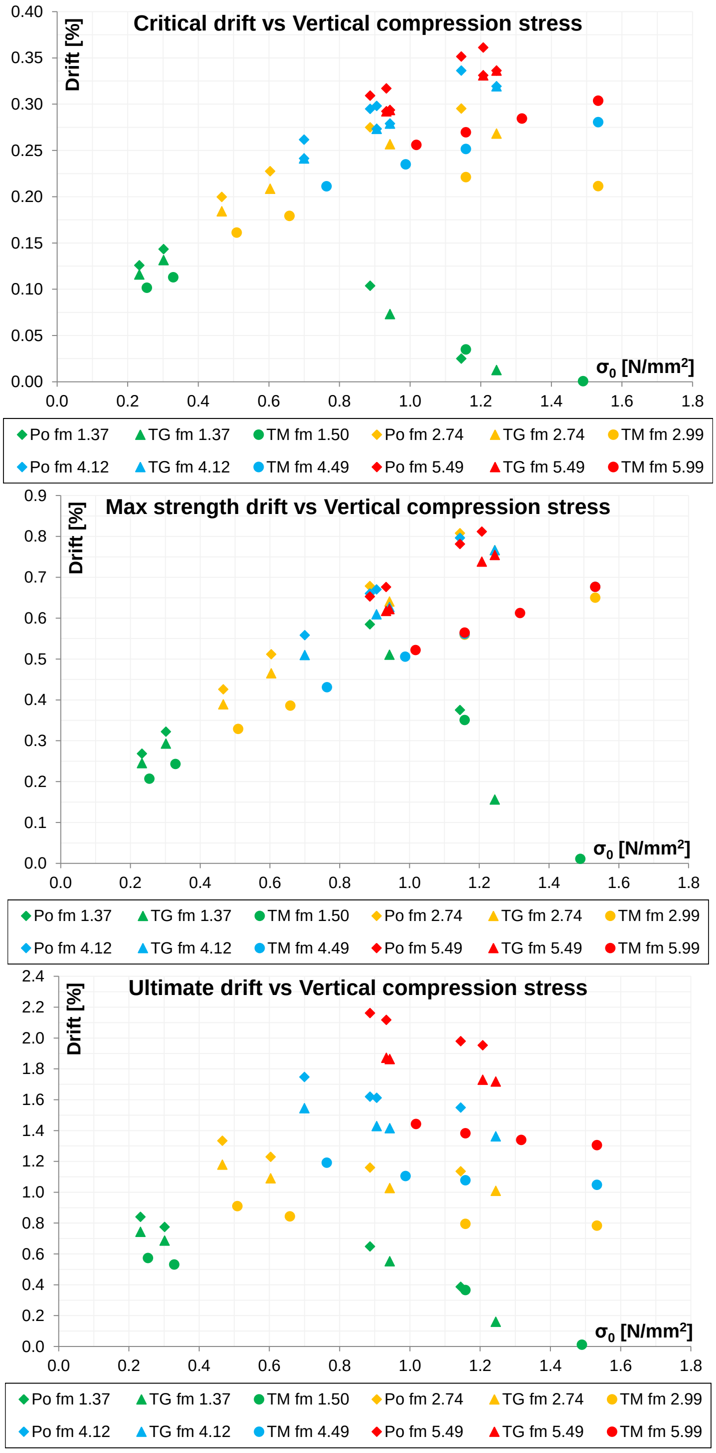

Fig. 5.45. Unreinforced masonry. Critical drift versus Vertical stress (above).
Drift at maximum strength versus Vertical stress (middle).
Drift at maximum displacement versus Vertical stress (below).

Furthermore it can be noted the influence of masonry strength itself, observing that TM masonry critical drift was in general lower than TG and Po masonry which had lower compressive strength.

Drift at maximum horizontal shear force strength (ψ_{Fmax}) of wall showed a similar trend (graph in the middle of Fig. 5.45).

Nonlinear trend showed by ψ_{cr} is less noticeable for ψ_{Fmax} and nonlinearity can be highlighted only when unit with compressive strength of 5 N/mm^2 and higher vertical stress were used. In these analyses, drift ranges between about 0.2% and 0.8% thus two times the range of ψ_{cr}.

The lower graph of Fig. 5.45 shows maximum drift (ψ_{dmax}) reached by walls during the analyses done. In this case the trend of ψ_{dmax} with different vertical loads is more disperse. But, as expected, with a first approximation can be considered that maximum drift decreases when vertical compression stress is increasing. In these analyses, ψ_{dmax} ranges between 0.4% and 2% again about two times ψ_{Fmax}.

Fig. 5.46 shows the drift variations at main limit states of analyses done when masonry compressive strength changes. The results were grouped by masonry vertical compression stress (using different colors) and by masonry type (using different marker sign).

The upper graph of Fig. 5.46 clearly shows that critical drift has linear relation with masonry compressive strength when the same vertical load ratio (in blue and red) was used. Furthermore if vertical load was kept constant the compressive strength of masonry had less influence on critical drift, but there is a strong nonlinear decrease when $f_{cu} \leq 10$ N/mm^2 confirming the considerations made for Fig. 5.45.

When considers ψ_{Fmax}, graph in the of Fig. 5.46 shows similar trend of ψ_{cr}, but in this case when vertical stress was kept constant also the drift can be considered in first approximation as constant, except for walls which had unit compressive strength lower than 10 N/mm^2 which manifest same nonlinear drift decrease as mentioned before. Furthermore this decrease is more important when higher compression stress was applied (see yellow versus green markers).

The lower part of Fig. 5.46 shows maximum drift capacity of masonry walls analyzed. In this case relation between f_{cu} and ψ_{dmax} is almost linear when constant vertical load ratio and also when magnitude of vertical load was kept constant. Besides, when higher vertical stress and lower masonry unit compressive strength is considered drift presents the non-linear decrease as showed in previous limit states.

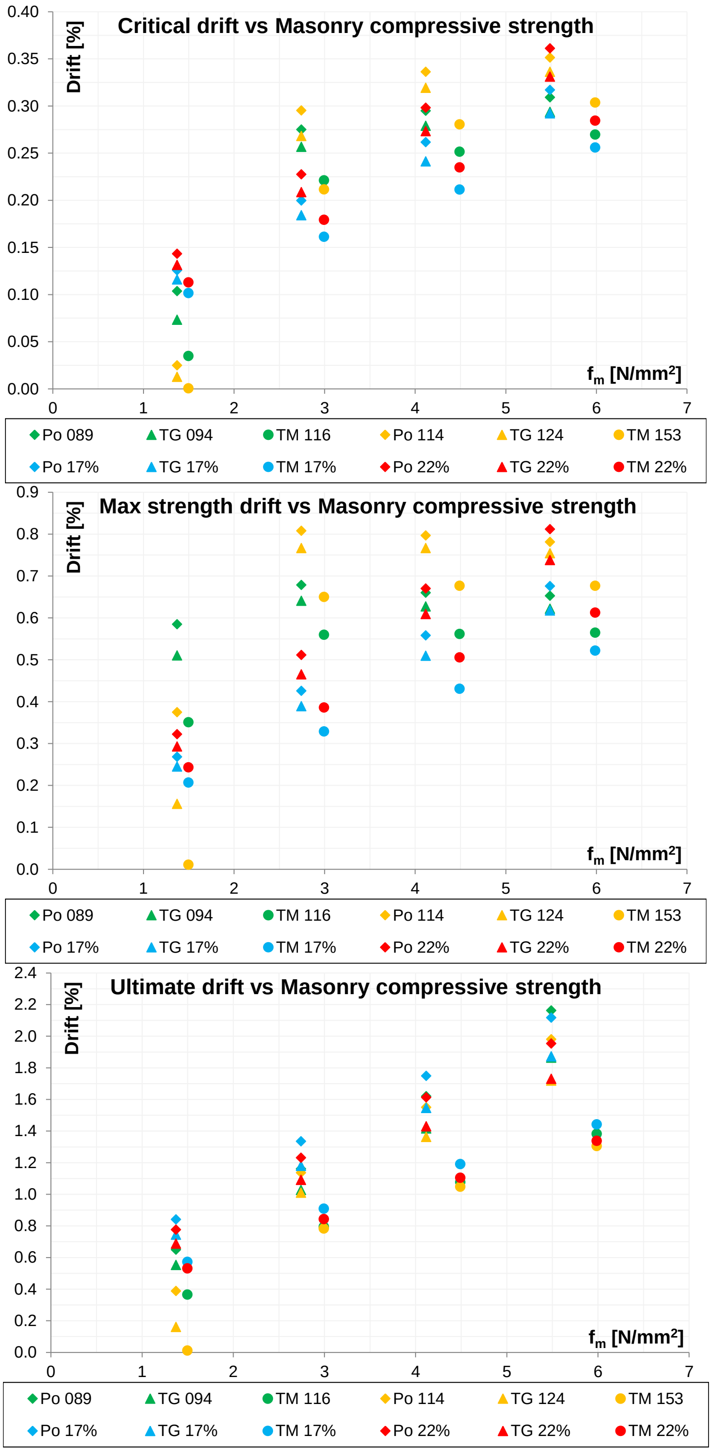

Fig. 5.46. Unreinforced masonry. Critical drift versus Masonry compressive strength (above).
Drift at maximum strength versus Masonry compressive strength (middle).
Drift at maximum displacement versus Masonry compressive strength (below).

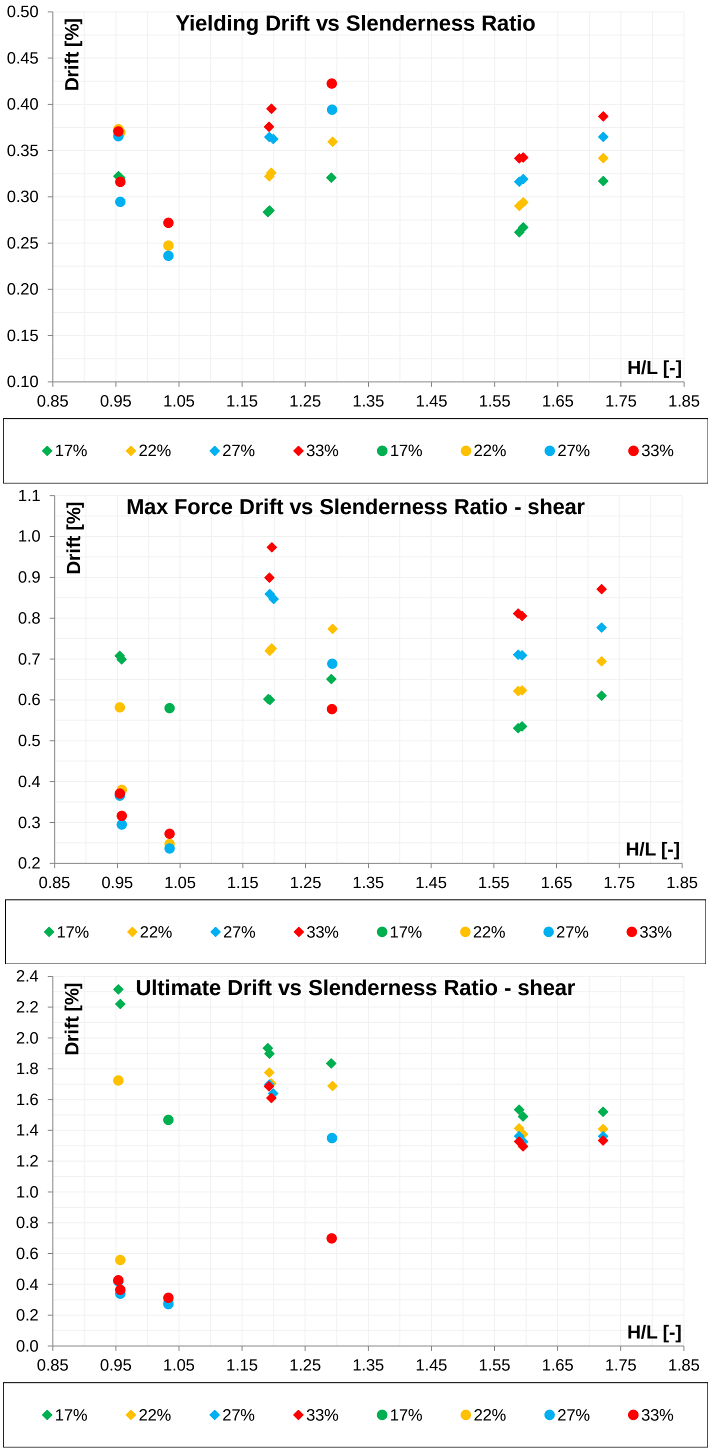

Fig. 5.47. Unreinforced masonry. Critical drift versus Slenderness ratio (above). Drift at maximum strength versus Slenderness ratio (middle). Drift at maximum displacement versus Slenderness ratio (below). Rhombus: flexure failure, Dots: shear failure.

Fig. 5.47 shows results of analyses done with slenderness ratio variation in terms of drift. The analyses were grouped by vertical load applied (using colors) and by different failure modes (rhombuses indicate flexure failure, dots diagonal shear failure).

The upper graph of Fig. 5.47 presents drift at critical limit state. It shows that in case of flexural failure critical drift tends to slightly decrease with the increasing of H/L ratio. When shear failure occurred critical drift was lower. Furthermore, when vertical stress ratios were 27% and 33% all squatter walls had critical point that coincided with maximum horizontal strength indicating a very brittle failure. In general higher compression stress ratio implies higher drift. In these analyses ψ_{cr} ranges about between 0.25% and 0.4%.

Drift at maximum horizontal strength of walls is showed in middle graph of Fig. 5.47 Walls failing in flexure showed the same trend explained before and ψ_{Fmax} decreases with increasing of slenderness ratio. Also here, the observation that higher compression stress ratio implies higher drift is still valid, but with some exceptions in case of shear failure. When shear failure occurred drift at maximum strength was lower. In these analyses ψ_{Fmax} ranges between 0.5% and 0.9% in case of flexure failure, when for shear failure it ranges between 0.25% and 0.7%.

The last graph of Fig. 5.47 shows the trend of maximum drift. Different from previous limit state, here it can be seen that lower compression stress ratio implies lower maximum drift. While still valid for walls with flexural failure a decreasing trend with the increasing of H/L ratio. On contrary the few walls that fail in shear seem to increase their ψ_{dmax} with slenderness. In these analyses, ψ_{dmax} ranges between 1.3% and 2.4% in case of flexural failure, when for shear failure it ranges between 0.25% and 1.3%.

5.6.2. Reinforced Masonry Walls

In this section analysis results in terms of drift ($\psi=\delta/H$), at each main limit state will be presented, comparing different parameters which were varied in order to see the influence of these mechanical and geometrical conditions on displacement capacity of reinforced masonry walls under in-plane actions.

Fig. 5.48 shows vertical stress variation when critical drift was achieved (above), at maximum horizontal strength of wall (middle) and at maximum displacement (below). The results can be grouped by slenderness (green and yellow for slender walls, and blue and red for squat walls) or by vertical compression ratio (green and blue for minimum reinforcement required by Italian code, and yellow and red for experimental reinforcement ratio).

Critical drift (ψ_{cr}) was limited by masonry diagonal shear strength when lower vertical compression stress was kept, on contrary ψ_{cr} was limited by achievement of masonry compressive strength at compressed toe of walls when higher compression stress was used.

In first case the function with vertical load is about linear, while in the second case the function seems nonlinear descending with increasing of σ_0.

Squat walls with higher vertical reinforcement ratio showed shear failure. In this case ψ_{cr} was lower but still have the same trend. Excluding very high compression stress, critical drift ranges about between 0.2% and 0.5%.Drift at maximum shear strength of wall can be seen in the middle graph of Fig. 5.48. Almost linear function can be seen between ψ_{Fmax} and vertical compression stress for all analyses. This fact is still true until ψ_{Fmax} was limited by achievement of yielding at reinforcement bar in compression.

In this case ψ_{Fmax} corresponds also with ψ_{dmax} for limitations imposed by assumptions of this model.

Furthermore also in this case, as previous highlighted, walls with shear failure had lower ψ_{Fmax}. In general, walls with higher reinforcement ratio exhibited a high ψ_{Fmax} compared to same walls with lower vertical reinforcement ratio (if shear failure did not occur).

Drift at maximum shear strength of walls ranges between 0.5% and 3.5%.

In this case walls under very high and very low compression stress had similar ψ_{Fmax}. Considering observations done for ψ_{cr} appears that in walls with very low vertical load ratio, ψ_{Fmax}/ψ_{cr} is close to 1, while for very high vertical load this ratio is greater, but walls reaches ψ_{cr} very early.

The third graph of Fig. 5.48 shows drift at maximum displacement capacity varying applied vertical stress. The general trend was similar to that described for ψ_{Fmax} with the difference that when vertical stress is lower than 0.6 N/mm^2, ψ_{dmax} change its trend and increases with the decrease of vertical load (left part of graph).

Fig. 5.49 shows limit state drifts of analyses performed varying slenderness ratio. They were grouped by vertical stress applied and by vertical reinforcement ratio. Critical drift was limited by masonry shear strength (V_m) when H/L was low (and increases almost linearly with slenderness ratio), while it is limited by achievement of maximum masonry compressive strength (f_m) when $H/L \geq 1.6$. Furthermore, ψ_{cr} was lower in case of shear failure and with higher vertical reinforcement ratio. In general, ψ_{cr} ranges between 0.1% and 0.5%

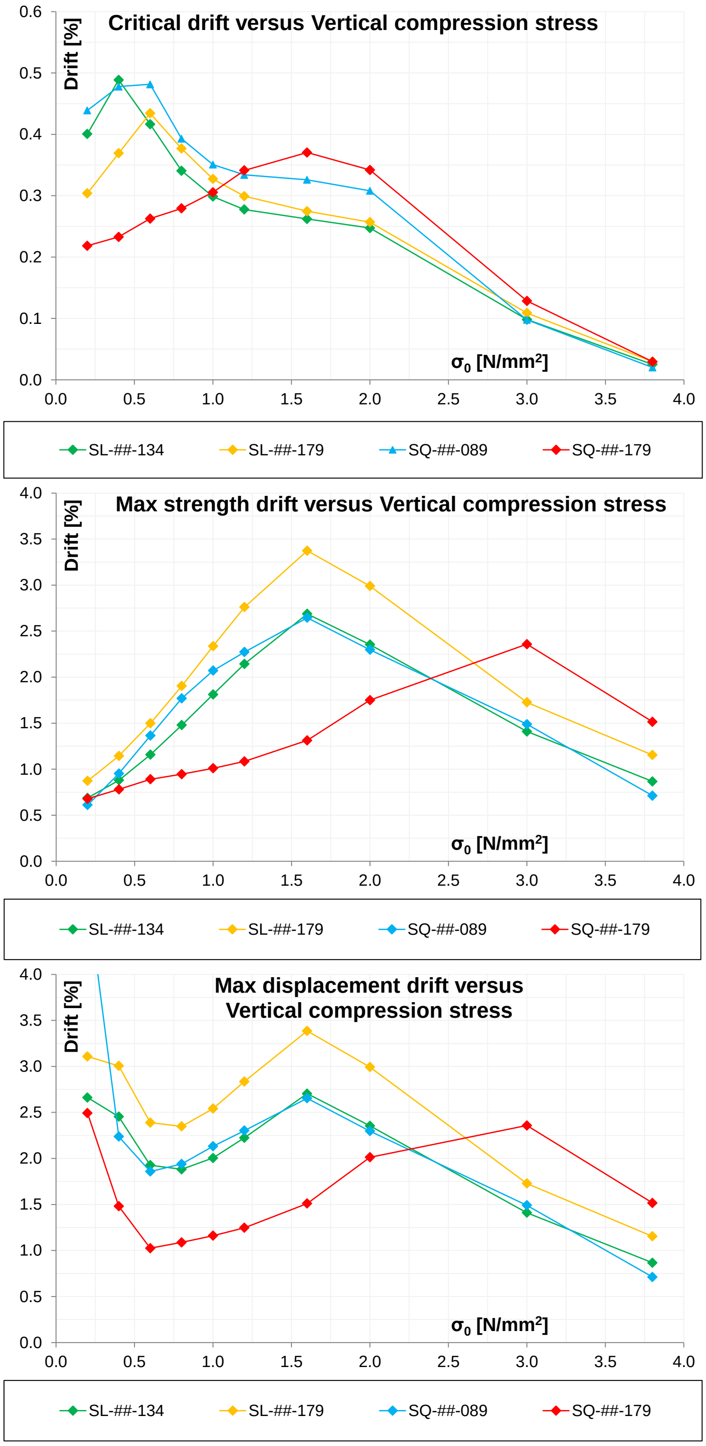

Fig. 5.48. Reinforced masonry. Critical drift versus Vertical stress (above). Drift at maximum strength versus Vertical stress (middle). Drift at maximum displacement versus Vertical stress (below).

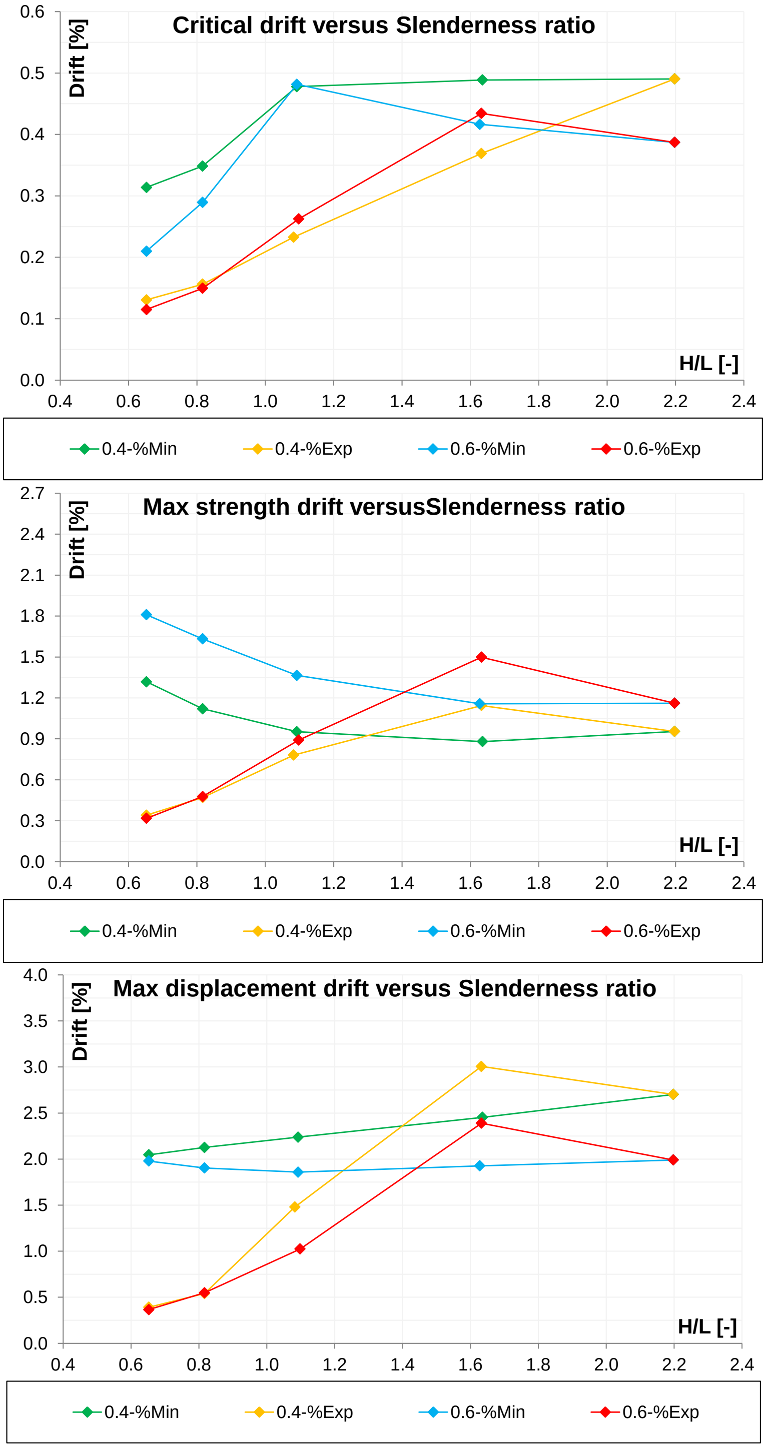

Fig. 5.49. Reinforced masonry. Critical drift versus Slenderness ratio (above). Drift at maximum strength versus Slenderness ratio (middle). Drift at maximum displacement versus Slenderness ratio (below).

Second graph of Fig. 5.49 refers to drift at maximum shear strength of walls. In general ψ_{Fmax} showed a decrease trend with increasing of slenderness ratio. Besides, ψ_{Fmax} is limited when shear failure occurred and in this case drift is lower but increases with slenderness ratio of walls. This happened for walls with higher vertical reinforcement ratio in similar way for both vertical stress considered.

Drift ranges between 0.9% and 1.8% in case of flexural behavior, while it ranges between 0.3% and 0.9% in case of shear failure.

Maximum drift in case of slenderness variation can be seen in lower graph of Fig. 5.49. For this limit state, when minimum reinforcement ratio is kept, flexural failure occurred and ψ_{dmax} was still almost constant at level of 2%. This limit appears to be acceptable also in case of higher vertical reinforcement ratio as that used in experimental tests if shear failure did not occur.

When shear failure occurred, this limits ψ_{dmax} which had an almost linear increase with H/L ratio. In this case, ψ_{dmax} ranges between 0.35% and 1.6%.

In Fig. 5.50 can be analyzed the influence of vertical reinforcement ratio on drift at main limit states. In the first graph, critical drift had a general decrease with increasing vertical reinforcement ratio (it was limited by achieving of V_m). However, in case of low vertical reinforcement ratio, masonry compression yielding limits critical drift, because it is in linear relation with reinforcement ratio.

Critical drift ranges between 0.15% and 0.5%. It can be noted that if no vertical reinforcement is used, ψ_{cr} was still around 0.15%.

The trend of drift with vertical reinforcement ratio can be seen in middle graph of Fig. 5.50. In this case the failure mechanism affects the drift capacity and the slope of ψ_{Fmax} trend. In left part drift is related to a flexure behavior, in the right part drift refers to diagonal shear behavior.

ψ_{Fmax} ranges between 0.5% and 1.5%. It can be noted that if no vertical reinforcement was used ψ_{Fmax} still around 0.3%.

Maximum drift (with reference to lower graph of Fig. 5.50) had similar trend of ψ_{Fmax} and different slopes in left part refers to a flexural failure of walls when in right part the slope changes in relation to shear failure occurring.

ψ_{dmax} ranges between 0.5% and 3.0%. It can be noted that if no vertical reinforcement was used ψ_{dmax} still around 1%.

In first graph of Fig. 5.51 can be noted as practically horizontal reinforcement had no influence on critical drift and which was more affected by influence of vertical compression and vertical reinforcement ratio.

Critical drift ranges around between 0.35% and 0.5% except for squat walls with higher vertical reinforcement ratio. In the last case ψ_{cr} was around 0.25%.

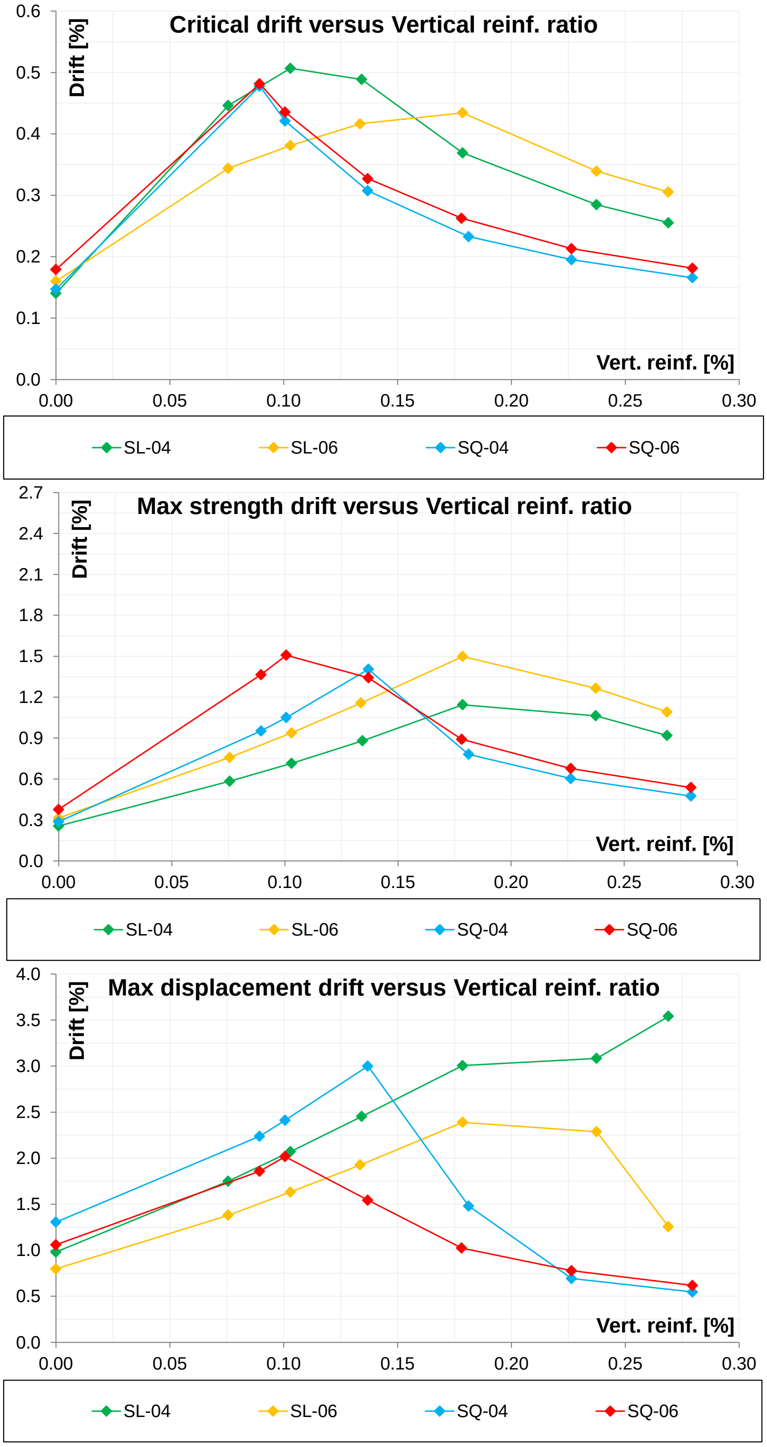

Fig. 5.50. Reinforced masonry. Critical drift versus Vertical reinforcement ratio (above). Drift at maximum strength versus Vertical reinforcement ratio (middle). Drift at maximum displacement versus Vertical reinforcement ratio (below).

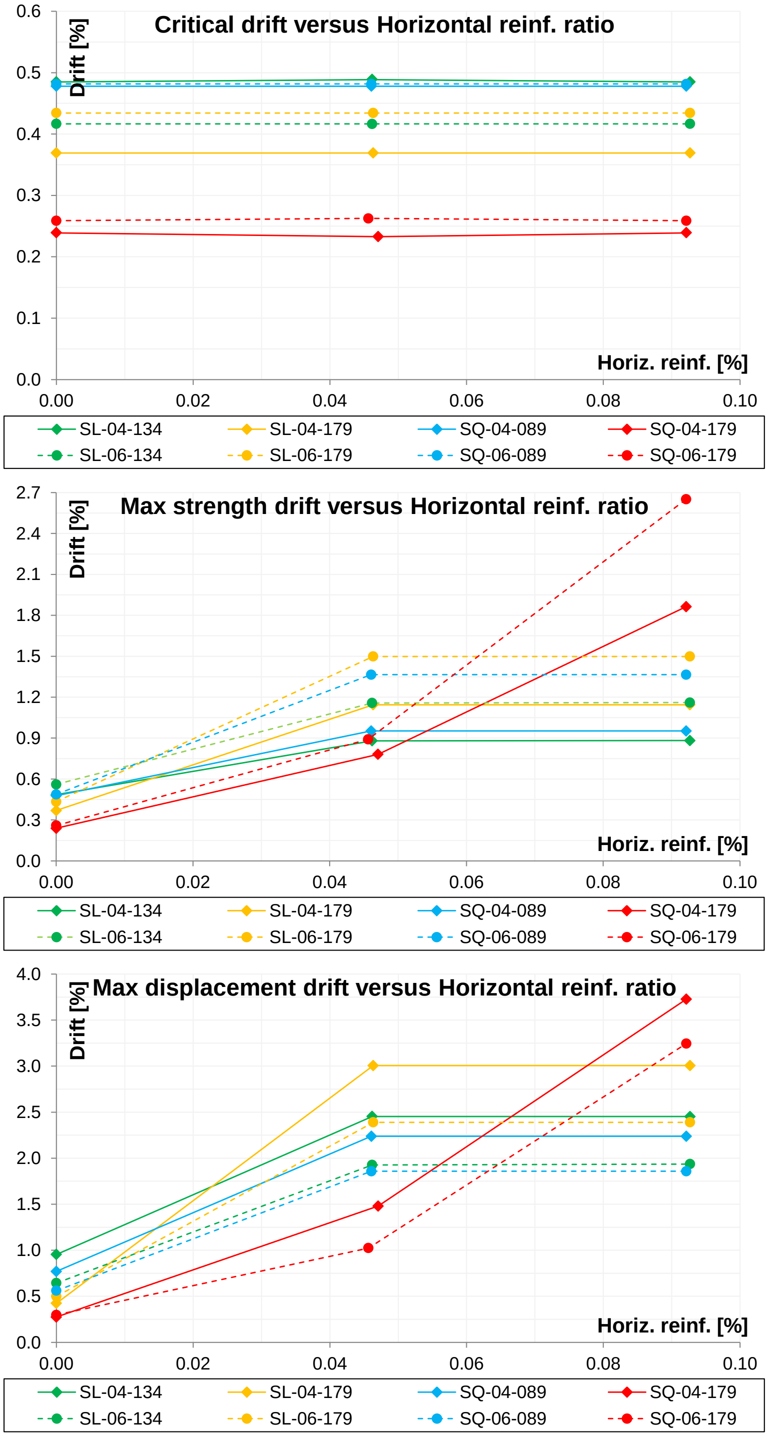

Fig. 5.51. Reinforced masonry. Critical drift versus Horizontal reinforcement ratio (above). Drift at maximum strength versus Horizontal reinforcement ratio (middle). Drift at maximum displacement versus Horizontal reinforcement ratio (below).

The middle graph of Fig. 5.51 reports drifts at maximum shear strength of walls. In this case it can be noted that with increasing of horizontal reinforcement ratio increases also ψ_{Fmax}. The range of ψ_{Fmax} is between 0.3% and 2.7%. But if, at least one every two horizontal joint was reinforced, lower bound of range raises to 0.8%.

The lower graph of Fig. 5.51 reports drifts at maximum displacement. Also in this case it can be noted that with increasing of horizontal reinforcement ratio, increases also ψ_{dmax}. The range of ψ_{dmax} is between 0.3% and 3.7%. But if, at least one every two horizontal joint was reinforced, lower bound of range raises to 1.0%.

Furthermore it worth to point out that with low horizontal reinforcement ratio both for ψ_{Fmax} and ψ_{dmax}, if vertical reinforcement ratio increases the drift decreases, but this trend changes if a good horizontal reinforcement was provided. Moreover slender walls showed better drift performances in case of no horizontal reinforcement, but squat walls can achieve the best performances if balanced vertical and horizontal reinforcements were used.

5.6.3. Summary and conclusions

It was built a model for masonry wall (S.D.o.F. structure) under in plane vertical and horizontal forces, able to take in to account the load-displacement capacity curve (also considering non-linear shear deformation) and to reproduce both flexural and shear failures. The model presented was validated reproducing experimental tests (see 5.4.1 and 5.5.1)

The modeling results of these analyses carried out with the above mentioned model were discussed and the main results are summarized in the following:

- In general modeled walls are greatly influenced by shear deformation and shear deformation is controlled to a great extent by shear modulus (G). Despite this sensitivity, model was in good agreement with experimental G obtained from shear-compression tests and with lower bound of values provided by (Circolare 2/02/2009 n. 617 C.S.LL.PP., 2009)
- As expected, in general, flexural behavior was fairly well reproduced by model achieving both strength and displacement showed in experimental tests, despite some inconsistencies present for unreinforced masonries.
- Shear strength formulation adopted was able to correctly forecast experimental walls subjected to shear failure and also, with acceptable approximation, their loads and displacements.
- model was able to describe the achievement of various limit states which represent the performances of masonry walls relating with cross-section (e.g. when masonry pier reach compressive strength at base section) or whole panel limit states (e.g. when wall reach shear strength provided by masonry).

Three types of load-bearing un-reinforced masonry walls, made with perforated clay units and differing types of head and bed joints were modeled under in-plane cyclic loads. The modeling results of these analyses were discussed.

- Parametric analyses showed how wall performance under combined shear and compression depend on unit strength, slenderness and masonry type.
- In general, maximum horizontal load and drift at ultimate state decrease with unit strength. The decrease in unit strength also corresponds to a change in dominant failure mode, from flexure/rocking to brittle flexure. In all masonry types, critical behavior arises at unit strengths between 10 and 5 N/mm^2 as found with FEM approach.
- If the ratio of applied vertical load to masonry compressive strength is kept constant, maximum drift decreases at lower unit strength, as vertical load decreases but not affect the failure mechanism (this fact differs from results of FEM analyses). In any case, the displacement capacity of thin-layer joint masonry remains lower than in other masonry types.

Reinforced masonry systems were modeled under in-plane cyclic loads. The modeling results of these analyses were discussed and the main results are in the following:

- increment of axial load leads to increase of shear capacity at the expense of ductility, in particular related to the post peak phase - variation of axial load allows to control the failure mode: from brittle shear failure to ductile flexural failure, and from more to less ductile flexural failure;
- the higher the aspect ratio (slender wall) the higher the ductility, where displacement capacity is concentrated in post peak phase;
- slenderness ratio influence failure mode and allows to control if shear or flexure prevails, but in general has less influence if minimum vertical reinforcement ratio is applied (flexure failure prevails);
- vertical reinforcement ratio allows to control the failure mode from brittle shear failure to ductile flexural failure, but in general has less influence on slender walls (flexure failure prevails in this way);
- in case of no horizontal reinforcement, slender walls showed better drift performances compared to squat walls; even though the latter achieve the best performances, when balanced vertical and horizontal reinforcements were used. In general, the higher horizontal reinforcement ratio the higher displacement capacity, within the range analyzed.

6. DYNAMIC ANALYSES

6.1. Introduction

In this chapter are presented the analysis method utilized to simulate the dynamic behavior of masonry systems under investigation and also the results of these analyses.

The non-linear dynamic analyses were carried out with the main aim of providing the Hysteretic Damping (ξ_{hys}) factor, for the proposed masonry systems, at designers, so that the design process with these systems is safe and easy through linear elastic analyses.

Non-linear dynamic analyses required the use of cyclic non-linear mechanical models, as also indicated by (DM 14/01/2008, 2008). It was applied the hysteretic model available after (da Porto et al., 2009c) which was developed during the DISWall European Project (DISWall, 2008) and based on model of (Tomaževič & Lutman, 1996).

Were carried out non-linear dynamic analyses of one degree of freedom systems characterized with experimental data available from (da Porto et al., 2009c) and (da Porto, 2005) respectively for reinforced masonry (RM) and unreinforced masonry (URM) systems.

Were applied 10 spectrum-compatible accelerograms with different Peak Ground Acceleration (PGA) in order to catch the performances at different displacements (or drifts, or ductility). Furthermore the analyses took in to account also different soil properties according to classification of (DM 14/01/2008, 2008).

6.2. A Hysteretic Model for Masonry Walls

6.2.1. Experimental Cyclic Shear-Compression Tests Modeling

The idealized envelope curves on which the construction of the hysteresis loops was based, were taken as the quadri-linear curves defined by the four experimental limit states given in paragraph 3.3.3 and available after (Mosele et al., 2008) and also reproduced by analytical model presented previous in Chapter 5.

The experimental observations on which the model is based are the following:

1. The loading phase can be divided in two parts: the first part, with low displacement, and high stiffness (until the point A in Fig. 6.1) and a second part with lower stiffness (until the point B in Fig. 6.1). The former still almost unchanged among different loading cycles, with only low decay of stiffness values; conversely, the second phase presented a high decay of stiffness. Furthermore, the transition between these two parts occurred when forces and displacements were close to first limit state (the point 1 in Fig. 6.1) and decreases with the increase of cycle amplitudes.
2. The un-loading phase can be subdivided in three parts: the first characterized by a high value of stiffness which determines the breadth of cycle and the dissipated energy (until the point C in Fig. 6.1); the second in which stiffness still almost the same as in second loading phase (until the point D in Fig. 6.1); finally, the third phase where the stiffness increase again and still constant in the succeeding loading phase of next loading cycle. The latter increase of stiffness happened when forces were similar to the stiffness change during the loading phase (points A and D in Fig. 6.1), giving the typical S form of hysteresis cycle.
3. Repeated amplitude cycles showed high strength decay during loading phase, when the unloading phase strength still almost unchanged respect to first cycle of that amplitude. Hence following cycles with the same amplitude were smaller and gave less dissipated energy amount compared to first cycle.

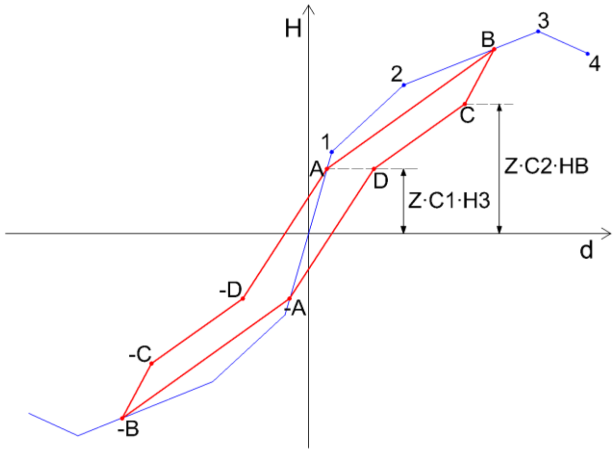

Fig. 6.1. Idealized envelope curve (1-2-3-4) and scheme of the hysteresis loop (A-B-C-D).

Starting from these observations, the construction of the hysteresis loops has been based on the definition of four symmetrical points (A, B, C, D). These points are found by means of two coefficients: C_1 and C_2, which are calculated by imposing the equivalence of the input energy and the dissipated energy in the experimental and modeled loops during a cycle (see Fig. 6.1).

The modeling of the first cycles at each displacement level is carried out as follow. System still linear elastic until the cycles reaches the first limit state (point 1 in Fig. 6.1) the opening of a cycle start after this amplitude. Hence, for little displacements system still moves over the envelope until the loading reversal (which is the point B). The point A is always placed on the idealized envelope curve. Its ordinate is a function of the maximum resistance (H_{max}) using the coefficient C_1 and the parameter Z (Eq. 6.5), which is a ductility parameter and is used to define H_A and $H_{C,}$ respectively the forces of point A and C. The point B is found on the four-limit-states idealized envelope curve, and placed at the defined displacement d_B of given cycle. The slope of the first unloading branch (K_{BC}) changes according to the amplitude of the cycle under consideration and the ordinate of the point C (H_C), where the first unloading branch ends, is defined by the coefficient C_2 and the parameter Z. K_{BC} (Eq. 6.2) is determined on the basis of another parameter, called C_K (Eq. 6.1). This parameter allows obtaining a linear variation of the slope of branch B-C, starting from elastic stiffness K_1 to a lower bound represented to the slope of the second branch of the envelope curve (K_{1-2}). The point D has the same ordinate of the point A, and is found imposing that the slope of K_{C-D} = K_{A-B}. The negative semi-cycle was built keeping the symmetrical point of A, B, C and D. Since point -A still almost constant, whereas point D increases the displacement along with the increase of cycle amplitude, K_{D-A} decreases at every cycle modeled Fig. 6.2.

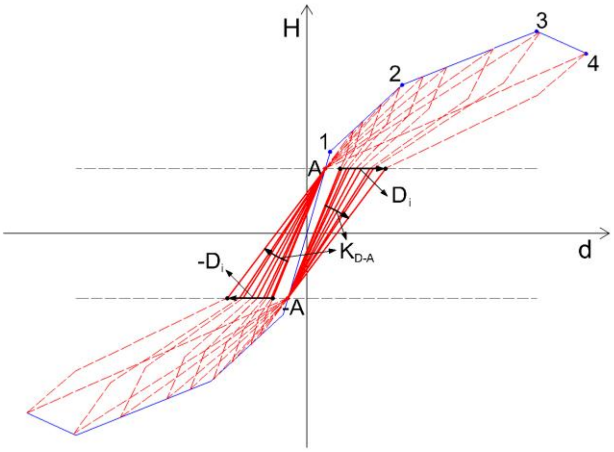

Fig. 6.2. Degradation of stiffness K_{D-A}.

$$C_k = \left(\frac{K_{1-2}}{K_1} - 1 \right) \Bigg/ \left(\frac{d_4}{d_1} - 1 \right) \tag{Eq. 6.1}$$

$$K_{BC} = K_1 \left[1 + C_k \left(\frac{d_B}{d_1} - 1 \right) \right] \tag{Eq. 6.2}$$

$$d_E = \frac{H_{max}}{K_1} \tag{Eq. 6.3}$$

$$C_z = \left(\frac{d_1}{d_E} - 1 \right) \Bigg/ \left(\frac{d_4}{d_E} - 1 \right) \tag{Eq. 6.4}$$

$$Z = 1 + 0.5 \cdot C_z \cdot \left(\frac{d_B}{d_E} - 1 \right) \le 1 \tag{Eq. 6.5}$$

Squat walls	C_1	SD_{C1}	C_2	SD_{C2}
SRSa 0.4	0,402	0,050	0,836	0,070
TRSa 0.4	0,400	0,060	0,916	0,056
SRSa 0.6	0,424	0,025	0,846	0,035
TRSa 0.6	0,466	0,033	0,892	0,067
mean	0,423	0,042	0,873	0,057
Slender walls	**C_1**	**SD_{C1}**	**C_2**	**SD_{C2}**
SRSb 0.4	0,311	0,063	0,852	0,056
TRSb 0.4	0,311	0,069	0,803	0,064
SRSb 0.6	0,391	0,069	0,922	0,025
TRSb 0.6	0,396	0,043	0,950	0,019
mean	*0,352*	*0,061*	*0,882*	*0,041*

Table 6.1. Hysteretic model parameters C_1 and C_2.

From fitting of experimental tests the form coefficients C_1 and C_2 did not still constant during cycles with different magnitude, but they were almost constant at first cycles and decreasing with the increase of cycle magnitude, because H_A and H_C tend to decrease.

Model introduces Z parameter that provides an estimate coefficient C_1 and C_2 variation, allowing to considers constant these parameters and rely on it to control their variation. Z is evaluated on the basis of C_Z (Eq. 6.4) and d_E (Eq. 6.3). With displacements lower than d_E, Z is considered equal to 1. After d_E, Z decreases linearly. As example mean C_1 and C_2 values (using Z corrector) found for RM system are reported in Table 6.1 with corresponding standard deviations (SD).

Further details on model are available on (DISWall, 2008) and (da Porto et al., 2009c).

6.2.2. Arrangement of Hysteretic Model for Random Seismic Input

The model, as it has been defined in the previous paragraph, assumes to know the amplitude of each cycle. Furthermore every cycle is greater than the previous, so the displacement at point B (d_B) is also the maximum reached displacement (d_{max}). Under these assumptions, it is possible to define for each cycle the stiffness of the branch A-B ($K_{A\text{-}B}$) as the stiffness that moves the system exactly from point A to point B, known a priori.

If we consider seismic action, it is impossible to assume a priori the amplitude of cycles. In fact, the earthquake induced displacement represents the unknown quantity. For this reason it has been necessary to define $K_{A\text{-}B}$ in order to establish how the system has to move when point A is exceeded. Furthermore the amplitudes of cycles are not certainly increasing, but random, so d_B usually does not overlaps d_{max}. Therefore Z parameter is referred to the maximum displacement, instead to point B.

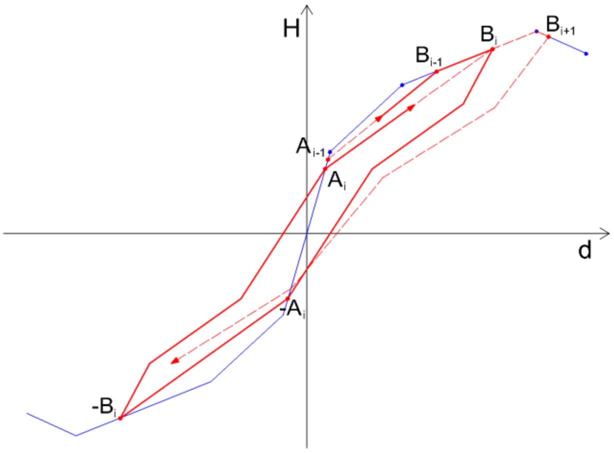

Fig. 6.3. Asymmetrical cycles.

The stiffness of branch A-B is implicitly defined in such a way to assure an increase in degradation with the increase of reached displacement. When the system starts to unload, the point B is detected. If the corresponding displacement is greater than the previous, Z parameter is updated and thus there is a degradation of point A. On the contrary, if d_B is less than d_{max}, neither Z changes nor A. So, the stiffness $K_{A\text{-}B}$ is defined as the slope of the secant to the point A and B.

This definition implies that, reproducing a cyclic test, asymmetrical cycles are obtained. In fact, with reference to Fig. 6.3 and considering the i-th cycle, the model initially considers $d_{max} = d_{Bi-1}$, because the higher displacement reached is represented by the amplitude of the previous cycle. The considered stiffness K_{A-B} is the secant to the points A_{i-1} e B_{i-1}. Therefore, the system moves from point A_{i-1} in order to reach point B_{i-1}, which is placed on the quadri-linear curve. Then it continues following the envelope until it reaches point B_i that represents the new d_{max}. It is now possible to update the parameter Z and calculate Ai. The asymmetry derives from the fact that the negative part of the cycle is carried out considering the i-th state. In this way the system, after the un-loading B-C and C-D, passes at first trough point $–A_i$ and then directly through point $–B_i$.

The stiffness of the section D-A (K_{D-A}), cannot be defined implicitly as the secant to points D and A, because for casual cycle amplitudes, the monotone degradation is not ensured. Therefore, if it is determined that the slope of the section D-A is lower than the current K_{D-A}, the latter is updated according to the secant to the points D and A and in this way the system pass through the point A. Otherwise, to move to point A the system should move with stiffness greater than current K_{D-A}, which however must not be exceeded. Therefore, exceeded point D, the system moves with the current stiffness K_{D-A} until it reaches the strength H_A, defining a new point, which is indicated by the letter E (Fig. 6.4). Beyond point E stiffness K_{A-B} is utilized.

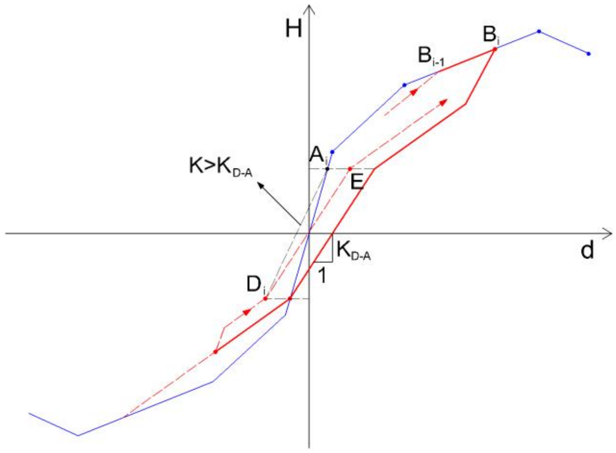

Fig. 6.4. Definition of point E.

The un-loading considered until now occurs in the section A-B, but this is merely a general condition. In fact, during a dynamic analysis the direction of the displacement can change its sign at any time. It is therefore possible to distinguish two cases: displacement inversion in the section B-C or C-D (Fig. 6.5 on the left), and displacement inversion in the section D-A (Fig. 6.5 on the right).

In the first case, the system simply changes its direction moving from the place where it is with stiffness $K_{A\text{-}B}$. In the second case, we have instead the opening of the cycle, still according to the parameter Z and the coefficient C_2, determined on the basis of amplitude Δ (Fig. 6.5). Hence we have two phases: a first branch B-C with stiffness $K_{B\text{-}C}$ and a second branch C-E with stiffness $K_{D\text{-}A}$. Once passed point E, the system moves with stiffness $K_{A\text{-}B}$.

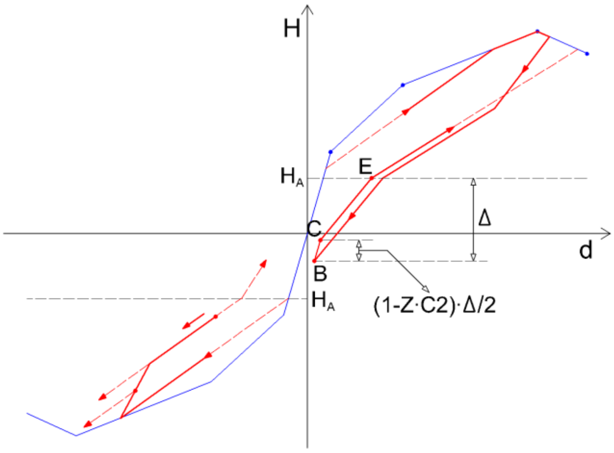

Fig. 6.5. Re-loading conditions.

6.2.3. Seismic Input used in the analyses

Dynamic analyses were carried out on 10 synthetic time-histories composed of 2048 points taken at a sampling frequency of 100 Hz. The time-histories were created in MATLAB™, and are compatible with the type 1 spectra of (EN 1998-1: 2004. Eurocode 8, 2004) with a lower bound and upper bound of 10% of deviation between generated and code-prescribed spectra in the period range from 0.10 to 2.00 s. Their Peak Ground Acceleration (PGA) is normalized to a_g (Fig. 6.6). Definition of the response spectra varies according to the different types of soils. The main five soil categories are: A, rock or other rock-like geological formation; B, very dense sand, gravel, or very stiff clay; C, medium-dense sand, gravel or medium stiff clay; D, loose-to-medium cohesionless soil or predominantly soft-to-firm cohesive soil; E, soil profile consisting of a surface alluvium layer.

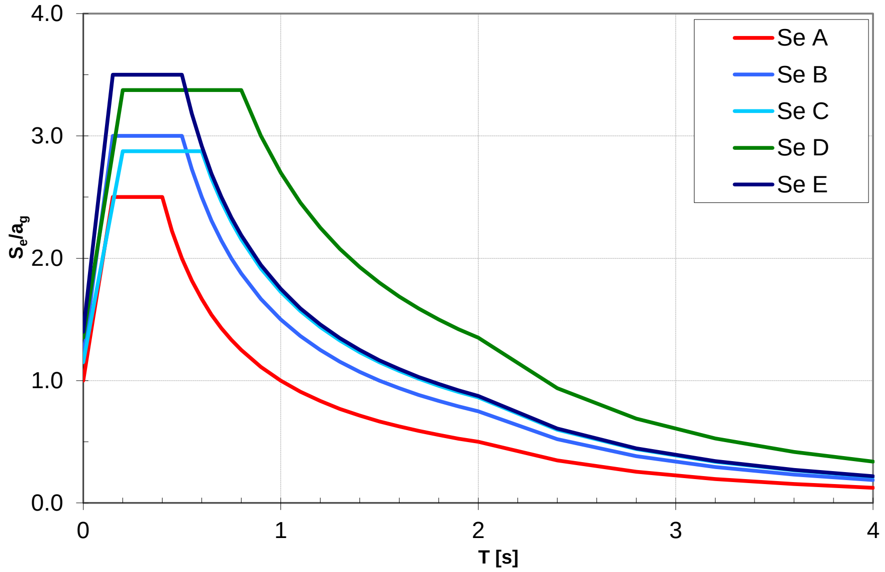

Fig. 6.6. Eurocode 8 recommended Type 1 spectra for ground Types A to E.

The analyses were repeated for the two limit soil group classified, i.e. soil A and soil D. Despite soil E has a peak spectral acceleration higher than soil D, the latter shows a larger plateau that has a bigger seismic demand at medium-high periods. Hence the effective response in the non-linear range determine an increase of effective periods, that often are beyond of T_C of soil E, to characterize the whole response until the ultimate capacity soil D spectrum appear more severe.

In Fig. 6.7 are reported the synthetic time-histories used in the analyses.

Fig. 6.8 shows the spectrum-compatibility between mean value of 10 accelerograms normalized to a_g and the corresponding spectra given from (EN 1998-1: 2004. Eurocode 8, 2004) for the two types of soil: A (rock soil) and D (soft soil), in the period range 0.15-2.0 s.

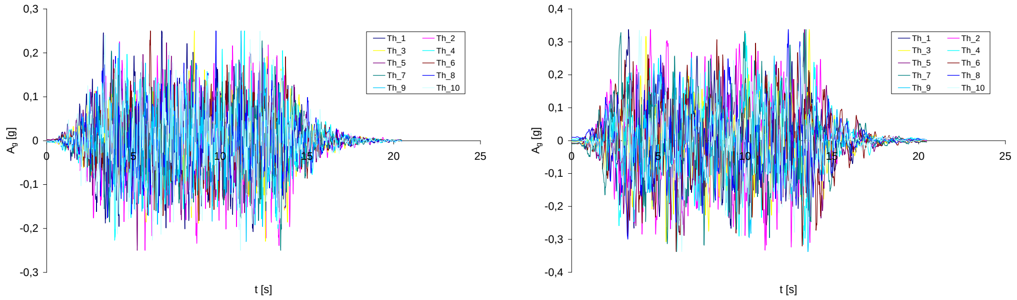

Fig. 6.7. Synthetic time-histories used in the analyses, generated respect soil A (above) and soil D (below).

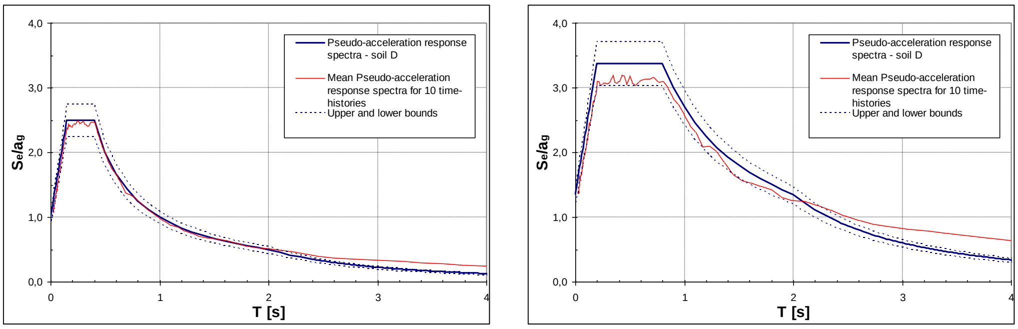

Fig. 6.8. Spectrum-compatibility between the mean value 10 time histories of accelerograms and Eurocode 8 type 1 spectra for soil A and D.

6.3. Analysis of Results and Conclusion

6.3.1. Application for Reinforced Masonry System

The hysteretic model calibration of cyclic shear compression test for RM system was already done in (da Porto et al., 2009c) and here were reported only the main results with the aim of providing details on model capability to catch experimental behavior and the parameters used for further seismic analyses carried out for this thesis. All 8 RM specimens were taken into account.

Fig. 6.10 shows the comparison between the experimental data and the modeled hysteretic loops. As can be seen, there is fair good agreement. From the comparison between experimental and modeled values of the ratio between dissipated and input energy (see Fig. 6.11) it can be seen that the model reproduces fairly well the energy balance of the tests. The differences are generally lower than 5% for the squat specimen, and 3% for the slender specimen.

Squat walls	C_1	C_2	C_K	C_Z
SRSa 0,4	0,402	0,836	-0,057	-0,135
TRSa 0,4	0,400	0,916	-0,047	-0,094
SRSa 0,6	0,424	0,846	-0,067	-0,157
TRSa 0,6	0,466	0,892	-0,101	-0,164
mean	*0,423*	*0,873*	*-0,068*	*-0,138*
Slender walls	C_1	C_2	C_K	C_Z
SRSb 0,4	0,311	0,852	-0,022	-0,048
TRSb 0,4	0,311	0,803	-0,026	-0,045
SRSb 0,6	0,391	0,922	-0,026	-0,055
TRSb 0,6	0,396	0,950	-0,028	-0,048
mean	*0,352*	*0,882*	*-0,025*	*-0,049*

Table 6.2. Hysteretic model parameters for reinforced masonry system.

Table 6.2 gives the values of the parameters found on the basis of these specimens. C_1 and C_2 coefficient are reported also in a graphical way in Fig. 6.9 from which is possible to see that these parameters can be assumed constant with its mean value for parameter C_2, when the C_1 parameter gave a significant difference between slender and squat walls. This can be useful in the case of extension of experimental results.

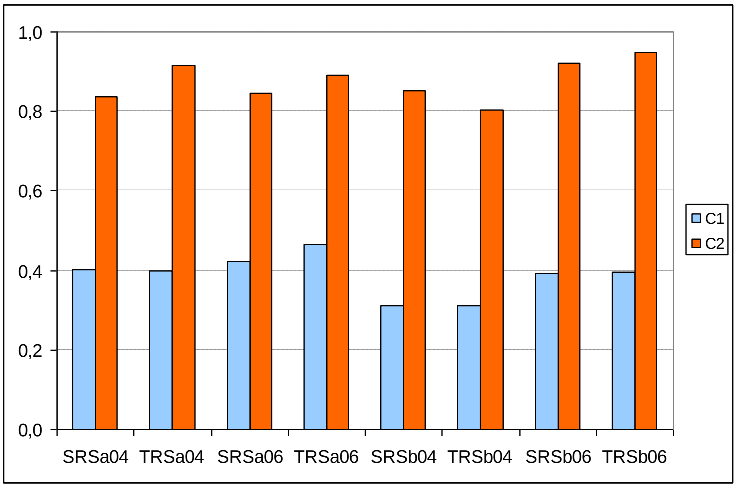

Fig. 6.9. C_1 and C_2 coefficients for RM.

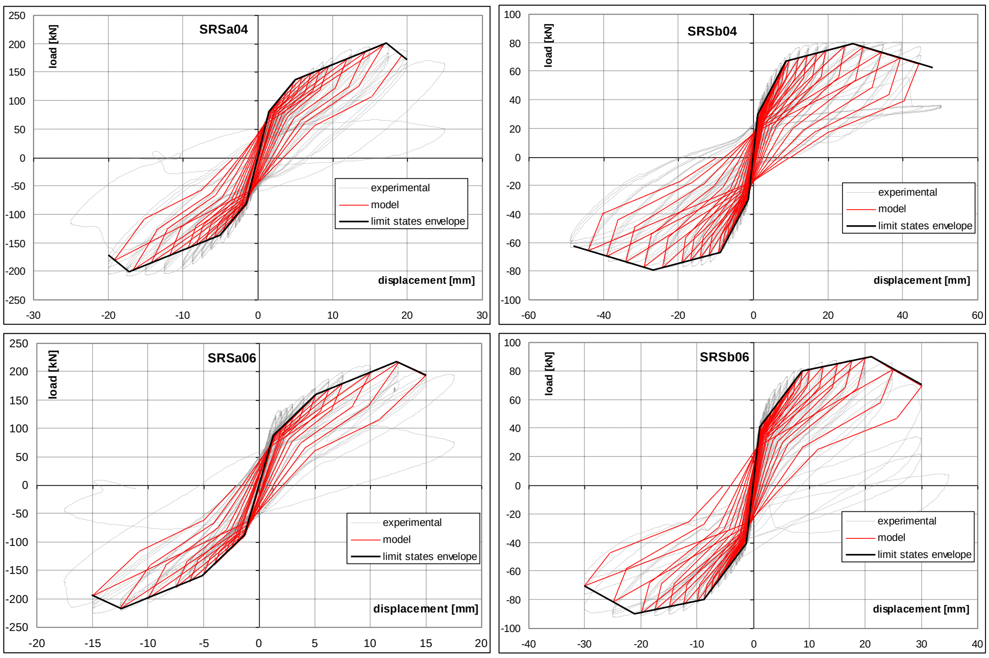

Fig. 6.10. Experimental hysteresis loops and loops from model. Squat (left) and slender (right) specimens; σ_0=0.4 N/mm^2 (above) and σ_0=0.6 N/mm^2 (below) vertical compression

load.

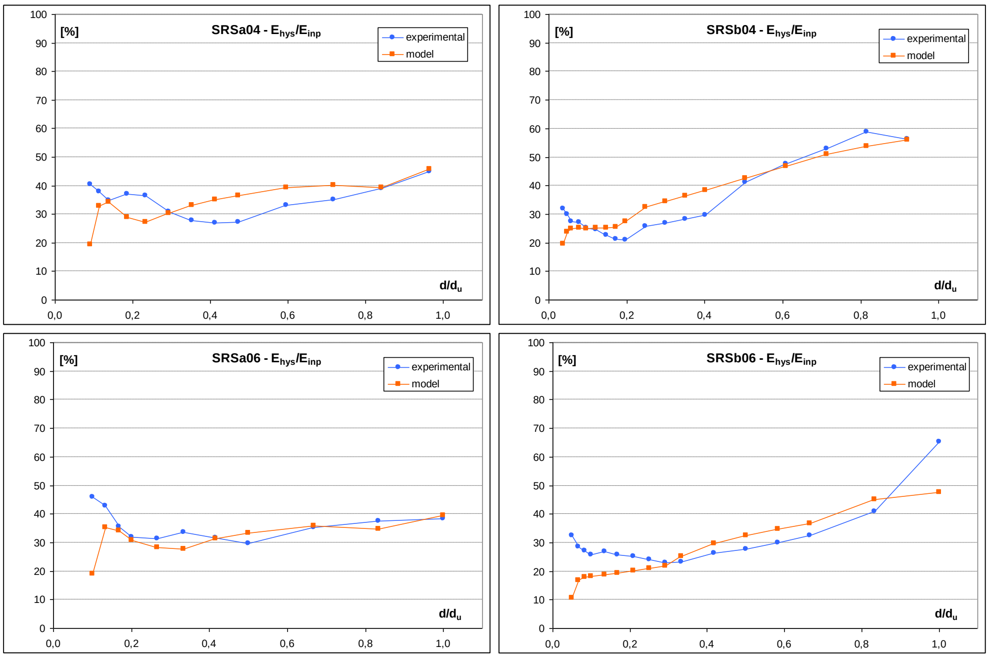

Fig. 6.11. Ratio of dissipated/input energy: comparison between experimental and modeled values. Squat (left) and slender (right) specimens; σ_0=0.4 N/mm^2 (above) and σ_0=0.6 N/mm^2 (below) vertical compression load.

In order to see the model capability to simulate also the seismic behavior of this RM system, in Fig. 6.12 are reported some cases of nonlinear time histories analyses (using the same TH to better confront other differences) done using different soil, different slenderness ratios and different PGA. In the firsts two rows of this figure, the squat specimen with 0.6 N/mm^2, soil A and PGA = 0.35 g is confronted changing respectively the soil (type D) and the slenderness ratio. The latter (slender) is confronted in the last row changing only the PGA from 0.35 g to 0.25 g. Other details will be reported in next the chapter 7 on which these results are used with the aim of estimate the damping factor for this RM system.

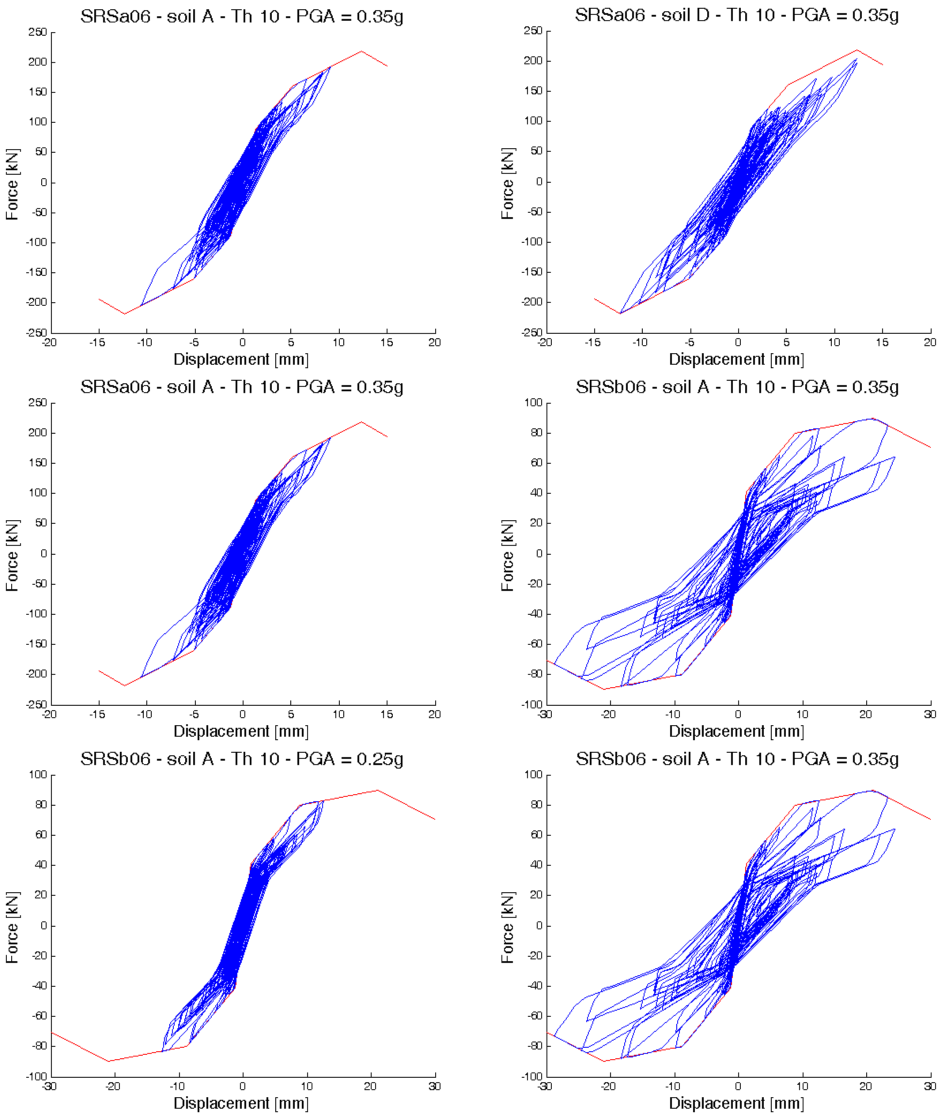

Fig. 6.12. Some example of model results given for different soil (above), different slenderness ratios (middle) and different PGA (below).

6.3.2. Application for Unreinforced Masonry System

For URM system under investigation in this thesis was done a similar calibration process using the hysteretic model done for RM. In this case from experimental tests can be seen that the behavior of the three typologies of masonry TM, TG and Po was similar. In particular for low vertical pre-compression level the specimens showed a flexural/rocking behavior with a low amount of dissipated energy.

The specimens tested under a vertical load of 0.27% of their masonry compressive strength, showed higher dissipated energy and also different failure modes. For these reason this hysteretic model was applied at this level of vertical compression load.

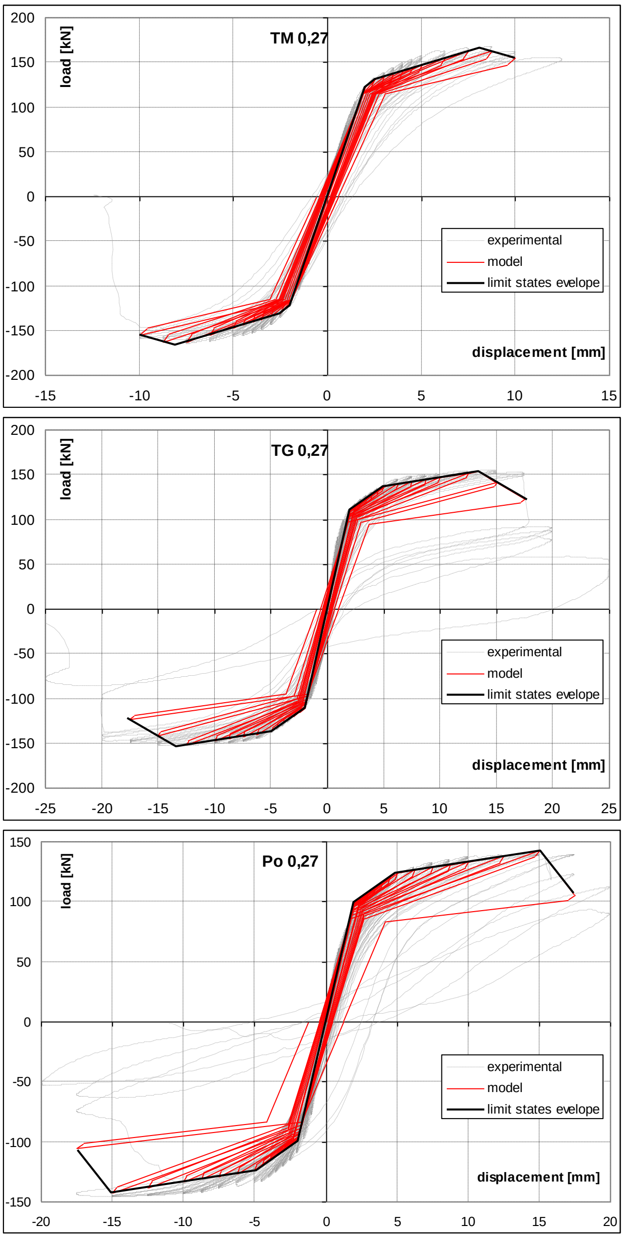

Fig. 6.13. Experimental hysteresis loops and loops from model. TM (above), TG (middle) and Po (below) specimens with vertical compression load of 0.27% of their compressive strength.

It worth to point out that from observation of experimental cycles the model needed to be revise in definition of Z parameter. In particular for URM, it was noted that the cycle opening represented by point C of model (and controlled by parameter C_2), tend to be proportional to force at point B. In the idealized behavior of model, this means that Z parameters (that control the variation of C_1 and C_2), for parameter C_2 is a constant and it does not vary with cycle amplitude. Provided this modification also in this case the hysteretic model was able to catch the experimental behavior fairly well.

In Table 6.3 are reported the model parameters and in Fig. 6.14 the coefficientsC_1 and C_2 graphically. In Fig. 6.13 and Fig. 6.15 respectively show the experimental and modeled loops and their energetic balance for the three masonry types.

URM	C_1	C_2	C_K	C_Z
TM 0.27%	0,735	0,949	-0,179	-0,098
TG 0.27%	0,718	0,965	-0,106	-0,052
Po 0.27%	0,691	0,962	-0,108	-0,059
mean	*0,715*	*0,959*	*-0,131*	*-0,070*

Table 6.3. Hysteretic model parameters for unreinforced masonry system.

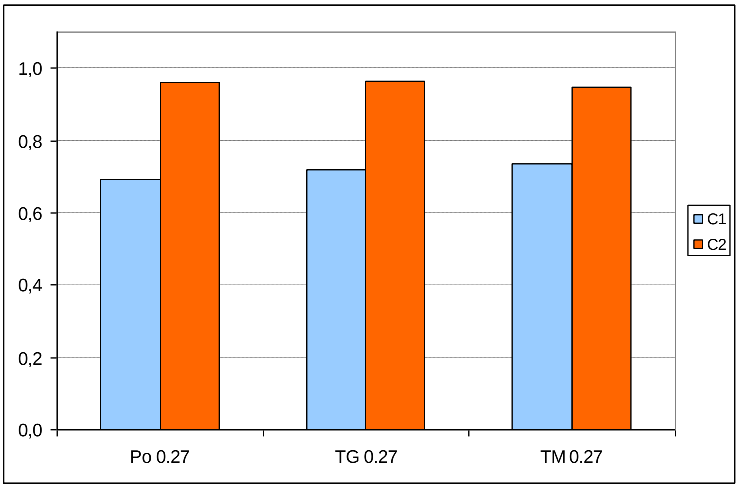

Fig. 6.14. C_1 and C_2 coefficients for URM.

In order to see the model capability to simulate also the seismic behavior of this URM systems, in Fig. 6.16 are reported some cases of nonlinear time histories analyses done using different masonry type, different soil and different PGA. Other details will be reported in next the chapter 7 on which these results are used with the aim of estimate the damping factor for this URM system.

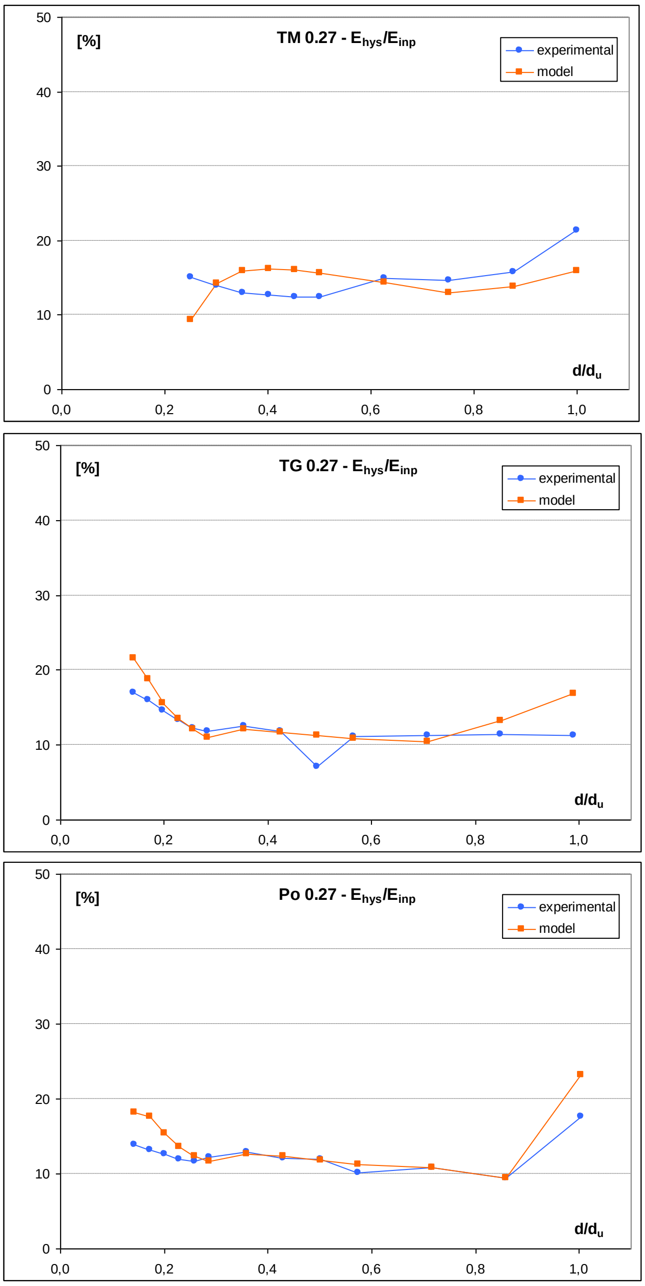

Fig. 6.15. Ratio of dissipated/input energy: comparison between experimental and modeled values. TM (above), TG (middle)s Po (below) specimens under vertical compression load of 0.27% of their compressive strength.

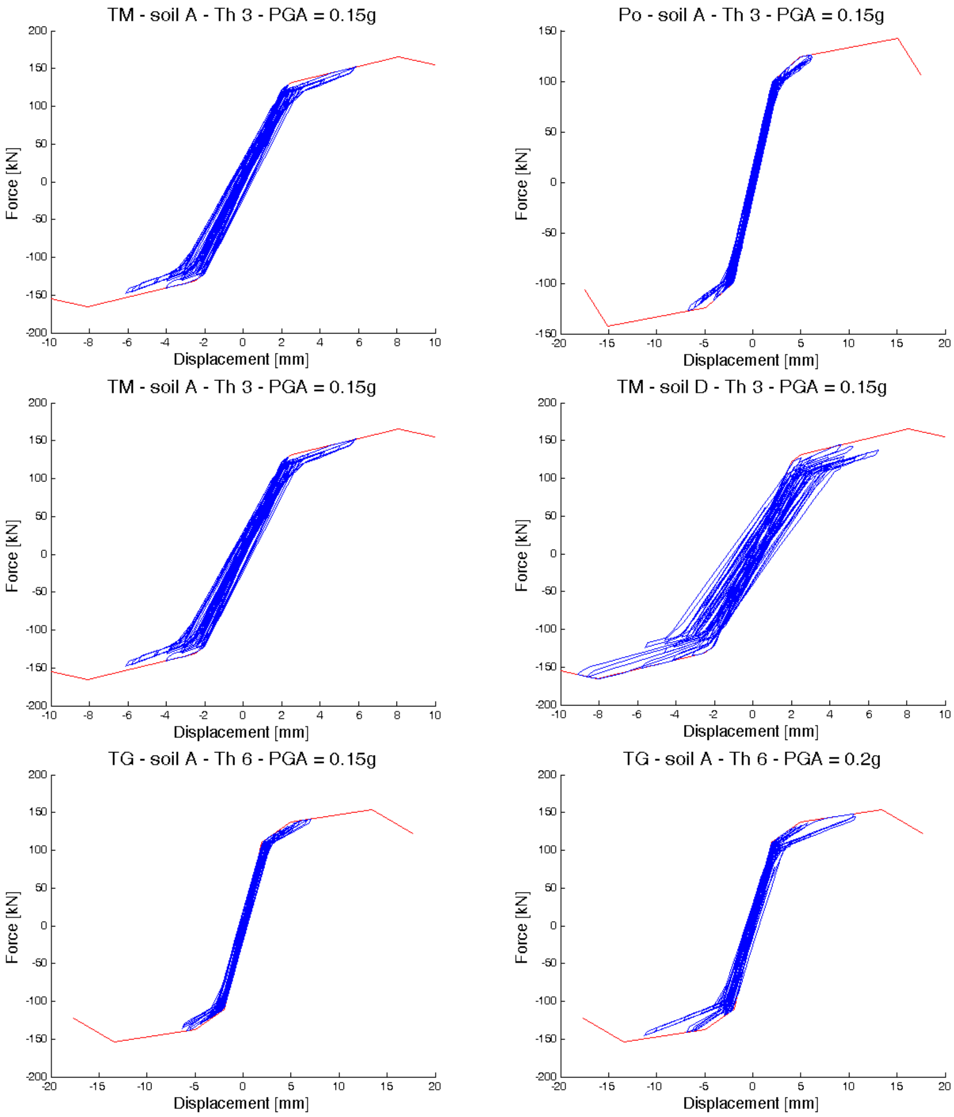

Fig. 6.16. Some example of model results given for different masonry type (above), different soil (middle) and different PGA (below).

7. DISPLACEMENT CONSIDERATIONS IN SEISMIC DESIGN OF MASONRY FOR SDOF STRUCTURES

7.1. Introduction and Performance-based Design Considerations

In last few years, has arose the possibility to being able to control the damage based on the probability of occurrence of an earthquake or base the design on different performance levels. The masonry still one of the widespread construction system for low-rise residential buildings even for countries prone to seismic risk, hence masonry needs to develop these design concepts.

Tailor seismic response to control risk requires a proper definition of performance indicators (they could be deformation limits, acceleration limits, etc.). Seismic codes usually are based on idea that controlling forces is the best way to control the damage induced by earthquake. However in the end of twentieth century (Moehle, 1992; Priestley, 1993) proposed the hypothesis that deformations is better than forces to control damage induced by earthquake. Hence, in the next years were developed design procedures based on that idea, the so called Displacement-Based Design (DBD) methods. For a wide summary on this argument can be seen the report of FIB Bulletin 25 ((editor) Calvi, 2003) and (Sullivan et al., 2003).

One of the most promising and developed DBD methods available in literature is the so called Direct Displacement-Based Design (DDBD) from (Priestley et al., 2007). Its main idea is to identify, at beginning of design process, the design displacement which can assure an acceptable damage for considered earthquake intensity. The method assumes that the design displacement can be found without to know the strength of structure. Another important concept of this procedure is the Substitute Structure given from (Gulkan & Sozen, 1974) and (Shibata & Sozen, 1976) which represent the non-linear behavior of complex structure with an equivalent Single Degree of Freedom (SDoF) structure that uses linear effective (secant) properties. In this way, when parameters of SDoF structures were defined, the design deformation limit and the equivalent damping of equivalent substitute structure can be calculated and the effective period (T_{eff}, related to base shear) obtained from them through displacement spectra.

An advantage of this method is that it permits to design a structure directly for different seismic risk levels. Knowledge of them was recently improved in term of displacement from (Cauzzi et al., 2008). Clearly, together with the design intensity level, another important aspect is the deformation limit considering not only the structural damage but also non-structural element limits. For some materials this deformation limits have only few references in literature. This can be imputed to design methods that usually gave more importance to forces than displacements.

DDBD method requires also a definition of an Equivalent Viscous Damping (EVD) which relates to dissipated energy during an earthquake and varies in relation to structural typology.

When were known both design displacement and EVD, the displacement spectrum is abated relating with equivalent damping, obtaining the T_{eff} of substitute structure. From the effective period it is easy to give the effective stiffness of the SDoF equivalent structure ($K_{eff} = 4 \cdot \pi^2 \cdot m_{eff} / T_{eff}^2$) and design base shear is finally obtained multiplying effective stiffness for design displacement. The use of effective stiffness permits that inelastic forces develop in relation to strength assigned at each structural element. This is another innovative aspect of DBD method.

In Italy, one topic (Linea 4) of the recent RELUIS project further developed DDBD method for different structural typologies involving many Italian Universities. The results were heterogeneous due to different available state-of-the-art, in fact DDBD was deeply developed for some structural typologies (e.g. reinforced concrete structures) whereas for others it was at first application (e.g. for masonry and retaining structures). The results are available in RELUIS project final report ((editors) Calvi & Sullivan, 2009).

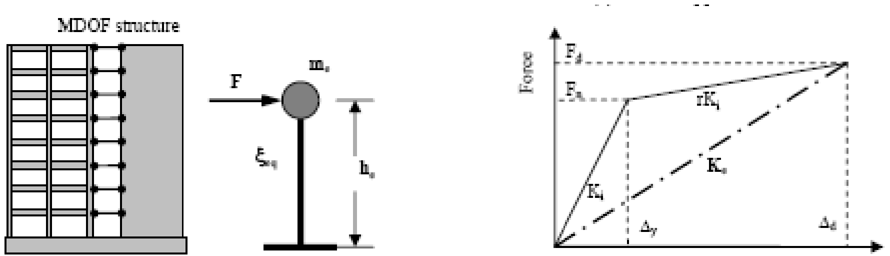

(a) SDOF Rappresentazione

(b) Effective Stiffness K_e

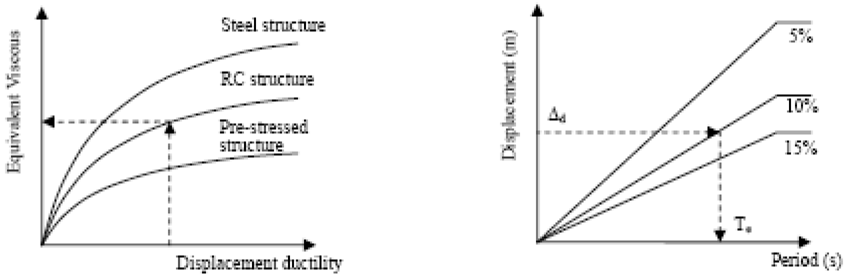

(c) Equivalent damping vs. ductility

(d) Design displacement spectra

Fig. 7.1. DDBD method from (Priestley et al., 2007)

In this field, the present work can be able to give some indications about displacements as performance indicators for masonry structures and furthermore complete the information for DDBD method with EVD curves.

7.2. Drift Limit Proposal

The proposed analytical model is able to interpret the performances of panels linking them with limit states resulting from integration of cross-section equilibrium equations (see chapter 5).

Analytical model results were here generalized proposing some design equations directly relating both geometrical and mechanical properties of URM panels to performance levels (Similar further developments are awaited for RM systems).

Different to what is present in RELUIS proposals, but according to experimental evidences and Italian building code (DM 14/01/2008, 2008) the present work defines four different limit states for masonry piers. Two of them are serviceability limit states and other two are ultimate limit states. They are respectively: guarantees to being operative immediately after the earthquake (the structure still substantially in the elastic range); damage control limit state (guarantees the structural resistance and controls damage on non-structural elements), life safety (guarantees structural strength and ductility) and collapse prevention (which is convenient only for the assessment of existing structures).

7.2.1. Further Parametrical Investigation for Unreinforced Masonry

Considering the parametrical analyses done for unreinforced masonry systems using the model developed in this thesis (explained in paragraphs 5.4.2 and 5.6.1) which changed the masonry unit strength, the three typologies of masonry showed a similar behavior and TG and Po masonry had the same compressive strength having the same strength of mortar and of unit (they were different only for different elastic modulus, E_m and elastic shear modulus, G in those parametrical analyses).

Furthermore is possible to represent these analyses of TG masonry in Fig. 7.2(a) which summarize the drift at different limit states in a compact form and Table 7.1 which represent, as example, the drift achieved by model at maximum horizontal strength of walls.

Especially in Table 7.1 can be seen that, despite the wide range of different configurations considered in these parametrical analyses, still some holes in the table. In order to describe better the drift relates to those parameters (f_m and σ_0) the holes must be filled.

Thus further parametrical analyses were done for the overall number of 32 combinations for TG masonry (16 from previous analyses). Then the corresponding Table 7.1 become Table 7.2 and Fig. 7.2(a) becomes Fig. 7.2(b)

TG	f_m [N/mm^2]			
σ_0 [N/mm^2]	1.37	2.74	4.12	5.49
0.23	0.116			
0.30	0.131			
0.47		0.184		
0.60		0.209		
0.70			0.241	
0.91			0.273	
0.93	0.077	0.256	0.277	0.292
1.21	0.016	0.269	0.315	0.331

Table 7.1. Drift at maximum strength for TG masonry. Parametrical analyses of chapter 5.

TG	f_m [N/mm^2]			
σ_0 [N/mm^2]	1.37	2.74	4.12	5.49
0.23	0.245	0.254	0.270	0.288
0.30	0.293	0.295	0.307	0.323
0.47	0.401	0.389	0.393	0.403
0.60	0.474	0.465	0.462	0.468
0.70	0.512	0.517	0.510	0.512
0.91	0.522	0.621	0.609	0.605
0.93	0.514	0.636	0.622	0.617
1.21	0.230	0.753	0.750	0.738

Table 7.2. Drift at maximum strength for TG masonry. Parametrical analyses of chapter 5.

In this way was possible to improve the accuracy of fitting process in order to provide some formulae able to directly give the drift limit states without perform the whole model analysis, and of course, can make faster the design process.

Next to mechanical parameters, also the slenderness geometrical parameter (H/L) was investigated in previous paragraphs 5.4.2 and 5.6.1 (overall number of analyses 36). See Fig. 7.3 for a concise presentation of results consistent with Fig. 7.2. These analyses represent the results in terms of drift with variation of main factors that affect the behavior of unreinforced masonry systems under investigation.

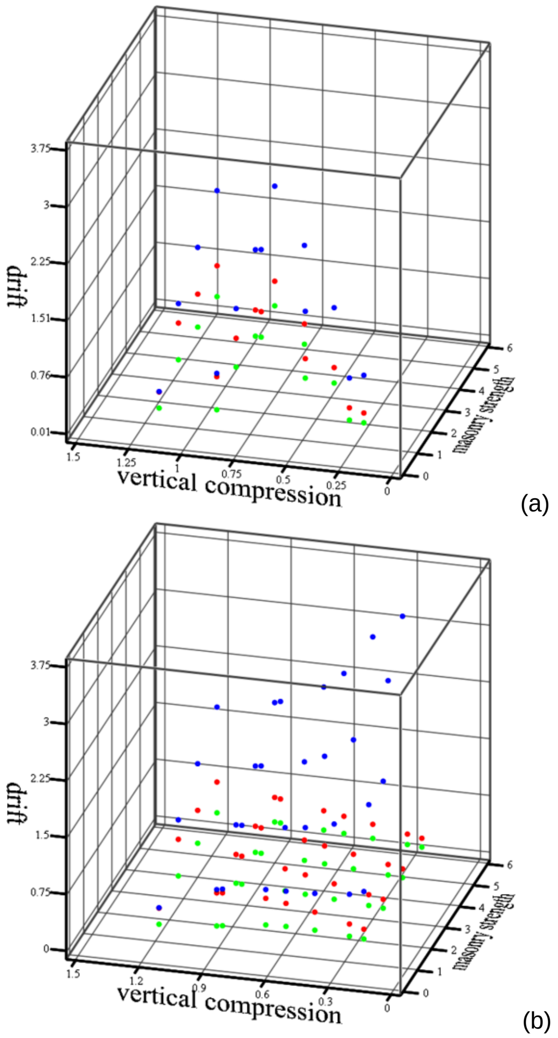

Fig. 7.2. Graphical view of different drift limit states for TG masonry. Analyses of chapter 5 (a), further analyses (b). Maximum drift (blue), drift at F_{max} (red) and critical drift (green).

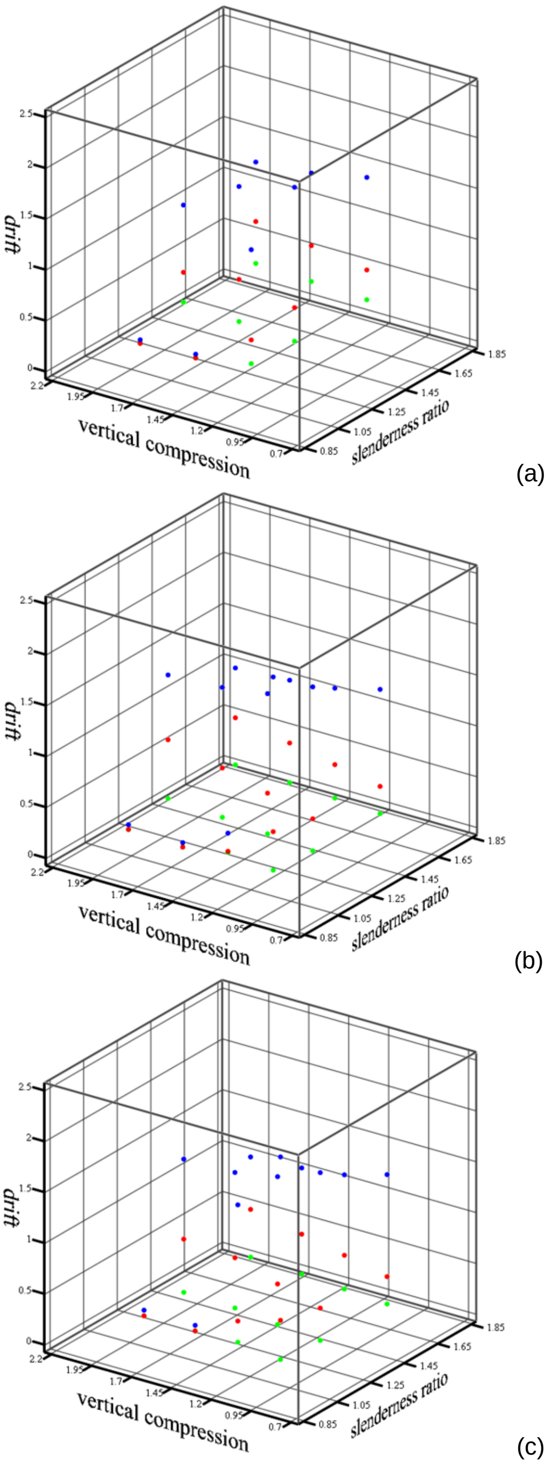

Fig. 7.3. Graphical view of different drift limit states for TM (a), TG (b) and Po (c) masonries. Slenderness analyses of Chap. 5. Max drift (blue), drift at F_{max} (red) and critical drift (green).

7.2.2. Some Drift Limit State Design Proposals for URM

From observation that loadbearing unreinforced masonry are not usually used for building with class of importance (or class of use) with high occupancy level, the limit states which govern the acceptable risk are the damage control and the life safety (and collapse limit states if consider also existing structures) according to (DM 14/01/2008, 2008). Therefore only these limit states were considered in the next.

Two main failure mechanisms influenced the experimental specimens and, thus were considered in the model: flexure and diagonal shear failure mechanism. These failure modes also influence the response in terms of drift as explained in paragraphs 5.4.2 and 5.6.1 showing different shape and slope in curves (e.g. Fig. 5.47). From this fact, it was chosen to subdivide the fitting process for walls showed flexure failure from walls showed a diagonal shear failure. The smaller resulting drift form these two relations will be the drift for the specific limit state.

In the light of experimental tests, FEM and analytical modeling results it was assumed that the response of unreinforced masonry walls, under combined vertical and horizontal in-plane forces, is characterized form three main parameters (as mentioned before) that are: masonry compressive strength, vertical compression stress (mechanical parameters) and the slenderness ratio (geometric parameter).

It has to be noted that all parametrical analyses given for TG masonry by changing masonry strength (on the basis of unit strength) and vertical compression load ratio had flexural failure. Whereas, the analyses done by changing slenderness ratio had flexural failure in 18 cases over the 32 combinations tested for the three masonry types. Furthermore, 7 walls in the group of walls that presented diagonal shear failure (14 walls) gave a very brittle response, in facts the maximum shear force was limited by reaching shear limit strength before masonry in compression reached the f_m limit (also at the base of wall).

The mechanical parameters were taken as independent for the reason that they present non-linear relation due to non-linear stress-strain constitutive law adopted and, in general, for the non-linearity of response. Hence, considering only their ratio cannot fully represent the wall response.

The fitting was performed with a trial and error process taking in to account not only the goodness of single limit state function, but the consistence with the others. For example, were constrained the curve of first limit state have a drift lesser than the drift at maximum strength limit state, which must be lower than maximum drift.

The fitting procedure in first few trials fixed all parameters except one in order to simplify the understanding of global shape of otherwise complex iper-surface (in facts the drift was considered dependent from three variables). Following, two parameters were released and one fixed in order to catch the cross-correlation between them (and in a broad sense the covariance).

The resulting formulae are reported in the following (Eq. 7.1) to (Eq. 7.5). Where ψ_{cr} is the critical drift and the ψ_{Fmax} and ψ_{dmax} are respectively the drift at maximum strength and at maximum displacement. The suffix “fl” means function refers to flexural failure, when suffix “sh” refers to diagonal shear failure relation.

Obviously the drift that has to be considered is the lesser between flexure failure and diagonal shear failure at corresponding limit state.

$$\psi_{cr} = \left[-0.8 \cdot \frac{{\sigma_0}^6}{{f_m}^4}\right] + \left[(0.16 \cdot \sigma_0) \cdot \left(\frac{1.2}{H/L}\right)^{1.2}\right] + \left[\left(0.07 \cdot {f_m}^{0.4}\right) \cdot \left(\frac{H/L}{1.2}\right)^{0.6}\right] \leq \psi_{Fmax\_sh}$$

(Eq. 7.1)

$$\psi_{Fmax\_fl} = \left[-0.6\frac{{\sigma_0}^6}{{f_m}^4}\right] + \left[(0.55 \cdot \sigma_0) \cdot \left(\frac{1}{H/L}\right)\right] + \left[0.17 \cdot {f_m}^{0.1}\right]$$

(Eq. 7.2)

$$\psi_{Fmax\_sh} = \left[0.82 \cdot \left(\frac{6.9}{f_m}\right)^{1.125} \cdot \left(\frac{\sigma_0}{f_m}\right) \cdot \left(\frac{H}{L}\right)\right] + \left[\left(\frac{4.4}{H/L}\right) \cdot \left(\frac{6.9}{f_m}\right) \cdot e^{-\left[\left(\frac{9.5}{H/L^{2.2}}\right) \cdot \left(\frac{f_m}{6.9}\right)^{1.5} \cdot \left(\frac{\sigma_0}{f_m}\right)\right]^{\left(\frac{2.1}{H/L}\right)}}\right]$$

(Eq. 7.3)

$$\psi_{dmax\_fl} = \left[1 + 0.13 \cdot \left(\frac{f_m}{\sigma_0}\right)^{1.5}\right] \cdot \left[\left(-0.5 \cdot \frac{{\sigma_0}^6}{{f_m}^4}\right) + (0.5 \cdot \sigma_0) \cdot \left(\frac{1}{H/L}\right) + \left(0.17 \cdot {f_m}^{0.1}\right)\right]$$

(Eq. 7.4)

$$\psi_{dmax\_sh} = \left[0.92 \cdot \left(\frac{6.9}{f_m}\right)^{1.125} \cdot \left(\frac{\sigma_0}{f_m}\right) \cdot \left(\frac{H}{L}\right)\right] + \left[\left(\frac{5.9}{H/L}\right) \cdot \left(\frac{6.9}{f_m}\right) \cdot e^{-\left[\left(\frac{6.75}{H/L^{2.2}}\right) \cdot \left(\frac{f_m}{6.9}\right)^{1.5} \cdot \left(\frac{\sigma_0}{f_m}\right)\right]^{\left(\frac{4.4}{H/L}\right)}}\right]$$

(Eq. 7.5)

Taking the previous representation from Fig. 7.2(b) and Fig. 7.3 is possible to give a concise representation of results provided by (Eq. 7.1) to (Eq. 7.5) simply adding surfaces generated by change of two parameters over the three considered.

In Fig. 7.4 it can be seen the approximation provide by the proposed equations when was fixed the slenderness ratio (was used the experimental H/L ratio) and varied the two main mechanical parameters considered in the case of TG unreinforced masonry.

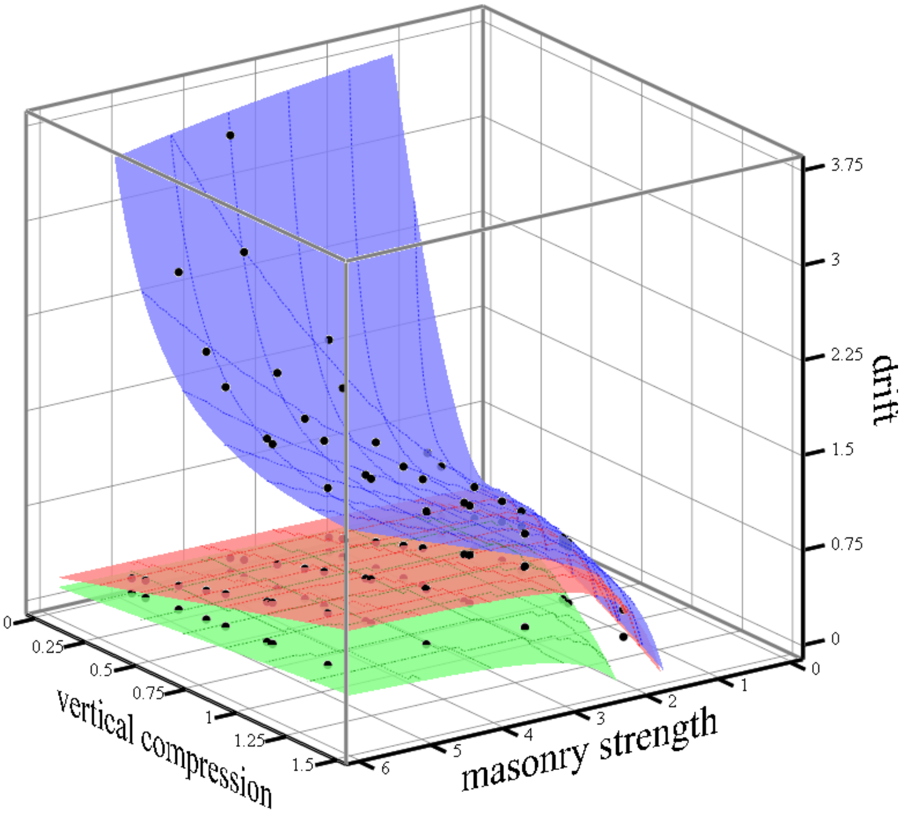

Fig. 7.4. Graphical view of different drift limit states (black dots) for mechanical parameters variation (TG masonry). Surfaces deriving from (Eq. 7.1) to (Eq. 7.5): maximum drift (blue), drift at F_{max} (red) and critical drift (green).

The complex shapes well represent the trends of analyses results. It easy to observe that masonry with low compressive strength have low displacement capacity and in particular very low or negligible post-peak ductility (ψ_{dmax}/ψ_{Fmax}) when vertical load increase. Vice versa, for masonry with good compressive strength the ratio ψ_{dmax}/ψ_{Fmax} increases. In particular, it can be seen that low level of vertical stress induces high ultimate drift capacity, but also that ductility concentrates in the post-peak branch with a low ratio between drift at maximum wall strength and critical drift (ψ_{Fmax}/ψ_{cr}).

Fig. 7.5, Fig. 7.6 and Fig. 7.7 represent the curves generate by the proposed functions fixing the masonry compressive strength respectively to the value valid for TM, TG and Po masonry. In these graphs the parametrical results are presented with black dots and the different limit state curves using different colors.

In these analyses model gave also diagonal shear failure and the equations proposed are substantially able to catch not only when shear failure arises but also give an estimation of the wall drift capacity in these cases.

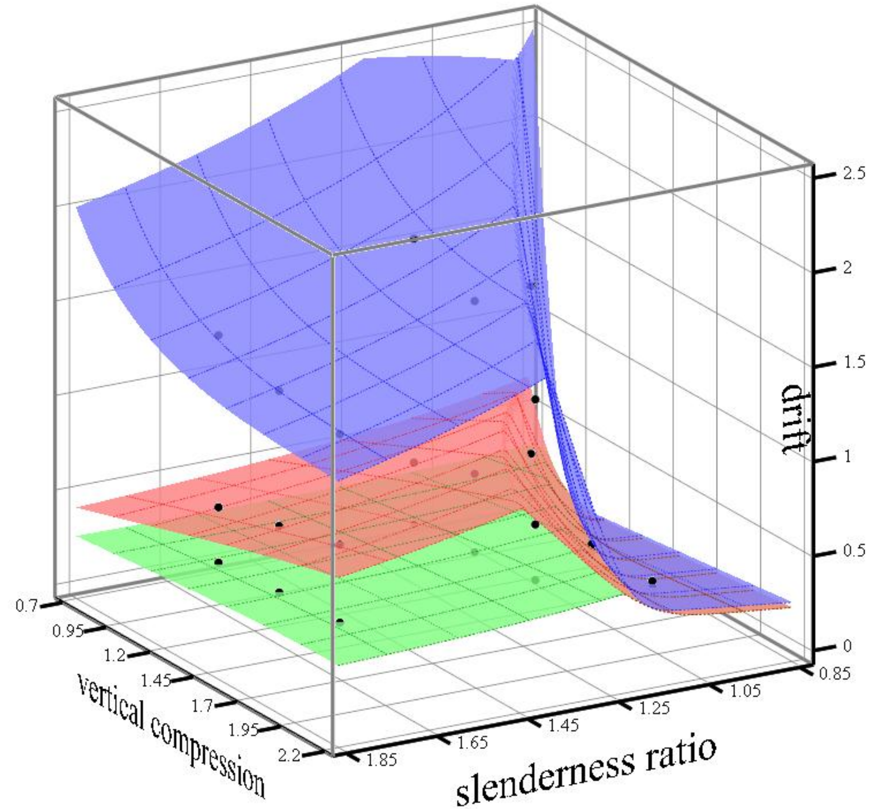

Fig. 7.5. Graphical view of different drift limit states (black dots) for slenderness variation (TM masonry). Surfaces deriving from (Eq. 7.1) to (Eq. 7.5):
maximum drift (blue), drift at F_{max} (red) and critical drift (green).

The fitting process leaded to good approximation for ψ_{Fmax} and ψ_{cr} curves, but for ψ_{dmax} the masonry TM (it has the higher compressive strength) the proposed equations lead to an overestimation of this drift capacity, when TG and Po showed only a slightly underestimation of ψ_{dmax}.

Also here in general, the effect of low vertical load is concentrate the ductility capacity in post-peak phase, lowering ψ_{Fmax}/ψ_{cr} ratio and increasing ψ_{dmax}/ψ_{Fmax}.

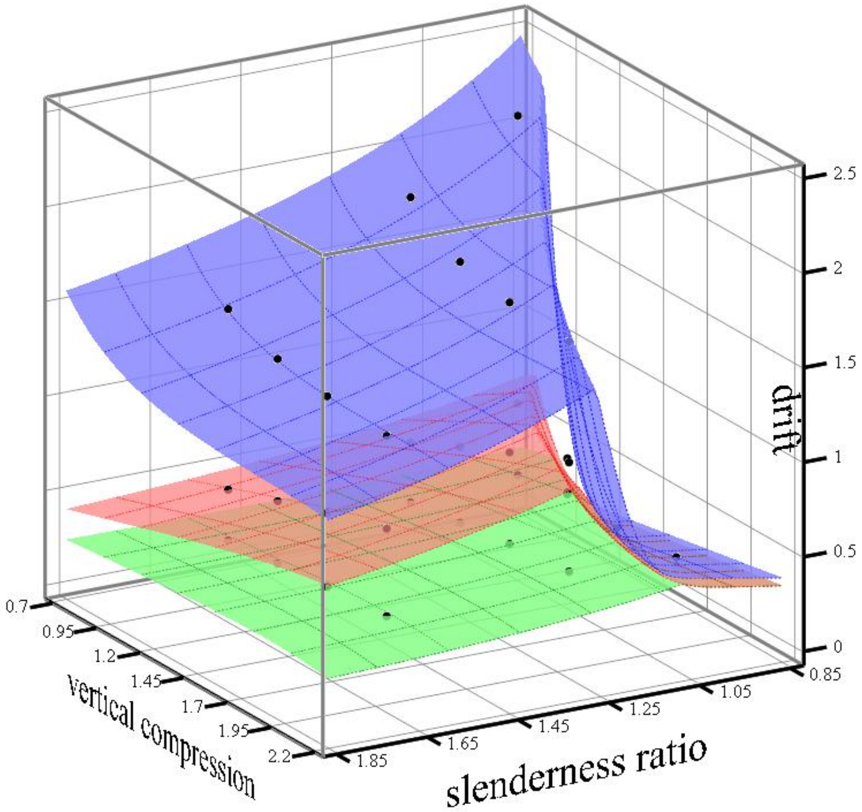

Fig. 7.6. Graphical view of different drift limit states (black dots) for slenderness variation (TG masonry). Surfaces deriving from (Eq. 7.1) to (Eq. 7.5):
maximum drift (blue), drift at F_{max} (red) and critical drift (green).

Shear failure affects the wall response lowering drift capacities and ductility ratios and this occurs more when vertical load tends to increase.

Whereas increasing the slenderness ratio leads to lower ductility ratios, in particular when low vertical stress was applied. This last statement still valid until diagonal shear failure occurs, in this case a decrease in slenderness ratio leads very quickly to a coarse displacement capacity and ductility ratios. Finally very brittle diagonal shear failures can be distinguished in the graphs when green curve encounter the red curve, or in other words when ψ_{Fmax} was fixed as equal to ψ_{cr} because walls failed in shear before stress concentration at compressed to of walls reached f_m.

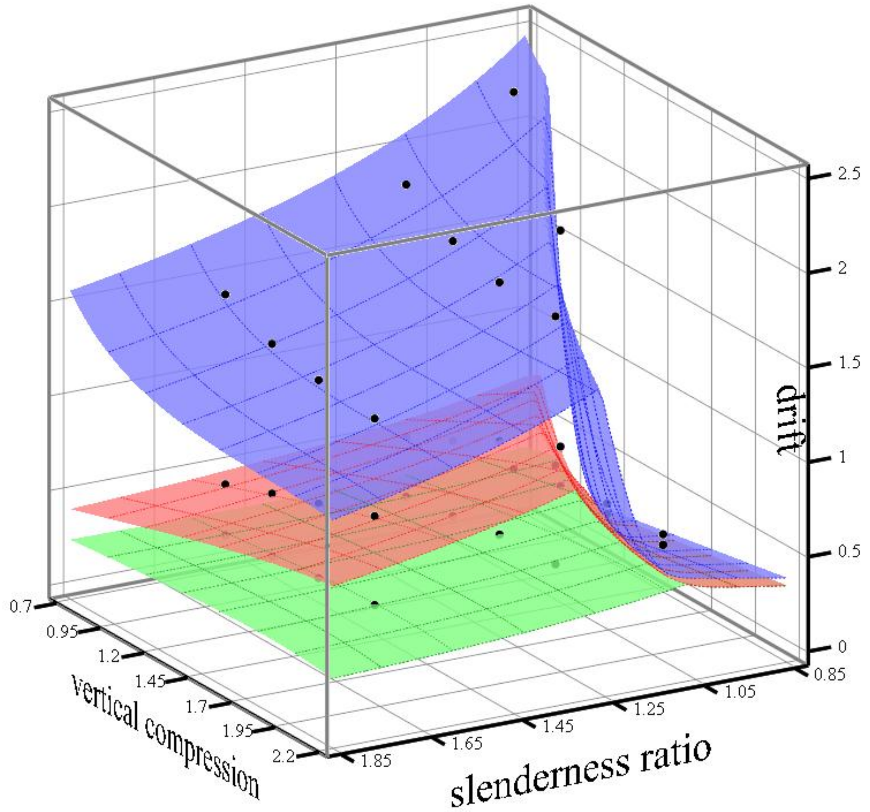

Fig. 7.7. Graphical view of different drift limit states (black dots) for slenderness variation (Po masonry). Surfaces deriving from (Eq. 7.1) to (Eq. 7.5):
maximum drift (blue), drift at F_{max} (red) and critical drift (green).

7.2.3. Error Estimation for Drift Formulae Proposed

In order to provide an estimation of errors introduced by this further simplification step, were calculated some statistical parameters, such as the Pearson product-moment correlation coefficient (denoted by R), the standard deviation (usually denoted by σ, but to avoid confusion, here denoted by SD) and finally the relative standard deviation (RSD).

It was assumed that analytical model data as true and they were confronted with corresponding values obtained by proposed equations (i.e. when obtained with the same f_m, σ_0 and H/L were used). The Pearson correlation coefficient indicates the strength of a linear relationship between two variables (Eq. 7.6). The covariance (COV) is calculated with (Eq. 7.7).

$$R(X,Y) = \frac{COV(X,Y)}{SD(X) \cdot SD(Y)} \qquad \text{(Eq. 7.6)}$$

$$COV(X,Y) = \frac{1}{N \cdot M} \cdot \sum_{j=1}^{M} \sum_{i=1}^{N} \left[\left(X_{i,j} - mean(X) \right) \cdot \left(Y_{i,j} - mean(Y) \right)^{T} \right] \quad \text{(Eq. 7.7)}$$

R can vary between -1 and +1 and a value of 1 implies that a linear equation describes the relationship between X and Y perfectly, with all data points lying on a line for which Y increases as X increases. Anyhow, R value generally does not completely characterize their relationship (Anscombe, 1973; Wilcox, 2005).

Therefore, the information was completed by the use of SD and RSD (which is SD divided by mean) that can better represent together with R, not only the linear relationship between drift derived from model and from equation, but also a gauge of their dispersion. It worth to point out that, in this case, the SD was not calculated using residual from difference between equation result and the mean of series results, but from difference between equation result and the corresponding (i.e. calculated using the same parameters) result of analytical model. In this way were constructed the graphs presented on left side of figures from Fig. 7.8 to Fig. 7.11.

Table 7.3 present the values of Pearson correlation coefficient for each drift limit state (in the rows) and for different parametrical analyses that were taken in to account and summarized in previous figures and tables (in the columns). It was added also the averaged values of R both for drift limit state and for analysis. The global average Pearson correlation is 0.969 that is a very high value even though in one case this correlation had the lower value of 0.759. This is due to two analyses were the equations provided a underestimation of critical drift for masonry Po with a slenderness ratio and vertical compression stress induced a fragile failure (see Fig. 7.7 and Fig. 7.11c). In the Table 7.4 can be seen the results of the comparison in terms of standard deviation (with the dimension of drift). Also in this case the critical drift of masonry Po showed higher value respect others. It can be noted that in this case averaging the SD value between different limit states does not have sense because they refers to different mean drift. On contrary, these comparison can be done using RSD values provided in Table 7.5 (with are dimensionless and expressed in percentage), because in this case the SD were “weighed” using the mean value. Anyway, the RSD showed a tendency to increase with the increase of drift in absolute magnitude. This is partially due to the facts that mean values are not fully representative of drift limit states (otherwise this design proposal equations would been meaningless).

From Fig. 7.8 to Fig. 7.11 are presented the graphical views of differences between model and equations results (left) and the corresponding distribution of deviations from model results (right) at different limit states. In other words with the continuous blue lines are showed the model drift both in horizontal and vertical axis, and with red crosses the results of equations proposed (gray lines represent the shift due to SD).

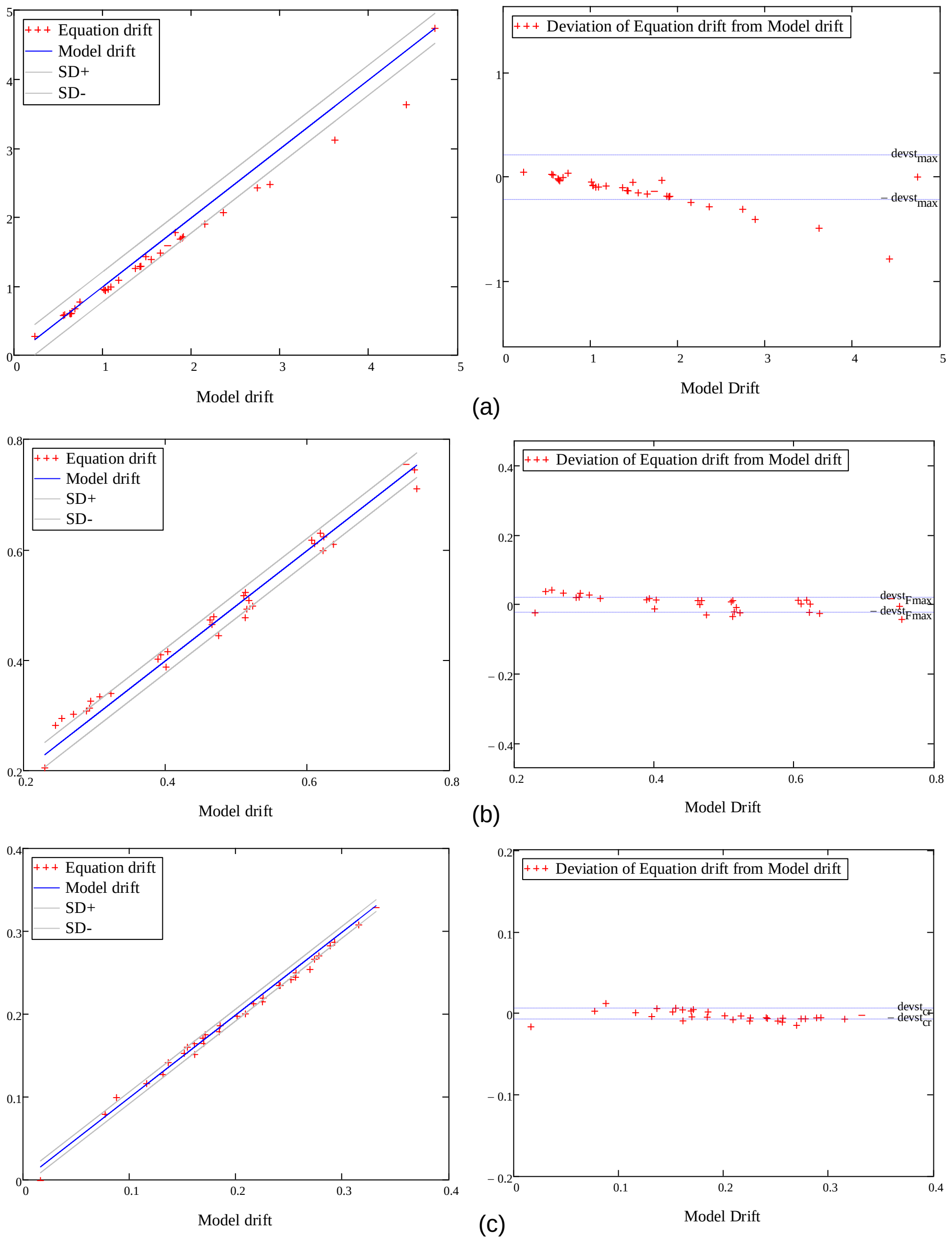

Fig. 7.8. Mechanical parameters variation (TG masonry). Graphical view of differences between model and equations results (left) and the corresponding distribution of deviations from model results (right). At maximum drift (a), drift at F_{max} (b) and critical drift (c).

In Fig. 7.8 can be noted a trend in the residuals, anyhow the equation tend to be conservative and provide a lower value of drift that with this analyses were fairly high.

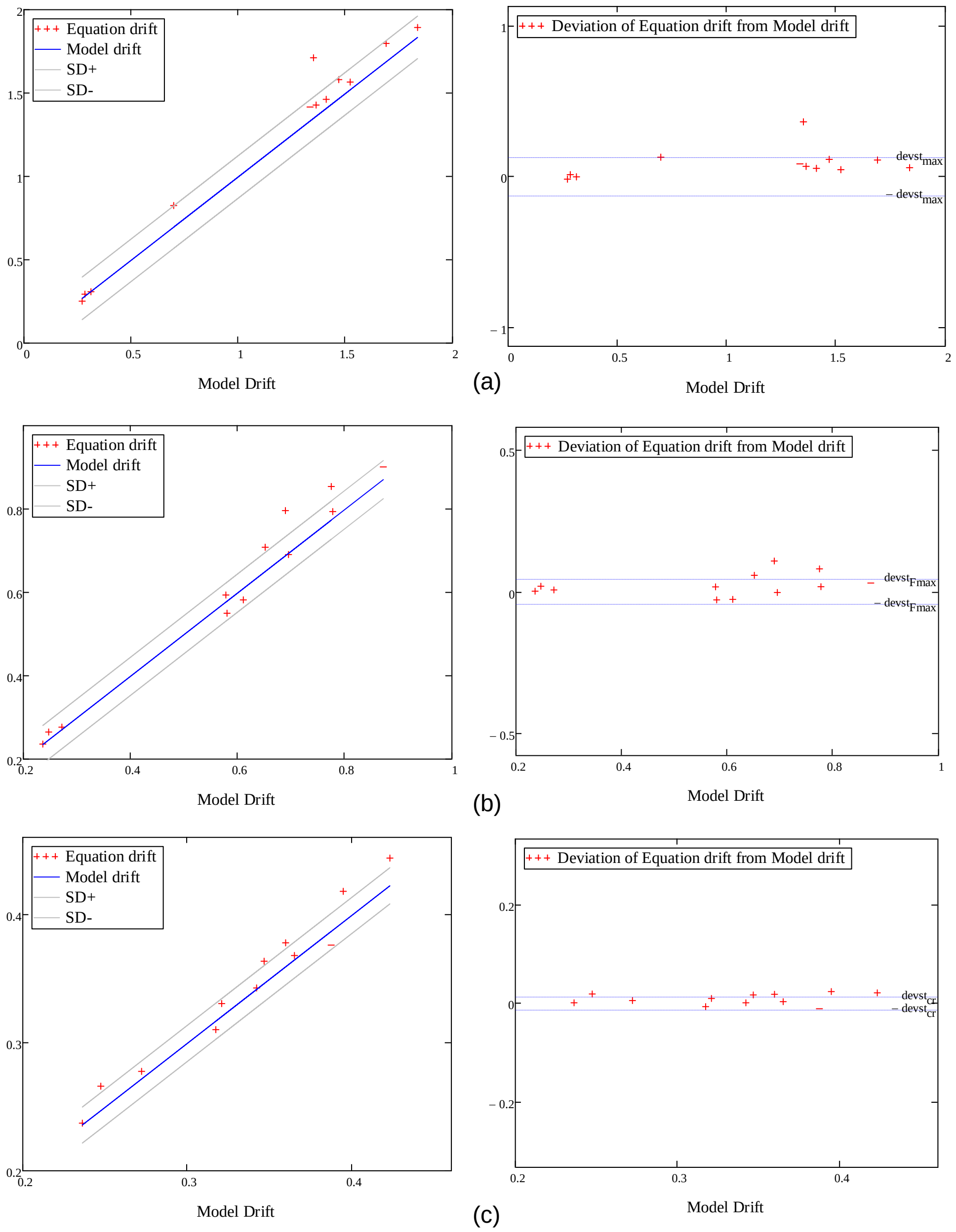

(a)

(b)

(c)

Fig. 7.9. Slenderness variation (TM masonry). Graphical view of differences between model and equations results (left) and the corresponding distribution of deviations from model results (right). At maximum drift (a), drift at F_{max} (b) and critical drift (c).

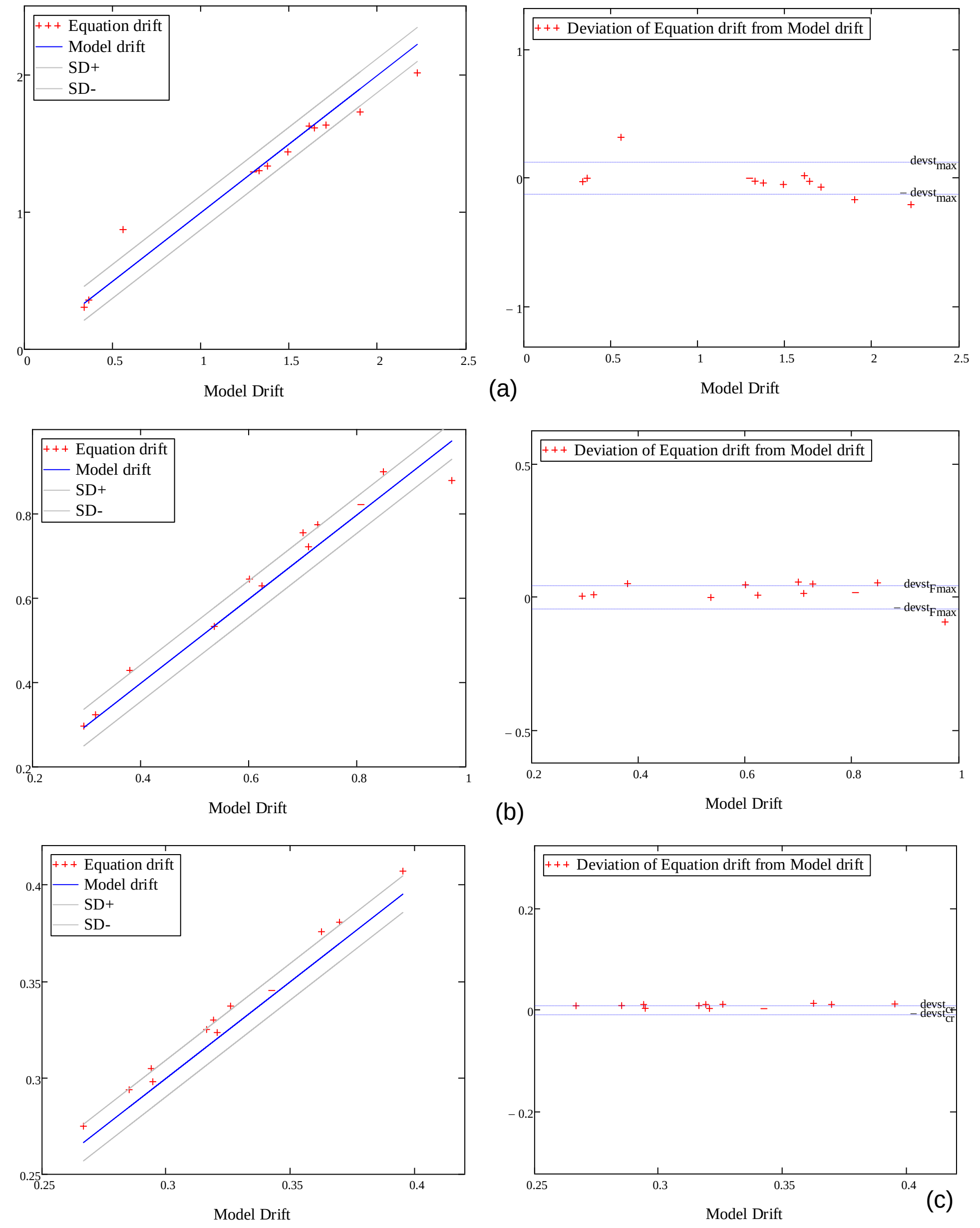

Fig. 7.10. Slenderness variation (TG masonry). Graphical view of differences between model and equations results (left) and the corresponding distribution of deviations from model results (right). At maximum drift (a), drift at F_{max} (b) and critical drift (c).

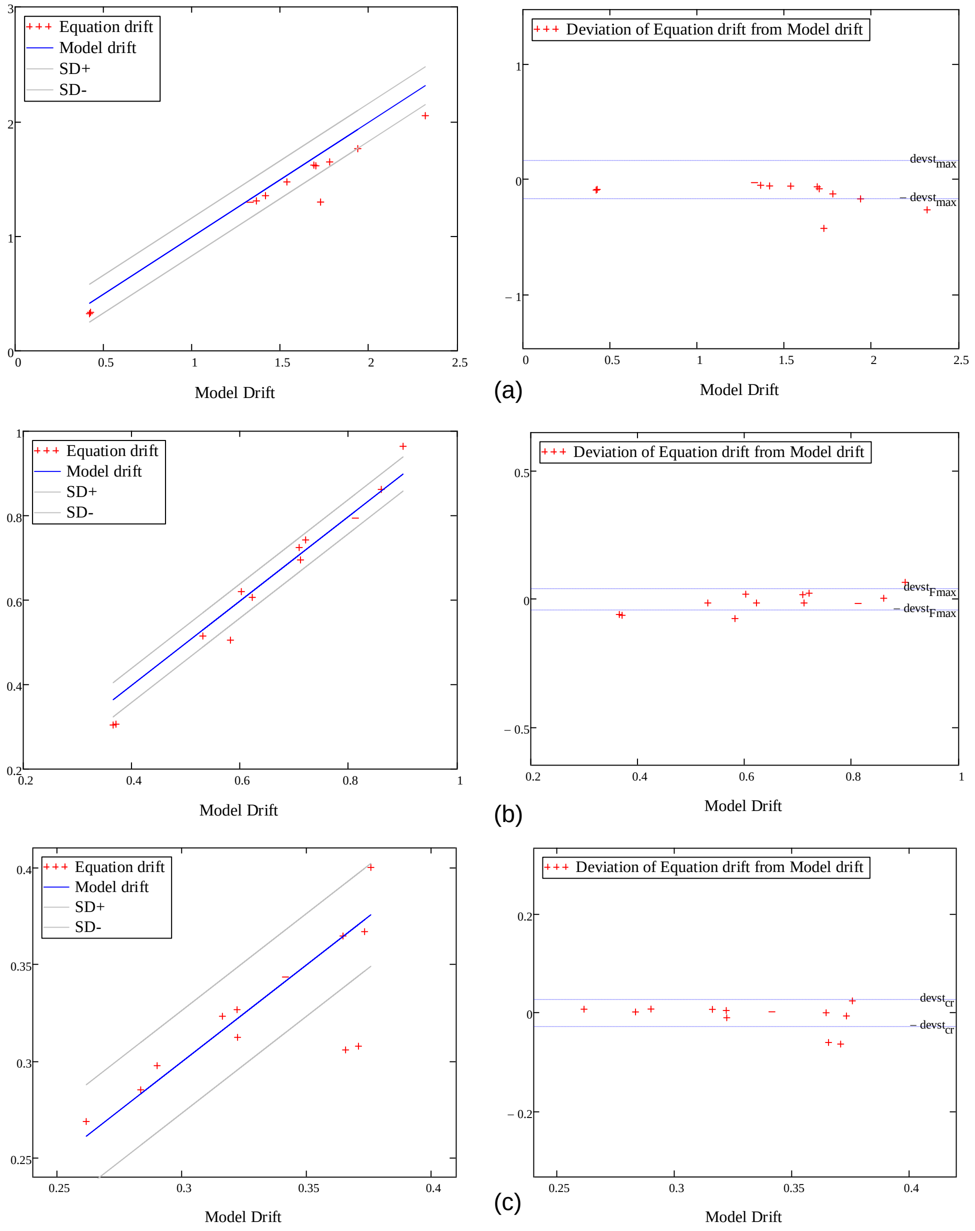

Fig. 7.11. Slenderness variation (Po masonry). Graphical view of differences between model and equations results (left) and the corresponding distribution of deviations from model results (right). At maximum drift (a), drift at F_{max} (b) and critical drift (c).

R [-]	f_m-σ_0 (TG)	H/L-σ_0 (TM)	H/L-σ_0 (TG)	H/L-σ_0 (Po)	*mean*
ψ_{cr}	0.997	0.983	0.996	0.759	*0.934*
Ψ_{Fmax}	0.991	0.986	0.981	0.991	*0.987*
ψ_{max}	0.993	0.989	0.983	0.980	*0.986*
mean	*0.994*	*0.986*	*0.987*	*0.910*	*0,969*

Table 7.3. Summary of R. Columns refer to analyses type, rows refer to different limit states.

SD [%]	f_m-σ_0 (TG)	H/L-σ_0 (TM)	H/L-σ_0 (TG)	H/L-σ_0 (Po)	*mean*
ψ_{cr}	0.007	0.014	0.009	0.026	*0.014*
Ψ_{Fmax}	0.022	0.046	0.043	0.040	*0.038*
ψ_{max}	0.218	0.127	0.123	0.165	*0.158*

Table 7.4. Summary of SD. Columns refer to analyses type, rows refer to different limit states.

RSD [%]	f_m-σ_0 (TG)	H/L-σ_0 (TM)	H/L-σ_0 (TG)	H/L-σ_0 (Po)	*mean*
ψ_{cr}	3.5	4.2	2.9	8.0	*4.7*
Ψ_{Fmax}	4.7	7.9	6.9	6.2	*6.4*
ψ_{max}	13.4	11.3	9.4	11.2	*11.3*
mean	*7.2*	*7.3*	*6.4*	*8.5*	*7.5*

Table 7.5. Summary of RSD. Columns refer to analyses type, rows refer to different limit states.

7.3. Equivalent Viscous Damping

7.3.1. A Procedure to Find Hysteretic Damping of the Equivalent Elastic Substitute Structure

Hysteretic model and analyses described in previous Chapter 6 allow to build relation curves between ductility and Equivalent Viscous Damping (EVD) which are useful in DDBD design process when the displacement elastic spectrum needs to be scaled in agreement to EVD showed by the structure at the performance chosen when defining the design displacement (Priestley et al., 2007).

In the algorithm defined with this purpose, can be distinguished two phases. In the first nonlinear time history (NLTH) analyses are carried out using hysteretic model described in previous chapter; in the second phase, through an equivalent elastic system (substitute structure) can be defined the EVD. The latter is obtained by imposing the equality, in displacement, between response of NLTH analysis and the linear elastic equivalent system.

For each time history considered the procedure the following steps:

1. Definition of target displacements.

   Hysteretic model considers the system response as elastic until the achievement of first limit state. Hence, target displacements are placed from first limit state until the ultimate displacement capacity. n equal-spaced points subdivide the non-linear part of envelope curve (it was chosen n = 7).

2. Research of PGA multiplier factor.

   For each target displacement it carries out NLTH analyses using the 10 synthetic accelerograms utilizing an elastic damping close to zero. These analyses are repeated scaling the TH using a multiplier factor of PGA until the maximum displacement achieved by NLTH is equal to target displacement with a specified tolerance. It is a iterative procedure and at each iteration the PGA is updated from previous one taking in to account the difference between the actual maximum displacement found and the target.
3. Determination of secant stiffness and effective period.

   When target displacement achieved is knows the multiplier factor of PGA to achieve it. Thus can be calculated the corresponding secant stiffness which is found relating point on envelope curve at target displacement. Knowing the secant stiffness it is easy to obtain the effective period ($T_{eff} = 2 \cdot \pi \cdot \sqrt[2]{m_{eff}/K_{eff}}$).
4. Definition of equivalent linear elastic system

   The linear elastic equivalent system is defined through effective period (or the corresponding secant stiffness) given from previous step and from hysteretic dumping equal to elastic damping used in point 2. On this system is carried out a TH scaled using PGA in point 2. Maximum displacement obtained from this analysis represents the linear response of equivalent system for the considered hysteretic damping.
5. Research of equivalent hysteretic damping

   Equivalent hysteretic damping means the value of damping which is able to make equal the displacement of linear elastic system to target displacement. Hence, for each iteration, linear elastic analysis is repeated varying the damping value, starting from previous one and taking in to account the difference between obtained displacement and the target displacement.

Elastic damping coefficient used in point 2 of procedure is close to zero because the aim is find the damping component due to hysteretic dissipation. To avoid numerical problems the starting value of elastic damping was set at very low value, but not zero. It was chosen a conventional value of 0.5% (one tenth of usual elastic damping component). The tolerance imposed in NLTH analyses to find the PGA was set to 2% of target displacement, while for linear elastic analyses was set to 1%.

7.3.2. Discussion of Results on Experimental Walls

The procedure explained in previous paragraph was repeated for each tested specimen (8 for RM system and 3 for URM system), for each target displacement (7), for the 10 synthetic accelerograms, for the 2 groups of soils, giving a total number of 1540 NLTH analyses as many linear elastic analyses.

In the figures Fig. 7.12 and Fig. 7.13 are presented the results for reinforced masonry system of this procedure divided for soil type. Each line in figures represents one experimental wall. Each one of seven dots composing the line is the mean value of 10 NLTH plus 10 equivalent linear analyses at corresponding target displacement. The ductility is defined respect to second limit (2nd LS) state consistent with experimental results and previous analysis approaches used. Hence, the first limit state (1st LS), fixed when masonry wall lives the elastic range, has ductility less than one. Therefore hysteretic model start to open cycles from 1st thus hysteretic damping start to increase from this limit state.

In Fig. 7.12 are presented the results in terms of equivalent hysteretic damping versus drift. It can be seen that obviously the damping is almost zero at elastic limit (not zero because elastic component was set to 0.5%) and, in general, the damping shows a logarithmic trend with the increasing of target displacement. In these curves walls characterized by shear failure (red and orange) at the same drift have a higher damping value respect the curves that represent the walls failed in flexure (blue and azure). When shear failure occurs, it can be noted also that for drift beyond drift of maximum strength (3rd LS) the damping shows a sudden change of trend. In facts beyond 3rd LS the damping increased a lot, even of 50%, going from values around 10% to value around 15%.

With reference to Fig. 7.13, that represent the damping respect to ductility variation, can be noted the curves with different failure tend to be superimposed. This fact is valid with reference to different failures and for both soil considered.

Furthermore, from results of equivalent elastic systems the effective periods (T_{eff}) of walls failed in shear gone about from 0.1 s for the first limit state (ductility less than one) to 0.35s for the ultimate displacement capacity. For walls showed a flexure behavior the previous range is about from 0.15 (1st LS) to 0.7 s (4th LS). Observing the spectra for soil type A and D from Eurocode 8 (given in Fig. 6.6) all walls still about on plateau of those spectra excluding the walls that fail in flexure and on soil type A (T_C = 0.4 s).

Therefore, this can be seen in the Fig. 7.13 because for soil A and flexure behavior (blue and azure lines) after a ductility of about 2 the damping tends to stabilize around the value of 12%. On contrary, for soil type D which have T_C = 0.8s can be noted trend that always increasing until average values of damping around 20%.

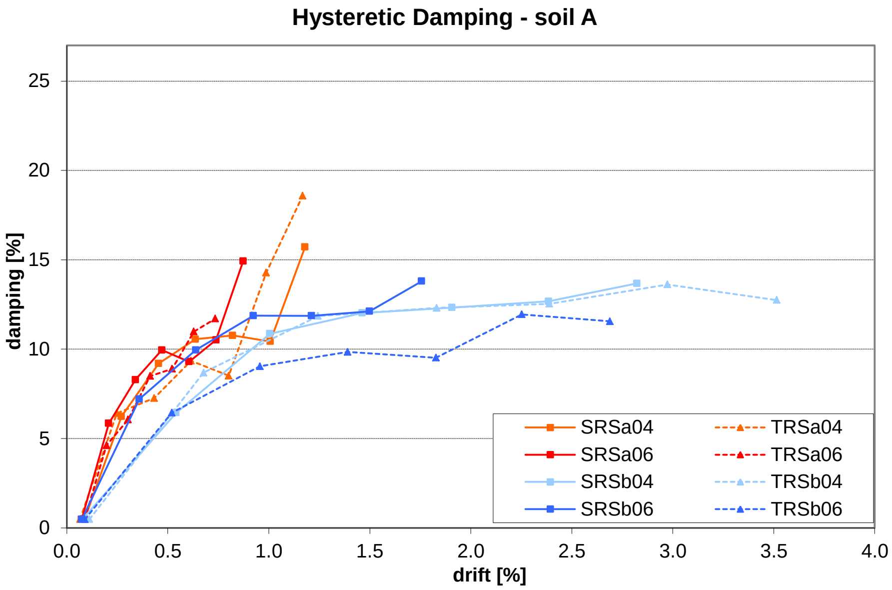

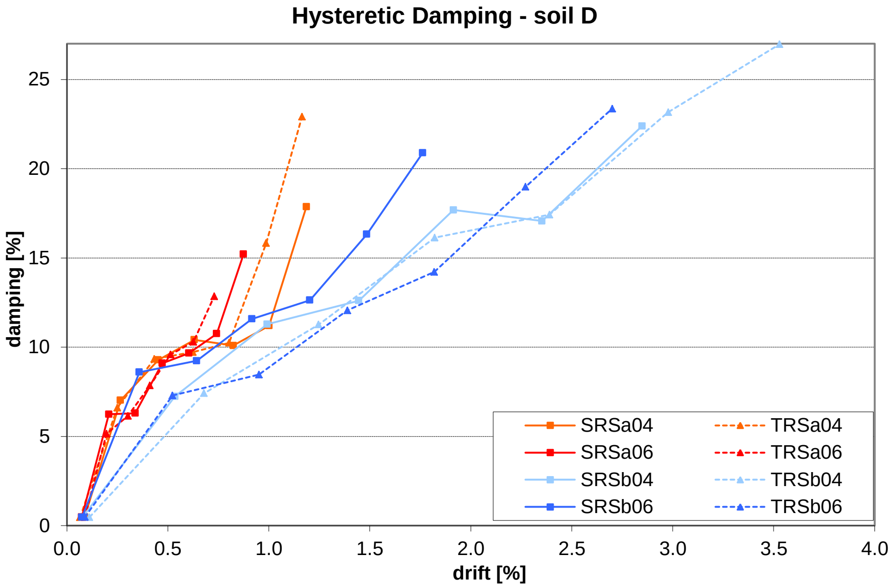

Fig. 7.12. Equivalent Hysteretic Damping versus Drift curves. Experimental RM walls under soil type A (above) type D (below).

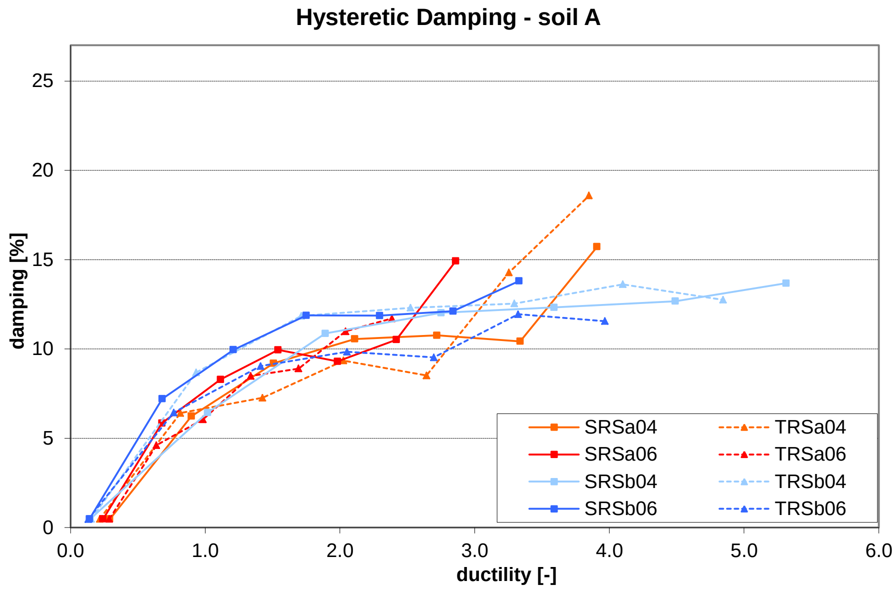

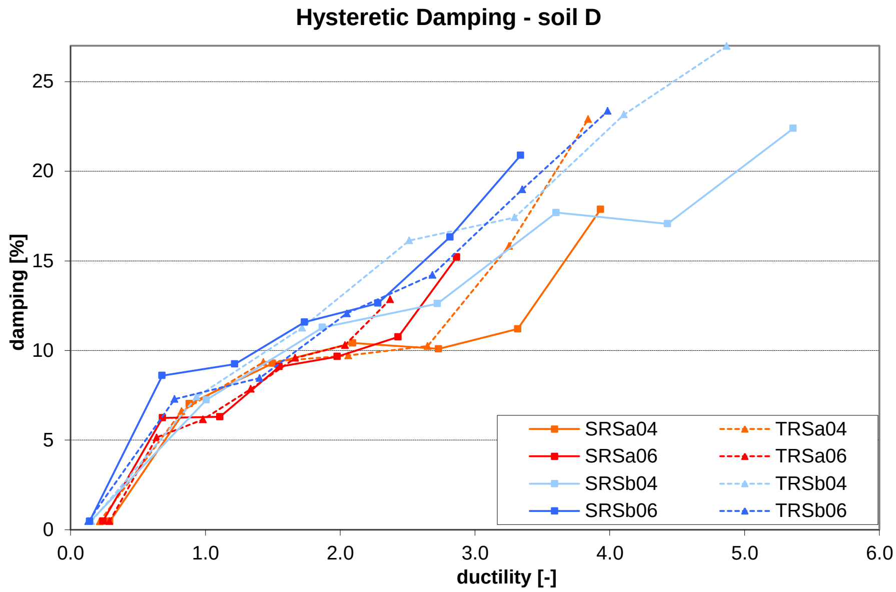

Fig. 7.13. Equivalent Hysteretic Damping versus Ductility curves. Experimental RM walls under soil type A (above) type D (below).

In Fig. 7.14 are presented the obtained results for URM masonry. It is easily to note that the obtained curves for Po and TG typologies results perfectly superimposed, for both soil typologies. It can be show a different trend in base of different soil, logarithmic trend for A soil and linear for D soil. Instead, TM typology gives an increasing trend for both type soils. Furthermore, at the same drift level, for this typology the damping is greater, with a mean difference on two soils of about 15%.

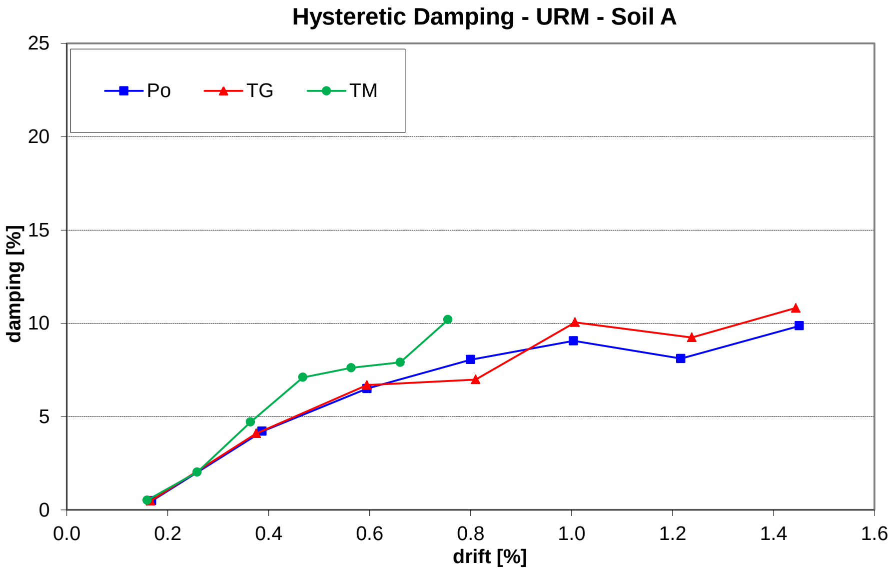

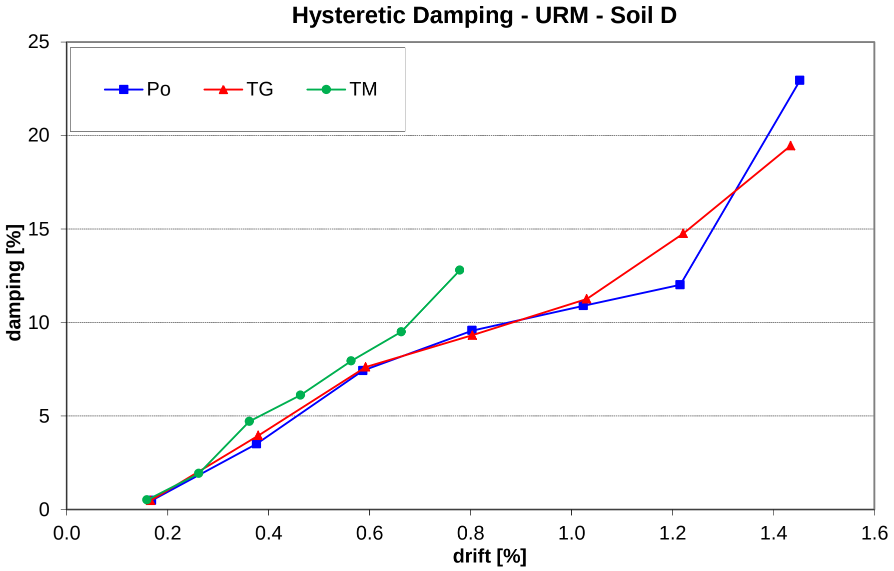

Fig. 7.14. Equivalent Hysteretic Damping versus Drift curves.
Experimental URM walls under soil type A (above) type D (below).

Observing the same results in function of ductility (see Fig. 7.15), there is again an optimum superimposition for Po and TG, whereas the curves obtained for TM, at the same ductility level, are smaller of about 50% for both soils. Furthermore, as the ultimate drift for TM are approximately an half of the ones obtained for the other two typologies (0.75% vs 1.5%), in terms of ductility it results similar ultimate capacity for all three typologies (3.5-4).

This phenomenon can be explained if considers that the displacement at 2nd LS, at which the ductility is referred to, is about of 5 mm for Po and TG and practically the half for TM. So, even if TM typology has a displacement capacity almost two times lower respect the others, it can reach a similar ultimate ductility.

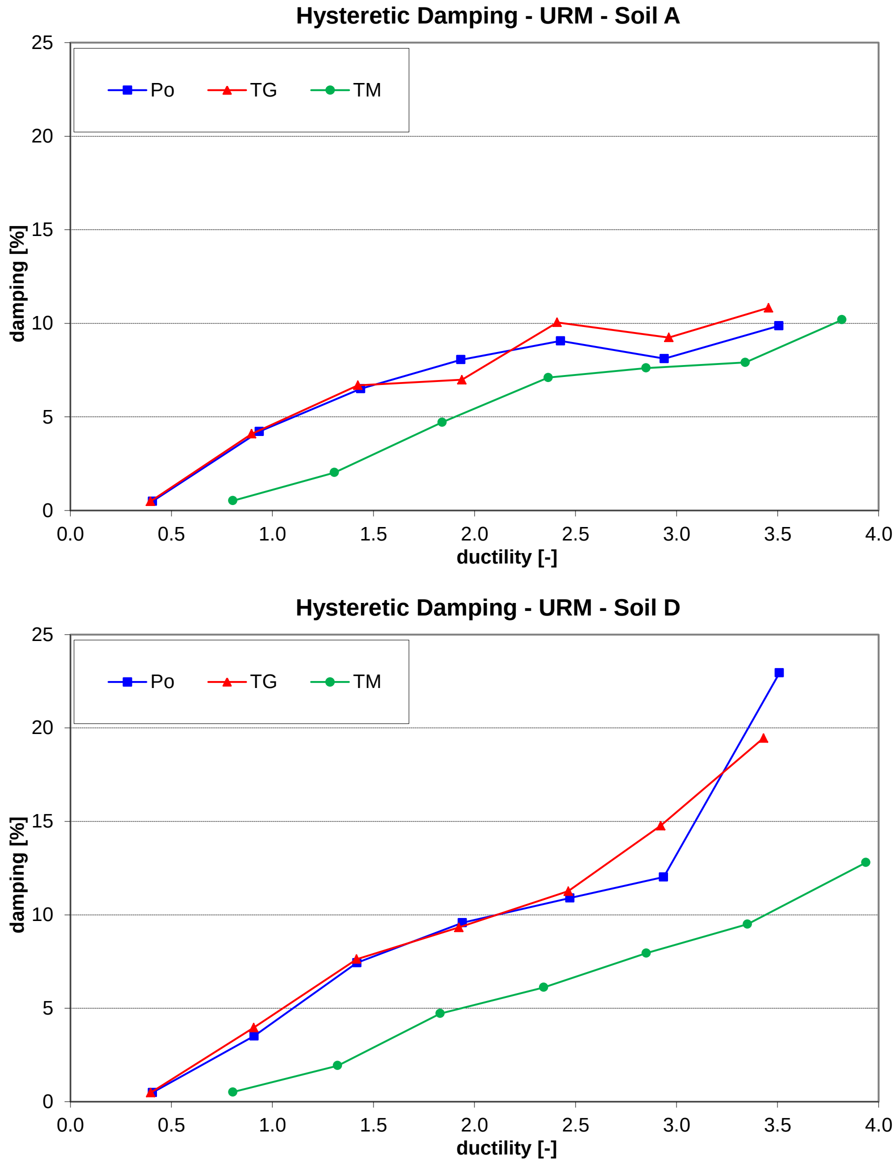

Fig. 7.15. Equivalent Hysteretic Damping versus Ductility curves. Experimental URM walls under soil type A (above) type D (below).

In reference to already done considerations for RM about variation of effective period, it is interesting to notice that the elastic period is about 0.2 s for all three typologies, whereas the one at ultimate LS is about 0.5 s for Po and TG and 0.4 s for TM. For the A soil, the first two typologies show a logarithmic trend that reach a plateau round a damping value of 9% beyond a ductility of about 2.5. For D soil the trend is linear until a value of 20%. The TM typology give linear trend for both soil and reach values of about 10% for A soil and 12 % for D soil.

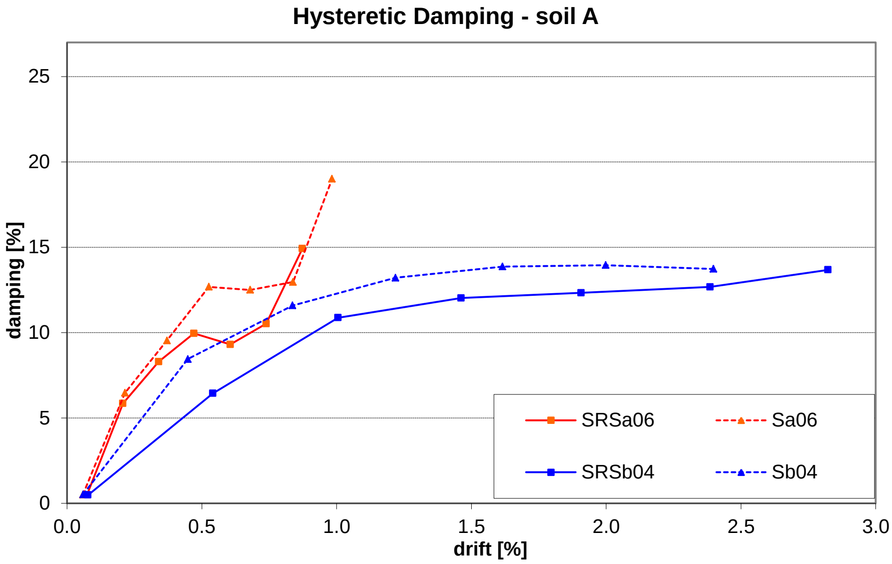

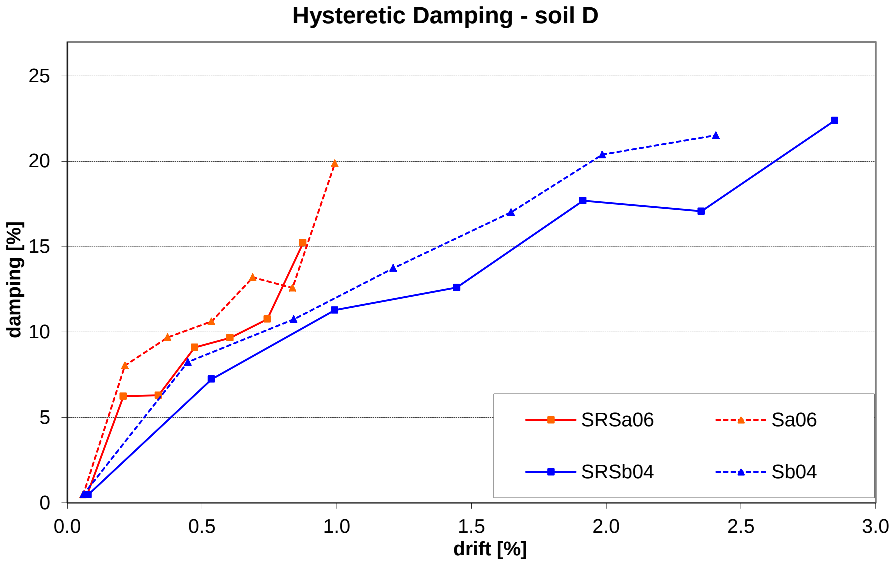

Fig. 7.16. Equivalent Hysteretic Damping versus Drift curves.RM walls under soil type A (above) type D (below). Experimental (continuous lines), analytical model (dash-dot lines).

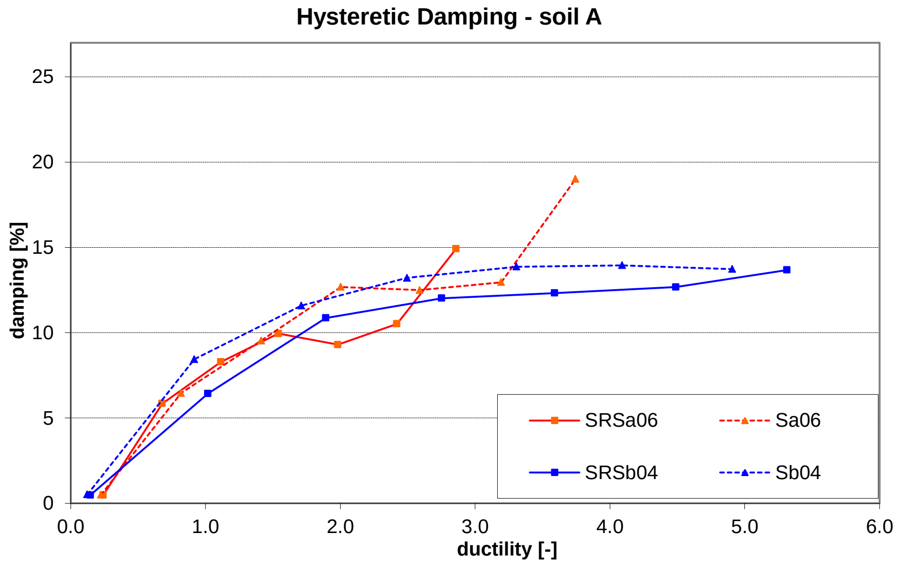

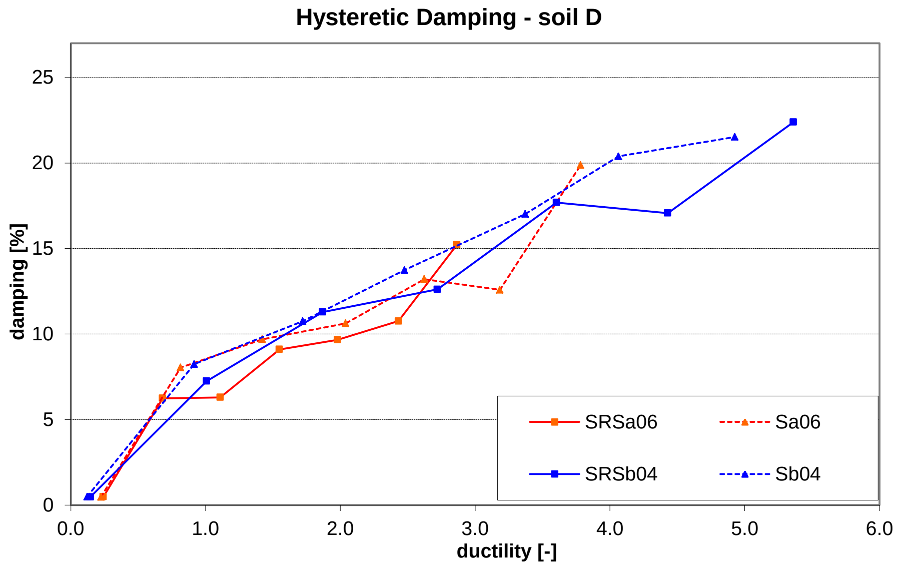

Fig. 7.17. Equivalent Hysteretic Damping versus Ductility curves.RM walls under soil type A (above) type D (below). Experimental (continuous lines), analytical model (dash-dot lines).

7.3.3. Extension of Results Using Analytical Model Envelopes

In order to test the capacity of analytical model (presented previous in Chapter 5) coupled with the hysteretic model to represent the non-linear dynamic in-plane behavior of masonry walls were carried out a series of analyses using the hysteretic model on the basis of four limit states provided by the developed analytical model.

This kind of correlation is a hard task because is done after a series of successive approximations made first from calibration of model which can represent the capacity curve and the limit state and after applying a hysteretic model and a series of dynamic random seismic excitations. These lead to a response which is sensitive to capacity of dissipate energy from hysteretic cycles and it is also sensitive to assignment of limit states.

Two walls that represent the extremes of behaviors showed during experimental tests of reinforced masonry system were taken in to account, namely the squat wall with higher vertical compression load and the slender wall with lower precompression. Those are respectively the red and blue continuous lines of Fig. 7.16 and Fig. 7.17. Instead, the dash dotted lines are the curves which refer to analytical model envelopes.

All the observation made before still valid here because globally the general form of the curves from analytical model show an almost perfect correlation with curves referring to experimental limit states and fully calibrated with hysteretic model used.

Conversely the curves from analytical model present in general a higher hysteretic damping and the relative errors with curves from experimental model can reach 20%, but in the most of cases range around 15%.

7.4. Conclusions

7.4.1. Drift Limit

In this chapter some formulations aimed to provide drifts for unreinforced masonry panels directly related with limit states model presented in chapter 5 were proposed. These formulations use simple geometrical and mechanical properties of URM panels to find drifts at different performance levels. They are able to catch both flexural and shear failure drift limits. Similar further developments are awaited for RM systems.

These formulations derive from an extrapolation process and were validated with specific experimental tests that cover a limited number (even though indicative) of new unreinforced masonry types and in with results of numerical models shown in chapter 5.

The proposed formulae have a complex form, however, they only depend on a limited number of engineering parameters (such as masonry compressive strength, vertical compression stress and wall slenderness). Therefore, although they need to be simplified in the light of practical use and further validated with other experimental tests, it appears that they follow the engineering criteria generally adopted in DDB design methods. They can be thus regarded as a first indication in the case of unreinforced masonry systems.

7.4.2. Equivalent Damping

In this chapter a procedure to evaluate the hysteretic component of Equivalent Viscous Damping (EVD), of both unreinforced and reinforced masonry walls, in relation to masonry drift and ductility is presented. The analyses were repeated for two extreme types of soils (A and D) of Eurocode 8. In addition, analyses aimed to compare the damping deduced form experimental limit states with that given from analytical model limit states were performed.

The results show a general logarithmic trend in drift-damping and ductility-damping curves, with a more linearized trend for walls having small displacement capacity.

The damping at ultimate displacement capacity ranges around 12%-15% for RM and around 10% for URM with soil A. While, damping reaches values around 20%, both RM and URM on soil D.

In the comparison of results given by analyses carried out on the basis of experimental and numerical envelopes, the latter tend to have a greater damping for both soils. The average error is around 15%, although the correlation between the two curves is very good (98%). This shows in one hand, the hysteretic model applied is robust, and on the other hand, adopting the numerical envelope curves obtained by means of the developed analytical model (chapter 5) leads to acceptable errors.

Finally, the results of the dynamic analyses shows that, in the case of RM walls, the ductility-damping curves of walls failed in shear and flexure can be almost superimposed, apart for the higher ductility values available only when flexural failure occurred.

8. CONCLUSIONS

8.1. Introduction

Some general remarks about the research carried out and the main conclusions obtained by the analyses are presented in this chapter.

The observations on the modeling approaches are given with the aim to define their reliability. Next, the results achieved by the analyses are discussed also with reference to the parametrical analysis extensions. Remarks were given for analyses on different masonry systems made with perforated clay units both reinforced and unreinforced, with different joint typologies.

In addition, observations about feasibility of displacement-based design for masonry are given on the basis of proposed formulae and results of dynamic analyses carried out.

Finally, the open issues, standing from the present work, are described as further possible field which needs further research and investigation.

8.2. About Reliability of Modeling Approaches

8.2.1. FEM Models

Four different types of non-linear models, which follow macro- and micro-modeling strategies and implement isotropic damage or orthotropic plastic criteria for materials, were calibrated. The main mechanical parameters were extracted by common tests, used in practice to characterize materials and simulate actual loading conditions in structural masonry walls, and were applied without arbitrary corrections.

Some simple criteria to evaluate mechanical properties of expanded units in micro-models and to obtain orthotropic parameters from isotropic ones were defined. The first criterion is based on the net area ratio that characterizes masonry cross-sections and influences masonry anisotropy when perforated units are used. The second allows micro-model interface parameters to be found and they can be applied to the analyses without any correction, by systematically introducing the experimental correction due to mortar joint and mortar-unit interface irregularity into the numerical models.

In the case of uniaxial compression, three out of the four models reproduced experimental behavior fairly well. Orthotropic models and the isotropic micro-model are more suitable. Experimental behavior under diagonal compression was properly described only by micro-models, both orthotropic and isotropic. In particular the isotropic micro-model described shear compression tests accurately. The type of test that is being simulated influences the accuracy of numerical results more than masonry type itself. In general, at least one modeling strategy simulated each type of test very well, and allowed differences in stress distribution and behavior due to the type of masonry bond arrangement to be appreciated.

Analyses confirmed that the various test configurations used to study the shear behavior of masonry walls (i.e., diagonal compression and shear compression tests) leads to different stress distributions, clearly, but they also showed that the types of tested masonry could emphasize this effect (i.e. unit dimension and joints arrangements).

8.2.2. Analytical Models

It was built a model for masonry wall (S.D.o.F. structure) under in plane vertical and horizontal forces, able to take in to account the load-displacement capacity curve (also considering non-linear shear deformation) and to reproduce both flexural and shear failures. The model was validated reproducing experimental tests (see 5.4.1 and 5.5.1)

As expected, in general, flexural behavior was fairly well reproduced by model achieving both strength and displacement showed in experimental tests, despite some inconsistencies for unreinforced masonries. However, they can partially be imputed to test variability of masonry specimens themself.

In general, modeled walls are greatly influenced by shear deformation and, obviously, shear deformation is controlled to a great extent by shear modulus (G). Despite this sensitivity, model was in good agreement with experimental G obtained from shear-compression tests and with lower bound of values provided by (Circolare 2/02/2009 n. 617 C.S.LL.PP., 2009). Shear strength formulation adopted was able to correctly forecast experimental walls subjected to shear failure and also, with acceptable approximation, their loads and displacements.

Model was able to describe the achievement of various limit states, which represent the performances of masonry walls relating with cross-section (e.g. when masonry pier reach compressive strength at base section) or whole panel limit states (e.g. when wall reach shear strength provided by masonry).

8.3. About Results of Analyses Carried Out

8.3.1. Unreinforced Masonry systems

Thanks to the methodical modeling approach followed, it was possible to define a reliable modeling strategy for analysis of in-plane loaded masonry, able to reproduce the experimentally observed masonry behavior.

Parametric analyses showed how wall performance under combined shear and compression depend on unit strength and masonry type.

If the ratio of applied vertical load to masonry compressive strength is kept constant, FEM model and analytical model results may differs. Maximum drift may increase at lower unit strength, as vertical load decreases and rocking behavior prevails in FEM analyses; when maximum drift decreases at lower unit strength, without affecting the failure mechanism in analytical analyses. In any case, the displacement capacity of thin-layer joint masonry remains lower than in other masonry types.

In general, maximum horizontal load and drift at ultimate state decrease with unit strength. The decrease in unit strength also corresponds to a change in dominant failure mode, from flexure/rocking to brittle flexure. In all masonry types, critical behavior arises at unit strengths between 10 and 5 N/mm^2. This fact was confirmed with both FEM and Analytical approaches.

Masonry units with compressive strength close to lower limit provided by codes leads to brittle failures with limited load and displacement capacities. Also in this case Italian code appears on the safe side because it fix the limit on the basis of characteristic strength ($f_m > f_{ck} \geq 5$ N/mm^2) when Eurocode 8 fix this limit on the basis of normalized unit strength (for this kind of unit geometry, in accordance with EN 772-1:2000 (2007), result $f_m < f_b \geq 5$ N/mm^2).

To avoid brittle failure vertical load need to be limited in ratio to masonry compressive strength. Italian code (NTC 2008) appears more conservative than Eurocode 8, when provides construction rules for “simple” masonry buildings, because it requires a basic verification of mean storey compressive stress, on contrary Eurocode 8 does not require this control.

Eurocode 8 allows the use of masonry made by mortarless head joints, while in the Italian seismic code (NTC 2008) this is not yet regulated. Although, were taken in to account, e.g. by means of FEM analyses, the actual joint arrangement conditions, results of analyses on masonry systems showed a similar behavior under combined vertical and horizontal loading. Hence, thin layer bed joints and vertical ungrouted joints with mechanical interlocking between masonry system does not present significant differences on global behavior from traditional head and bed joint masonry systems, despite showed lower ductility performances.

8.3.2. Reinforced Masonry Systems

Modeled RM system and experimental results were compared and good agreement was found in terms of load, displacements, failure modes and, for FEM models, also the crack patterns.

Calibrated models were used to carry out parametric analyses in order to investigate the influence of vertical load, slenderness and vertical reinforcement ratio (also horizontal reinforcement ratio with the analytical model) on the behavior of the masonry system under investigation.

Maximum horizontal load capacity of the walls changes, as expected, with the variation of these parameters and their combinations. In general, it was possible to find linear relation between the maximum shear stress and both the vertical load and the vertical reinforcement percentage. Maximum shear stress presented a non-linear decrease with increase of H/L ratio.

Increment of axial load leads to increase of shear capacity at the expense of ductility, in particular related to the post peak phase. Thus, variation of axial load allows to control the failure mode. The same can be said for also vertical reinforcement ratio. Italian code prescription about vertical reinforcement assigns limits both for minimum percentage (0.05% of gross sectional area) and for maximum percentage (1%). In the light of the obtained results, maximum limit appears high to avoid brittle failure modes; even though it is more conservative than Eurocode 8 provisions that indicate only a lower bound limit for vertical reinforcement ratio.

Slenderness ratio influence failure mode and allows to control if shear or flexure prevails. In general, the higher the aspect ratio (slender wall) the higher the ductility, where displacement capacity is concentrated in post peak phase.

In case of no horizontal reinforcement, slender walls showed better drift performances compared to squat walls; even though the latter achieve the best performances, when balanced vertical and horizontal reinforcements were used. In general, the higher horizontal reinforcement ratio the higher displacement capacity, within the analyzed range.

8.4. About Feasibility of Displacement-Based Design for Masonry

8.4.1. Drift limits

Some formulations aimed to provide drifts for unreinforced masonry panels, directly related with limit states model presented in chapter 5 using simple geometrical and mechanical properties, were proposed. They are able to catch both flexural and shear failure drift limits.

The proposed formulae have a complex form; however, they only depend on masonry compressive strength, vertical compression stress and wall slenderness. Therefore, it appears that they follow the engineering criteria generally adopted in DDB design methods. They can be thus regarded as a first indication in the case of unreinforced masonry systems.

8.4.2. Damping

A procedure to evaluate the hysteretic component of Equivalent Viscous Damping (EVD), of both unreinforced and reinforced masonry walls, in relation to masonry drift and ductility is presented in chapter 7.

The results show a general logarithmic trend in drift-damping and ductility-damping curves, with a more linearized trend for walls having small displacement capacity.

The damping at ultimate displacement capacity ranges around 12%-15% for RM and around 10% for URM with soil A. While, damping reaches values around 20%, both RM and URM on soil D.

The comparison of results given by analyses carried out on the basis of experimental and numerical envelopes, shows in one hand, that the hysteretic model applied is robust, and on the other hand, that adopting the numerical envelope curves obtained by means of the developed analytical model (chapter 5) leads to acceptable errors (around 15%).

Finally, the results of the dynamic analyses show that, in the case of RM walls, the ductility-damping curves of walls failed in shear and flexure can be almost superimposed, apart for the higher ductility values available only when flexural failure occurs. Therefore, also in this case the results follow the engineering criteria generally adopted in DDB design methods. They can be thus regarded as a first indication in the case of reinforced masonry systems.

8.5. Future Work and Developments

Further developments of the research carried out on reinforced and unreinforced masonry system could be aimed both at integrating the modeling program and completing the validation part of the present thesis.

Drift formulations at different limit states provided also for reinforced masonry systems would be an immediate development of thesis work.

Next, with the aim of validate and further extend the different modeling approaches, experimental data on different masonry systems available from literature can be drawn. This can be done also in order to further validate and extend both formulation proposed for drift and ductility-damping curves.

Analytical model would be improved introducing at material constitutive level, at one hand, an interaction of non-linear shear deformation effects also including transverse reinforcement (thus, avoiding phenomenological interpretation of them) and on the other hand, a hysteretic law allowing for the modeling under reversed-cyclic loading.

Evaluating both displacements and dynamical effects on whole structure would be another development of presented S.D.o.F. model. This can be useful in the light of DDB design method, which need the displacement profile of structure to be evaluated and to calibrate the damping-ductility curves for the equivalent substitute structure.

9. BIBLIOGRAPHY

(editor) Calvi G. M. (2003) "*Displacement-Based Seismic Design of Reinforced Concrete Buildings*". FIB Bulletin No. 25. 192pp, Lausanne.

(editors) Calvi G. M. and Sullivan T. J. (2009) "*Development of a Model Code for Direct Displacement Based Seismic Design*". Atti di Linea IV, Convegno Finale del progetto RELUIS.: 31pp, Napoli, Italy.

Abrams D. P. (2001) "*Performance-based engineering concepts for unreinforced masonry building structures*". Progress in Structural Engineering and Materials. 3(1): 48-56pp.

Ahmad N., Crowley H., Pinho R. and Ali Q. (2010) "*Simplified formulae for the displacement capacity, energy dissipation, and characteristic vibration period of brick masonry buildings*". Proceedings of the 8IMC-International Masonry Conference. Dresden, Germany, 4-7 July 2010. 11(2), pp. 1385-1394.

Anderson D. L. and Priestley M. J. N. (1992) "*In plane shear strength of masonry walls*". Proceedings of the 6th Canadian Masonry Symposium. Saskatoon, Saskatchewan, Canada, June, 1992. pp 657-662.

Anscombe F. J. (1973) "*Graphs in Statistical Analysis*". The American Statistician. Vol. 27(No. 1): 17-21pp.

Benedetti A. and Steli E. (2008) "*Analytical models for shear-displacement curves of unreinforced and FRP reinforced masonry panels*". Construction and Building Materials. 22(3): 175-185pp.

Benedetti D., Binda L. et al. (1982) "*Comportamento statico e sismico delle strutture murarie*". Clup: Milano.

Bernardini A., Modena C., Lazzaro G. and Valluzzi M. R. (1997) "*Cyclic behaviour and modelling of reinforced masonry panels*". Proceedings of the 11th International Brick/Block Masonry Conference. Shangai, China, October 14-16, 1997.

Bernardini A., Modena C., Turnšek V. and Vescovi U. (1982a) "*A comparison of laboratory test methods used to determine shear resistence of masonry*". Proceedings of the 7th World Conference on Earthquake Engineering. Istambul, Turkey. Vol. 7. pp. 181-184.

Bernardini A., Modena C. and Vescovi U. (1982b) "*An Anisotropic Biaxial Failure Criterion for Hollow Clay Brick Masonry*". International Journal of Masonry Constructions. Vol. 2, no. 4: 165pp.

Bosiljkov V. (2001) "*Failure modes for in-plane mono and biaxially loaded brickwork masonry*". Proceedings of the 9th Canadian Masonry Symposium. Canada. Vol. CD-Rom.

Calderini C. and Lagomarsino S. (2008) "*Continuum Model for In-Plane Anisotropic Inelastic Behavior of Masonry*". ASCE (Journal of Structural Engineering). 134(2)pp.

Cauzzi C., Faccioli E. and Paolucci R. (2008) "*Deliverable D2 – A reference model for prediction of long-period response spectral ordinates*". Project S5 – Seismic input in terms of expected spectral displacements. Convenzione INGV - DPC 2004 – 2006.: 50pp, Politecnico di Milano, Italy.

Ceresa P., Petrini L., Pinho R. and Sousa R. (2009) "*A fibre flexure–shear model for seismic analysis of RC-framed structures*". Earthquake Engineering & Structural Dynamics. 38(5): 565-586pp.

Chaimoon K. and Attard M. M. (2007) "*Modeling of unreinforced masonry walls under shear and compression*". Engineering Structures. 29(9): 2056-2068pp.

Circolare 2/02/2009 n. 617 C.S.LL.PP. (2009) "*Instrucions for Application of DM 14/01/2008 - Technical Standards for Constructions*". Infrastructure Ministry, Official Gazette of the Italian Republic, February, 2 2009.

Cosenza E., Manfredi G. and Verderame G. M. (2006) "*A fibre model for push-over analysis of underdesigned reinforced concrete frames*". Computers & Structures. 84(13-14): 904-916pp.

Costa A. A., Penna A., Magenes G. and Galasco A. (2008) "*Seismic performance assessment of autoclaved aerated concrete (AAC) masonry buildings*". Proceedings of the 14th WCEE. Beijing, China.

da Porto F. (2005) "*In-plane cyclic behavior of thin layer joints masonry walls*". PhD Thesis. University of Trento, February, 2005.

da Porto F., Garbin E., Modena C. and Valluzzi M. R. (2005) "*Failure modes for in plane loaded masonry walls made with thin layer mortar*". Proceedings of the 10th Canadian Masonry Symposium. Banff, Alberta, June 8 - 12, 2005. Vol. CD-Rom.

da Porto F., Grendene M. and Modena C. (2009a) "*Estimation of load reduction factors for clay masonry walls*". Earthquake Engineering & Structural Dynamics. 38(10): 1155-1174pp.

da Porto F., Guidi G., Garbin E. and Modena C. (2010a) "*In-Plane Behavior of Clay Masonry Walls: Experimental Testing and Finite-Element Modeling*". Journal of Structural Engineering. 136(11): 1379-1392pp.

da Porto F., Mosele F. and Modena C. (2009b) "*Reinforced clay masonry walls under shear-compression loads: experimental behaviour*". Proceedings of the 11th Canadian Masonry Symposium, Organized by: McMaster University (Canada). Toronto, Ontario, Canada, May 31 - June 3, 2009. Vol. CD-Rom.

da Porto F., Mosele F. and Modena C. (2010b) "*Compressive behaviour of a new reinforced masonry system*". Materials and Structures: 1-17pp.

da Porto F., Nicolini L., Grendene M. and Modena C. (2009c) "*Modelli di comportamento ciclico ed analisi dinamiche per la valutazione di fattori di riduzione delle forze per muratura armata*". Proceedings of the ANIDIS 2009, Italian National Association of Seismic Engineering. Bologna, Italy, 28th June - 2nd July. Vol. CD-Rom.

De Witte F. and Kikstra W. (2005) "*DIANA finite element analysis. User's manual*". Analysis Procedurespp.

Decanini L., De Sortis A. et al. (2004) "*Performance of Masonry Buildings During the 2002 Molise, Italy, Earthquake*". Earthquake Spectra. 20(S1): S191-S220pp.

Del Piero G. (1983) "*Il consolidamento delle costruzioni*". CISM, Udine.

DISWall. European Community, 2005-2007, COOP-CT-2005-18120. (2008) "*Developing innovative systems for reinforced masonry walls*". Scientific coordinator: C. Modena. University of Padova, http://diswall.dic.unipd.it/.

DM 14/01/2008. (2008) "*Technical Standards for Constructions*". Infrastructure Ministry, Official Gazette of the Italian Republic, February, 4 2008.

Drysdale R. G. and Hamid A. A. (2008) "*Masonry Structures Behavior and Design - 3rd edition*". The Masonry Society: Boulder, Colorado.

EN 772-1: 2000. (2007) "*Methods of test for masonry units - Determination of compressive strength*". European Committee for Standardization, Brussels, Belgium, June 2007.

EN 1992-1-1. (2004) "*Eurocode 2 - Design of concrete structures - Part 1-1: General rules and rules for buildings*". CEN, December 2004.

EN 1996-1: 2005. Eurocode 6. (2005) "*Design of masonry structures - Part 1-1: General rules for reinforced and unreinforced masonry structures*". European Committee for Standardization, Brussels, Belgium.

EN 1996-2: 2006. Eurocode 6. (2006) "*Design of masonry structures - Part 2: Design considerations, selection of materials and execution of masonry*". European Committee for Standardization, Brussels, Belgium.

EN 1998-1: 2004. Eurocode 8. (2004) "*Design of Structures for Earthquake Resistance. Part 1: General Rules, Seismic Actions and Rules for Buildings*". European Committee for Standardization, Brussels, Belgium.

EN 1998-3: 2005. Eurocode 8. (2005) "*Design of Structures for Earthquake Resistance. Part 3: Strengthening and Repair of Buildings*". European Committee for Standardization, Brussels, Belgium.

ESECMaSE. European Community, 2005-2007. (2008) "*Enhanced Safety and Efficient Construction of Masonry Structures in Europe*", http://www.esecmase.org.

Feenstra P. H. (1993) "*Computational Aspects of Biaxial Stress in Plain and Reinforced Concrete*". Ph.D. Thesis. Delft University of Technology. Delft, The Netherlands

FIP CEB. (1991) "*Model Code 90–Design Code*". CEB Comite Euro-International du Betonpp.

Gambarotta L. and Lagomarsino S. (1997a) "*Damage model for the seismic response of brick masonry shear walls. Part I: the mortar joint model and its applications*". Earthquake Engineering & Structural Dynamics. 26(4): 423-439pp.

Gambarotta L. and Lagomarsino S. (1997b) "*Damage model for the seismic response of brick masonry shear walls. Part II: the continuum model and its applications*". Earthquake Engineering & Structural Dynamics. 26(4): 441-462pp.

Ganz H. and Thürlimann B. (1982) "*Tests on the biaxial strength of masonry*". Report 7502-4, Inst. Of Struct. Engrg.pp, ETH Zurich, Zurich, Switzerland

Ganz H. and Thürlimann B. (1984) "*Test on masonry walls under normal and shear loading*". Report No. 7502-4, Inst. Of Struct. Engrg.pp, ETH Zurich, Zurich, Switzerland.

Giambanco G., Rizzo S. and Spallino R. (2001) "*Numerical analysis of masonry structures via interface models*". Computer Methods in Applied Mechanics and Engineering. 190(49-50): 6493-6511pp.

Giuffrè A. (1980) "*Requisiti delle costruzioni in muratura nelle zone sismiche*". Proceedings of the 15th Congress of ANDIL (italian association of clay brick and tile producers). Italy.

Guedes J. and Pinto A. V. (1997) "*A numerical model for shear dominated bridge piers*". Proceedings of the Second Italy–Japan Workshop on Seismic Design and Retrofit of Bridges. Rome, Italy.

Guidi G. (1954) "*Confronto di resistenze fra murature in mattoni pieni e semipieni con vari tipi di malta*". L'industria italiana dei laterizi. n° 1pp.

Guidi G. (2006) "*Sistemi di muratura portante in laterizio: calibrazione di modelli numerici sulla base di risultati sperimentali*". Graduation Thesis. Dept of Structural and Trasportation Engineering, University of Padova. Padua, December 2006.

Gulkan P. and Sozen M. A. (1974) "*Inelastic response of reinforced concrete structures to earthquake motions*". ACI Journal. Vol. 71(No.12): 604-610pp.

Hamid A. A. and Drysdale R. G. (1980) "*Concrete Masonry Under Combined Shear and Compression Along the Mortar Joints*". ACI Journal. 77(5): 314-320pp.

Hamid A. A. and Drysdale R. G. (1981) "*Proposed Failure Criteria for Concrete Block Masonry under Biaxial Stresses*". Journal of the Structural Division, ASCE. 107(8): 1675-1687pp.

Hegermeir G. A., Nunn R. O. and Arya S. K. (1978) "*Behaviour of concrete masonry under biaxial stresses*". Proceedings of the North American Masonry Conference, University of Colorado. Boulder, USA. 1.1-1.28.

Hendry E. A. W. (2001) "*Masonry walls: materials and construction*". Construction and Building Materials. 15(8): 323-330pp.

Jiang H. and Kurama Y. (2010) "*Analytical Modeling of Medium-Rise Reinforced Concrete Shear Walls*". pp.

Kent D. C. and Park R. (1971) "*Flexural members with confined concrete*". Journal of Structural Engineering. 97(7): 1964-1990pp.

Lagomarsino S., Galasco A. and Penna A. (2007) "*Non-linear macro element dynamic analysis of masonry buildings*". Proceedings of the ECCOMAS Thematic Conference on Computational Methods in Sructural Dynamics and Earthquake Engineering. Rethymno, Greece, 13-16 June 2007. Vol. CD-Rom.

Latina C. (1999) "*Murature in laterizio e resistenza sismica*". Costruire in Laterizio, May-June 1999. 69, pp56-69, bi-mountly.

Lotfi H. R. and Shing P. B. (1994) "*Interface Model Applied to Fracture of Masonry Structures*". ASCE (Journal of Structural Engineering). 120(1): 63pp.

Lourenço P. B. B. (1996a) "*Computational strategies for masonry structures*". PhD-Thesis. Delft University of Technology. Delft, 1996.

Lourenço P. B. B. (1996b) "*A user/programmer guide for the micro-modelling of masonry structures*". Report. 3(1.31): 35pp.

Lourenço P. B. B., De Borst R. and Rots J. G. (1997) "*A plane stress softening plasticity model for orthotropic materials*". International Journal for Numerical Methods in Engineering. 40(21): 4033-4057pp.

Lourenço P. B. B. and Rots J. G. (1997) "*Multisurface Interface Model for Analysis of Masonry Structures*". Journal of Engineering Mechanics. 123(7): 660-668pp.

Magenes G. (2006) "*Masonry building design in seismic areas: Recent experiences and prospects from a European standpoint - Keynote 9*". Proceedings of the 1st European Conference on Earthquake Engineering and Engineering Seismology, SYMPORG SA. Geneva, Switzerland, 3-8 September 2006. Vol. CD-Rom.

Magenes G. (2010) "*Earthquake resistant design of masonry structures: rules, backgrounds, latest findings*". Proceedings of the 8th International Masonry

Conference, Organized by: International Masonry Society and Technische Universitat Dresden. Dresden, Germany, 4-7 July 2010. Vol. CD-Rom. 29-45.

Magenes G., Calvi G. and Gaia F. (1996) "*Shear tests on Reinforced Masonry Walls.*". Report RS-03/96. Department of Structural Engineering, University of Paviapp, Pavia.

Magenes G. and Calvi G. M. (1997) "*In-plane seismic response of brick masonry walls*". Earthquake Engineering & Structural Dynamics. 26(11): 1091-1112pp.

Magenes G. and Della Fontana A. (1998) "*Simplified Non-linear Seismic Analysis of Masonry Buildings*". Proceedings of the British Masonry Society, October 1998. 8. 190-195.

Magenes G., Morandi P., Penna A. and Ferrata V. (2008) "*D 7.1 c Test results on the behaviour of masonry under static cyclic in plane lateral loads*". pp.

Magenes G., Remino M. et al. (2006) "*SAM II, Software for the Simplified Seismic Analysis of Masonry buildings*". University of Pavia and EUCENTRE.

Marini A. and Spacone E. (2006) "*Analysis of Reinforced Concrete Elements Including Shear Effects*". ACI Structural Journal. 103(5): 645-655pp.

Marmo F. (2008) "*A fiber-free approach to the inelastic analysis of reinforced concrete structures*". pp.

Matsumura A. (1988) "*Shear strength of reinforced masonry walls*". Proceedings of the 9th Worrld Conference of Earthquake Engineering. Tokyo, Japan, August 2-6, 1988. Vol. 6. pp. 121-126.

Moehle J. P. (1992) "*Displacement-based design of RC structures subjected to earthquakes*". Earthquake Spectra. 8(3): 403-428pp.

Morandi P. and Magenes G. (2008) "*Seismic Design of Masonry Buildings: Current Procedures and New Perspectives*". Proceedings of the 14 th World Conference on Earthquake Engineering, International Association for Earthquake Engineering. Beijing, China, October 12-17, 2008.

Mosele F. (2004) "*Comportamento meccanico della muratura: sperimentazione e modellazione*". Degree Thesis. Department of Structural and Trasportation Engineering, University of Padova. Padova, Italy.

Mosele F. (2009) "*In-Plane And Out-Of-Plane Cyclic Behaviour of Reinforced Masonry Walls*". PhD Thesis. University of Trento, March, 2009.

Mosele F., da Porto F., dalla Benetta M. and Modena C. (2008) "*Experimental behaviour of newly developed systems for load bearing reinforced masonry walls*". Proceedings of the 14th International Brick and Block Masonry Conference, Organized by: The University of Newcastle - Australia. Sydney, Australia, February 17-20, 2008. Vol. CD-Rom.

Mostafaei H. and Vecchio F. J. (2008) "*Uniaxial Shear-Flexure Model for Reinforced Concrete Elements*". Journal of Structural Engineering. 134(9): 1538-1547pp.

Ordinanza P.C.M. n. 3274: 2003. (2005) "*Norme tecniche per il progetto, la valutazione e l'adeguamento sismico degli edifici*". - and following updating, Official Gazette of the Italian Republic, March, 20 2003.

Page A. W. (1980) "*A biaxial failure criterion for brick masonry in the tension-tension range*". Int. J. Masonry Constr. 1(1): 20-29pp.

Page A. W. (1981) "*The biaxial compressive strength of brick masonry*". Proc. Inst. Civ. Eng. Pt. 2 71,(Sept), 893, 1981pp.

Page A. W. (1982) "*An experimental investigation of the biaxial strength of brick masonry*". Proceedings of the 6th IBMAC. Rome, Italy. 3-15.

Page A. W. (1983) "*The strength of brick masonry under biaxial compression-tension*". Int. J. Masonry Constr. 3(1): 26-31pp.

Paulay T. and Priestley M. J. N. (2009) "*Seismic Design of Reinforced Concrete and Masonry Buildings - Chapt. 7: Masonry Structures*". John Wiley & Sons, Inc.

Petrangeli M., Pinto P. E. and Ciampi V. (1999) "*Fiber Element for Cyclic Bending and Shear of RC Structures. I: Theory*". Journal of Engineering Mechanics. 125(9): 994-1001pp.

Priestley M. J. N. (1986) "*Flexural strengthening of rectangular unconfined masonry shear walls with distribuited reinforcement*". Journal of Masonry Society. 5(2)pp.

Priestley M. J. N. (1993) "*Myths and Fallacies in Earthquake Engineering – Conflicts Between Design and Reality*". Bulletin of NZ National Society for Earthquake Engineering, New Zealand. Vol.26, No.3, 329-341pp.

Priestley M. J. N. and Bridgeman D. O. (1974) "*Seismic resistance of brick masonry walls*". Bulletin of NZ National Society for Earthquake Engineering, New Zealand. Vol. 7, No.4, Wellingstone: 167-178pp.

Priestley M. J. N., Calvi G. M. and Kowalsky M. J. (2007) "*Displacement Based Seismic Design of Structures*": Pavia, Italy.

Priestley M. J. N., Verma R. and Xiao Y. (1994) "*Seismic Shear Strength of Reinforced Concrete Columns*". Journal of Structural Engineering. 120(8): 2310-2329pp.

Roca P. (2006) "*Assessment of masonry shear-walls by simple equilibrium models*". Construction and Building Materials. 20(4): 229-238pp.

Rots J. G. (1997) "*Structural masonry an experimental/numerical basis for practical design rules*". Balkema: Rotterdam, The Netherlands.

Samarasinghe W. and Hendry A. W. (1980) "*The strength of brickwork under biaxial tensile and compressive stress*". Proceedings of the International Symposium on Load-Bearing Brickwork. London, UK. 129-139.

Saritas A. and Filippou F. C. (2009) "*Inelastic axial-flexure-shear coupling in a mixed formulation beam finite element*". International Journal of Non-Linear Mechanics. 44(8): 913-922pp.

Shibata A. and Sozen M. A. (1976) "*Substitute Structure Method for Seismic Design in Reinforced Concrete*". Journal of the Structural Division, ASCE. Vol. 102(No. ST1)pp.

Shing P. B., Brunner J. and Lofti H. R. (1993) "*Evaluation of shear strength of reinforced masonry walls*". Journal of Masonry Society. 12(1): 61-76pp.

Shing P. B., Schuller M. and Hoskered V. S. (1990) "*Strength and ductility of reinforced masonry shear walls*". ASCE (Journal of Structural Engineering). 116(3): 619-640pp.

Spacone E., Filippou F. C. and Taucer F. F. (1996) "*Fibre beam-column model for non-linear analysis of R/C frames: part I. Formulation*". Earthquake Engineering & Structural Dynamics. 25(7): 711-725pp.

Sullivan T. J., Calvi G. M., Priestley M. J. N. and Kowalsky M. J. (2003) "*The limitations and performances of different displacement based design methods*". Journal of Earthquake Engineering. 7(2003): 201pp.

Sveinsson B. I., Mayes R. L. and McNiven H. D. (1985) "*Cyclic loading of masonry single piers*". Earthquake Engineering Research Center. Vol-4, Additional test with height to width ratio of 1, Rep. No. UCB/EERC-85/15: 90pp, Berkley, California, US.

Tassios T. P. (1988) "*Meccanica delle murature*". Liguori Editore: Napoli.

Tassios T. P., Vintzileou E. and Trohanis A. (1984) "*Reinforced masonry squat walls under horizontal monotonic and cyclic loading*". Proceedings of the 8th World Conference on Earthquake Engineering (WCEE). San Francisco, US, 21-28 July 1984. pp 565-572.

Taucer F. F., Spacone E. and Filippou F. (1991) "*A fiber beam-column element for seismic response analysis of reinforced concrete structures*". Report EERC. 91: 17pp.

Tomaževič M. (1978) "*The computer program POR*". Report of ZRMK.: 42pp, Ljiubliana, Slovenia.

Tomaževič M. (1999) "*Earthquake-resistant design of masonry buildings*". Imperial college press London.

Tomaževič M. (2009) "*Shear resistance of masonry walls and Eurocode 6: shear versus tensile strength of masonry*". Materials and Structures. 42(7): 889-907pp.

Tomaževič M. and Lutman M. (1988) "*Seismic resistance of reinforced masonry walls*". Proceedings of the 9th World Conference on Earthquake Engineering Tokyo-Kyoto, Japan, August 2-9, 1988. Vol. VI. pp. 97-102.

Tomaževič M. and Lutman M. (1996) "*Seismic Behavior of Masonry Walls: Modeling of Hysteretic Rules*". Journal of Structural Engineering. 122(9): 1048-1054pp.

Tomaževič M. and Lutman M. (1997) "*Influence of reinforcement and block strength on seismic behavior of reinforced masonry walls*". Proceedings of the 11th International Brick/Block Masonry Conference, Tongji University. Shangai, China, October 14-16. Vol. 14. pp.217-226.

Tomaževič M., Lutman M. and Bosiljkov V. (2006) "*Robustness of hollow clay masonry units and seismic behaviour of masonry walls*". Construction and Building Materials. 20(10): 1028-1039pp.

Tomaževič M., Lutman M. and Petcovič L. (1996) "*Seismic Behavior of Masonry Walls: Experimental Simulation*". ASCE (Journal of Structural Engineering). vol. 122(n.9): 1040-1047pp.

Tomaževič M. and Weiss P. (2010) "*Displacement capacity of masonry buildings as a basis for the assessment of behavior factor: an experimental study*". Bulletin of Earthquake Engineering. 8(6): 1267-1294pp.

Turnšek V. and Čačovič F. (1971) "*Some experimental results on the strength of brick masonry walls*". Proceedings of the 2nd International Brick Masonry Conference, Stoke on Trent ,British Ceramic Research Association. London, UK. pp.149-156.

UNI EN 1052-3. (2007) "*Methods of test for masonry - Determination of initial shear strength*". Ente Nazionale Italiano di Unificazione (UNI).

van Zijl G. P. A. G. (2004) "*Modeling Masonry Shear-Compression: Role of Dilatancy Highlighted*". Journal of Engineering Mechanics. 130(11): 1289-1296pp.

Vecchio F. J. and Collins M. P. (1986) "*The modified compression field theory for reinforced concrete elements subjected to shear*". ACI Journal. 83(22): 219-231pp.

Vermeltfoort A. T. (2005) "*Brick–mortar interaction in masonry under compression*". Ph.D. Thesis. Eindhoven University of Technology. Eindhoven, the Netherlands.

Voon K. C. and Ingham J. M. (2007) "*Design Expression for the In-Plane Shear Strength of Reinforced Concrete Masonry*". Journal of Structural Engineering. 133(5): 706-713pp.

Wakabayashi M. and Nakamura T. (1984) "*Reinforcing principle and seismic resistance of brick masonry walls*". Proceedings of the 8th World Conference on Earthquake Engineering (WCEE). San Francisco, US, 21-28 July 1984. pp. 661–668.

Wilcox R. R. (2005) "*Introduction to Robust Estimation and Hypothesis Testing, Second Edition (Statistical Modeling and Decision Science)*". Academic Press.